Universidade de Aveiro
2022

ISABEL MARINHO CARVALHO BJØRGE

Micro-scaffolds avançados injectáveis para engenharia de tecido ósseo

Advanced injectable micro-scaffolds for modular bone tissue engineering

/

Universidade de Aveiro
2022

ISABEL MARINHO CARVALHO BJØRGE

Micro-scaffolds avançados injectáveis para engenharia de tecido ósseo

Advanced injectable micro-scaffolds for modular bone tissue engineering

Tese apresentada à Universidade de Aveiro para cumprimento dos requisitos necessários à obtenção do grau de Doutor em Ciência e Engenharia de Materiais, realizada sob a orientação científica do Doutor João F. Mano, Professor Catedrático do Departamento de Química da Universidade de Aveiro, e Doutora Clara R. Correia, Investigadora Doutorada, Diretora de Investigação na Tech4Med.

Modalidade alternativa à apresentação de Tese, nos termos do artigo 63.º e 64.º do Regulamento de Estudos da Universidade de Aveiro.

Financial support by the Portuguese Foundation for Science and Technology (FCT) with doctoral grant SFRH/BD/129224/2017. Financed by national funds (OE) through FCT/MCTES in the scope of the projects “TETRISSUE” (PTDC/BTM-MAT/3201/2020), and “CIRCUS” (PTDC/BTM-MAT/31064/2017), supported by the Programa Operacional Competitividade e Internacionalização, in the component FEDER (POCI-01-0145-FEDER-031064 and POCI-01-0145-FEDER-031210). Supported by the European Research Council grant agreement for the project “ATLAS” (ERC-2014-ADG-669858) and developed within the scope of the project CICECO-Aveiro Institute of Materials, UIDB/50011/2020 & UIDP/50011/2020, financed by national funds through the FCT/MEC and when appropriate co-financed by FEDER under the PT2020 Partnership Agreement. Apoio financeiro da FCT e do FSE no âmbito do III Quadro Comunitário de Apoio.

To my mother, who will probably try to read this.

o júri

Presidente

Doutor **Vasile Staicu**
professor catedrático da Universidade de Aveiro

Vogais

Doutora **Jenneke Klein Nulend**
professora catedrática, Universidade de Amesterdão

Doutor **João Filipe Colardelle da Luz Mano** (orientador)
professor catedrático da Universidade de Aveiro

Doutora **Cristina Carvalho Barrias**
investigadora principal, Universidade do Porto

Doutora **Ana Maria Pissarra Coelho Gil**
professora associada, Universidade de Aveiro

Doutor **Nicholas Agung Kurniawan**
professor assistente, Eindhoven University of Technology

Acknowledgement

I am happily presenting this doctoral thesis because of several people who believed in me and coached me towards success – to them I am extremely grateful.

I acknowledge my supervisors, Professor João Mano and Doctor “Chefinha” Clara Correia. I thank them for their leadership and support over the years, and for giving me the best possible conditions. It has been a privilege to work with them and I am a better researcher today because of them.

I also want to thank the remainder of the COMPASS Research Group – the initial “Texugos”, who welcomed me as their own, and everyone else who came along as the years went by. A special appreciation for Paulo, our lab technician, who guaranteed everything was running smoothly. I especially want to thank Sara Nadine, my PhD accomplice, Sara Vilabril, for being my greatest cheerleader, Marta Maciel, for her contagious love of research, and Sofia Silva, for being a big sister in science.

From my time in Boston, I thank Professor Christopher Chen for accepting me in his lab during difficult pandemic times, and I thank Subra Sundaram for teaching me novel techniques and thinking outside the box. To Diana, thank you for being my weekend buddy, fellow foodie, and always going along with my crazy plans.

I cannot begin to express my gratitude towards my mother, my role model, the person who supports me the most and always drives me to do better. To my grandparents, Lisa e Velino, I thank them for ever encouraging me and giving me the tools to thrive. To my aunt, Cristina, who actually guided me towards biomedical engineering – without her, I would probably be studying rocks right now, not that there is anything wrong with that, cells are just more interactive. I thank my father, Bestemor og Bestefar, for their continued support and for always being there. I thank my not-so-little rascals, João, Hedda, and Birk.

To Carlos, my partner in crime, my best friend, I thank you for your patience and for always making me laugh when I need my spirit lifted.

palavras-chave

Engenharia de tecidos, biomateriais, mecanotransdução, propriedades biofísicas, tecido ósseo, topografia de superfície, osteogénese, angiogénese

Resumo

A estrutura e organização do tecido nativo são aspetos chave que condicionam o funcionamento a nível celular. As estratégias baseadas em sinais geométricos e topográficos são opções atrativas para controlar e guiar o comportamento celular. No entanto, estas estratégias estão limitadas a contextos 2D, que não mimetizam o ambiente celular nativo. Microestruturas com propriedades físicas manipuladas surgem para modular o ambiente 3D em estratégias celulares, para engenharia de tecidos, e como veículos para aplicações sem células. Com foco em sinais geométricos, o ajuste do rácio área de superfície e volume de partículas de hidrogel esferoidais com circularidade ajustável influencia a cinética de libertação de substâncias ativas, bem como o comportamento celular, sendo por isso utilizadas como plataformas para libertação controlada e encapsulamento de células. Com foco em sinais topográficos, um modelo quasi-3D de cultura sandwich, que permite um estímulo ventral e dorsal da célula, permitiu analisar o efeito da topografia e respetiva orientação relativa de modo simultâneo e independente em ambos os lados da célula. Este estudo permitiu expor o efeito impactante do contacto inicial para guiar a resposta celular em estratégias de engenharia de tecidos usando estratégias de mecanotransdução. Independentemente, microestruturas 3D discoides com topografia superficial de nanoranhuras (topodiscs) foram concebidos e produzidos, para aplicação em estratégia “bottom-up”, mediada por células. Aplicados em engenharia de tecido ósseo, topodiscs levaram a um aumento da proliferação celular e permitiram a formação de agregados semelhantes ao osso, sem requerer fatores osteoindutivos. Quando combinados com uma co-cultura de células estaminais/estromais e células endoteliais dentro de cápsulas liquefeitas, os topodiscs demonstraram um grande potencial em induzir osteogénese e estimular a criação de pré-vascularização. Conjuntamente, os estudos efetuados elucidam a importância dos sinais biofísicos para estratégias de medicina regenerativa e ilustram como obter uma histoarquitetura funcional poderá estar dependente da combinação de microestruturas com geometrias e sinais topográficos definidos.

keywords

Tissue engineering, biomaterials, mechanotransduction, biophysical cues, bone tissue, surface topography, osteogenesis, angiogenesis

abstract

Structure and organization are key aspects of the native tissue environment, which ultimately condition cell fate. Engineered geometrical and topographical cues appear as attractive options to control and guide cell behavior, yet such strategies are limited to a 2-dimensional approach, which differs from the native cell environment. Physically tuned microcarriers appear as attractive vehicles for cell-based tissue engineering strategies aiming to modulate this 3D environment, but also as vehicles for cell-free applications. On the geometry side, the varying surface area to volume ratio of designed spheroidal hydrogel particles with adjustable circularity was proven to impact drug release and cell viability, demonstrating its applicability for drug delivery or as cell encapsulation platforms. On the topography side, the developed quasi-3D sandwich culture model, enabling both ventral and dorsal cell surface stimulation, allowed to study the effect of grooved surface topography in a simultaneous and independent manner on two cell sides. Here, the pivotal role of initial cell-biomaterial contact on cellular alignment was highlighted, providing important insights for tissue engineering strategies aiming to guide cellular response through mechanotransduction approaches. In turn, 3D disc-shaped microcarriers featuring nanogrooved surface topography (topodiscs) were designed and produced, aiming to be applied as a bottom-up cell-mediated strategy. Applied to bone tissue engineering, topodiscs were shown to enhance cell proliferation and direct the formation of bone-like aggregates, even in the absence of osteoinductive factors. When combined with co-culture of stem/stromal cells and endothelial cells within liquefied core capsules, topodiscs demonstrated great potential in not only directing osteogenic, but also in the achieving a pre-vascularized construct. Taken together, our studies highlight the importance of physical cues in regenerative medicine strategies and illustrate how achieving a functional histoarchitecture may depend on a combination of fine-tuned geometrically shaped microcarriers presenting intricately tailored topographical cues.

Table of Contents

Section 3: Results & Discussion

Section 4: Conclusion

List of Abbreviations and Acronyms

0-9	
2D	Two-dimensional
3D	Three-dimensional
A	
ACN	Acetonitrile
AHSG	α2-HS glycoprotein
ALG	Alginate
α-MEM	Minimum Essential Medium Eagle - Alpha Modification
B	
BAS	Basal cell culture medium (no osteogenic factors)
BMP-2	Bone morphogenetic protein-2
BP	Biological Process
BSA	Bovine serum albumin
C	
$CaCl_2$	Calcium chloride
$CaCO_3$	Calcium carbonate
CD	Optical media substrate
CHT	Chitosan
CO	Co-culture
COL1A2	Collagen type I α2
CVD	Chemical vapour deposition
D	
DEX	Dexamethasone
DReg-TopoBAS	Downregulated proteins by topography in basal medium
DReg-TopoOST	Downregulated proteins by topography in osteogenic medium
ds	Double-stranded
E	
EBL	Electron beam lithography
EC	Endothelial cell
ECM	Extracellular matrix
EDTA	Ethylenediamine tetraacetic acid
ELISA	Enzyme-linked immunosorbent assay
ERK–MAPK	Extracellular signal-regulated kinase–mitogen-activated protein kinase
F	
FA	Focal adhesion
F-actin	Actin filaments
FAK	Focal adhesion kinase
FBS	Fetal bovine serum
Flat microdiscs	Microdiscs without grooves
FTIR-ATR	Fourier Transformed Infrared Spectroscopy – Attenuated Total Reflectance
G	
GO	Gene ontology
GTPases	Small guanosine triphosphate hydrolases
H	
hASCs	Human adipose-derived stromal cells
HCD	High-energy collisional dissociation
hFOB	Human fetal osteoblastic cells
hMSC	Human mesenchymal stromal cells
HUVECs	Human umbilical vein endothelial cells
I	
IBL	Ion beam lithography

L	
LbL	Layer-by-Layer
LUM	Lumican
M	
MC3T3-E1	Pre-osteoblastic cell line
MF	Molecular Function
MLC	Myosin light-chain II
MONO	Monoculture
MTS	3-(4,5-dimethylthiazol-2-yl)5-(3-carboxymethoxy-phenyl)-2-4-sulfophenyl)-2- 4-sulfophenyl)-2H-tetrazolium
MVs	Extracellular microvesicles
MYH9	Myosin-9
N	
NaCl	Sodium chloride
nanoESI	Nanoelectrospray ionization
nanoLC-MS/MS	Nano Liquid Chromatography coupled to tandem Mass Spectrometry
O	
OSP	Osteopontin
OST	Cell culture medium supplemented with osteogenic factors
P	
PBS	Phosphate-buffered saline
PCL	Poly(ε-caprolactone)
PEG	Poly(ethylene glycol)
PEG-DA	Poly(ethylene glycol) diacrylate
Pen-strep	Penicillin-streptomycin
pFAK	Phosphorylated focal adhesion kinase
PLL	Poly(L-lysine)
PP	Polypropylene
PVA	Poly(vinyl alcohol)
R	
ROCK	RhoA kinase
RT	Room temperature
S	
SEM	Scanning electron microscopy
SW	Sandwich
T	
TAZ (or WWTR1)	Transcriptional coactivator with PDZ-binding motif
TCEP	Tris-(2-carboxyethyl)-phosphine
TE	Tissue engineering
TEOS	Tetraethyl orthosilicate
TERM	Tissue Engineering and Regenerative Medicine
THBS1	Thrombospondin-1
Topodisc	Nanogrooved microdisc
U	
UReg-TopoBAS	Upregulated proteins by topography in basal medium
UReg-TopoOST	Upregulated proteins by topography in osteogenic medium
UV	Ultraviolet
μCT	Microtomography
μSphere	Spherical microparticle
V	
VEGF	Vascular endothelial growth factor
vWF	von Willebrand Factor
Y	
YAP	Yes-associated protein

List of Tables

Section 1: General Introduction

Section 3: Results & Discussion

Table VI.S5. Microvesicles' proteins upregulated by topography in osteogenic medium (UReg-TopoOST). Abundance ratio, ratio of the relative protein abundance in the topodiscs condition against the μspheres condition. Abundance ratios of 100: proteins only detected in topodiscs condition and not in μspheres condition. Proteins were considered significantly upregulated by Volcano plot analysis: abundance ratio > 2 and p-value < 0.05.

Table VI.S6. Microvesicles' proteins downregulated by topography in osteogenic medium (DReg-TopoOST). Abundance ratio, ratio of the relative protein abundance in the topodiscs condition against the μspheres condition. Abundance ratios of 0.01: proteins only detected in μspheres condition and not in topodiscs condition. Proteins were considered significantly downregulated by Volcano plot analysis: abundance ratio < 0.05 and p-value < 0.05.

List of Figures

Section 1: General Introduction

Chapter I. Exploring topography and geometry of non-spherical microcarriers in biomedical applications – a review

with light-induced drug. C. Geometry-dependent assembly of "daughter/parent" particles for localised cell transfection.

Section 2: Materials & Methods

Chapter II. Experimental methodologies and materials

Scheme II.1. Illustration of the production method for topodiscs. I. Production of polyvinyl alcohol (PVA) counter-moulds of CDs by solvent evaporation of a 12% w/v PVA solution at 40ºC. II. Production of PCL particles via oil/water emulsion and subsequent sieving to collect particles with diameters comprised between 25-40 μm microparticles ($\mu spheres_{25\text{-}40}$) by sieving. III. Micro-moulding of $\mu spheres_{25\text{-}40}$ between nanogrooved PVA membranes at an optimised applied force, time, and temperature. IV. Successive topodisc washings to remove all traces of PVA. V. Topodisc recovery by centrifugation.

Scheme II.2. Schematic representation of the production method of liquefied-core, multi-layered capsules. I. Dropwise addition of ALG solution containing core components (illustrated: hASC and topodisc microaggregates, combined with suspended HUVECs) into an aqueous calcium chloride solution. II. ALG bead collection and sequential immersion in PLL, ALG, CHT, and ALG solutions to obtain a 12-layered membrane. III. ALG core liquefaction with EDTA. IV. Ultimately, core contents are remodelled to for a microtissue.

Section 3: Results & Discussion

Chapter III. Tuneable spheroidal hydrogel particles for cell and drug encapsulation

Figure III.1. Schematic representation of oblate spheroidal particle production method. Inset: Axis (*x, y, z*) and semi-axis (*a, c*) representation. M-CHT liquid precursor was squeezed between superamphiphobic surfaces separated using a known spacer height, followed by UV-crosslinking. Representative SEM image of topographical features present on superamphiphobic surfaces (scale bar corresponding to 10 μm).

Figure III.2. A: Geometry predicted by numerical studies of the shape of the elastic liquid droplet upon deformation. B: Effect of decreasing spacer height on particle format. Dotted

red lines correspond to the profiles of predicted particle geometry by numerical studies. C: Spheroidal particle shape acquired upon removal of upper superamphiphobic surface. Dotted green lines correspond to the *yz* plane representation of spheroids. The particle on the left was used as a spherical control with no deformation and was only in contact with the lower superamphiphobic surface. Increasing deformation was used for the following particles. Scales bars on both sets of images correspond to 1 mm.

Figure III.3. Effect of chitosan concentration on UV-crosslinked spheroidal particles. Particles were produced with concentrations of 2, 3, and 4%, and with equal deformations of 0, 48, 62, and 76%. Scale bars correspond to 1 mm.

Figure III.4. Correlation of particle deformation with circularity (•, n>8) and surface area (▪, n>4). The values of circularity and surface area were obtained from particle images. Second order polynomial fittings are represented only as guidelines for the eye.

Figure III.5. A: Cumulative BSA release from 2% M-CHT spheres (•) and spheroids (62% deformation) (▪), up to 216 hours, with a zoom-in for the initial 2 hours (n=3). Values plotted are the mean ± error for 3 samples. Both experimental and curve fittings using Korsmeyer-Peppas equation are presented in the figure (lines with the same colour of the corresponding symbols). Statistical significance of $p<0.05$ (*), $p<0.01$ (**), and $p<0.001$ (***) are represented for time-points when applicable. B: Numerical modelling studies for the release of a compound from spherical versus spheroidal particles with varying particle height. Variation in height of spheroidal particles (¾, ½, and ¼) is presented relatively to spherical particles, corresponding to 1.

Figure III.6. Live/Dead assay of L929 cells encapsulated within 2% M-CH particles 24 hours after seeding. Spherical (0%) and spheroidal (48%, 62%, and 76%) particles are represented. A: Top views of particles and image magnifications in inset. Scale bars correspond to 750 μm for main images, and 440 μm for inset images. B: Quantification of the relative number of live cells per condition.

Chapter IV. Cell behaviour within nanogrooved sandwich culture systems

Scheme IV.1. Schematic representation of the different assembly conditions tested. MC3T3-E1 cells were seeded on polystyrene substrates with or without grooves and placed in

sandwich-culture (SW) conditions. Cell seeding was performed on lower substrates unless marked with a star symbol. Relative orientations correspond to the angle between the nanogrooves of the upper and lower substrates. [Box 1] Control conditions without (A) or with (B) nanogrooves. [Box 2] SW conditions with cell-seeded lower substrates (single-seeding). The orientation of the nanogrooves between the upper and lower substrates is varied between 0º (C) and 90º (D). SW conditions with both substrates without nanogrooves (E) or presenting the nanogrooves on the upper (F) or lower (G) substrate. [Box 3] SW conditions with cell-seeded upper substrates (single-seeding). SW conditions with relative orientation of 0º (H) or 90º (I), and upper (J) or lower (K) grooved substrates. [Box 4] SW conditions with cell-seeded upper and lower substrates (double seeding). Cells adhered to upper or lower substrates are stained with DiO (green) or DiD (red) lipophilic dyes, respectively. SW conditions with the grooves only on the upper substrate (L), or with relative orientations of 0º (M) or 90º (N).

Figure IV.1. MC3T3-E1 cells seeded on 2D substrates or in SW conditions. F-actin stained in red and cell nuclei in blue. Cells seeded on lower substrates unless marked with a star. Images correspond to the substrate where cells were seeded (50 μm scale bars). Cells painted in red in SEM images for conditions (A) and (B) (20 μm scale bars). White dotted lines indicate nanogroove orientation of cell seeded substrates.

Figure IV.2. Analysis of 2D substrates ((A) and (B)) and single-seeded SW conditions ((C)-(K)). I. Orientation color-coded F-actin and corresponding orientation plots (n=2), ranging from -90 to 90º (circular color-coding map inset) (100 μm scale bars). Cells seeded on lower substrates unless marked with a star. White dotted lines indicate nanogroove orientation of cell seeded substrates. II. Cells for conditions (B) and (C) stained with vinculin (red) and nuclei (blue), with corresponding orthogonal views (left) and counterstaining of F-actin in green (right). III. Quantification via ELISA of total FAK (ng/mL) and phosphorylation of FAK at Tyr-397 (units/mL) for conditions (B) and (C) ($n \geq 11$) with corresponding pFAK/FAK ratio. Statistical significance of $p \leq 0.0001$ (****). IV. Cell elongation factor ($n \geq 8$). Statistical significance of $p \leq 0.05$ (*), $p \leq 0.01$ (**) and $p \leq 0.001$ (***) are represented when applicable. Statistical significance was observed between condition (B) and every other condition except (C), represented with # to facilitate reading.

Figure IV.3. Double-seeded SW conditions (L)-(N) (100 μm scale bars). I. Confocal images of closed sandwich conditions: DiO (green) and DiD (red) stained cells, previously seeded on upper and lower substrates, respectively, with corresponding channel merging and orthogonal views. 3D projection of condition (L). II. Open SW orientation color-coded F-actin and corresponding orientation plots (n=2), ranging from -90 to 90º (circular color-coding map inset). White dotted lines indicate nanogroove orientation.

Figure IV.S1. Fluorescence images of SW conditions (L), (M), and (N) demonstrating the relative orientation of cells seeded on upper and lower substrates stained with DiO (green) and DiD (red), respectively. Some cells from the upper substrate tend to migrate and attach more firmly to the lower substrate, yet the opposite does not occur. Scale bars correspond to 200 μm.

Figure IV.S2. Fluorescence confocal image of cells seeded in a closed SW condition stained with DiO (green) and DiD (red) for upper and lower substrates, respectively. Along the *z* axis it is possible to observe that cells from distinct substrates are in fact not in contact and opposing substrate stimulation will not impact cell behavior. In order to guarantee substrate contact, additional measures were taken to prevent this occurrence. Scale bar corresponds to 200 μm.

Chapter V. Nanogrooved microdiscs for bottom-up modulation of osteogenic differentiation

Scheme V.1. Schematic representation of production method for topodiscs. (I) Polyvinyl alcohol (PVA) counter-molds of CDs were produced by dispensing 12% w/v solution on top of CDs and allowing to dry at 40ºC. (II) PCL particles produced by oil/water emulsion were sieved to obtain [25-40] μm microparticles (μspheres). (III) Subsequently, μspheres were micro-molded between the patterned PVA membranes at an optimized time, temperature, and applied force. (IV) Topodiscs were subjected to several washings to eliminate the PVA counter-mold. (V) Recovery of topodiscs by centrifugation. Topodiscs sustained cell adhesion and proliferation via cell-mediated topodisc aggregation.

Figure V.1. μsphere and topodisc characterization. (A) SEM images from left to right of: PVA counter-mold; PCL grooved topodisc with higher magnification of topodisc patterning

on border (1) and center (2). (B) μsphere and topodisc dimensions: μsphere diameter (left); topodisc length and width (center); topodisc and μsphere surface area (right).

Figure V.2. Pre-osteoblastic MC3T3-E1 culture on topodiscs and μspheres. (A) Fluorescence images of stained F-actin filaments (red) and nuclei (blue) of cells seeded on topodiscs or μspheres at timepoints 1, 7, 14, and 21 days. Cells were seeded at a density of 40 000 cells/cm^2, calculated according to the average surface area of topodiscs, and cultured in basal medium. Scale bars correspond to 100 μm. (B) SEM images of cells seeded on topodiscs and μspheres on days 7 and 21 of culture in basal medium. Day 21 images from left to right correspond to cells and topodiscs/μspheres aggregation; cross-sections of respective aggregates with cells; and higher magnification of ECM. (C) SEM images of cells (red) cultured on μspheres or topodiscs, highlighting the 3D cell-mediated aggregation and alignment, for the case of topodiscs, upon 7 days in culture. Control image of cell cultured on a commercially available 2-dimensional polystyrene substrate. (D) Cell metabolic activity determined using an MTS colorimetric assay and (E) cell proliferation determined by DNA quantification. Cells were cultured up to 21 days in basal medium. Mean ± standard deviation for each condition (n=3). All results were significantly different unless marked with ns ($p > 0.05$), indicating no statistically significant differences between samples.

Figure V.3. hASCs seeded on topodiscs and μspheres after 21 days of culture in basal (BAS) or osteogenic (OST) medium. Staining of histological cuts with Masson's Trichrome and von Kossa was performed. For Masson's Trichrome, tissue is marked in red and collagen fibers in blue. Von Kossa staining of tissue (blue) and phosphate deposits (black), with arrow exemplifying the identification of deposits. Hydroxyapatite was fluorescently stained in green, whilst cell nuclei were stained in blue (DAPI). Black scale bars correspond to 20 μm, whereas white scale bars correspond to 100 μm.

Figure V.S1. SEM image of topography of the used optical media substrate (CD).

Figure V.S2. Schematic representation of the potential of topodiscs as injectable cell-carriers for bone regeneration upon fracture due to their adaptability to multi-shaped defects. Right: topodisc-cell aggregates acquire the shape of 2D patterned regions with circular, hexagonal, and squared geometries. Scale bars correspond to 200 μm.

Figure V.S3. Hydroxyapatite staining in MC3T3-E1 cell line and μsphere or topodisc aggregates. Fluorescence images of MC3T3-E1 cells seeded on topodiscs and μspheres after 21 days of culture in basal (BAS) or osteogenic (OST) medium. Hydroxyapatite stained in green, whilst cell nuclei are stained in blue (DAPI). Scale bars correspond to 100 μm.

Chapter VI. Bioengineered hierarchical bone-like compartmentalized microconstructs using nanogrooved microdiscs

Figure VI.1. Schematic representation of the envisioned modular and hierarchical strategy to produce pre-vascularized, bone-like constructs. Nanogrooved microdiscs (topodiscs) interact with cells at the nanoscale level and are assembled into microaggregates containing various cells and particles, by cell-mediated action. Microaggregates of hASC-topodisc are placed in contact with suspended endothelial cells and compartmentalized within macrocapsules, whose core is further liquefied, promoting endothelial cell adhesion to living microaggregates. For initial culturing periods, the interaction of capsule core contents is promoted, leading to the formation of larger constructs. Upon prolonged culture, these capsules may rupture, and the core contents of several capsules become free to interact and create larger mineralized tissues interweaved with endothelial cells.

Figure VI.2. Particle populations (μspheres and topodiscs) sustain formation of homogeneous cell-mediated microaggregates, that are successfully encapsulated within liquefied-core capsules. A. SEM image of μspheres. B. SEM images of topodiscs. C. Brightfield image of microaggregates composed of hASCs and topodiscs or μspheres upon 24h within AggreWell400 plates. D. Characterization of microaggregates concerning longest axis (μm) and circularity for each type of microparticle. E. Schematic representation of liquified-core, multi-layered capsule: *I.* Dropwise addition of ALG solution containing solely microaggregates (hASC-topodisc or hASC-μsphere) or combined with suspended HUVECs into an aqueous calcium chloride solution. *II*. ALG bead collection and sequential immersion in PLL, ALG, CHT, and ALG solutions to obtain a 12-layered membrane. *III.* ALG core liquefaction with EDTA. Brightfield image of capsules containing hASC microaggregates (topodiscs or μspheres) and HUVECs on encapsulation day (day 0).

Figure VI.3. HUVECs interact and adhere to hASC-particle microaggregates (topodiscs and μspheres), forming larger aggregates, particularly under dynamic conditions. Left and

center: Tracking of HUVECs (green) and hASCs (red), pre-stained with lipophilic dyes, at day 1 and day 7 post-encapsulation, under static and dynamic culturing, using confocal microscopy. Corresponding projections along the *x* and *y*-axis are shown. Right: brightfield images for samples at day 7.

Figure VI.4. Topography impacts mineralization, collagen structure, and pre-vascularization. A. Fluorescent staining of hydroxyapatite (green) counterstained with nuclei (blue) in dynamic and static environments for monoculture (MONO) and co-culture (CO) conditions, in basal (BAS) and osteogenic (OST) medium, with topodiscs or μspheres. B. Assessment of structural organization of secreted collagen matrix: Masson's Trichrome staining of collagen (purple) and surrounding tissue (red), with the corresponding deconvolution of ATR-FTIR spectra within the amide I region (absorbance in arbitrary units, A.U.). C. Contribution (%) of leading absorption bands assigned to triple helix, random coil, α-helix, β-turns, and β-sheets, for each dynamic versus static culturing of μsphere and topodisc CO BAS conditions. D. Microtomography (microCT) 3D reconstructions and 2D projections for topodisc and μsphere conditions in dynamic CO OST. E. Immunohistochemistry staining of CD31 (green), podocalyxin (green), laminin (red), von Willebrand Factor (vWF, red), and actin filaments (F-actin, green), counterstained with nuclei (blue).

Figure VI.5. Topodiscs topography induces changes in the proteome of microvesicles (MV) released by co-cultured cells. A. ClueGo analysis of proteins upregulated (UReg-TopoBAS) and downregulated (DReg-TopoBAS) by topography (topodiscs-to-μsphere relative abundances ratios) in basal (BAS) medium. B. Significant relevant pathways where UReg-TopoBAS proteins intervene. C. Significant relevant pathways where DReg-TopoBAS proteins intervene. D. ClueGo analysis of proteins upregulated (UReg-TopoOST) and downregulated (DReg-TopoOST) by topography (topodiscs-to-μsphere relative abundances ratios) in osteogenic (OST) medium. E. Significant relevant pathways where UReg-TopoOST proteins intervene. F. Significant relevant pathways where DReg-TopoOST proteins intervene. Functionally grouped networks in 'A' and 'D' represent Biological Process (BP) and Molecular Function (MF) terms as circular and hexagonal nodes, respectively. Terms are linked based on their kappa score level (>0.4). The node size represents the term enrichment significance. Each node shows the % of UReg and Dreg

proteins per term has a 'pie-chart'. UReg and DReg proteins and related terms/pathways are in blueish and reddish colors, respectively. The bar length refers to the 'entities ratio', i.e., the number of proteins from each dataset that belong to the pathway divided by total number of *Homo sapiens* proteins known to belong to the pathway. Grey lines represent the -log10 (p-value), where the p-value represents the probability that the overlap between each dataset and the pathway has occurred by chance.

Scheme VI.S1. Illustration of the production method for topodiscs. I. Production of polyvinyl alcohol (PVA) counter-moulds of CDs by solvent evaporation of a 12% w/v PVA solution at 40ºC. II. Production of PCL particles via oil/water emulsion and subsequent sieving to collect particles with diameters comprised between 25-40 μm microparticles ($\mu spheres_{25\text{-}40}$) by sieving. III. Micro-moulding of $\mu spheres_{25\text{-}40}$ between nanogrooved PVA membranes at an optimised applied force, time, and temperature. IV. Successive topodisc washings to remove all traces of PVA. V. Topodisc recovery by centrifugation.

Figure VI.S1. A. SEM image of 12% w/v polyvinyl alcohol countermold of initial CD molds. B. Frequency distribution (%) of topodiscs' length (μm) and width (μm). C. Comparison of surface area for $\mu spheres_{50\text{-}80}$ (diameter ranging between 50-80 μm) and topodiscs.

Figure VI.S2. Flow cytometry analysis of surface marker expression for isolated hASCs and HUVECs.

Figure VI.S3. Live/dead staining (live cells in green and dead cells in red) and corresponding brightfield images for hASC monoculture (MONO) and hASC-HUVEC co-culture (CO) with μspheres or topodiscs, on day 21 post-encapsulation under static culturing conditions. An apparent higher percentage of dead cells is visible in bigger aggregates, as expected.

Figure VI.S4. Fluorescence images of hydroxyapatite (stained in green) and nuclei (in blue) in hASC monoculture (MONO) and hASC-HUVEC co-culture (CO) conditions, using flat microdiscs as particles, with (OST) or without (BAS) osteoinductive factors, in both static and dynamic environments. SEM image of a flat microdisc. Scale bars: 100 μm.

Figure VI.S5. Osteopontin expression (red) of hASC-HUVEC co-cultures (CO) with topodiscs or μspheres, cultured in medium with (OST) or without (BAS) osteoinductive factors, under dynamic conditions. Nuclei counterstained in blue.

Section 4: Conclusion

Chapter VII. Conclusions and future perspectives

Figure VII.1. Surface versus bulk properties of biomaterials for tissue regeneration. Surface properties, such as pore size and geometry, exposure of biochemical domains to guide the cellular behaviour (e.g., signalling biomolecules, growth factors, drugs, and reprogramming factors), topography (e.g., random or aligned patterns, roughness), surface chemistry, including charge and wettability, and local stiffness, have low dependence on the quantity/volume of material used to produce the bioengineered scaffold. On the contrary, bulk properties, such as mechanical performance, porosity, degradation, and the release rate of absorbed biomolecules, are highly dependent on the quantity/volume of material.

Figure VII.2. Approaches to engineer low-material based bioengineering systems according to their dimension ranging from "zero-dimensional" (0D) to "three-dimensional" (3D). Dotted lines connect each building block to the correspondent higher hierarchical order structure, namely *(i)* microparticles (0D) can be incorporated within liquefied systems to provide cell adhesion cells or used to produce template-based systems (3D), *(ii)* cells containing nanoparticles (0D) can be used to produce magnetic cell sheets (2D), and *(iii)* fibres (1D) can be assembled to produce fibre mats (2D).

List of Publications

A – Publications resulting from work performed during the PhD thesis

A1 – International peer-reviewed journals

1. I.M. Bjørge, B.M. de Sousa, S.G. Patrício, A.S. Silva, L.P. Nogueira, L.F. Santos, S.I. Vieira, H.J. Haugen, C.R. Correia, J.F. Mano. Bioengineered hierarchical bone-like compartmentalized microconstructs using nanogrooved microdiscs, *submitted*.
2. I.M. Bjørge,* C.R. Correia,* J.F. Mano.* Exploring geometrical and topographical cues of non-spherical microcarriers for biomedical applications, **Materials Horizons** (2022) (**DOI**: 10.1039/D1MH01694F) (*corresponding authors)
3. C.R. Correia, I.M. Bjørge,* S. Nadine,* J.F. Mano (*authors contributed equally). Minimalist tissue engineering approaches using low material-based bioengineered systems, **Advanced Healthcare Materials**, 10 (2021) e2002110. (**DOI:** 10.1002/adhm.202002110)
4. I.M. Bjørge, M. Salmerón-Sánchez, C.R. Correia, J.F. Mano. Cell behavior within nanogrooved sandwich culture systems, **Small**, 16 (2020) 2001975. (**DOI:** 10.1002/smll.202001975)
5. I.M. Bjørge, I.S. Choi, C.R. Correia, J.F. Mano. Nanogrooved microdiscs for bottom-up modulation of osteogenic differentiation, **Nanoscale**, 11 (2019) 16214-16221. (**DOI:** 10.1039/C9NR06267J)
6. I.M. Bjørge, A.M.S. Costa, A.S. Silva, J.P.O. Vidal, J. M. Nóbrega, J.F. Mano. Tuneable spheroidal hydrogel particles for cell and drug encapsulation, **Soft Matter**, 14 (2018) 5622-5627. (**DOI:** 10.1039/C8SM00921J)

A2 – International and national conferences

A2.1 – Oral communications

1. I.M. Bjørge, B.M. de Sousa, S.G. Patrício, A.S. Silva, L.P. Nogueira, L.F. Santos, S.I. Vieira, H.J. Haugen, C.R. Correia, J.F. Mano, "Nanogrooved microdiscs and liquefied-core capsules as platforms for the development of vascularised bone tissue constructs", **31st Conference of the European Society for Biomaterials (ESB)**, September 5th-9th, 2021.

2. I.M. Bjørge, C.R. Correia, J.F. Mano, "Topographical cues to induce microbone formation in a liquefied 3D context", **VII International Conference IMFAHE (International Mentoring Foundation For The Advancement Of Higher Education)**, May 31st, 2021.
3. I.M. Bjørge, C.R. Correia, J.F. Mano, "Nanogrooved microdiscs for a bottom-up co-culture of ASCs and HUVECs within liquefied-core capsules", **World Biomaterials Congress (WBC)**, Glasgow, Scotland, December 11th-16th, 2020.
4. I.M. Bjørge, M. Salmerón-Sánchez, C.R. Correia, J.F. Mano, "Nanogrooved sandwich culture model to study cell behaviour", **WBC**, Glasgow, Scotland, December 11th-16th, 2020.
5. I.M. Bjørge, C.R. Correia, J.F. Mano, "Groovy", **Research Summit** – University of Aveiro, Aveiro, Portugal, June 24th-26th, 2020.
6. I.M. Bjørge, C.R. Correia, J.F. Mano, "Biodegradable microparticles as cell supports for bottom-up tissue engineering", **Aveiro-Osaka Universities joint symposium on advanced biomaterials and cell-based bioengineering strategies**, University of Aveiro, Aveiro, Portugal, October 31st, 2019.
7. I.M. Bjørge, C.R. Correia, J.F. Mano, "Let's get physical", **Research Summit** – University of Aveiro, Aveiro, Portugal, July 3rd-5th, 2019.
8. I.M. Bjørge, C.R. Correia, J.F. Mano, "Patterned discoidal microfilms modulate osteogenic differentiation", **TERMIS-EU**, Rhodes, Greece, May 27th-31st, 2019.

A2.2 – Poster communications

1. I.M. Bjørge, B.M. de Sousa, S.G. Patrício, A.S. Silva, L.P. Nogueira, L.F. Santos, S.I. Vieira, H.J. Haugen, C.R. Correia, J.F. Mano, "3D nanogrooved living platforms for vascularised bone-like microtissue manufacture", **CICECO Jornadas** – University of Aveiro, Aveiro, Portugal, October 6th-7th, 2021.
2. I.M. Bjørge, M. Salmerón-Sánchez, C.R. Correia, J.F. Mano, "Cell behaviour within nanogrooved sandwich-culture models", **TERMIS-EU**, Manchester, UK, May 26th-29th, 2020.
3. I.M. Bjørge, C.R. Correia, J.F. Mano, "Nanogrooved microdiscs modulate response of co-cultured stromal and endothelial cells within liquefied-core capsules in dynamic conditions", **TERMIS-EU**, Manchester, UK, May 26th-29th, 2020.

4. I.M. Bjørge, C.R. Correia, J.F. Mano, "Patterned Microfilms for Bone Tissue Engineering", **CICECO Jornadas** – University of Aveiro, Aveiro, Portugal, June 11th-13th, 2019.
5. I.M. Bjørge, C.R. Correia, J.F. Mano, "Nanopatterned micro-scaffolds for bone tissue engineering applications", **European Society for Biomaterials (ESB)**, Maastricht, Netherlands, September 9th-13th, 2018.
6. I.M. Bjørge, A.M.S. Costa, A.S. Silva, J.P.O. Vidal, J.M. Nóbrega, J.F. Mano, "Spheroidal hydrogel particles as vehicles for cell and drug encapsulation", **ESB**, Maastricht, Netherlands, September 9th-13th, 2018.
7. I.M. Bjørge, C.R. Correia, J.F. Mano, "Advanced Injectable Nanopatterned Micro-Scaffolds for Modular Bone Tissue Engineering", **5th World Congress TERMIS**, Kyoto, Japan, September 4th-7th, 2018.
8. I.M. Bjørge, A.M.S. Costa, A.S. Silva, J.P.O. Vidal, J.M. Nóbrega, J.F. Mano, "Tuneable Spheroidal Hydrogel Particles for Cell and Drug Encapsulation", **5th World Congress TERMIS**, Kyoto, Japan, September 4th-7th, 2018.
9. I.M. Bjørge, A.M.S. Costa, A.S. Silva, J.P.O. Vidal, J.M. Nóbrega, J.F. Mano, "Spheroidal hydrogel particles with controllable shape for cell and drug encapsulation", **CICECO Jornadas** – University of Aveiro, Aveiro, Portugal, June 11th-12th, 2018.

B – Publication in international peer-reviewed journal resulting from collaborative work performed during the present PhD thesis

1. C.R. Correia, I.M. Bjørge, J. Zeng, M. Matsusaki, J.F. Mano. Liquefied microcapsules as dual-microcarriers for 3D+3D bottom-up tissue engineering, **Advanced Healthcare Materials**, 8 (2019) 1901221. (**DOI:** 10.1002/adhm.201901221)

C – Book chapter resulting from collaborative work performed during the present PhD thesis

J. Borges, C.F.V. Sousa, I.M. Bjørge, S. Nadine, C.R. Correia, S.G. Patrício and J.F. Mano. "Shaping Soft Structures using Bottom-up Layer-by-Layer Assembly Technology for Biomedical Applications", Chapter 18, **Soft Matter for Biomedical Applications**, Volume 13, Royal Society of Chemistry (2021). (**DOI:** 10.1039/9781839161124-00444)

Thesis Outline

This thesis is divided into four main sections, comprised of a total of seven chapters. Sections 1 and 3 are based on scientific papers published or submitted to international peer-reviewed journals. The corresponding original publication is cited at the beginning of each chapter.

Section 1 is a general introduction to biophysical cues and the mechanotransduction mechanisms behind cellular response to such cues, with particular emphasis towards topography and geometry. Microcarriers are introduced as platforms for cell-free and bottom-up tissue engineering strategies. Methodologies to produce microcarriers are described. The current advances in specific tissue engineering strategies employing these microcarriers and the role of microcarrier geometry in cell-free biomaterial-based strategies are reviewed.

Section 2 complements and summarizes the Materials and Methods subsection for each chapter in Section 3.

Section 3 contains four experimental chapters related to the application of biophysical cues, namely geometry and topography, in a 3D context. In Chapter III, the role of increasing surface area and varying shape of spheroidal hydrogel particles was assessed regarding drug release rate and cell viability. In Chapter IV, sandwich culture methodologies are applied to assess the effect of grooved topography upon simultaneous dorsal and ventral stimulation to determine the impact of initial contact on cell behavior. In Chapter V, the methodology behind the production of nanogrooved microdiscs (topodiscs) is addressed and the role of these particles in directing osteogenesis is evaluated. In Chapter VI topodiscs and liquefied core capsules are applied towards the production of pre-vascularized bone-like microtissues.

Section 4 summarizes the results obtained in this thesis, addresses recent progresses in the field, and briefly discusses future directions in the field.

1

General Introduction

Chapter I

Exploring topographical and geometrical cues of non-spherical microcarriers in biomedical applications

Chapter I: Exploring topographical and geometrical cues of non-spherical microcarriers in biomedical applications[1]

Abstract

Structure and organisation are key aspects of the native tissue environment, which ultimately condition cell fate via a myriad of processes, including the activation of mechanotransduction pathways. By modulating the formation of integrin-mediated adhesions and consequently impacting cell contractility, engineered geometrical and topographical cues may be introduced to activate downstream signalling and ultimately control cell morphology, proliferation, and differentiation. Microcarriers appear as attractive vehicles for cell-based tissue engineering strategies aiming to modulate this 3D environment, but also as vehicles for cell-free applications, given the ease in tuning their chemical and physical properties. In this review, geometry and topography are highlighted as two preponderant features in actively regulating interactions between cells and the extracellular matrix. While most studies focus on the 2D environment, we focus on how the incorporation of these strategies in 3D systems could be beneficial. The techniques applied to design 3D microcarriers with unique geometries and surface topographical cues are covered, as well as specific tissue engineering approaches employing these microcarriers. In fact, successfully achieving a functional histoarchitecture may depend on a combination of fine-tuned geometrically shaped microcarriers presenting intricately tailored topographical cues. Lastly, we pinpoint microcarrier geometry as a key player in cell-free biomaterial-based strategies, and its impact on drug release kinetics, the production of steerable microcarriers to target tumour cells, and as protein or antibody biosensors.

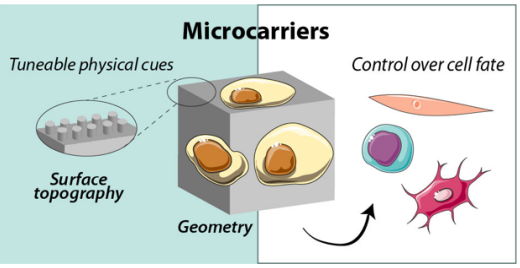

[1] Based on the publication: I.M. Bjørge, C.R. Correia, J.F. Mano. Hipster microcarriers: Exploring topographical and geometrical cues of non-spherical microcarriers in biomedical applications, **Materials Horizons** (2022), DOI: 10.1039/D1MH01694F

1. Introduction

The cell microenvironment is a complex and hierarchical environment, where distinct cell populations interact and organise in specific architectures, in a tissue-dependent manner. Single cells give rise to functional subunits ranging anywhere between 100 µm and 1 mm that form the basis for each tissue.[1] Each cell is constantly exposed to biophysical and biochemical factors emerging from the direct and indirect contact with the extracellular matrix (ECM), neighbouring cells, soluble factors, and physical forces.[2] Although stable in the presence of minor perturbations, the cell phenotype is in fact pliable to external cues, which play a crucial role in regulating gene expression.[1] Within each tissue building block, ubiquitous physical cues guide cellular organisation and ultimately impact behaviour.[2] The capability of cells to translate the physical and mechanical cues delivered by the ECM into biochemical signals is a central aspect of how external cues modulate cellular functions and tissue organisation.[3] At the nanometric scale, aligned collagen fibrils form the basic building block for both bone and tendon, where the key difference lies in the mineralised hydroxyapatite component of bone.[4] Cardiomyocytes similarly align and elongate along fibrillar collagen and elastin bundles to form cardiac tissue.[5] Geometry is a distinctive feature of hepatic lobules, characterised by their hexagonal form containing a central vein from which hepatic cords radiate, separated by vascular sinusoids.[6] The distinctive design of each tissue highlights the importance of structural organisation in the native cell environment and point towards the advantage of applying physical cues and constraints to develop functional histoarchitectures.[7,8]

From a tissue engineering perspective, biological factors such as growth factors remain the gold standard to induce cellular processes towards a functional regeneration. *In vitro*, biochemical factors can be easily introduced as a component of the cell culture medium, yet the transposal to *in vivo* studies is more complex. With each targeted therapy, achieving a localised administration at an adequate concentration is still a necessary hurdle to overcome to reach the desired results in a clinical setting.[9] An example is the controversy around the use of osteoinductive factor bone morphogenetic protein-2 (BMP-2) during spine fusion procedures, for which the FDA later issued a Public Health Notification due to life-threatening complications.[10] The presentation of biophysical cues as opposed to biochemical signals has the advantage of bypassing such issues, while delivering similar outcomes. For

instance, mesenchymal stromal cell differentiation can be guided towards distinct lineages simply by altering the physical/mechanical environment to which cells are exposed, such as tuning substrate stiffness[11] or introducing topographical features.[12]

It is well established that physical and mechanical aspects of a synthetically bioengineered ECM alter integrin-mediated cell adhesion and accordingly activate distinct downstream signalling pathways.[13,14] As such, the role of surface cues on determining cell fate has been explored at the subcellular level using topographical features[15] (grooves, pillars, and pits) and at a single cell or multicellular level via the application of geometrical features.[16] These studies have elucidated the impacting and crucial role of both topographical and geometrical cues on the modulation of cell behaviour. However, these studies have been mainly performed in 2-dimensional (2D) environments, which fail to fully mimic the native cell environment. Options to take these studies into the third dimension rely mostly on bottom-up tissue engineering strategies using micrometric constructs, termed microcarriers. While microcarriers originally referred to spherical microparticles applied for adherent cell expansion in bioreactors, this term has since been broadened to range from cell-based tissue engineering approaches to drug delivery applications.

With this review, we aim to explore the current applications and advantages of non-spherical microcarriers, focusing on microcarriers with unique geometries and surface topographical features. Due to their modular, hierarchical context, we additionally include macroscale cell encapsulation approaches that rely on bottom-up assembly into larger constructs. While there are several recent research articles focusing on spherical microcarriers,[17,18] and even microcarriers with distinct biochemical and biophysical cues,[19,20] here we take a step further to delve deeper into the role of topography and geometry in directing cell fate, while addressing the mechanotransduction pathways inherently involved in this regulation and the impact of their transposal to the 3D context. To this end, relevant 2D studies are included that address the impact of cell-substrate interactions at the cellular level and mechanotransduction of geometrical/topographical cues to complement what is known, since the inclusion of such cues in a 3-dimensional (3D) setting is an emerging field. Numerous techniques can be employed to design and produce these vehicles, as will be described further along in this review (Figure I.1). We will also report the 3D applications and outcomes of advanced microcarriers opposing the classical spherical systems, which are

recently being employed in TE, drug delivery, cell targeting, and biosensors. A special focus will be given to the role of geometrical and topographical cues not only in a 2D setting, as they are commonly applied, but the importance of transposing these cues into a 3D context, particularly for regenerative medicine applications.

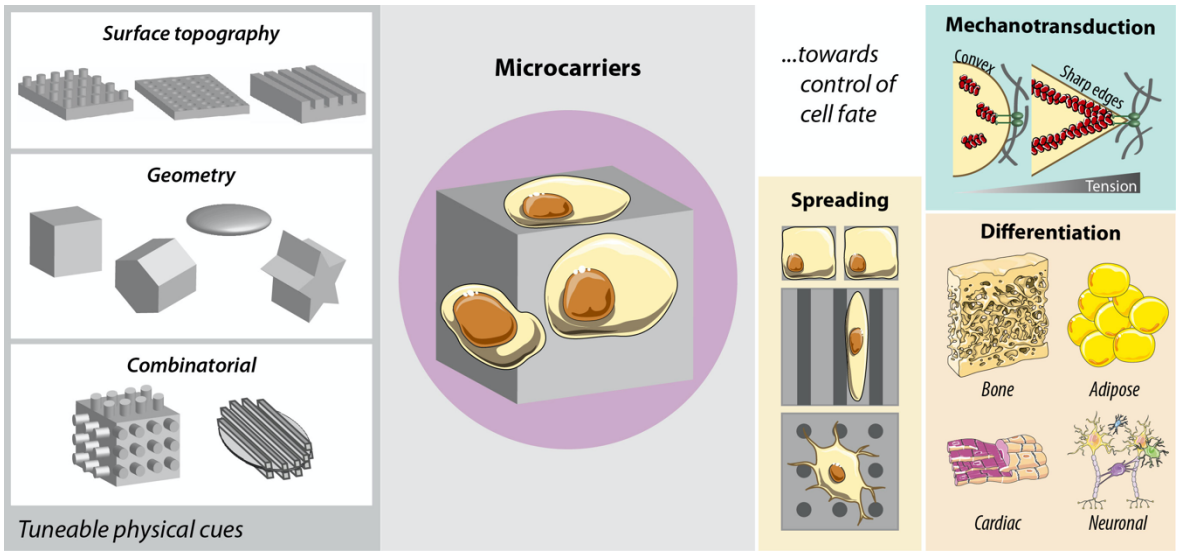

Figure I.1. Microcarriers can be endowed with tuneable physical cues such as surface topography and geometry, or a combination of both, to modulate cell spreading and fate via mechanotransduction pathways to impact cell differentiation.

2. Impact of Cell-ECM interactions at the cellular level

In the native tissue environment, exchanges of biochemical and biophysical cues between neighbouring cells and cells from distinct lineages are mediated via interaction with the ECM.[21] In a process termed mechanotransduction, physical and mechanical cues from the ECM are translated into biochemical signals.[3] In general terms, most cell-ECM adhesions can be simplified into two major components, namely *(i)* transmembrane proteins, such as integrins that bind to the ECM or cadherins that bind to neighbouring cells, and *(ii)* actin fibres, which bind indirectly to transmembrane proteins via adaptor proteins.[22,23] Upon integrin-mediated cell adhesion to the ECM, mechanical loading is exerted on adhesion sites with consequent force transmission.[21] Force acts as a key regulator of the stability and lifetime of ligand-bound integrins and can lead to eventual bond dissociation for certain types of bonds [22]. Via force-induction, protein conformational changes or enzymatic reactions occur, which in turn direct biochemical signalling via integrin clustering and

downstream signalling of integrin-mediated events. These include focal adhesion kinase (FAK) activation or recruitment of adaptor proteins such as vinculin.[21,22]

The molecular clutch controls tissue remodelling by regulating the transmission of force and cell migration.[23] The molecular clutch model considers that myosin contractility continuously powers actin flow towards the centre of the cell, termed retrograde flow.[24,25] Upon integrin-based adhesion to the ECM, the elastic resistance to deformation offered by the ECM counters myosin contractility, which in turn slows down the actin retrograde flow (Figure I.2). This however increases the force loading rate on the integrin-based adhesion complex.[14,23] Depending on the type of bond behaviour for a given protein-protein interaction, the increased force loading rate can lead to either bond lifetime shortening or prolongation, for slip bonds and catch bonds, respectively.[21,26] For example, rigid substrates induce higher loading rates, which in turn direct the unfolding of force-sensitive protein talin via catch bond formation, and consequent vinculin recruitment, decreased actin flow, growth of adhesion sites, and downstream signalling. Conversely, soft substrates with lower loading rates promote integrin detachment from the ECM prior to talin unfolding and bond reinforcement with vinculin.[13,21] Due to this fact, whereas for cells adhered to rigid substrates the disruption of multiple actin stress fibres via laser nanoscissor severing only minimally disrupts cell morphology, a single fibre disruption for cells on soft substrates may greatly alter cell behaviour.[27] The molecular clutch model has also been demonstrated to govern cell sensing of substrate viscosity, with higher viscosity increasing loading rates and consequent talin unfolding and downstream signalling, which does not occur for lower viscosity. Lower matrix viscosity has also been linked to a rounded cell morphology due to an increasing ligand mobility and resulting reduction in cytoskeletal tension.[14] Varying substrate coating density also impacts the rigidity threshold required for downstream signalling. For example, a reduction in coating density (e.g., with fibronectin) will decrease the number of available clutches. With actomyosin contractility distributed among fewer clutches, the loading force per clutch will increase accordingly, thus inducing talin unfolding and reinforcement at a lower rigidity threshold.[13]

Cells' capability to generate tension is thus impacted by the mechanical properties of the ECM, which in turn influences cell spreading, nuclear shape, activation of intercellular signalling pathways, and modulation of gene expression and transcription factors.[28,29] Focal

adhesions (FAs) are dynamic multiprotein complexes governed by external cues and cellular responses.[30] These may include integrins, as well as cytoskeletal and signalling proteins, such as talin, actinin, vinculin, zyxin, paxillin, and focal adhesion kinase (FAK).[31] Furthermore, it has been suggested that cell adhesion in a 3D context may in fact differ from 2D focal and fibrillar adhesions in both molecular composition and localisation. FAs are mainly composed of separately localised $\alpha_v\beta_3$, paxillin, vinculin, and FAK, whereas fibrillar adhesions mostly contain $\alpha_5\beta_1$ integrin and tensin. Whereas tyrosine-phosphorylated FAK and paxillin are present in focal adhesions, a distinct trend is observed in fibrillar and 3D adhesions. Fibroblasts seeded in a 3D environment presented triple co-localisation of α_5 integrin, paxillin, and fibronectin, with $\alpha_5\beta_1$ integrin playing a critical role. Additionally, even though 3D matrix adhesions present co-localisation of α_5 integrin with paxillin and FAK, as well as α_5 integrin co-localised with tyrosine-phosphorylated paxillin, the presence of tyrosine-phosphorylated FAK is only punctually observed, indicating another key difference between 2D and 3D adhesions.[32]

Upon initial integrin-mediated adhesion, the increased local tension induces integrin clustering and phosphorylation of FAK. This activates small guanosine triphosphate hydrolases (GTPases) of the Rho-family such as RhoA, which in association with effector RhoA kinase (ROCK), phosphorylates myosin light-chain II (MLC). Subsequently, MLC binds and enhances non muscle myosin II heavy-chain activity, inducing actomyosin contractility.[33] Actomyosin contractility increases tension within the cytoskeleton with consequent enlargement and maturation of focal adhesion (FA) complexes and an ensuing greater traction on the ECM.[28,34] Increasing matrix rigidity leads to upregulated myosin II contraction, which recruits and activates FAK.[35] Actin polymerisation, protease activation or secretion, and assembly/disassembly of focal contacts are regulated by FAK activity and downstream signalling.[30] Whereas Rho activation leads to the formation of FAs and may also activate FAK, a regulatory circuit exists where FAK in turn induces Rho down-regulation to prevent the formation of excessive adhesions. FAK-mediated Rho inhibition is hence required for FA turnover and cell migration.[31] This is performed via direct interaction or phosphorylation of Rho GTPase protein activators or inhibitors.[30] FAK activation has also been linked to the activation of intracellular signalling cascades such as extracellular signal-regulated kinase–mitogen-activated protein kinase (ERK–MAPK) pathway, which impacts

cell migration and proliferation.[36,37] Aside from responding to ECM mechanical properties, cells may also induce ECM stiffening, hence directing matrix-mediated intercellular mechanical communication and collective durotaxis.[38]

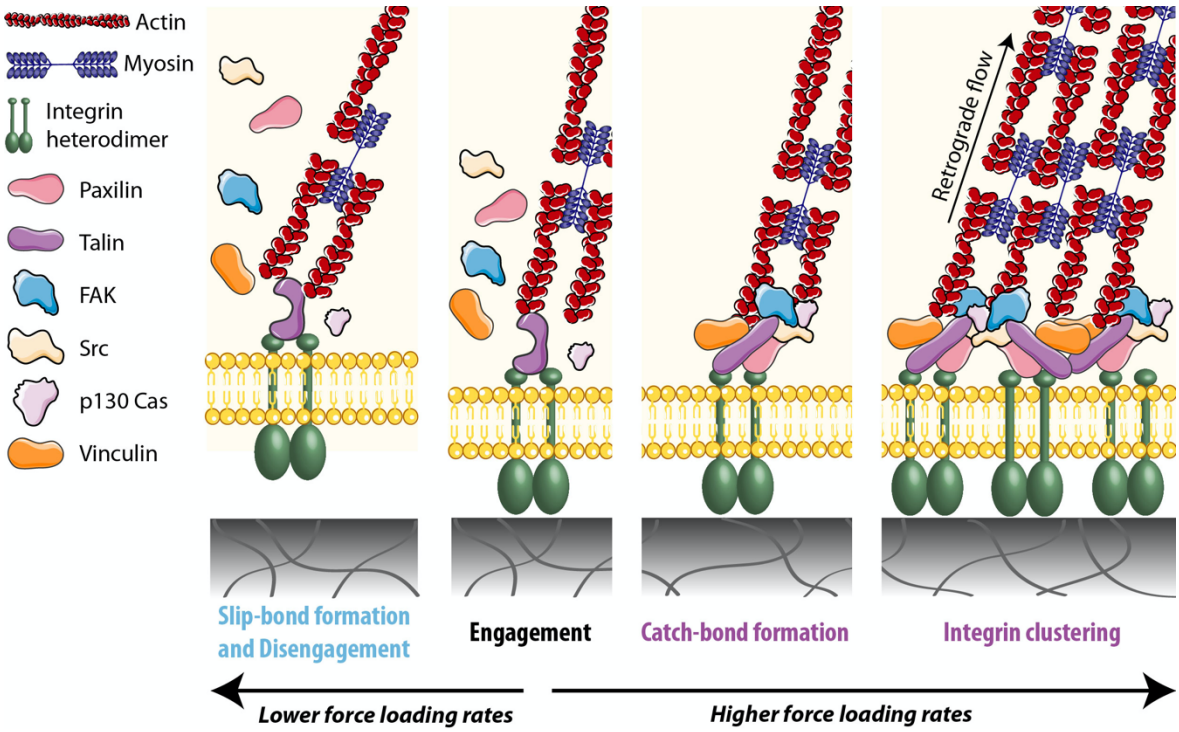

Figure I.2. Molecular clutch model: upon integrin-mediated adhesion to the ECM, the increase in force loading rate on the integrin-based adhesion complex may direct the unfolding of force-sensitive protein talin via catch bond formation, and consequent vinculin recruitment, decreased actin flow, growth of adhesion sites, and downstream signalling. Impacting factors to integrin-mediated adhesions. Conversely, lower force loading rates lead to slip-bond formation and disengagement from the substrate. Integrin-mediated adhesions are impacted by substrate rigidity, ligand concentration, viscoelasticity, stress relaxation, topographical, and geometrical cues.

2.1. Cell spreading and migration

Cell spreading is similarly controlled by FA response to force and downstream regulation of Rho-family GTPases.[37] Changes in cell shape and cytoskeletal tension brought upon by cell adhesion are required for the activation of ROCK. Modulation via cell culture density or micro-island size can both impact cytoskeletal tension and consequently alter RhoA and ROCK expression.[39] Rho-family GTPases are involved in cell motility, adhesion, and cytoskeletal dynamics.[15] They are also involved in the initiation of actin polymerisation and actin assembly with consequent formation of protrusions, in association with paxillin as a major regulator of protrusion growth. The formation of stress fibres, lamellipodia, and filopodia is directed by RhoA, Rac, and Cdc42 (cell division cycle 42), respectively.[30,37] Cell

spreading also impacts cell proliferation and appears as a requirement for anchorage-dependent cells to enter the S phase of the cell cycle.[40]

Whereas cell migration on 2D substrates and nonlinearly elastic 3D environments is governed by the protrusion of lamellipodia, migration in a linearly elastic 3D structure, mimetic of the native cell environment, appears to occur via the extension of lobopodia. The formation and maintenance of lobopodia requires actomyosin contractility. In conjunction with nucleoskeleton-intermediate filament linker protein nesprin-3, a high cytoplasmic hydrostatic pressure in front of the nucleus is generated that drives the lobopodial membrane forward [41]. In fact, migration in a 3D environment has been proposed to be similar to migration in a 1D environment, such as the one simulated by single fibres, as opposed to migration in 2D. Specifically, fibroblast migration on 1D fibrillar lines has been shown to be independent of ECM ligand density, but dependent on myosin II contractility and microtubules, similarly to cell migration within a 3D fibrillar cell-derived matrix. Whereas in 2D inhibition of contractility increases cell migration speed, speed in 1D and 3D is markedly hampered. Furthermore, fibroblasts in 1D demonstrate rapid spreading, polarisation, motility, and uniaxial phenotype, as would be expected in 3D.[42] Moreover, hydrogel stress relaxation affects the spreading and proliferation of encapsulated fibroblasts, which are both increased with faster stress relaxation rates.[43]

2.2. ECM mechanics as an impacting factor

In response to ECM mechanics, Rho GTPase activity and actomyosin tension induce YAP (Yes-associated protein) and TAZ (transcriptional coactivator with PDZ-binding motif or WWTR1) shuttling to the nucleus, which play a role in ECM remodelling.[3,44] YAP/TAZ act as regulators of cell spreading and proliferation, shuttling from the cytoplasm to the nucleus in response to a soft or stiff environment, respectively.[45] Furthermore, YAP transcriptionally controls the formation of FAs and hence the degree of cell adhesion with consequent impact over cytoskeleton stability.[44] A study culturing MSCs on fibronectin-coated micropillars pinpointed nuclear localisation of YAP/TAZ as being primarily regulated by cell spreading/area and not cell-ECM contact area. Furthermore, rigid micropillars resulted in nuclear YAP/TAZ whereas elastic micropillars led to cytoplasmic localisation.[3] Another study using surface micropatterning for single-cell analysis, determined that a reduction in

contact area led to a decrease in the number of FAs and a lower nuclear to cytoplasmic YAP localisation. However, for a constant cell spreading/area with decreasing contact area and consequent decrease in FAs, YAP nuclear localisation was not affected. This implies that cell area is in fact more crucial for YAP nuclear accumulation than the number of FAs formed during adhesion to the ECM.[44] In a 2D versus 3D encapsulation study of YAP/TAZ nuclear translocation in environments with identical substrate chemistry and varying stiffness, cell spreading was enhanced on stiffer 2D substrates, while softer substrates proved to enhance spreading within a 3D matrix. Correlating with YAP/TAZ relative nuclear intensity, increased nuclear localisation was observed for rigid substrates in 2D, while in 3D this was observed for softer and medium stiff hydrogels. When comparing MSCs seeded within same stiffness degradable or non-degradable hydrogels, it was demonstrated that cells acquired a more rounded morphology and presented a lower nuclear YAP/TAZ for non-degradable hydrogels. Hence, this highlighted the role of degradation on YAP/TAZ localisation, independently of hydrogel stiffness.[46]

Notably, substrate rigidity has been linked to lineage-specific differentiation of MSCs, with soft gels (0.1-1 kPa) predominantly directing neurogenesis, while intermediately stiff gels (11 kPa) lead to myogenesis, and stiff gels (34 kPa) primarily induce osteogenesis. These stiffness-driven results were demonstrated to be linked with non-muscle myosin II expression [11]. Furthermore, the role of substrate stiffness on MSC osteogenic differentiation has been associated with the downstream up-regulation of specific proteins such RhoA, YAP, and TAZ.[14] Nuclear lamin-A overexpression has also been found to impact YAP1 nuclear localisation, indicating lamin-A as a modulator of several transcription pathways. Lamin-A expression has been implied as mechanosensitive, with high lamin-A concentrations stabilising the nucleus against stress on stiff surfaces. Furthermore, lamin-A knockout on soft substrates directed MSC differentiation into the adipogenic lineage, whereas overexpression on stiff substrates led to osteogenic differentiation.[47]

Nevertheless, in 3D environments MSC commitment has been shown to occur even when cell and nuclear morphology were unaltered by substrate rigidity. Cell differentiation does still occur in response to mechanical stimulation, which regulates integrin binding and the reorganisation of adhesion ligands.[48] For instance, a similar cell morphology was observed between MSCs encapsulated within hydrogels with identical initial elastic modulus but with

quite distinct stress relaxation rates, evidencing enhanced osteogenesis for faster stress relaxation. For slow-relaxing gels, an analogous trend in cell morphology was observed, with commitment to the adipogenic lineage ensuing with lower substrate elastic modulus, whereas osteogenesis occurred with higher elastic modulus. Generally, MSC commitment to the osteogenic lineage was observed in initially stiffer, faster relaxing hydrogels, while adipogenesis was promoted in initially softer hydrogels with slower stress relaxation. Faster relaxing viscoelastic matrices reportedly allow for a greater matrix mechanical remodelling, which expedites adhesion-ligand clustering and adjustment of cell shape. ECM ligands were shown to mediate the effect of stress relaxation in the context of osteogenic differentiation, with an increased localisation of β_1 integrin at the cell periphery for faster relaxing gels. Furthermore, stiffer gels with faster stress relaxation presented an enhanced integrin clustering and greater actomyosin contractility, coincident with increased osteogenesis.[43] Yet, contrarily to previous studies stating the co-localisation of $\alpha_5\beta_1$ integrin, paxillin, and fibronectin in 3D matrix adhesions,[32,49] paxillin was absent in the 3D environment for all levels of stress relaxation.[43] For both initial elastic moduli assessed, an increased YAP nuclear translocation was observed with faster stress relaxation. However, a similar nuclear to cytoplasmic YAP ratio was observed independently of elastic modulus, indicates that YAP localisation alone does not control MSC differentiation in 3D culture.[43] In both proteolytically degradable hydrogels as well as dynamic viscoelastic hydrogels, the enhancement of hMSC spreading, YAP/TAZ nuclear translocation, and osteogenic differentiation, has been shown to be mediated by cellular adhesion to nascent proteins. Upon inhibition of adhesion to nascent proteins or impaired remodelling, cell spreading was effectively reduced, which impacted downstream cellular outcomes such as YAP/TAZ nuclear translocation, and ultimately favoured commitment to the adipogenic lineage.[49]

In fact, not only stromal cells are affected by the mechanical aspects of their environment. Morphology and function of hepatocytes have been shown to be impacted by substrate rigidity. Strikingly, increasing gel rigidity resulted in enhanced proliferation and dedifferentiation, whereas decreasing rigidity led to growth arrest and maintenance of phenotype.[50] When factoring in both rigidity and ligand concentration, a greater cell spreading was correlated with increased rigidity and ligand concentration. Conversely, albumin secretion, a downstream measure of hepatocyte function, followed the opposite

trend with higher secretion rates for softer gels with lower ligand concentration, which was linked to decreased spreading.[51] Interestingly, stiffness has also been pinpointed as a crucial factor in modulation of the immune response by leading to an altered function and phenotype of both immature and mature dendritic cells (DCs). Whereas substrate stiffness reportedly altered C-type lectin expression and consequently antigen internalisation in immature DCs, mature DCs presented altered CCR7 expression, which was linked to changes in migration towards chemokine CCL21 and a potentially hampered cell ability to reach lymph vessels.[52]

Even though ECM mechanics have been the focus of several 2D and cell encapsulation studies, research on their impact for cell microcarriers is lacking. Considering current studies, it would be interesting to evaluate whether the same effects emerge in the more adaptable microcarrier environment. The same rational applies to geometrical and topographical cues where, considering the impact of mechanical properties on the formation of FAs and consequent generation of tension by cells with corresponding onset of mechanotransduction events, it would be logical that such cues would also play a crucial role. Curiously, in a 2D study, microtopography and stiffness showed an isolated but not combinatory impact on cell proliferation and differentiation.[53] It would be relevant to study further combinations of topography or geometry with stiffness or stress relaxation.

3. Mechanotransduction of topographical and geometrical cues in 2D and 3D contexts

A vast range of topographical cues have been explored in a 2D context. Topographical features such as pillars/columns,[54] pits,[55] roughness gradients,[56] localised curvature,[57] grooves,[58] and even random algorithm-generated topographies,[59–61] condition cell morphology and impact cell behaviour. The most widely studied feature may in fact be nano- and microgrooves, which have been shown to direct the alignment of several types of cells, among which MSCs,[58] fibroblasts,[62] cardiomyocytes,[63] osteoblasts,[64] and macrophages.[65] Similarly, geometrical features can restrict cell spreading and model cell morphology via the use of adhesive/non-adhesive spots to study the effects on single[66] or multiple[67] cells at a time. By tuning the size of adhesive spots, these can also be used to selectively target and modulate cell adhesion at the integrin-level,[15] or model the cell as a whole.[16] Hence, the question arises of which mechanotransduction pathways these topographical and

geometrical cues trigger (Figure 3). Additionally, how this information may be leveraged and introduced to microcarrier-based approaches for 3D strategies.

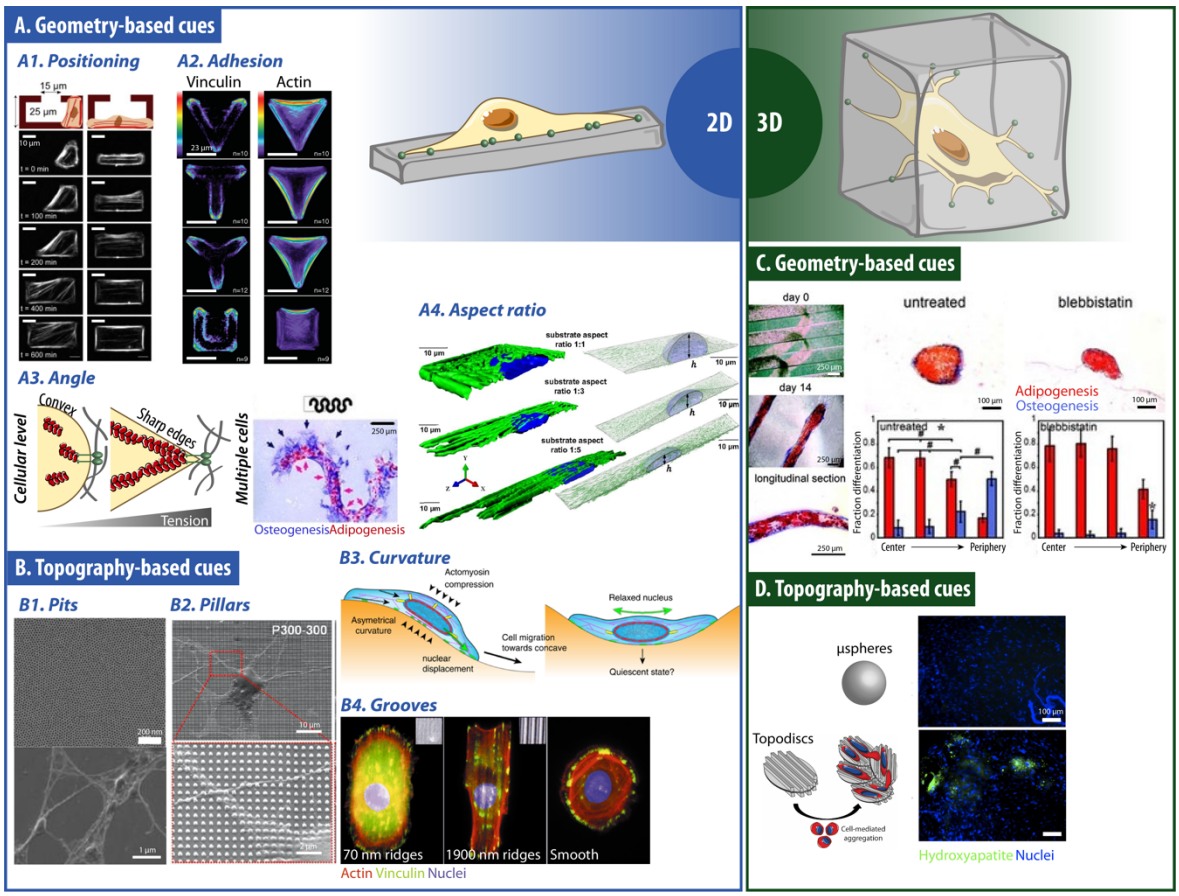

Figure I.3. Geometrical and topographical cues applied in 2D and 3D to modulate cell behaviour. 2D – A. Geometry-based cues: Positioning (A1) [Reprinted with permission from [92], Copyright (2019) Elsevier]. Adhesion (A2) [Reprinted with permission from [91], Copyright (2006) John Wiley & Sons]. Angle (A3) [Reprinted with permission from [67], Copyright (2009) John Wiley & Sons]. Aspect ratio (A4) [Reprinted with permission from [250], Copyright (2019) National Academy of Sciences]. B. Topography-based cues: Pits (B1) [Reprinted with permission from [81], Copyright (2014) American Chemical Society]. Pillars (B2) [Reprinted with permission from [80], Copyright (2013) American Chemical Society. Curvature (B3) [Reprinted with permission from [57], Copyright (2018) Springer Nature]. Grooves (B4) [Reprinted with permission from [73], Copyright (2003) Company of Biologists Ltd.]. **3D** – C. Geometry-based cues [Reprinted with permission from [67], Copyright (2009) John Wiley & Sons]. D. Topography-based cues [Reprinted with permission from [117], Copyright (2019) Royal Society of Chemistry].

3.1. Topographical cues

Given the micrometric breadth of integrin-based adhesions, cells are able to sense subcellular alterations in local ECM properties.[68] For instance, contact guidance of fibroblasts on grooved surface topography has been shown to be non-existent below features with a height of 35 nm,[69] yet an independent study demonstrated that fibroblasts can respond to nanopillars

with a height as low as 8 nm.[70] Endothelial cells have been shown to spread substantially faster on grooved substrates than on flat substrates, particularly for groove depths below 1 μm (1 μm ridge/groove widths). Grooved topographical features accelerate initial cell spreading via integrin dependent FAK signalling, which in turn initiates downstream signalling for FA complex formation. Subsequently, contact guidance relies on ROCK and myosin II dependent cell contractility for maturation of FAs.[71] The regulation of FA size is hence force-dependent and relies on actomyosin contractility.[72] There are however contrasting reports on the effect of grooves on the size of FAs quantified using distinct parameters, such as area, width, or elongation. These differences may be attributed to varying groove dimensions such as groove/ridge width and depth, or even due to divergent responses of distinct cell populations. FA area was reportedly larger for endothelial cells seeded on grooves (1 μm ridge/groove/depth) than on flat substrates, yet by decreasing the depth to 800 nm these differences were abolished.[71] Smaller and more elongated FAs were observed for hMSCs seeded on nanogrooves (250 nm) versus larger and less elongated FA on microgrooves (10 μm) or flat substrates.[72] Similarly, FA width of human corneal epithelial cells was highest for flat substrates and decreased in correspondence with decreasing ridge and groove widths, reaching a low for 70 nm ridges and 330 nm grooves.[73] Grooved (350 nm width) versus non-grooved substrates with distinct mechanical properties have illustrated the topography-dependent decrease in expression of integrin subunits α_1, α_2, α_6, α_V, β_2, β_3 and β_4 for the specific case of hMSCs cultured on grooves. This may indicate that differential integrins govern the transduction of grooved topographical cues to FA signalling components.[74] Initial contact also plays an important role in modulating cell behaviour. In quasi-3D sandwich cultures, cells were shown to maintain their morphology and spreading orientation even when stimulated with opposing physical cues to their dorsal region.[75] Interestingly, aside from the well documented induction of cell alignment by grooved surface topography, 12.5 μm wide grooves have also been shown to prompt the reorganisation of the nuclear lamina of fibroblasts, which provides structural support for the nucleus. Nuclear elongation in combination with cytoskeletal forces on the nucleus impact by repositioning chromosomal territories, primarily at the telomeric regions of the larger chromosomes. Transposing this to osteoblasts and considering that the major genes contributing to osteoblast functionality such as osteocalcin, osteopontin, Runx2, among

others, are located within the telomeric regions of larger chromosomes, could explain a groove-induced facilitated accessibility to transcription factors.[76]

Shallow nanoscale pits (14 and 29 nm) have been shown to increase spreading and cell attachment of human fetal osteoblastic cells (hFOB) when compared to deep pits (45 nm) or flat substrates. On shallower pits, hFOB integrin expression was demonstrated to be selective on specific integrin subunits, namely α_v, which has been linked to cell area and attachment. In combination with the presence of highly tensioned actin stress fibres anchored to paxillin, this points to an integrin α_v-paxillin-actin mediation of nanoscale topography. Changes in FAK autophosphorylation at tyrosine-397 on nanopits may also be linked to changes in integrin α_v and paxillin.[77] On columns (100 nm diameter), fibroblasts presented markedly fewer stress fibres and a rounded cell morphology, when compared with fibroblasts on flat surfaces. Interestingly, columns induced a slightly higher number of filopodia, which cells use to probe the surrounding environment.[54]

Substrate curvature, convex or concave, has likewise been presented as an impacting factor on fibroblast behaviour. Fibroblasts cultured on top of glass spheres with diameters ranging from 5 μm to 2 mm embedded at the surface of hydrogels demonstrated that cell attachment rates and migration speeds declined as the sphere's diameter decreased. This was interrelated with a decrease in cell spreading, likely due to the increasing surface convexity inherent to smaller diameters.[78] The term "curvotaxis" has been attributed to the mechanism by which adherent cells react to curvature variations, specifically migrating towards negative curvatures. MSCs were shown to avoid convex regions during migration and position themselves in concave regions, with the nucleus positioned at the most concave areas. Whereas short-lived and less-tensed FA were formed on convex curvatures, concave curvatures were marked by more stable FA due to the increased intracellular tension, contributing to preferential cell positioning in concave areas. Rho activity and its regulation of cell migration, actomyosin contractility, and FA is hence required for curvotaxis. Additionally, actin-dependent compression of the nucleus and consequent high lamin-A to stabilise the nucleus are required for curvature-induced nuclear movements and cell migration. Furthermore, curvotaxis requires LINC (Linkers of the Nucleoskeleton to the Cytoskeleton) complexes, given their role in enabling force transmission within the cell through the nucleus by bridging the nuclear lamina and cytoskeleton.[57] Correspondingly,

actomyosin contractility was required for the alignment of endothelial cells and stress fibres on concave microgrooves (50 μm width). This effect was diminished upon treatment with blebbistatin, a myosin II inhibitor, which impacts cell contractility.[79]

Interfacial roughness impacts mechanotransduction pathways and controls MSC adhesion and fate via FA formation, activation of signalling proteins, generation of nuclear tension, chromatin remodelling, and transcriptional activity. For roughness gradients ranging from 50 nm to 1.2 μm, cell spreading decreased and cell circularity increased with increasing substrate roughness. An intermediate interfacial roughness was associated with an increased adhesion due to an increased cellular contractility, evidenced via the formation of more pronounced actin stress fibres, paxillin localisation, and densest filopodia. Nuclear conformation was markedly impacted by distinct roughness gradients, reporting large smooth nuclei with higher lamin A/C intensity on low to intermediate roughness, versus small wrinkled nuclei with low lamin A/C for high roughness. Considering the impact of nuclear conformation and effects on chromatin remodelling and alteration of transcriptional activity, the differences stated may in fact play a role in the modulation of cell phenotype. Accordingly, YAP nuclear localisation peaked for intermediate roughness values. In mixed medium containing both osteoinductive and adipogenic factors, osteogenesis was favoured and adipogenesis supressed. When solely containing osteoinductive or adipogenic factors, osteogenesis or adipogenesis were respectively induced, indicating the possible activation of distinct pathways.[56]

In fact, it is well established that topographical cues do not only impact osteogenesis and adipogenesis via mechanotransduction. Accordingly, alignment and acquisition of an elongated morphology has been observed for human neural stem cells (hNSCs) cultured on substrates with nanogrooves alone (300 nm width with incremental spacing between features)[80] and on combination substrates with both microgrooves (1.5 μm width) with nanopits (10 nm diameter).[81] When seeded on 300 nm diameter pillars with incremental spacing, cells became radially aligned.[80] With a 300 nm spacing between features, neuron differentiation was enhanced on nanogrooves comparatively to nanopillars, which was correlated with an enhanced FA formation and upregulation of phosphorylated FAK. This was also observed when comparing substrates with a greater spacing between features. FAK phosphorylation in turn can activate downstream intracellular signalling of MEK-ERK

pathways, which are involved in neurite outgrowth during stem cell differentiation.[80] Interestingly, hNSCs differentiation into functional neurons was enhanced on combination substrates featuring both microgrooves and nanopits when compared with flat substrates and substrates presenting only microgrooves or nanopits. These combination substrates presented an enhanced vinculin staining, as well as colocalization of integrin β_1 and neural cell adhesion molecule, even when compared with substrates presenting only a single feature. β_1 integrin-mediated binding in conjunction with ROCK-mediated intracellular signalling pathways promoted FA formation and FAK pathway activation, which enhanced differentiation of hNSCs. Furthermore, increased neurite sprouting from cell bodies was observed, which is known to augment cell-cell interactions and enhance hNSC differentiation via cell-cell signalling.[81] ROCK downstream signalling has been associated with an increased actomyosin contractility. In particular, the up-regulated gene expression of neuronal markers in human embryonic stromal cells has been attributed to a higher actomyosin contractility on nanogrooves (250 nm).[72,82] However, the expression level of microtubule-associated protein 2 (MAP2), a marker for mature neurons, was reduced via inhibition of myosin II, yet not by ROCK inhibition, indicating a ROCK-independent regulatory pathway of myosin II.[82] Furthermore, the increased FAK phosphorylation and higher pFAK/FAK ratio on nanogrooved versus flat substrates was correlated with the increased MAP2 expression. The higher MAP2 expression was attributed to early FAK activation via topographical cues and not alterations in cell shape *per se*. A plausible explanation is that by regulating the spatial organisation and elongation of FA, grooves impact the pulling angle of actomyosin contractility within the cell.[72]

For osteogenic differentiation, the selected cell population has been demonstrated to be an impacting factor with pre-osteoblastic cell line MC3T3-E1, hASCs, and periodontal ligament-derived stromal cells (PDLSCs) presenting commitment to the osteogenic lineage with distinct groove and ridge dimensions. Interestingly, the enhanced commitment to the osteogenic lineage for each cell type was linked with the maximum cell elongation, which may be linked to the tensile stress required for osteogenic differentiation.[58] On the micrometric scale with a fixed groove width of 5 μm, hMSCs cultured with supplements for specific lineage commitment, preferentially differentiated into the adipogenic lineage with increasing ridge width (15 μm), whereas decreasing ridge width (2 μm) preferentially

induced osteogenesis. Interestingly, 600 nm wide grooves with 650 nm ridges directed both adipogenic and osteogenic differentiation of MSCs, yet no significant upregulation was observed in the absence of lineage commitment factors. Furthermore, YAP localisation remained unaffected on grooved versus flat substrates.[83] Another study featuring grooves (300 nm width) or pillars (450 nm diameter with hexagonal or square organisation) with surface immobilised bone morphogenetic protein-2 (BMP-2) observed an increase in mineralisation and upregulation of osteogenic markers for these distinct topographical features as opposed to flat substrates. This result may in fact be linked to an augmented FA formation on substrates with topographical features, supported by an enhanced gene expression of FA assembly proteins such as vinculin and FAK.[84] Substrates with highly ordered topographical features have thus shown promising results in strategies aiming osteogenic differentiation. Interestingly, cell adhesion and osteogenic differentiation of osteoprogenitor cells was shown to be enhanced on nano-displaced pits (120 nm diameter pits, 100 nm deep), in contrast to a negligible effect observed for highly ordered nanotopographies.[55] Varying topographical cues have been shown to play a role in mineralisation, which could in fact be correlated with *in vivo* bone bonding to titanium implant.[60]

3.2. Geometrical cues

While topographical features actively modulate cell morphology to some extent (e.g., cell alignment with grooves), they generally do not fully control single cell geometry. A practical approach to study the effects of 2D geometry on cell behaviour is via microcontact printing to create adhesive and non-adhesive regions. These regions can be tailored in size, biochemical composition and spatial localisation, and shape, from less to more complex geometries. Microcontact printing of linear cell adhesive fibronectin elements with varying line alignment, density, and width, demonstrated that cell alignment altered the number and location of protrusive edges initiated by active Rac1, and that a high alignment was correlated with a rapid directional cell migration.[15] To assess the effects of anisotropic versus isotropic ligand arrangement on cytoskeletal organisation, circular and square geometries with distinct peripheral fibronectin localisation were patterned. An anisotropic ligand arrangement was shown to enhance actomyosin contractility and consequently redirected cell differentiation from adipogenic to osteogenic.[66]

In endothelial cells, cell shape and spreading proved to be impacting factors in directing cell proliferation or apoptosis. Using multiple FA-sized islands versus islands accommodating an entire cell, an increased cell spreading with a constant cell-matrix contact area was enabled by further distancing FA-sized islands. Increasing cell spreading was correlated with an increased cell proliferation and abrogated apoptosis.[16] While cell spreading is required for the formation of FAs and an increased spreading is correlated with a greater number of FAs, cytoskeletal tension has also been proven to play a role in moulding the shape and distribution of FAs and not integrin-ECM contact alone.[85] Also, by simply decreasing or increasing island size and hence the available surface area for cells to adhere, MSC fate could be directed to either adipogenic or osteogenic, respectively.[86] Cell shape reportedly modulated endogenous RhoA activity with osteogenic differentiation occurring only for spread cells with active RhoA, and adipogenic commitment requiring dominant-negative RhoA and unspread round cells. However, osteogenesis could be induced independently of cell shape by directly inducing actomyosin contractility via ROCK activation.[87]

Other major osteogenesis-promoting cues are cell aspect ratio and subcellular curvature. For example, commitment to the osteogenic lineage was boosted for single cells on rectangles (4:1 aspect ratio) versus squares (1:1). Concerning subcellular curvature, adipogenesis was favoured on flower shapes with large convex curves, while osteogenesis was preferentially induced on star-shapes with concave edges and sharp vertices. Star shapes reportedly induced larger FAs and stress fibres, with a consequent increase in actomyosin contractility and cytoskeletal tension. Actomyosin contractility stimulates MAPK cascades and Wnt signalling, via Wnt associated transcripts such as Rac1, Cdc42, RhoA, ROCK2, among others, which regulate differentiation into the osteogenic lineage. Geometries that led to lower contractility rendered cells more susceptible to adipogenic soluble factors, while downregulating Wnt signalling. Blocking selective cell surface integrin receptors also led to inhibition of osteogenesis due to the decreased tension exerted by the cell on the substrate. Furthermore, in the absence of lineage guidance soluble factors, stars expressed higher expression of GTPases involved in cell motility, Rac, and Cdc42, linked to greater polarity and protrusion.[86] Furthermore, high cell contractility has been shown to favour lipid raft formation, which triggers Akt recruitment to the plasma membrane and pathway activation towards osteogenic differentiation.[88]

Convex features on 2D substrates were shown to promote the assembly of lamellipodia, whereas concave features led to the assembly of stress filaments, which was linked to changes in polarity of rat melanoma cells.[89] On non-adherent regions, specifically negative/concave curvatures, cell migration mediated by a combination of leading-edge actin cables and the local induction of a tension anisotropy gradient. Whereas protrusions on cell-sized positive/convex curvatures occurs via retrograde flow, on negative/concave curvatures actin cables were formed due to an anterograde flow towards the cell edge.[90] On T, Y, and U-shaped spots, cells initially acquired the shape of micropattern, and secondly generated contractile stress fibres to minimise the distance between apices. Accordingly, stronger contractile stress fibres spanned over non-adhesive edges than over adhesive edges.[91] Aside from geometry, initial cell positioning is another preponderant factor for cell spreading, where corners require cell rotation and hence slow down cell spreading.[92]

On multicellular islands, similar trends regarding low or high cellular tension and selective differentiation have been observed. Whereas osteogenic differentiation was induced at island edges, adipogenesis was stimulated at the centre, regardless of geometry (mixed osteogenic and adipogenic soluble factors). To isolate the effect of curvature, undulating geometries were assessed, and it was observed that cells on convex edges underwent osteogenic differentiation while concave edges directed adipogenesis. Cells on convex edges were subjected to forces in a magnitude three-fold higher than concave edges. Hence, high stress regions with increased actomyosin contractility were associated with osteogenic differentiation, whereas low contractility on low stress regions induced adipogenesis. In a 3D microcarrier-based context, cells encapsulated within a collagen hydrogel also presented enhanced osteogenesis on the edge of constructs and adipogenesis in the core.[67] Particularly due to the effects of local curvature on cell fate, it would be interesting to explore the impact of microcarrier geometry upon implantation *in vivo*.

In a cell sheet model, a higher cell proliferation was localised in regions with enhanced tractional stress generated within the cell sheet. The geometry-dependent cell contraction originated patterns of mechanical stress which affected cell growth and highlighted the importance of tissue architecture.[93] Another approach using microfabricated tissue gauges (μTUGs) allowed to produce collagen-embedded microtissues between a desired number of micropillars. Micropillars acted as anchoring points and allowed to control matrix alignment,

measure microtissues' contractile forces and apply tensile strain. The mechanical stiffness of micropillars and collagen matrix impacted cellular contractile forces and matrix protein deposition, consequently altering tissue remodelling.[94] Pillar isotropic or anisotropic arrangement allowed to control matrix alignment between unaligned and aligned, respectively. Whereas higher microtissue stiffness was observed in aligned regions, this was not dependent on active cellular contractility, but was rather dictated by the collagen matrix and the cellular actin cytoskeletal network.[95]

Taken together, these studies underline the relevance of both topographical and geometrical cues on the mediation and activation of mechanotransduction pathways, which subsequently govern multiple cellular actions, such as migration, proliferation, and differentiation, ultimately overseeing tissue composition and architecture. However, it is to note that a good degree of uncertainty and unpredictability still surround the influence of physical cues on cell behaviour. Furthermore, the question arises whether such physical cues are sensed only upon direct contact with the substrate or if cells indirectly transfer these cues to neighbouring cells. As the main adhesion proteins at intercellular junctions, cadherins also play their part in mechanosensing of fluctuations in actomyosin cytoskeletal tension and subsequent mechanotransduction.[96] It would be expected that such mechanisms would play a role in the indirect transmission of topographical and geometrical cues. With the evolution of biofabrication tools enabling an even tighter control over feature design, endless iterations of feature dimensions become possible. Combined with inherent differences for distinct cell populations, it becomes difficult to reach a universal consensus. High-throughput studies aim to bridge this gap by combining large scale screening with machine learning to rationally design biomaterial surfaces.[59–61,97,98]

4. Microcarrier production methods

The application of microcarriers, particularly spherical microcarriers, in the regenerative medicine field is vast. Spherical microcarriers have been applied as vehicles for cell proliferation and expansion within bioreactors,[99] their biochemical surface properties have been tailored to enable the production of larger constructs via cell-mediated aggregation,[100] they have been utilised as cell encapsulation vehicles to direct localised *in vivo* tissue formation,[101] among others. The scope of this review lies in exploring the applications and

advantages of non-spherical microcarriers, focusing on microcarriers with unique geometries and surface topographical features.

Non-spherical microparticles may be produced via distinct microfabrication techniques. To produce spheroids and ellipsoids simpler techniques such as uniaxial stretching within sacrificial templates,[102–108] emulsion-based,[109–111] superhydrophobic surface-based,[112] and conventional continuous-flow microfluidic-based set-ups[113,114] have been applied. To produce other standard geometric shapes, such as cylinders, rectangular, and triangular prisms, or even more complex geometries, alternative methods have been applied. Methods for production of these geometries include photolithography,[115] and soft lithography techniques, such as replica moulding[116] and imprinting[117]. Microfluidics-based strategies with continuous flow[118] or stop-flow lithography,[119] as well as optofluidics[120] are popular alternatives. Figure I.4 highlights select examples for each of the fabrication methods described in this section, namely photolithography (photomask-based and digital mirror device (DMD)-based), soft lithography (replica moulding and imprinting), multiphoton lithography electrodeposition, electron beam and ion beam lithography (EBL and IBL), microfluidics, and optofluidics. Additionally, Table I.1 summarises the methods and respective materials used to produce microcarriers with variable geometries and topographical cues.

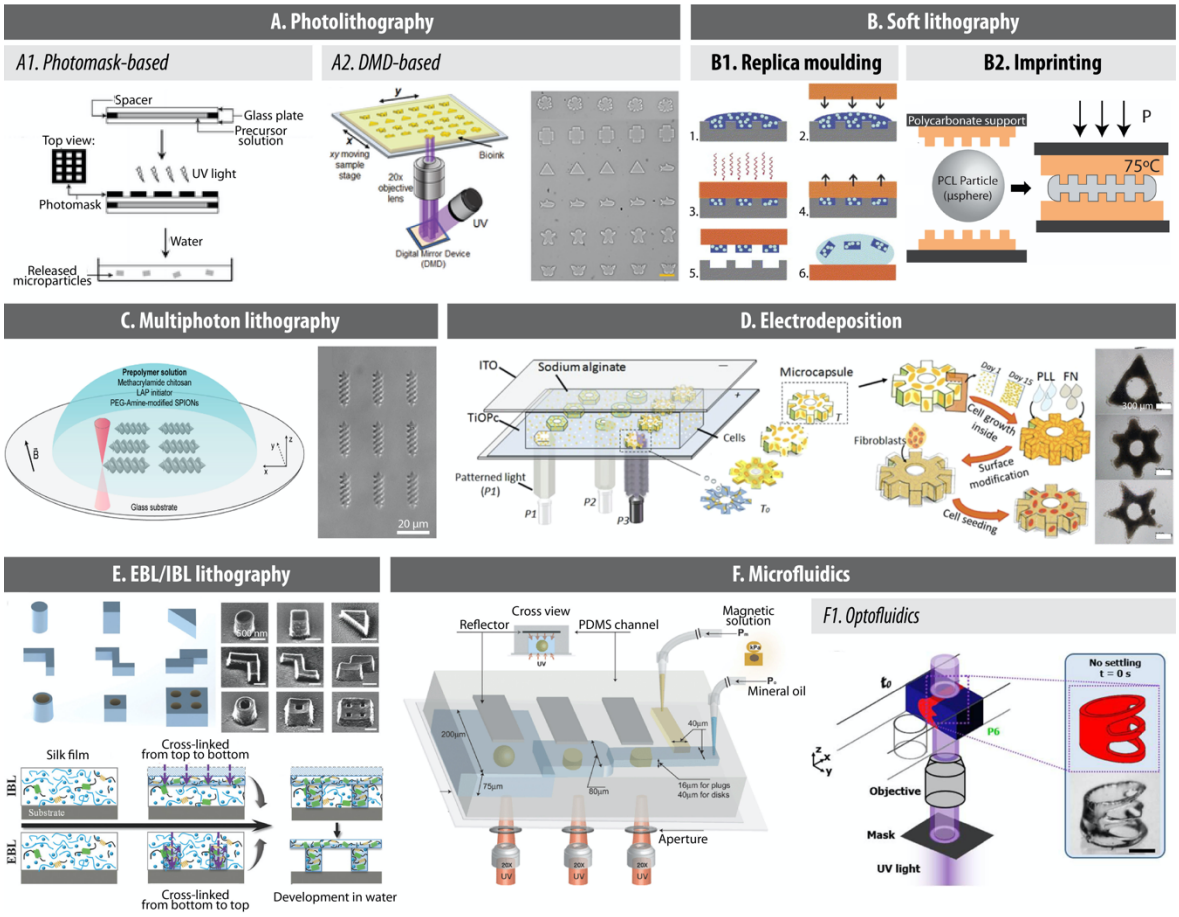

Figure I.4. Microcarrier production methods. A. Photolithography: photomask-based (A1) and DMD-based (A2) [Reprinted with permission from [167], Copyright (2007) American Chemical Society. Reprinted with permission from [168], Copyright (2019) John Wiley & Sons]. B. Soft lithography: replica moulding (B1) and imprinting (B2) [Reprinted with permission from [128], Copyright (2006) Elsevier. Reprinted with permission from [117], Copyright (2019) Royal Society of Chemistry]. C. Multiphoton lithography [Reprinted with permission from [170], Copyright (2018) American Chemical Society]. D. Electrodeposition [Reprinted with permission from [142], Copyright (2019) American Chemical Society]. E. EBL/IBL lithography. [Reprinted with permission from [138], Copyright (2018) John Wiley & Sons]. F. Microfluidics and optofluidics (F1) [Reprinted with permission from [189], Copyright (2008) Royal Society of Chemistry. Reprinted with permission from [120], Copyright (2016) Royal Society of Chemistry].

4.1 Photolithography

Photolithography relies on a projection-printing system where relief patterns are created via the projection of radiation within or near the UV-visible section of the electromagnetic spectrum. The technology uses an illumination system composed of a source and condenser lens assembly, as well as a photomask for region selective projection. The main limitation of photolithography hinges on the resolution, which is approximately half the wavelength of the illuminating light and is governed not only by the illuminating light but also the aperture of the projection lens. Initially dependent on visible g-line (436 nm) and UV i-line (365 nm)

sources, current technologies may resort to extreme-UV light (13.5 nm), which greatly increases resolution.[121,122] To produce hydrogel-based microcarriers, and in particular microcarriers aiming towards cell encapsulation, photolithography is an attractive and widely applied technique. Cells can be uniformly dispersed throughout the construct, and the control over spatial and temporal reaction kinetics can be easily achieved. However, both UV exposure time and photoinitiator concentration should be taken into consideration as they impact cell viability due to the generation of cytotoxic free radicals.[123] Nonetheless, taking advantage of current biotechnology solutions, these issues can be easily minimised, and interesting applications developed. For instance, fibroblast-encapsulating PEGDA-based microunits were produced via photolithography and further assembled into larger constructs via polypeptide-based crosslinkers present on the microunits' surface.[124] As an example of a specific tissue engineering strategy, the technique was applied for the fabrication of methacrylated chitosan and hydroxyapatite based osteon-like structures encapsulating osteoblast-like MG63 cells and HUVECs in a spatially controlled manner.[125] Photolithography can be further employed as a secondary technique for microcarrier production. For instance, electrospun fibres dispersed in a PEGDA precursor solution yielded cylindrical fibre-entrapped microgels upon localised photolithography and bare fibre dissolution. The main advantage here lies in the possibility to produce distinct compartment combinations within the same unit by sequentially stacking electrospun fibres with tailored compositions and/or bound growth factors.[126]

4.2 Soft lithography

Soft lithography relies on printing and moulding mainly using elastomeric masters, which present the patterns of interest in bas-relief.[127] It encompasses several techniques such as microcontact printing, replica moulding, imprinting, microtransfer moulding, micromoulding in capillaries, and solvent-assisted moulding. For the production of microcarriers, replica moulding and imprinting are the most commonly applied soft lithography techniques. Both techniques can be used on a broader range of materials than photolithography. During replica moulding, the pre-polymer solution is cast onto the master and subsequently crosslinked. The resulting structure is dependent on the van der Waals interactions, wetting, and kinetic factors during mould filling.[122] Replica moulding has been applied as a strategy to produce geometrically tuneable microconstructs encapsulating cells

via photocrosslinking of a cell-laden pre-polymer solution.[128] A variation on replica moulding, particle replication in non-wetting templates (PRINT) produces isolated particles as the non-wetting surface confines the liquid precursor within the features of the mould. This technique may even be applied for a continuous, roll-to-roll production of high-resolution particles.[129,130] Imprinting in turn relies on the thermoplastic properties of polymers and bypasses the need for photoinitiators. Due to the high temperatures generally required for the plastic deformation of a polymer, this technique is not compatible with cell encapsulation but presents itself as an attractive technique to produce microcarriers for cell anchorage.[117] Replica moulding and imprinting are both simple and inexpensive methods to obtain microconstructs with a nanometric resolution, which can include topographical features.[122] Nonetheless, the initial stamp generally relies on methods such as photolithography[127] or rapid prototyping techniques such as stereolithography[131] to be produced. Interestingly, mould fabrication via an etching process originates Bosch etch lines as an artefact of the process. This may generally be considered a disadvantage of the process, yet it is in fact a relatively simple approach to tune geometry and topography simultaneously. Upon PRINT, resulting cuboidal particles presented ridges on four faces, corresponding to the etch lines in the mould.[132,133] A limitation of the imprinting and replica moulding technologies is the removal process of constructs. Options to circumvent this issue include sacrificial templates[117,134] or responsive moulds with pneumatic-aid to enable recovery and minimise shape distortion.[135,136]

4.3 Electron beam, ion beam, and multiphoton lithography

A further decrease in feature size and increase in nanoscale complexity requires the employment of alternative technologies. Electron beam and ion beam lithography are both maskless patterning techniques that allow to produce constructs with nanoscale precision. Electron beam lithography (EBL) provides a higher resolution and penetration depth than ion beam lithography (IBL), yet electron beam projections are susceptible to pattern distortion.[137] IBL presents the advantage of reduced scattering, resulting in higher patterning precision. These two techniques have in fact been combined where an initial EBL writing step was applied to produce nanopillars, which were subsequently sculpted via IBL. By leveraging the induction of structural changes in spider silk upon ion penetration,

asymmetric complex microconstructs with nanoscale precision were produced while bypassing the need for potentially cytotoxic photoinitiators.[138]

Another option is single-photon lithography, which applies a UV laser that photopolymerises a specific area in proximity with the focal point. A submicrometric x,y-resolution can be obtained, yet z-resolution is typically above 25 µm given the occurrence of initiation reactions above and below the focal plane. Using a near-infrared (NIR) laser source, multiphoton lithography relies on the two-photon absorption of NIR light to confine photoreactions to the focal plane, improving z-resolution to 2-3 µm. Multiphoton lithography enables a deeper sample penetration, yet is more time consuming and costly than single-photon lithography.[139,140] The main limitation to produce cell encapsulating hydrogels via multiphoton lithography currently lies in the limited efficiency of available two-photon initiators, which should ideally be hydrophilic, water soluble, and present a molar absorptivity within the NIR range (800 nm).[141]

4.4 Electrodeposition

Electrodeposition is a versatile tool to produce cell encapsulating, geometrically diverse thin structures according to an exposure pattern that can be changed in real time by using a digital mirror device (DMD)-based system projecting CAD files. The system is composed of a photoconductive electrodeposition chip, a visible light supply coupled to a DMD, and a direct-current (DC) power supply.[142] Alginate is a commonly applied biomaterial for the electrodeposition method given the non-cytotoxic and facile process of alginate crosslinking with divalent ions, such as calcium. Calcium-alginate electrodeposition is triggered at the electrode surface by the electrochemically induced release of calcium ions from calcium carbonate particles included in the initial alginate solution. Upon application of a direct current voltage to the photoconductive chip, the DMD-based system limits light projection to a restricted area where ionic crosslinking of alginate occurs.[143] Crosslinked alginate structures, which may be laden with cells, can then be used as templates for liquefied-core capsule formation. Upon build-up of a multi-layered membrane via layer-by-layer technique with alginate, chitosan, and PLL, the alginate core is liquefied using calcium chelation. The final structure is a liquefied-core microcapsule that maintains the original form of the electrodeposited alginate.[142–146]

4.5 Microfluidics

Microfluidics is the technique by which fluids are manipulated within channels with dimensions below the micrometric range. Via the manipulation of multiphase flows it enables the production of polymer particles, emulsions, and foams.[147] Commonly applied for the production of spheres, this technique may be employed to produce sphere deformation geometries such as rods, ellipsoids, and discs.[118] Furthermore, by increasing the complexity of the system, more intricate shapes can be fabricated.[120] Coupling of the microfluidics system with photopolymerisation enables crosslinking of a photocurable resin or photosensitive polymer and subsequent collection of the produced particles. Continuous flow lithography supports the continuous generation micrometric hydrogels via photopolymerisation in a free-floating manner, where microgels are not adhered to a substrate, as opposed to what occurs in regular photolithography. Both the optical resolution and depth of field of the microscope objective condition the dimensions of obtained particles.[118] However, this technique demands either short polymerisation times or slow flow rates, which requires highly concentrated prepolymer solutions and raises cytotoxicity issues. Stop-flow lithography appeared as an alternative to overcome this setback of continuous flow lithography while allowing cell-laden microgel production at a rapid rate. This technique relies on three steps, namely interruption of the liquid flow, followed by polymerisation of the patterned solution, and lastly particle flowing out of the device.[119]

Initially proposed systems for both continuous and stop-flow lithography within microfluidic channels relied on photomasks. Currently, microfluidics is combined with DMD-based technologies, termed optofluidics. High-speed optical projection systems are coupled with two-dimensional micromirror arrays, which control and projects UV exposure patterns according to linked computer aided design (CAD) files, circumventing the need for photomasks.[148] Furthermore, by inserting obstacles such as pillars and varying microchannel geometry, these systems are able to control inertial flow shaping, gravity-induced flow shaping, and UV light patterns to create truly complex geometries.[120,149–152]

Table I.1. Microcarrier geometries applied for drug delivery and tissue engineering strategies with corresponding material and production method.

Shape	Material	Production	Ref
Dimpled spheres	Polystyrene (PS)	Dispersion polymerisation	[153]
Spheroids, ellipsoids, and rods	Poly (lactide-co-glycolide) (PLGA)	Emulsion solvent evaporation	[109–111,154]
Capped ellipsoids	Alginate with magnetic nanoparticles	Hanging drop crosslinking	[155]
Spheroids, cylinders, heart-shaped, rectangular, hexagonal, triangular prisms	Methacrylated chitosan, alginate, PCL	Superhydrophobic/superhydrophilic surfaces	[112,156,157]
Spheroids, ellipsoids, compartmentalised rods	Poly(methyl methacrylate) (PMMA), PS, polycaprolactone (PCL), ethoxylated trimethylolpropane triacrylate (ETPTA) and magnetic nanoparticles	Uniaxial stretching within sacrificial matrix	[102–105,108,158]
Hollow ellipsoids	Polydopamine, PS	Uniaxial stretching within sacrificial matrix. Posterior gas foaming or coating with polydopamine and PS leaking with tetrahydrofuran	[106,107]
Barrel-, dumbbell-, and funnel-shaped	PEG, gelatin-methyl acrylate (GelMA), polyacrylamide (PAAm)	Material-dependent crosslinking while applying liquid bridge phenomenon between two surfaces	[159]
Cylinders	PLLA	Electrospinning and aminolysis	[160]
Rods and spheres with single or multiple protruding fibres	PLGA	Single and multiplexed electrospray	[161]
Cylinders, cubes, rectangular, hexagonal, and triangular prisms, arrow-, star-, Z-, cross-, donut-, plus sign-, and saw-shaped	Photocurable epoxy-resin SU-8, PEG, PEGDA, silk proteins (fibroin and sericin), alginate, gelatin, methacrylated hyperbranched polyglycerol, hydroxyapatite	Photolithography	[115,124,125,162–167]
Cylinders, cubes, triangular prism, animal-(octopus, shark, butterfly), plus sign-shaped	ETPTA, PEG methacrylate, GelMA, and PAAm	Photolithography system with DMD	[168,169]
Multi-compartmentalised cylinders	PEGDA hydrogel containing PLGA fibres	Electrospinning and photolithography	[126]

LEGO bricks and complex geometries	Genetically engineered spider silk	Combination of IBL and EBL	[138]
Helicoids	Methacrylamide chitosan or GelMA containing iron oxide nanoparticles	Multiphoton lithography	[170,171]
Helicoids	Alginate/PEGDA containing magnetic nanoparticles	Microfluidic spinning and coiling technology	[172]
Cylinders, hexagonal, triangular and rectangular prisms, keyboard character-shaped, complex shapes (characters, puzzles, barcodes, smiling faces, ring-over-disc, cross, yin–yang, three-discs-over-a-bar, circle-over-wrench, assembled triangular, assembled zigzag, and assembled quadrilateral)	Collagen type I, sPEG-A with SPIONs, methacrylated hyperbranched polyglycerol, hyaluronic acid, PEGDA, PLGA, commercial photosensitive resin	Replica moulding	[67,116,128,167,173–176]
Cylinders and rectangular prisms	Agarose	Replica moulding with thermoresponsive PNIPAAm moulds	[177]
Cylinders	PLGA	Solvent/non-solvent plasticization replica moulding	[178]
Cylinders, pentagonal, triangular and quadrangular prisms, plus- and hepatic lobule-shaped. Cylinders with cylindric, rectangular, and triangular cut-outs	Collagen type I, gelatin, agarose, and matrigel	Pneumatic-aided replica moulding	[135,136]
Cubes, cylinders, grooved cubes	PEG; combination of ETPTA, cystaminebisacrylamide, aminoethyl methacrylate, doxorubicin, and hydroxycyclohexylphenyl ketone; combination of albumin and insulin	PRINT	[132,133,179]
Nanogrooved microdiscs ("topodiscs"), cubes, donut-, and LEGO-shaped	PCL, poly(d,l-lactic acid) (PDLLA)	Imprinting	[117,134]
"Spiky" microparticles	Alginate, polyethylene glycol (PEG) and dextran	Aqueous two-phase based microfluidics	[180]
Ellipsoids, truncated spheres, hemispheres, tear-, and bullet-shaped, rods, cylinders, rectangular, hexagonal, and triangular	Alginate, PEGDA, PEGDA with magnetic nanoparticles, PLGA, tripropyleneglycol diacrylate, ethyleneglycol dimethacrylate, 1,6-	Continuous flow lithography microfluidics	[113,114,188,189,118,181–187]

prisms, rings, keyhole-shaped	hexanediol diacrylate, dimethacrylate oxypropyl dimethylsiloxane, divinylbenzene, ethyleneglycol diacrylate, pentaerythritol triacrylate		
Cylinders, cubes, rectangular, pentagonal, hexagonal, and triangular prisms, donut-, cross-, and S-shaped	PEGDA, 3-(trimethoxysilyl)propyl acrylate:ethoxy trimethylolpropan	Stop-flow lithography microfluidics	[119,190–192]
Bell-, bullet-shaped	PEGDA with magnetic nanoparticles	Non-uniform UV stop-flow lithography microfluidics	[193]
Wrinkled-surface cylinders, heart- and deformed rhombus-shaped	PEGDA	Stop flow lithography with wrinkling post-process	[194]
Complex shapes, cubes, triangular and rectangular prisms, star- and L-shaped	PEGDA, GelMA	Optofluidic fabrication in regular or non-rectangular microfluidic channels	[120,149–152]
Hollow hexagonal-, gear-, donut, square frame-, dumbbell-, rod-, and hepatic lobule-shaped	Alginate, chitosan, and PLL	Photo-induced electrodeposition and layer-by-layer	[142–146]

5. 3D application of geometrical and topographical cues

5.1. Tissue engineering

5.1.1. Top-down versus bottom-up

Tissue engineering strategies for 3D cell culture can roughly be divided into two approaches: top-down and bottom-up. In top-down strategies, a prefabricated scaffold is populated with cells, which are expected to migrate within the scaffold and create their own extracellular matrix (Figure 5). Scaffolds are often coupled with systems for aided perfusion, bioactive molecules such as growth factors, and even mechanical stimulation.[195] However, the restrictive architecture and geometry of top-down scaffolds are an impediment for optimal cell culture, limiting mass transfer and hindering the production of a functional histoarchitecture.[196] Cell migration is also restricted within these systems, resulting in an inhomogeneous cell distribution throughout the scaffold.[134] Furthermore, when considering engineering vascular tissues, vascularisation of top-down fabricated constructs has proven to be challenging.[196] In fact, one of the major difficulties in TE is to develop a vascular network, capable of sustaining the requirements of the engineered tissue. Whereas perfusion

bioreactors can be used *in vitro* to enable an adequate diffusion within large constructs, upon implantation, a functional vasculature is required to supply oxygen and nutrients to the entire engineered construct. Since vascular ingrowth of host blood vessels to the construct is a slow process, cells within large-scale, non-vascularised constructs will likely suffer from nutrient deficiencies and/or hypoxia.[197]

Bottom-up appears as an alternative to the traditional top-down approaches, where smaller, often micrometric carriers, are assembled, either in a random or controlled manner, to form larger structures (Figure I.5).[195] With these microcarriers, cells can either be encapsulated within the core (Figure I.5A), or adhere to the exterior of the microcarriers (Figure I.5B). Bottom- up strategies enable a homogeneous cell seeding and have the added advantage of allowing to spatially control the distribution of cell-laden modules with the aim of acquiring a functional histoarchitecture.[196,198] Recent trends point towards the use of minimalist "low material" approaches, which enable cell self-organisation while delivering biochemical and biophysical cues for an optimal tissue regeneration.[199] Polymeric spherical systems for both cell encapsulation and cell anchorage have been extensively studied and reviewed previously.[200,201] Materials used in such systems range from naturally derived materials, such as chitosan[202] and alginate,[203] to synthetic materials, such as polycaprolactone[204] and poly(ethylene) glycol–vinyl sulphone.[205]

Cell encapsulation within micron-sized hydrogels for minimal invasive implantation is an example of a bottom-up approach. Micron-sized hydrogels were first reported in 1980 for the immunoisolation of pancreatic islets.[206] Since then, developing and exploring microencapsulation techniques has received increasing interest. Due to their tuneable mechanical properties and degradability, hydrogels present themselves as optimal vehicles for cell encapsulation. Encapsulated cells are protected from the exterior environment and, via engraftment of polymer chains with peptide motifs, when necessary, cell attachment and long-term proliferation is enabled.[207] Typically applied for encapsulation of multiple cells simultaneously, these systems may also be used to envelope single cells.[208] However, for constructs typically above a maximum diffusion distance of 200 μm, diffusion of oxygen and nutrients to cells within the hydrogel core is impaired, leading to the formation of a necrotic core.[209,210] To overcome this drawback, strategies to include pores within hydrogels, such as porogen leaching, electrospinning, among others, have been explored.[199] Another

option is to use chemical bonding via PEG-NHS annealing of previously produced cell-laden microgels, resulting in an inherently porous structure due to the interstitial spaces formed between spherical microgels.[211] Such structures are commonly referred to as bead-based or granular scaffolds and have been recently reviewed elsewhere.[212] Liquefied-core capsules are likewise an attractive option where cells are cultured in a compartmentalised liquid environment, with facilitated diffusion comparatively to jellified environments.[210] The embedding of microfluidic networks within the hydrogel network via bioprinting, soft lithography, or fibre templating may also improve diffusion.[213]

Whereas polymeric microparticles of spherical or other geometries may be applied for cell encapsulation, an alternative is to use these platforms as anchoring points.[19,214,215] The surface of microcarriers may be tuned both biochemically and physically.[216] Selective cell anchoring capabilities have been imparted onto spherical microcarriers via the immobilisation of specific monoclonal antibodies for either endothelial or stem/stromal cells, allowing to separate and capture the desired cell population.[202] Via physical modification, anchorage microcarriers can be imparted with topographical and geometrical cues to control cell fate. To this end, nanogrooved microdiscs, "topodiscs", directed cell fate towards the osteogenic lineage simply due to the topographical cues present on the surface of these tailored disc-shaped particles.[117] Whereas the assembly of anchorage-dependent bottom-up approaches may be cell-mediated,[202] they may also rely on chemical crosslinking. Both enzyme- and ultraviolet light-mediated annealing of spherical microgels have been previously applied to develop injectable bead-based scaffolds with tuneable geometry, which could anchor cells. The size of applied microgels governs pore size and consequently controls cell migration throughout the scaffold.[205,217]

A combination of cell encapsulation and anchorage was established where cell-laden microgels were subsequently coated with a distinct cell population. This strategy aimed to produce a pre-vascularised network that could anastomose upon implantation.[218] Ultimately, bottom-up strategies can be used to interweave a pre-vascularised network between cell-seeded micrometric structures in a precise manner, something which would not be possible with top-down strategies.[219]

Due to the micrometric nature of units applied for bottom-up strategies and their proximity in size to cell dimensions, this unlocks several opportunities to tailor and guide cell response via biophysical signals such as geometrical, mechanical, and topographical cues. An interesting approach relied on the use of microcontact printing to spatially position polyelectrolyte multilayers or PLGA microfilms. The geometry for these thin films ranged from 2 μm microparticles to millimetre long fibres. Upon cell adhesion to micropatterned sections, the temperature-sensitive sacrificial layer allowed to collect cell-loaded constructs, which then assembled as cell-microparticle aggregates or mesh-supported cell sheets.[220] Considering the fibrous environment of the ECM, microfibres appear as attractive biomimetic tissue engineering substrates. The techniques used to produce these fibres and their applications have been previously reviewed.[221] Additionally, fibres can be tailored via the introduction of topographical features, such as grooves, which opens up a multitude of possibilities.[222]

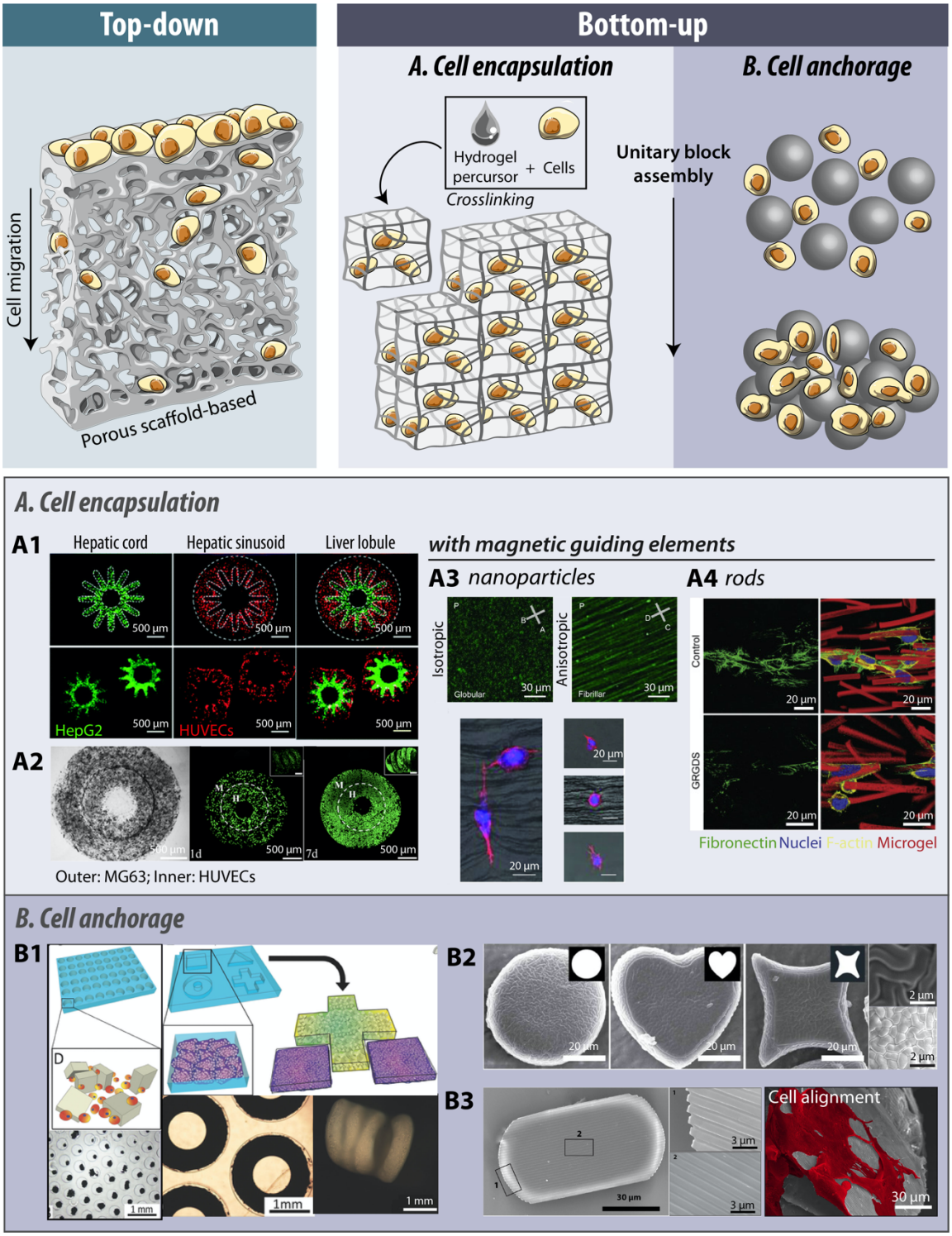

Figure I.5. Schematic representation of top-down versus bottom-up tissue engineering strategies. Bottom-up cell encapsulation (A) and cell anchorage (B) approaches. [A1. Reprinted with permission from [135], Copyright (2016) Royal Society of Chemistry. A2. Reprinted with permission from [125], Copyright (2015) American Chemical Society. A3. Reprinted with permission from [173], Copyright (2018) Elsevier. A4. Reprinted with permission from [224], Copyright (105) John Wiley & Sons. B1. Reprinted with permission from [115], Copyright (2014) John Wiley & Sons. B2. Reprinted with permission from [194], Copyright (2016) Springer Nature. B3. Reprinted with permission from [117], Copyright (2019) Royal Society of Chemistry.]

5.1.2. Cell encapsulation

Living tissues are generally composed of different cell types, which are organised in tissue specific conformations. In order to mimic these geometrical patterns, tissue engineering approaches must resort to strategies that allow to spatially control cell organisation.[165] As has been previously stated, several techniques can be used to produce cell-laden constructs with relevant geometries.

Cell-encapsulating hydrogels with varying geometry have to some extent been explored as proof of concept and produced using distinct techniques. For example, oxidised methacrylated alginate cylindric microgels produced via microfluidics have been shown to be a viable option for chondrocyte encapsulation.[113] Pneumatic-aided replica moulding has been applied to produce cell-laden microgels with well-defined geometries, bypassing replica moulding issues related with deforming constructs upon production.[135,136] DMD coupled photolithography enables the cell encapsulation within butterfly- and cross-shaped microgels (approx. 300 μm width).[168] Cylindric and rectangular prism shaped liquefied capsules produced via a combination of electrodeposition, layer-by-layer, and core liquefaction are too promising candidates for cell culture.[145] Another approach relies on the use of superhydrophobic surfaces with hydrophilic regions with different shapes. This method granted the encapsulation of cells within thin alginate microgels of various shapes (cylinders, heart-shaped, rectangular, hexagonal, and triangular prisms) with diameter/length of 3 mm. Comparatively to bulk hydrogels with 2 mm thickness, thin alginate films produced via this method presented a significantly increased cell viability and metabolic activity.[156] Furthermore, the inclusion of magnetic nanoparticles enabled cell-laden microgel manipulated by an external magnetic field.[155,156,223]

Even though mentioned studies produce microgels with specific geometries, few or no comparisons have been made between geometries on aspects such as cell viability or proliferation. To this end, the effect of varying circularity of methacrylated chitosan hydrogels from spheres to spheroids on the viability of encapsulated L929 cells was studied. Specifically, oblate ellipsoidal hydrogels with smaller short axis presented a higher cell viability than spheroids with longer short axis or spheres. Since spheroids possessed a higher

surface area to volume ratio, this likely facilitated oxygen and nutrient diffusion to encapsulated cells.[112]

Co-culture cell encapsulation strategies have similarly been explored. Replica moulding with PDMS moulds was employed to produce adhered or free-standing collagen hexagonal prisms with encapsulated fibroblasts. By seeding a second collagen precursor to fill the gaps between crosslinked hexagons, the authors produced coplanar arrays of fibroblasts pre-labelled with distinct fluorescent dyes, demonstrating its potential for the inclusion of distinct populations of cells. Moreover, several layers could be stacked to form a larger construct.[116] In turn, thermoresponsive poly(N-isopropylacrylamide) dynamic micromoulds were applied to fabricate compartmentalised cell-laden microgels shaped as cylinders or rectangular prisms. The strategy involved crosslinking fibroblast- or HepG2-laden agarose microgels within the mould and subsequently leveraging its thermoresponsive behaviour to induce expansion, allowing for the deposition and crosslinking of an outer HUVEC-laden layer.[177] Similarly, pneumatic-aided replica moulding was applied to produce cylindrical collagen microgels containing single or multiple channels with distinct geometries (squares, triangles, or circles) to ensure a higher oxygen and nutrient diffusion. Multi-compartmental microgels were similarly produced, containing at the core cylindric, rectangular, or triangular prism shaped hydrogels encapsulating HepG2 cells, fibroblasts, or A549 cells, and enveloped by a semi-spherical HUVEC laden microgel.[135] Alternatively, HUVEC coating of collagen type I cylinders encapsulating HepG2 cells, assembled within a larger construct and perfused with cell culture medium or whole blood, demonstrated that HUVEC presence led to an increased clotting time and reduced thrombogenicity.[174]

Aside from microunit fabrication, another key aspect of the bottom-up strategy lies in the assembly process. To this end, “lock and key” assembly is an option to group compatible shapes that have been previously produced via methods such as photolithography,[164,165] electrodeposition combined with layer by layer and core liquefaction,[143] crosslinking within two surfaces (liquid bridge phenomenon),[159] or microfluidics.[151] By placing microgels under agitation, compatible shapes aggregate via a “lock and key” type assembly.[165] Similarly, acoustic waves induce microgel self-assembly, where parameters such as acoustic frequency and amplitude can be optimised.[164] Optically induced dielectrophoretic manipulation likewise allows to assemble microgels with distinct geometries (cubes, triangular and

rectangular prisms, L- and star-shaped), laden with distinct cell populations, in a "tetris"-like manner.[151] Self-locking donut- and dumbbell-shaped liquefied microcapsules containing cells within the core have also been reported. For that, alginate constructs with the corresponding shape were produced via electrodeposition combined with layer by layer and core liquefaction. Whereas the layer-by-layer process caused shrinkage, which allowed to fit the dumbbell within the donut, liquefaction-induced microcapsule swelling allowed to achieve self-locking of both shapes.[143] Alternatively, chemical assembly can be applied to group cell-laden microgels with different geometries (cubes, cylinders, and star-shaped). This was performed via a Michael-type addition reaction between the acrylate groups on microgel surfaces and the thiol groups on the crosslinker. Interestingly, constructs fabricated by the assembly of star-shaped microgels presented higher porosity, permeability, and interconnectivity when compared with constructs produced with cubic and cylindric microgels. This technique could hence be useful to produce larger constructs with tuneable properties.[124]

Moreover, strategies to guide the spatial distribution of cells within hydrogel structures have been recently explored. These strategies generally include magnetic nanoparticles and rely on a magnetic field to control their distribution and orientation, upon which the hydrogel network is crosslinked in place. Moreover, the mechanotransduction pathways set in motion by these hydrogel-embedded cues have been subjected to a greater analysis than solely the role of geometry. Aligned topographical features were produced within a 3D hydrogel matrix via magnetic field directed self-assembly of magnetic nanoparticles into chains. Nanoparticles were coated with distinct proteins (fibronectin, laminin, or BSA) to mimic ECM fibres and parameters such as chain length, width, and interchain distance were controlled. In this case, fibroblasts encapsulated within aligned nanoparticle loaded Matrigel tended to have more extended dendrites directed parallelly or perpendicularly to chains as opposed to conditions with randomly distributed nanoparticles.[224] Using the same model, it was determined that the generation and length of fibroblast's protrusion was dependent on the expression of integrin β_1 and fascin, yet co-alignment with engineered fibrils was still verified independently of their knock-out. Conversely, protrusion length upon myosin II inhibition with blebbistatin remained unchanged, while protrusion orientation was markedly random (Figure I.5A3).[225] Given the role of myosin II in the deformation of cell shape by

generating contractile tension via actin filament pulling, this study links cell contractility with the sensing of topographical cues in a 3D environment.[225,226] Following a similar strategy, another study incorporated rod-shaped magnetic inert or peptide-coupled microgels within bioactive fibrin or inert PEG hydrogels (Figure I.5A4). Whereas fibroblasts in fibrin hydrogels aligned independently of microgel surface chemistry, a striking increase in fibronectin production was observed for bioinert microgels. Fibronectin co-localisation with vinculin led to conclude that with inert microgels, cells were required to produce their own ECM for attachment. Nuclear YAP localisation increased with higher microgel content and with peptide-coupled microgels, pointing to a stronger interaction of cells with peptide-coupled microgels. Within PEG hydrogels, biofunctionalized microgels were required for cell attachment and spreading, whereas almost no fibronectin was produced with inert microgels.[173]

Strategies for bone and liver tissue engineering have been particularly explored in the literature. Such approaches, which generally take advantage of geometry to replicate osteon- or lobule-like structures and feature compartmentalised distribution of distinct cell populations, are described in the following subsections in more detail.

5.1.2.1. Liver

Aiming to replicate the architecture of a biomimetic lobule-like microtissue, a system consisting of the compartmentalised encapsulation of HepG2 cells and HUVECs was developed. To this end, HepG2 cells were seeded within the core in a hepatic cord-like geometry whereas HUVECs were seeded in a hepatic sinusoid-like geometry (Figure I.5A1). Upon treatment with analgesic drug acetaminophen, which is known to induce hepatotoxicity, the lobule-like microtissue formed was shown to be more sensitive to acetaminophen when compared with a HepG2 monoculture in both 2D (monolayer) and 3D (encapsulation in collagen hydrogel) conditions. Hence, the developed microtissue could in fact be a useful 3D tissue model for *in vitro* drug toxicity screening.[135] However, the results obtained could be mostly attributed to the co-culture and not geometry of the constructs *per se*.

Another approach to produce hepatic lobule modules relied on a gear-shaped geometry, where alginate constructs containing RLC-18 rat liver cells were initially produced via electrodeposition. Upon detachment, modules were coated with PLL to form an outer shell and the alginate core was liquefied to originating microcapsules. When comparing gear-shaped modules (975 μm diameter with a 300 μm height) and cylindric modules (840 μm diameter and 400 μm height), an increased albumin and urea secretion was observed for gear-shaped modules at more advanced timepoints, demonstrating a higher hepatic function. This study in fact highlighted the role of geometry on hepatic function but failed to determine the mechanotransduction pathways activated in the process. In addition, gear-shaped modules could be further assembled into 3D four-layered hepatic lobule models.[144,146] Aiming to take this concept a step further into a co-culture system, the outer shell of fibronectin coated gear-shaped microcapsules containing HepG2 cells was posteriorly seeded with fibroblasts. Fibroblast adhesion to the exterior of constructs enabled a continuous increase in urea and albumin secretion and, upon lobule module stacking, mediated construct self-bonding.[142]

5.1.2.2. Bone

An approach to produce an osteon-like structure relied on the compartmentalised encapsulation of human osteoblast-like cells (MG63) and HUVECs within alginate and gelatine hydrogels. MG63 or HUVEC laden microgels were fabricated using photolithography and assembled via a "lock and key" assembly for cylindric and cross-shaped microgels, or a "concentric double-ring" assembly for donut-shaped microgels.[227] Taking this concept further, osteon-mimetic concentric double-ring structures (2 mm outer diameter) were produced using methacrylated chitosan and hydroxyapatite. The inner ring contained HUVECs whereas the outer ring contained MG63 cells (Figure I.5A2). The osteogenic and angiogenic potential of the co-culture system was evidenced by a significantly increased collagen I and VEGF expression, as well as a slight increase in ALP and osteocalcin expression when compared to the monoculture system.[125] The benefits of a co-culture system composed of osteoblasts or stromal cells in combination with endothelial cells for the formation of bone-like tissue have been previously proven.[228,229] Hence, an interesting approach would be to compare the expression of specific bone and

vascularisation markers for distinct geometries. By controlling cell localisation within hydrogels and playing with different geometries, it would be possible to take a step forward in pinpointing the role of geometry and its specific impact on the outcomes observed. Given the impact of actomyosin contractility in osteogenic differentiation, the effects of tension in a 3D context were studied. Using a combination of osteogenic and adipogenic factors, MSCs encapsulated within hydrogels preferentially differentiated into the osteogenic lineage at the edge of hydrogels, whereas cells localised in central regions underwent adipogenesis. Upon treatment with blebbistatin, a myosin II inhibitor, a considerable decrease in osteogenesis was observed, which allowed to link this occurrence to an increased actomyosin contractility in the hydrogel periphery. Moreover, by expressing ROCKΔ3 so as to increase myosin activity, a thicker layer of cells differentiated into the osteogenic lineage was observed.[67]

5.1.3. Cell anchorage

As previously stated, microcarriers as anchoring points for cells are another attractive option bottom-up approach. RGD-coupled PEGDA microrods (length 150-450 μm) were shown to enable fibroblast adhesion and led to the formation of larger aggregates via a cell-mediated bottom-up assembly.[188] Via reeling of magnetic alginate fibres, ring structures (diameters of 40 or 160 μm) were produced and seeded with fibroblasts, which aligned along the longitudinal direction of fibres and acquired a spindle-shaped morphology. Cell-seeded microrings could additionally be stacked via non-contact magnetic micromanipulation to form larger constructs (Figure 5B1).[230] In line with this, helicoidal cell-seeded microcarriers may be assembled via translational corkscrew motion, activated by a rotating magnetic field, to form double or triple helix structures, while staining cell survival.[172]

Cubes (40x40x40 μm^3), rectangular prisms (80x80x40 μm^3) and plus sign-shaped (90x90x40 μm^3) micro-objects produced using a photocurable resin have been demonstrated to enable a cell-mediated assembly of micro-objects into larger constructs. Upon placement of constructs into toroidal-shaped moulds, cells could further mediated construct fusion into millimetre-sized toroids, which could in turn be stacked to form tubular structures.[115] "Low material" strategies such as ultrathin PCL microparticles with varying geometry have also been shown to enable a cell-mediated assembly and even particle folding to generate 3D constructs.[157] When comparing donut-shaped and cubic geometries for culturing of hMSCs,

a similar cell viability with both types of micro-objects was observed. Theoretically, donut-shaped objects should introduce more pore volume into the resulting aggregate and consequently impact oxygen and nutrient diffusion, yet this appeared not to be the case. Upon mono or co-culture of hMSCs and HUVECs with cube-shaped objects, the authors concluded that cell type and order of cell seeding with cubes determined aspects such as compaction rate, cellular organisation, and cell survival. For instance, hMSC-only aggregates with cubes presented a higher compaction for increased object-to-cell ratios (e.g., more compact aggregates for a 1:20 than for a 1:8 ratio), whereas HUVEC-only conditions resulted in minimal aggregate formation for both ratios studied. For co-culture conditions, sequential seeding of HUVECs with pre-aggregated cubes and hMSCs led to more robust constructs with an increased HUVEC adhesion when compared with a simultaneous seeding of HUVECs, hMSCs, and cubes.[134]

An advantage of anchorage versus encapsulation systems is the fact that topographical cues can easily be introduced onto the surface of microcarriers. Whereas encapsulations systems are so far limited to the magnetic manipulation of rods or fibre-like structures to control cell alignment from within,[173,224,225] anchorage microcarrier systems can be modified prior to cell contact. Given the well-established impact in a 2D context of topographical features on cell orientation, migration, cytoskeletal organisation, differentiation, as well as inter- and intracellular signalling, transposing these cues to the third dimension is of the utmost importance, since it better mimics the native cell environment.[231,232] The role of nano and microscale topographical features in a 2D environment have been previously reviewed.[28,233,234] Yet to date, few strategies have incorporated topographical features onto microcarriers. Wrinkled topography has been introduced onto non-spherical particles by partial curing of the superficial polymer layer, which was subsequently wrinkled via plasma treatment (Figure I.5B2). An increased cell adhesion was observed for wrinkled surface particles and, considering that both smooth control and wrinkled particles were submitted to plasma treatment with no significantly different surface chemistry, this enhanced adhesion was attributed to the topographical cues.[194] Additionally, nanogrooved microdiscs, "topodiscs", have been proposed. These micron-sized platforms for a bottom-up cell-mediated assembly were produced via imprinting and possessed a disc-like shape featuring surface nanogrooves (Figure I.5B3). Due to the enhanced surface area to volume ratio when

compared with conventional spherical microparticles, topodiscs led to an increased cell proliferation. More importantly, these tailored microdiscs stimulated the osteogenic differentiation of hASCs without requiring supplemental osteoinductive factors added in the culture medium.[117]

5.2. Drug delivery and cell targeting

Spherical microparticles are among the most studied and widely applied geometries for controlled delivery of pharmaceuticals and bioactive agents. This is likely due to the ease of fabrication, whether by microfluidics,[235] oil-in-water emulsion,[236] solvent emulsion evaporation,[237] superhydrophobic surfaces,[238] electrospray,[239] among others. Drug-encapsulating microparticles may roughly be divided into two categories: reservoir/core-shell systems, and matrix/monolithic systems. Controlled release from microparticles is impacted by factors such as drug diffusion out of the device, polymer swelling or erosion, osmotic effects, *etc*. Initial drug concentration is also a preponderant factor, with differing release profiles for microparticles encapsulating drugs below or above their solubility.[240]

However, spherical microparticles may not always be the most advantageous geometry. For instance, distinct particle morphologies present altered polymer matrix degradation rates, consequently allowing to tailor drug release kinetics [161]. As such, for the same volume of a spherical microparticle, distinct geometrical shapes such as cubes or spheroids will present an increased surface area, which may facilitate diffusion across the particle surface. Taking only diffusion into consideration, numerical modelling studies assessed the impact of geometry for the same particle volume on the release profile of a specific compound. For modelled geometries (spheres and spheroids), it was determined that spheroids with smaller short axis presented a faster release and reached a plateau more rapidly than spheroids with larger short axis and even faster than spheres. This trend was experimentally corroborated, as the release kinetics of model protein BSA from chitosan spheroidal hydrogels was faster than from spherical hydrogels with the same volume.[112] The loading capability of PLGA spheroids and ellipsoids with paclitaxel,[109,110] BSA,[110] and model peptide drug octreotide acetate[111] has been established, still the impact of varying shape on the release profile has yet to be explored. Applying a sequential process, bi-compartmental fibre-entrapped cylindric hydrogels (approx. 200 μm diameter) were produced. Firstly, PLGA fibres loaded

with either bFGF or BMP-2 were produced via electrospinning and sequentially stacked. Secondly, PEGDA-entrapped fibres were produced via photolithography, which yielding individual cylindric microgels upon the dissolution of bare fibres. By using a distinct lactide/glycolide ratio for bFGF- or BMP-2-loaded fibres, a tailored release of either compound could be achieved.[126]

The selection of the production method is key so as not to interfere or diminish the activity of the encapsulated drug/bioactive agent. Since liquid phase organic solvents may impact drug activity, an option is to use solvent plasticisation with a vapour mixture. This method was applied to produce cylinders by the deformation of initially spherical VEGF-loaded PLGA microparticles within 200 μm diameter cylindric moulds, while successfully maintaining VEGF activity. When cultured with HUVECs it was anticipated that due to their higher surface area and thus expected faster VEGF release, cylinders would increase the sprout number comparatively to microspheres. This however did not occur and was attributed to the low aspect ratio of cylinders and to a possible degradation at longer culturing timepoints.[178]

Tumour tissues present highly reducing intracellular environments and high GSH (γ-glutamyl-cysteinyl-glycine tripeptide) levels, which can be harnessed for targeted delivery. Whereas disulfide bonds are stable in the presence of low GSH levels, a rapid cleaving via GSH-mediated thiol-disulfide exchange reaction occurs with high GSH levels.[241] Taking advantage of this fact, doxorubicin-loaded cuboidal particles (side length 2 μm) crosslinked with disulfide were applied to selectively target HeLa cervical cancer cells.[133] Alternative tumour targeting strategies have applied helicoidal magnetic microparticles, or "microswimmers", which showed promising results due to their steerability under a rotating magnetic field. These 20 μm long helicoidal structures composed of methacrylamide chitosan and magnetic nanoparticles were produced via two-photon polymerisation and could be loaded with doxorubicin, which was released locally on-demand under an external light stimulus (Figure I.6A).[170] This system has also been used for targeted cell labelling for therapeutic intervention of ErbB 2 overexpressing SKBR3 cancer cells. Taking advantage of the local elevated MMP-2 concentration in cancer sites and the degradability of gelatine to this enzyme, local delivery of anti-ErbB 2 antibody-tagged magnetic contrast agents may be induced by using magnetic gelatine methacryloyl microswimmers.[171] Synthetic

nano/micro-motors, capable of movement via bubble and acoustic propulsion or light-driven motion, are gaining significant interest in the biomedical field due to their response to external stimuli.[242,243]

A practical application for microcarriers with distinct geometries is their potential for shape-mediated, or "lock and key" assembly. Shapes such as cylinders, cubes, and triangular prisms are easily manufactured by a combination of photolithography with a dynamic photomask to generate compatible "parent" and "daughter" particles laden with different viruses. Initially, "parent" particles were assembled within PDMS moulds according to their shape. Subsequently, smaller "daughter" particles fit within the shape-dependent indentations of "parent" particles (e.g., triangular prism fits within larger rectangular prism with triangular cut-out). Cells seeded atop of the "daughter"/"parent" microscale self-assembling were spatially subjected to gene transfection. Due to the loading of "parent" and "daughter" particles with distinct viruses, it was possible to locally produce heterogeneous cell populations in a controlled manner (Figure I.6B).[169]

Taken together, considering geometry in the design of strategies for drug delivery and cell targeting presents several advantages. Yet it is crucial to assess the scalability and inherent costs of such strategies for a successful entry into the clinical setting.

5.3. Biosensors

One-step microfluidic biosensors have been based on the application of cylindric microgels. Microgels containing glucose oxidase and peroxidase were fabricated within the polymerisation chamber of a microfluidic chip and then sent via a pressure-driven flow to the connected reaction chamber. Upon feeding a glucose and Amplex Red solution to the microfluidic system, glucose oxidase mediated the conversion of glucose into gluconolactone and hydrogen peroxide, whilst the latter in conjunction with peroxidase reacted with Amplex Red to produce fluorescent resorufin. With this system, it was possible to correlate fluorescent intensity with glucose concentration over a physiologically relevant range. Additionally, for the same glucose concentration, smaller or larger microgels resulted in a rapid lower fluorescence intensity or slower high fluorescence intensity, respectively.[166]

Geometry has also been useful for multiplex assays, namely miRNA profiling using geometric barcoding. This strategy relied on the combination of high-resolution imaging with programmable DNA origami nanostructures presenting pre-designed nano-array patterns for multiplexed capture.[244] Similarly, surfaces with programmable wettability may be applied for 2D encryption of fluorescence information due to selective capture and release of hydrogel particles.[245] Furthermore, in response to the growing demand for high-throughput and high-content protein analysis, protein microarrays have been developed to identify different proteins simultaneously. Commonly used systems are composed of optically coded spherical microparticles, yet these are limited to the number of colour combinations and possible spectral overlaps. Hence, shape-coded suspension protein microarrays appear as an alternative to the traditional colour-coded options. Cylindric microgels were immobilised with IgG whereas rectangular prism microgels were immobilised with IgM. When reacted with samples containing varying mixtures of FITC-anti-IgG and FITC-anti-IgM, a simultaneous detection of IgG and IgM without crosstalk induced by the fluorescence indicator was possible (Figure I.6C).[162] In turn, biomimetic structural colours, which result from the physical interaction of light with nanostructures, have found application in the biomedical field. For example, hydrogels present distinct structural colours upon swelling or shrinking since a change in photonic band gap occurs.[246] This has been applied in multiplex assay based on stomatocyte-mimetic photonic crystal (PhC) colour barcodes. Stomatocyte morphology was achieved by quick solvent extraction and self-assembling of monodispersed silica nanoparticles in aqueous droplets. This highly ordered structure was replicated using a hydrogel with suspended ferric oxide nanoparticles and the cavity was filled with platinum nanoparticles. Such micromotors could hence be driven by magnetic force and, when exposed to hydrogen peroxide solution, catalytic bubbles. Barcodes rely on the characteristic reflection peaks originating from the photonic band gap. Hence, by using structural colour-barcode micromotors with characteristic reflection peaks at 458, 565 and 650 nm (blue, green, and red) modified with three distinct probes, a simultaneous detection of three kinds of DNA was performed (Figure I.6D).[247]

Taking advantage of geometry via surface patterning or using diverse building blocks has proven to be a useful tool in biosensor design, which paves the way for the development of further strategies and their employment in non-clinical and clinical research.

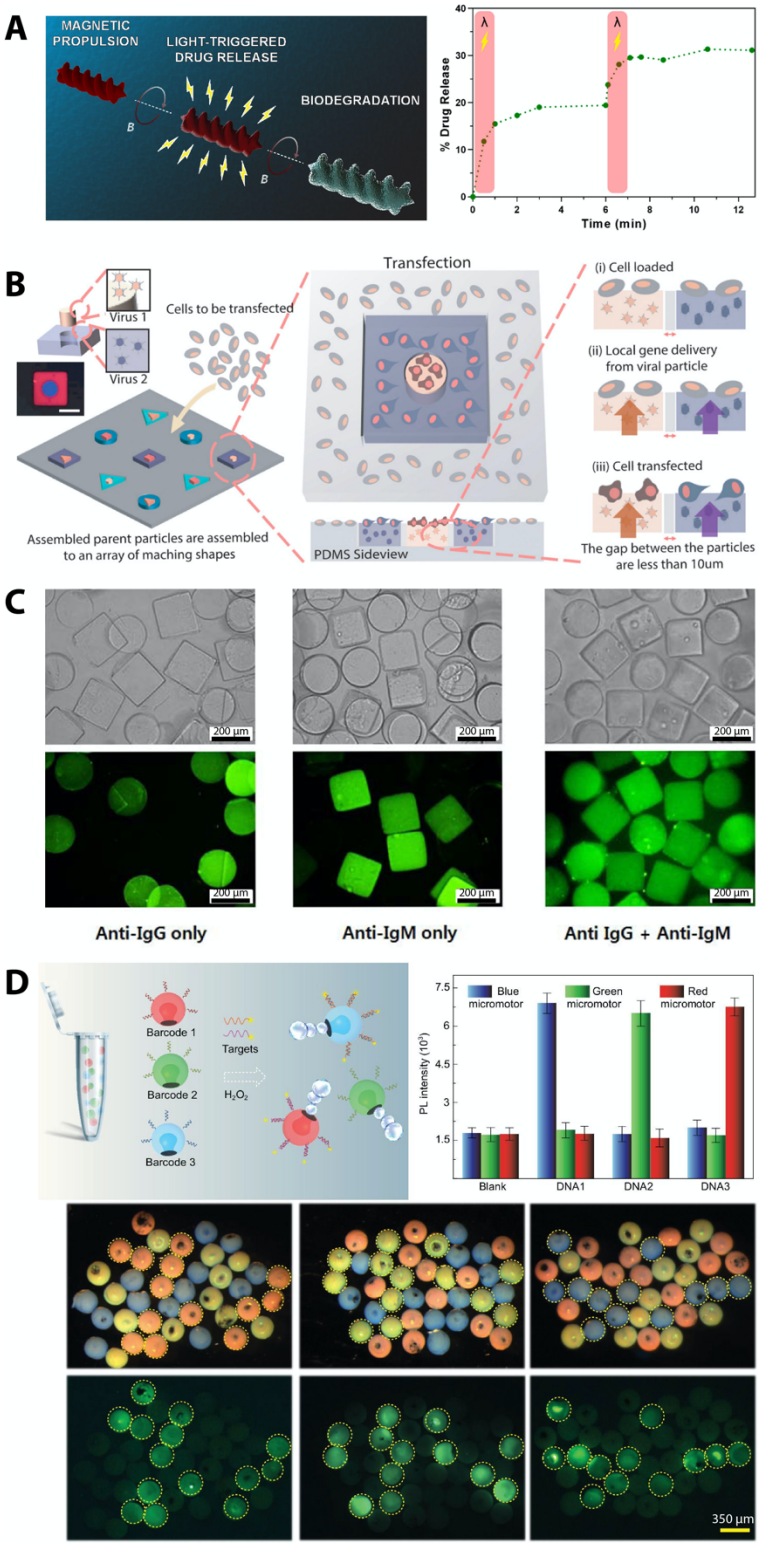

Figure I.6. A. Magnetically powered, double-helical microswimmers with light-induced drug [Reprinted with permission from [170], Copyright (2018) American Chemical Society]. B. Geometry-dependent assembly of "daughter/parent" particles for localised cell transfection [Reprinted with permission from [169], Copyright (2018) AIP Publishing]. C. Multiplexed immunoassays using shape-coded hydrogel microparticles immobilizing distinct proteins [Reprinted with permission from [162], Copyright (2012) MDPI]. D. Multiplex detection of three target DNA via fluorescence using structural color-barcode micromotors [Reprinted with permission from [247], Copyright (2020) Oxford University Press].

6. Conclusions

Recent advances in the tissue engineering and drug delivery fields have evidenced the impact of geometrical cues in controlling cell fate and tailoring drug release/cell targeting, respectively. Particularly in a 2D context, geometrical and topographical features have been highlighted as key moderators in controlling cell adhesion, morphology, and directing cell differentiation into specific lineages via their impact on mechanotransduction pathways. Topographical cues are associated with contact guidance and modulation of actomyosin contractility, while certain features have been shown to accelerate cell spreading. Consequently, differentiation is impacted by such cues and promising results have been evidenced for neurogenesis and osteogenesis applying grooves, pillars, and pits. Similarly, geometrical cues impact the generation of tension within the cell, which may be linked to alterations in cell proliferation, and cell fate towards adipogenic and osteogenic lineages, for instance.

Considering the more biomimetic 3D environment, microcarriers appear as attractive options for cell encapsulation and anchorage due to the possibility to easily modify and apply geometric and topographical features in combination with tuneable mechanical properties. Furthermore, microcarriers easily allow for a controlled cell spatial organisation for strategies featuring distinct cell populations, enabling “lock and key” assemblies. The application of these strategies has yielded promising reports in the literature, yet it is necessary to further study cell behaviour to pinpoint the mechanotransduction mechanisms in play in these 3D contexts. The role of topography in a 3D context has been greatly overlooked and warrants an advanced investigation, since results obtained in 2D do not easily transpose to what occurs in 3D. Similarly, microcarriers featuring distinct geometries have shown promising results for strategies aiming towards cell targeting, controlled drug delivery, and even production of biosensors, indicating that this strategy should be further pursued.

Recent advances in the field of biofabrication with new and improved techniques enable a growing control over feature morphology and intricacy of topographical details.[248] With these advances, novel microparticle systems are expected to emerge for an efficient control over cell behaviour. Of course, these innovations bring even more possibilities to a table

already full of options. Ultimately, *in silico* biomaterial design coupled with advanced fabrication techniques and high-throughput screening may be the way forward to test cellular response to such novel microcarriers.[60] In fact, high-throughput screening might evolve towards assessing the synergistic effect of both physical cues and material chemical of microcarriers.[249]

Acknowledgments

I. M. Bjørge acknowledges financial support by the Portuguese Foundation for Science and Technology (FCT) with doctoral grant SFRH/BD/129224/2017. This work was supported by the European Research Council grant agreement ERC-2014-ADG-669858 for the project "ATLAS". This work was financed by national funds (OE) through (FCT/MCTES) in the scope of the projects "TETRISSUE", reference PTDC/BTM-MAT/3201/2020 and "CIRCUS", reference PTDC/BTM-MAT/31064/2017 also supported by the Programa Operacional Competitividade e Internacionalização, in the component FEDER (POCI-01-0145-FEDER-031064). This work was developed within the scope of the project CICECO-Aveiro Institute of Materials, UIDB/50011/2020 & UIDP/50011/2020, financed by national funds through the FCT/MEC and when appropriate co-financed by FEDER under the PT2020 Partnership Agreement.

References

1. Nelson, C. M. & Bissell, M. J. Of Extracellular Matrix, Scaffolds, and Signaling: Tissue Architecture Regulates Development, Homeostasis, and Cancer. *Annu. Rev. Cell Dev. Biol.* **22**, 287–309 (2006).
2. Khetani, S. R. & Bhatia, S. N. Engineering tissues for in vitro applications. *Curr. Opin. Biotechnol.* **17**, 524–531 (2006).
3. Dupont, S. *et al.* Role of YAP/TAZ in mechanotransduction. *Nature* **474**, 179–183 (2011).
4. Fratzl, P. & Weinkamer, R. Nature's hierarchical materials. *Prog. Mater. Sci.* **52**, 1263–1334 (2007).
5. Dvir, T., Timko, B. P., Kohane, D. S. & Langer, R. Nanotechnological strategies for engineering complex tissues. *Nat. Nanotechnol.* **6**, 13–22 (2011).
6. Kline, T. L., Zamir, M. & Ritman, E. L. Relating Function to Branching Geometry: A Micro-CT Study of the Hepatic Artery, Portal Vein, and Biliary Tree. *Cells. Tissues. Organs* **194**, 431 (2011).
7. Brassard, J. A., Nikolaev, M., Hübscher, T., Hofer, M. & Lutolf, M. P. Recapitulating macro-scale tissue self-organization through organoid bioprinting. *Nat. Mater.* **20**, 22–29 (2021).
8. Lopes, D., Martins-Cruz, C., Oliveira, M. B. & Mano, J. F. Bone physiology as inspiration for tissue regenerative therapies. *Biomaterials* **185**, 240–275 (2018).
9. Vo, T. N., Kasper, F. K. & Mikos, A. G. Strategies for controlled delivery of growth factors and cells for bone regeneration. *Adv. Drug Deliv. Rev.* **64**, 1292–1309 (2012).
10. James, A. W. *et al.* A Review of the Clinical Side Effects of Bone Morphogenetic Protein-2.

Tissue Eng. - Part B Rev. **22**, 284–297 (2016).
11. Engler, A. J., Sen, S., Sweeney, H. L. & Discher, D. E. Matrix Elasticity Directs Stem Cell Lineage Specification. *Cell* **126**, 677–689 (2006).
12. Dalby, M. J., Gadegaard, N. & Oreffo, R. O. C. Harnessing nanotopography and integrin–matrix interactions to influence stem cell fate. *Nat. Mater.* **13**, 558–569 (2014).
13. Elosegui-Artola, A. *et al.* Mechanical regulation of a molecular clutch defines force transmission and transduction in response to matrix rigidity. *Nat. Cell Biol.* **18**, 540–548 (2016).
14. Bennett, M. *et al.* Molecular clutch drives cell response to surface viscosity. *Proc. Natl. Acad. Sci. U. S. A.* **115**, 1192–1197 (2018).
15. Wang, W. Y. *et al.* Extracellular matrix alignment dictates the organization of focal adhesions and directs uniaxial cell migration. *APL Bioeng.* **2**, 46107 (2018).
16. Chen, C. S., Mrksich, M., Huang, S., Whitesides, G. M. & Ingber, D. E. Geometric control of cell life and death. *Science.* **276**, 1425–8 (1997).
17. Huang, L., Abdalla, A. M. E., Xiao, L. & Yang, G. Biopolymer-Based Microcarriers for Three-Dimensional Cell Culture and Engineered Tissue Formation. *International Journal of Molecular Sciences* **21**, 1895 (2020).
18. Zhou, Z., Wu, W., Fang, J. & Yin, J. Polymer-based porous microcarriers as cell delivery systems for applications in bone and cartilage tissue engineering. *Int. Mater. Rev.* **66**, 77–113 (2021).
19. Neto, M. D., Oliveira, M. B. & Mano, J. F. Microparticles in Contact with Cells: From Carriers to Multifunctional Tissue Modulators. *Trends Biotechnol.* **37**, 1011–1028 (2019).
20. Maciel, M. M., Correia, T. R., Henriques, M. & Mano, J. F. Microparticles orchestrating cell fate in bottom-up approaches. *Curr. Opin. Biotechnol.* **73**, 276–281 (2022).
21. Sun, Z., Guo, S. S. & Fässler, R. Integrin-mediated mechanotransduction. *J. Cell Biol.* **215**, 445–456 (2016).
22. Gauthier, N. C. & Roca-Cusachs, P. Mechanosensing at integrin-mediated cell–matrix adhesions: from molecular to integrated mechanisms. *Curr. Opin. Cell Biol.* **50**, 20–26 (2018).
23. Elosegui-Artola, A., Trepat, X. & Roca-Cusachs, P. Control of Mechanotransduction by Molecular Clutch Dynamics. *Trends Cell Biol.* **28**, 356–367 (2018).
24. Mitchison, T. & Kirschner, M. Cytoskeletal dynamics and nerve growth. *Neuron* **1**, 761–772 (1988).
25. Chan, C. E. & Odde, D. J. Traction dynamics of filopodia on compliant substrates. *Science.* **322**, 1687–1691 (2008).
26. Hu, K., Ji, L., Applegate, K. T., Danuser, G. & Waterman-Storer, C. M. Differential Transmission of Actin Motion Within Focal Adhesions. *Science.* **315**, 111–115 (2007).
27. Kumar, S. *et al.* Viscoelastic retraction of single living stress fibers and its impact on cell shape, cytoskeletal organization, and extracellular matrix mechanics. *Biophys. J.* **90**, 3762–3773 (2006).
28. Nikkhah, M., Edalat, F., Manoucheri, S. & Khademhosseini, A. Engineering microscale topographies to control the cell–substrate interface. *Biomaterials* **33**, 5230–5246 (2012).
29. Bao, M., Xie, J. & Huck, W. T. S. Recent Advances in Engineering the Stem Cell Microniche in 3D. *Adv. Sci.* **5**, 1800448 (2018).
30. Mitra, S. K., Hanson, D. A. & Schlaepfer, D. D. Focal adhesion kinase: in command and control of cell motility. *Nat. Rev. Mol. Cell Biol.* **6**, 56–68 (2005).
31. Ren, X. D. *et al.* Focal adhesion kinase suppresses Rho activity to promote focal adhesion turnover. *J. Cell Sci.* **113**, 3673–3678 (2000).
32. Cukierman, E., Pankov, R., Stevens, D. R. & Yamada, K. M. Taking Cell-Matrix Adhesions to the Third Dimension. *Science.* **294**, 1708–1712 (2001).
33. Kimura, K. *et al.* Regulation of Myosin Phosphatase by Rho and Rho-Associated Kinase (Rho-Kinase). *Science.* **273**, 245–248 (1996).
34. Sao, K. *et al.* Myosin II governs intracellular pressure and traction by distinct tropomyosin-dependent mechanisms. *Mol. Biol. Cell* **30**, 1170–1181 (2019).
35. Pasapera, A. M., Schneider, I. C., Rericha, E., Schlaepfer, D. D. & Waterman, C. M. Myosin

II activity regulates vinculin recruitment to focal adhesions through FAK-mediated paxillin phosphorylation. *J. Cell Biol.* **188**, 877–890 (2010).
36. Zhu, X. & Assoian, R. K. Integrin-dependent activation of MAP kinase: a link to shape-dependent cell proliferation. *Mol. Biol. Cell* **6**, 273–82 (1995).
37. Miller, A. E., Hu, P. & Barker, T. H. Feeling Things Out: Bidirectional Signaling of the Cell–ECM Interface, Implications in the Mechanobiology of Cell Spreading, Migration, Proliferation, and Differentiation. *Adv. Healthc. Mater.* 1901445 (2020). doi:10.1002/adhm.201901445
38. Han, Y. L. *et al.* Cell contraction induces long-ranged stress stiffening in the extracellular matrix. *Proc. Natl. Acad. Sci. U. S. A.* **115**, 4075–4080 (2018).
39. Bhadriraju, K. *et al.* Activation of ROCK by RhoA is regulated by cell adhesion, shape, and cytoskeletal tension. *Exp. Cell Res.* **313**, 3616–23 (2007).
40. Folkman, J. & Moscona, A. Role of cell shape in growth control. *Nature* **273**, 345–349 (1978).
41. Petrie, R. J., Koo, H. & Yamada, K. M. Generation of compartmentalized pressure by a nuclear piston governs cell motility in a 3D matrix. *Science.* **345**, 1062–1065 (2014).
42. Doyle, A. D., Wang, F. W., Matsumoto, K. & Yamada, K. M. One-dimensional topography underlies three-dimensional fibrillar cell migration. *J. Cell Biol.* **184**, 481–490 (2009).
43. Chaudhuri, O. *et al.* Hydrogels with tunable stress relaxation regulate stem cell fate and activity. *Nat. Mater.* **15**, 326–334 (2016).
44. Nardone, G. *et al.* YAP regulates cell mechanics by controlling focal adhesion assembly. *Nat. Commun.* **8**, 15321 (2017).
45. Rose, J. C. & De Laporte, L. Hierarchical Design of Tissue Regenerative Constructs. *Adv. Healthc. Mater.* **7**, 1701067 (2018).
46. Caliari, S. R., Vega, S. L., Kwon, M., Soulas, E. M. & Burdick, J. A. Dimensionality and spreading influence MSC YAP/TAZ signaling in hydrogel environments. *Biomaterials* **103**, 314–323 (2016).
47. Swift, J. *et al.* Nuclear lamin-A scales with tissue stiffness and enhances matrix-directed differentiation. *Science.* **341**, 1240104 (2013).
48. Huebsch, N. *et al.* Harnessing traction-mediated manipulation of the cell/matrix interface to control stem-cell fate. *Nat. Mater.* **9**, 518–26 (2010).
49. Loebel, C., Mauck, R. L. & Burdick, J. A. Local nascent protein deposition and remodelling guide mesenchymal stromal cell mechanosensing and fate in three-dimensional hydrogels. *Nat. Mater.* **18**, 883–891 (2019).
50. Wells, R. G. The role of matrix stiffness in regulating cell behavior. *Hepatology* **47**, 1394–1400 (2008).
51. Semler, E. J., Lancin, P. A., Dasgupta, A. & Moghe, P. V. Engineering hepatocellular morphogenesis and function via ligand-presenting hydrogels with graded mechanical compliance. *Biotechnol. Bioeng.* **89**, 296–307 (2005).
52. Mennens, S. F. B. *et al.* Substrate stiffness influences phenotype and function of human antigen-presenting dendritic cells. *Sci. Rep.* **7**, 1–14 (2017).
53. Li, Z. *et al.* Differential regulation of stiffness, topography, and dimension of substrates in rat mesenchymal stem cells. *Biomaterials* **34**, 7616–7625 (2013).
54. Dalby, M. J., Riehle, M. O., Sutherland, D. S., Agheli, H. & Curtis, A. S. G. Changes in fibroblast morphology in response to nano-columns produced by colloidal lithography. *Biomaterials* **25**, 5415–5422 (2004).
55. Dalby, M. J. *et al.* The control of human mesenchymal cell differentiation using nanoscale symmetry and disorder. *Nat. Mater.* **6**, 997–1003 (2007).
56. Hou, Y. *et al.* Surface Roughness Gradients Reveal Topography-Specific Mechanosensitive Responses in Human Mesenchymal Stem Cells. *Small* **16**, 1905422 (2020).
57. Pieuchot, L. *et al.* Curvotaxis directs cell migration through cell-scale curvature landscapes. *Nat. Commun.* **9**, 3995 (2018).
58. Kim, C.-S. *et al.* A Specific Groove Pattern Can Effectively Induce Osteoblast Differentiation. *Adv. Funct. Mater.* **27**, 1703569 (2017).
59. Hulsman, M. *et al.* Analysis of high-throughput screening reveals the effect of surface topographies on cellular morphology. *Acta Biomater.* **15**, 29–38 (2015).

60. Hulshof, F. *et al.* Mining for osteogenic surface topographies: In silico design to in vivo osseo-integration. *Biomaterials* **137**, 49–60 (2017).
61. Unadkat, H. V *et al.* An algorithm-based topographical biomaterials library to instruct cell fate. *Proc. Natl. Acad. Sci. U. S. A.* **108**, 16565–70 (2011).
62. den Braber, E. T., de Ruijter, J. E., Ginsel, L. A., von Recum, A. F. & Jansen, J. A. Quantitative analysis of fibroblast morphology on microgrooved surfaces with various groove and ridge dimensions. *Biomaterials* **17**, 2037–2044 (1996).
63. Au, H. T. H., Cheng, I., Chowdhury, M. F. & Radisic, M. Interactive effects of surface topography and pulsatile electrical field stimulation on orientation and elongation of fibroblasts and cardiomyocytes. *Biomaterials* **28**, 4277–4293 (2007).
64. Lamers, E. *et al.* The influence of nanoscale grooved substrates on osteoblast behavior and extracellular matrix deposition. *Biomaterials* **31**, 3307–3316 (2010).
65. Moon, H. *et al.* Novel grooved substrata stimulate macrophage fusion, CCL2 and MMP-9 secretion. *J. Biomed. Mater. Res. Part A* **104**, 2243–2254 (2016).
66. Cabezas, M. D., Meckes, B., Mirkin, C. A. & Mrksich, M. Subcellular Control over Focal Adhesion Anisotropy, Independent of Cell Morphology, Dictates Stem Cell Fate. *ACS Nano* **13**, 11144–11152 (2019).
67. Ruiz, S. A. & Chen, C. S. Emergence of patterned stem cell differentiation within multicellular structures. *Stem Cells* **26**, 2921–7 (2008).
68. Kim, D. & Wirtz, D. Focal adhesion size uniquely predicts cell migration. *FASEB J.* **27**, 1351–1361 (2013).
69. Loesberg, W. A. *et al.* The threshold at which substrate nanogroove dimensions may influence fibroblast alignment and adhesion. *Biomaterials* **28**, 3944–3951 (2007).
70. McNamara, L. E. *et al.* Investigation of the limits of nanoscale filopodial interactions. *J. Tissue Eng.* **5**, 2041731414536177 (2014).
71. Franco, D. *et al.* Control of initial endothelial spreading by topographic activation of focal adhesion kinase. *Soft Matter* **7**, 7313 (2011).
72. Teo, B. K. K. *et al.* Nanotopography Modulates Mechanotransduction of Stem Cells and Induces Differentiation through Focal Adhesion Kinase. *ACS Nano* **7**, 4785–4798 (2013).
73. Teixeira, A. I., Abrams, G. A., Bertics, P. J., Murphy, C. J. & Nealey, P. F. Epithelial contact guidance on well-defined micro- and nanostructured substrates. *J. Cell Sci.* **116**, 1881–92 (2003).
74. Yim, E. K. F., Darling, E. M., Kulangara, K., Guilak, F. & Leong, K. W. Nanotopography-induced changes in focal adhesions, cytoskeletal organization, and mechanical properties of human mesenchymal stem cells. *Biomaterials* **31**, 1299–306 (2010).
75. Bjørge, I. M., Salmeron-Sanchez, M., Correia, C. R. & Mano, J. F. Cell Behavior within Nanogrooved Sandwich Culture Systems. *Small* **16**, 2001975 (2020).
76. McNamara, L. E. *et al.* The role of microtopography in cellular mechanotransduction. *Biomaterials* **33**, 2835–2847 (2012).
77. Lim, J. Y. *et al.* The regulation of integrin-mediated osteoblast focal adhesion and focal adhesion kinase expression by nanoscale topography. *Biomaterials* **28**, 1787–1797 (2007).
78. Lee, S. J. & Yang, S. Micro glass ball embedded gels to study cell mechanobiological responses to substrate curvatures. *Rev. Sci. Instrum.* **83**, 094302 (2012).
79. Sun, B., Xie, K., Chen, T.-H. & Lam, R. H. W. Preferred cell alignment along concave microgrooves. *RSC Adv.* **7**, 6788–6794 (2017).
80. Yang, K. *et al.* Nanotopographical Manipulation of Focal Adhesion Formation for Enhanced Differentiation of Human Neural Stem Cells. *ACS Appl. Mater. Interfaces* **5**, 10529–10540 (2013).
81. Yang, K. *et al.* Multiscale, Hierarchically Patterned Topography for Directing Human Neural Stem Cells into Functional Neurons. *ACS Nano* **8**, 7809–7822 (2014).
82. Ankam, S., Lim, C. K. & Yim, E. K. F. Actomyosin contractility plays a role in MAP2 expression during nanotopography-directed neuronal differentiation of human embryonic stem cells. *Biomaterials* **47**, 20–28 (2015).
83. Abagnale, G. *et al.* Surface topography enhances differentiation of mesenchymal stem cells towards osteogenic and adipogenic lineages. *Biomaterials* **61**, 316–326 (2015).

84. Kim, M. J. *et al.* BMP-2 Peptide-Functionalized Nanopatterned Substrates for Enhanced Osteogenic Differentiation of Human Mesenchymal Stem Cells. *Biomaterials* **34**, 7236–7246 (2013).
85. Chen, C. S., Alonso, J. L., Ostuni, E., Whitesides, G. M. & Ingber, D. E. Cell shape provides global control of focal adhesion assembly. *Biochem. Biophys. Res. Commun.* **307**, 355–361 (2003).
86. Kilian, K. A., Bugarija, B., Lahn, B. T. & Mrksich, M. Geometric cues for directing the differentiation of mesenchymal stem cells. *Proc. Natl. Acad. Sci. U. S. A.* **107**, 4872–7 (2010).
87. McBeath, R., Pirone, D. M., Nelson, C. M., Bhadriraju, K. & Chen, C. S. Cell Shape, Cytoskeletal Tension, and RhoA Regulate Stem Cell Lineage Commitment. *Dev. Cell* **6**, 483–495 (2004).
88. von Erlach, T. C. *et al.* Cell-geometry-dependent changes in plasma membrane order direct stem cell signalling and fate. *Nat. Mater.* **17**, 237–242 (2018).
89. Maduram, J. H., Goluch, E. D., Hu, H., Liu, C. & Mrksich, M. Subcellular curvature at the perimeter of micropatterned cells influences lamellipodial distribution and cell polarity. *Cell Motil. Cytoskeleton* **65**, 841–52 (2008).
90. Chen, T. *et al.* Large-scale curvature sensing by directional actin flow drives cellular migration mode switching. *Nat. Phys.* **15**, 393–402 (2019).
91. Théry, M., Pépin, A., Dressaire, E., Chen, Y. & Bornens, M. Cell distribution of stress fibres in response to the geometry of the adhesive environment. *Cell Motil. Cytoskeleton* **63**, 341–355 (2006).
92. Kassianidou, E. *et al.* Extracellular Matrix Geometry and Initial Adhesive Position Determine Stress Fiber Network Organization during Cell Spreading. *Cell Rep.* **27**, 1897-1909.e4 (2019).
93. Nelson, C. M. *et al.* Emergent patterns of growth controlled by multicellular form and mechanics. *Proc. Natl. Acad. Sci. U. S. A.* **102**, 11594–11599 (2005).
94. Legant, W. R. *et al.* Microfabricated tissue gauges to measure and manipulate forces from 3D microtissues. *Proc. Natl. Acad. Sci. U. S. A.* **106**, 10097–10102 (2009).
95. Bose, P., Eyckmans, J., Nguyen, T. D., Chen, C. S. & Reich, D. H. Effects of Geometry on the Mechanics and Alignment of Three-Dimensional Engineered Microtissues. *ACS Biomater. Sci. Eng.* **5**, 3843–3855 (2019).
96. Leckband, D. E. & De Rooij, J. Cadherin Adhesion and Mechanotransduction. *Annu. Rev. Cell Dev. Biol.* **30**, 291–315 (2014).
97. Hulshof, F. F. B. *et al.* NanoTopoChip: High-throughput nanotopographical cell instruction. *Acta Biomater.* **62**, 188–198 (2017).
98. Adler, A. F. *et al.* High-throughput screening of microscale pitted substrate topographies for enhanced nonviral transfection efficiency in primary human fibroblasts. *Biomaterials* **32**, 3611–3619 (2011).
99. Pettersson, S., Wetterö, J., Tengvall, P. & Kratz, G. Cell expansion of human articular chondrocytes on macroporous gelatine scaffolds - Impact of microcarrier selection on cell proliferation. *Biomed. Mater.* **6**, (2011).
100. Custódio, C. A. *et al.* Functionalized microparticles producing scaffolds in combination with cells. *Adv. Funct. Mater.* **24**, 1391–1400 (2014).
101. Yao, R., Zhang, R., Lin, F. & Luan, J. Injectable cell/hydrogel microspheres induce the formation of fat lobule-like microtissues and vascularized adipose tissue regeneration. *Biofabrication* **4**, 045003 (2012).
102. Keville, K. ., Franses, E. . & Caruthers, J. . Preparation and characterization of monodisperse polymer microspheroids. *J. Colloid Interface Sci.* **144**, 103–126 (1991).
103. Herrmann, C., Bannwarth, M. B., Landfester, K. & Crespy, D. Re-dispersible Anisotropic and Structured Nanoparticles: Formation and Their Subsequent Shape Change. *Macromol. Chem. Phys.* **213**, 829–838 (2012).
104. Friess, F., Roch, T., Seifert, B., Lendlein, A. & Wischke, C. Phagocytosis of spherical and ellipsoidal micronetwork colloids from crosslinked poly(epsilon-caprolactone). *Int. J. Pharm.* **567**, 118461 (2019).
105. Sahari, A., Traore, M. A., Scharf, B. E. & Behkam, B. Directed transport of bacteria-based drug delivery vehicles: bacterial chemotaxis dominates particle shape. *Biomed. Microdevices*

16, 717–725 (2014).
106. Zhang, P. *et al.* Ellipsoidal Colloids with a Controlled Surface Roughness via Bioinspired Surface Engineering: Building Blocks for Liquid Marbles and Superhydrophobic Surfaces. *ACS Appl. Mater. Interfaces* **9**, 7648–7657 (2017).
107. Orsi, S., Di Maio, E., Iannace, S. & Netti, P. A. Hollow micro- and nano-particles by gas foaming. *Nano Res.* **7**, 1018–1026 (2014).
108. Champion, J. A., Katare, Y. K. & Mitragotri, S. Making polymeric micro- and nanoparticles of complex shapes. *Proc. Natl. Acad. Sci.* **104**, 11901–11904 (2007).
109. Heslinga, M. J., Mastria, E. M. & Eniola-Adefeso, O. Fabrication of biodegradable spheroidal microparticles for drug delivery applications. *J. Control. Release* **138**, 235–242 (2009).
110. Heslinga, M. J., Willis, G. M., Sobczynski, D. J., Thompson, A. J. & Eniola-Adefeso, O. One-step fabrication of agent-loaded biodegradable microspheroids for drug delivery and imaging applications. *Colloids Surfaces B Biointerfaces* **116**, 55–62 (2014).
111. Fan, Q. *et al.* Direct and controllable preparation of uniform PLGA particles with various shapes and surface morphologies. *Colloids Surfaces A Physicochem. Eng. Asp.* **500**, 177–185 (2016).
112. Bjørge, I. M. *et al.* Tuneable spheroidal hydrogel particles for cell and drug encapsulation. *Soft Matter* **14**, (2018).
113. Wang, S. *et al.* An in-situ photocrosslinking microfluidic technique to generate non-spherical, cytocompatible, degradable, monodisperse alginate microgels for chondrocyte encapsulation. *Biomicrofluidics* **12**, 014106 (2018).
114. Wang, S. *et al.* In-situ photopolymerization of monodisperse and discoid oxidized methacrylated alginate microgels in a microfluidic channel. *Biomicrofluidics* **10**, (2016).
115. Leferink, A. *et al.* Engineered micro-objects as scaffolding elements in cellular building blocks for bottom-up tissue engineering approaches. *Adv. Mater.* **26**, 2592–2599 (2014).
116. Tang, M. D., Golden, A. P. & Tien, J. Molding of Three-Dimensional Microstructures of Gels. *J. Am. Chem. Soc.* **125**, 12988–12989 (2003).
117. Bjørge, I. M., Choi, I. S., Correia, C. R. & Mano, J. F. Nanogrooved microdiscs for bottom-up modulation of osteogenic differentiation. *Nanoscale* **11**, 16214–16221 (2019).
118. Dendukuri, D., Pregibon, D. C., Collins, J., Hatton, T. A. & Doyle, P. S. Continuous-flow lithography for high-throughput microparticle synthesis. *Nat. Mater.* **5**, 365–369 (2006).
119. Panda, P. *et al.* Stop-flow lithography to generate cell-laden microgel particles. *Lab Chip* **8**, 1056–1061 (2008).
120. Paulsen, K. S. & Chung, A. J. Non-spherical particle generation from 4D optofluidic fabrication. *Lab Chip* **16**, 2987–2995 (2016).
121. Sun, J. & Litchinitser, N. M. Toward Practical, Subwavelength, Visible-Light Photolithography with Hyperlens. *ACS Nano* **12**, 542–548 (2018).
122. Xia, Y. & Whitesides, G. M. Soft lithography. *Angew. Chemie Int. Ed.* **37**, 550–575 (1998).
123. Williams, C. G., Malik, A. N., Kim, T. K., Manson, P. N. & Elisseeff, J. H. Variable cytocompatibility of six cell lines with photoinitiators used for polymerizing hydrogels and cell encapsulation. *Biomaterials* **26**, 1211–1218 (2005).
124. Liu, B., Liu, Y., Lewis, A. K. & Shen, W. Modularly assembled porous cell-laden hydrogels. *Biomaterials* **31**, 4918–4925 (2010).
125. Zuo, Y. *et al.* Photo-Cross-Linkable Methacrylated Gelatin and Hydroxyapatite Hybrid Hydrogel for Modularly Engineering Biomimetic Osteon. *ACS Appl. Mater. Interfaces* **7**, 10386–10394 (2015).
126. Cho, K. *et al.* Multi-Compartmental Hydrogel Microparticles Fabricated by Combination of Sequential Electrospinning and Photopatterning. *Angew. Chemie Int. Ed.* **54**, 11511–11515 (2015).
127. Whitesides, G. M., Ostuni, E., Takayama, S., Jiang, X. & Ingber, D. E. Soft Lithography in Biology and Biochemistry. *Annu. Rev. Biomed. Eng.* **3**, 335–373 (2001).
128. Yeh, J. *et al.* Micromolding of shape-controlled, harvestable cell-laden hydrogels. *Biomaterials* **27**, 5391–5398 (2006).
129. Xue, B., Kozlovskaya, V. & Kharlampieva, E. Shaped stimuli-responsive hydrogel particles: syntheses, properties and biological responses. *J. Mater. Chem. B* **5**, 9–35 (2017).

130. Xu, J. *et al.* Future of the Particle Replication in Nonwetting Templates (PRINT) Technology. *Angew. Chemie Int. Ed.* **52**, 6580–6589 (2013).
131. Melchels, F. P. W., Feijen, J. & Grijpma, D. W. A review on stereolithography and its applications in biomedical engineering. *Biomaterials* **31**, 6121–6130 (2010).
132. Kelly, J. Y. & DeSimone, J. M. Shape-Specific, Monodisperse Nano-Molding of Protein Particles. *J. Am. Chem. Soc.* **130**, 5438–5439 (2008).
133. Petros, R. A., Ropp, P. A. & DeSimone, J. M. Reductively Labile PRINT Particles for the Delivery of Doxorubicin to HeLa Cells. *J. Am. Chem. Soc.* **130**, 5008–5009 (2008).
134. Leferink, A. M. *et al.* Shape-defined solid micro-objects from poly(d,l-lactic acid) as cell-supportive counterparts in bottom-up tissue engineering. *Mater. Today Bio* **4**, 100025 (2019).
135. Ma, C., Tian, C., Zhao, L. & Wang, J. Pneumatic-aided micro-molding for flexible fabrication of homogeneous and heterogeneous cell-laden microgels. *Lab Chip* **16**, 2609–2617 (2016).
136. Huang, P.-J. *et al.* Pneumatically Actuated Soft Micromold Device for Fabricating Collagen and Matrigel Microparticles. *Soft Robot.* **4**, 390–399 (2017).
137. Broers, A. N. Fabrication limits of electron beam lithography and of UV, X -ray and ion-beam lithographies. *Philos. Trans. R. Soc. A Math. Phys. Eng. Sci.* **353**, 291–311 (1995).
138. Jiang, J. *et al.* Protein Bricks: 2D and 3D Bio-Nanostructures with Shape and Function on Demand. *Adv. Mater.* **30**, 1705919 (2018).
139. Ruskowitz, E. R. & DeForest, C. A. Photoresponsive biomaterials for targeted drug delivery and 4D cell culture. *Nat. Rev. Mater.* **3**, 17087 (2018).
140. Nguyen, A. K. & Narayan, R. J. Two-photon polymerization for biological applications. *Mater. Today* **20**, 314–322 (2017).
141. Parkatzidis, K. *et al.* Multiphoton 3D Printing of Biopolymer-Based Hydrogels. *ACS Biomater. Sci. Eng.* **5**, 6161–6170 (2019).
142. Zheng, Z. *et al.* 3D Construction of Shape-Controllable Tissues through Self-Bonding of Multicellular Microcapsules. *ACS Appl. Mater. Interfaces* **11**, 22950–22961 (2019).
143. Liu, Y. *et al.* Programmable higher-order biofabrication of self-locking microencapsulation. *Biofabrication* **11**, 035019 (2019).
144. Liu, Z. *et al.* Batch Fabrication of Microscale Gear-Like Tissue by Alginate-Poly-L-lysine Microcapsules System. *IEEE Robot. Autom. Lett.* **1**, 206–212 (2016).
145. Liu, Z. *et al.* Shape-controlled high cell-density microcapsules by electrodeposition. *Acta Biomater.* **37**, 93–100 (2016).
146. Liu, Z. *et al.* Three-dimensional hepatic lobule-like tissue constructs using cell-microcapsule technology. *Acta Biomater.* **50**, 178–187 (2017).
147. Whitesides, G. M. The origins and the future of microfluidics. *Nature* **442**, 368–373 (2006).
148. Chung, S. E. *et al.* Maskless lithography techniques typically use computer-controlled programable two-dimensional spatial light modulators (SLMs). *Appl. Phys. Lett.* **91**, 041106 (2007).
149. Paulsen, K. S., Deng, Y. & Chung, A. J. DIY 3D Microparticle Generation from Next Generation Optofluidic Fabrication. *Adv. Sci.* **5**, 1800252 (2018).
150. Nam, S. M., Kim, K., Kang, I.-S., Park, W. & Lee, W. Generation of 3D Microparticles in Microchannels with Non-rectangular Cross Sections. *BioChip J.* **13**, 226–235 (2019).
151. Yang, W., Yu, H., Li, G., Wang, Y. & Liu, L. High-Throughput Fabrication and Modular Assembly of 3D Heterogeneous Microscale Tissues. *Small* **13**, 1602769 (2017).
152. Yang, W. *et al.* Modular and Customized Fabrication of 3D Functional Microgels for Bottom-Up Tissue Engineering and Drug Screening. *Adv. Mater. Technol.* 1900847 (2020). doi:10.1002/admt.201900847
153. Park, S. H., Kim, J., Lee, W.-E., Byun, D.-J. & Kim, M. H. One-Step Synthesis of Hollow Dimpled Polystyrene Microparticles by Dispersion Polymerization. *Langmuir* **33**, 2275–2282 (2017).
154. Li, R. *et al.* High-Yield Fabrication of PLGA Non-Spherical Microarchitectures by Emulsion-Solvent Evaporation Method. *Macromol. Rapid Commun.* **31**, 1981–1986 (2010).
155. Zhang, W. *et al.* Engineering ellipsoidal cap-like hydrogel particles as building blocks or sacrificial templates for three-dimensional cell culture. *Biomater. Sci.* **6**, 885–892 (2018).
156. Neto, A. I. *et al.* Fabrication of Hydrogel Particles of Defined Shapes Using

Superhydrophobic-Hydrophilic Micropatterns. *Adv. Mater.* **28**, 7613–7619 (2016).
157. Neto, M. D. *et al.* Fabrication of Quasi-2D Shape-Tailored Microparticles using Wettability Contrast-Based Platforms. *Adv. Mater.* **33**, 2007695 (2021).
158. Wu, Z. *et al.* Peanut-inspired anisotropic microparticles from microfluidics. *Compos. Commun.* **10**, 129–135 (2018).
159. Wang, L. *et al.* Fabrication of Microscale Hydrogels with Tailored Microstructures based on Liquid Bridge Phenomenon. *ACS Appl. Mater. Interfaces* **7**, 11134–11140 (2015).
160. Castro, A. G. B. *et al.* Top-Down Approach for the Preparation of Highly Porous PLLA Microcylinders. *ACS Biomater. Sci. Eng.* **2**, 2099–2107 (2016).
161. Almeria, B., Deng, W., Fahmy, T. M. & Gomez, A. Controlling the morphology of electrospray-generated PLGA microparticles for drug delivery. *J. Colloid Interface Sci.* **343**, 125–133 (2010).
162. Park, S., Lee, H. J. & Koh, W.-G. Multiplex Immunoassay Platforms Based on Shape-Coded Poly(ethylene glycol) Hydrogel Microparticles Incorporating Acrylic Acid. *Sensors* **12**, 8426–8436 (2012).
163. Pal, R. K. *et al.* Fabrication of precise shape-defined particles of silk proteins using photolithography. *Eur. Polym. J.* **85**, 421–430 (2016).
164. Xu, F. *et al.* The assembly of cell-encapsulating microscale hydrogels using acoustic waves. *Biomaterials* **32**, 7847–7855 (2011).
165. Zamanian, B. *et al.* Interface-Directed Self-Assembly of Cell-Laden Microgels. *Small* **6**, 937–944 (2010).
166. Choi, D., Jang, E., Park, J. & Koh, W.-G. Development of microfluidic devices incorporating non-spherical hydrogel microparticles for protein-based bioassay. *Microfluid. Nanofluidics* **5**, 703–710 (2008).
167. Oudshoorn, M. H. M. *et al.* Preparation and characterization of structured hydrogel microparticles based on cross-linked hyperbranched polyglycerol. *Langmuir* **23**, 11819–11825 (2007).
168. Hong, J., Shin, Y., Kim, S., Lee, J. & Cha, C. Complex Tuning of Physical Properties of Hyperbranched Polyglycerol-Based Bioink for Microfabrication of Cell-Laden Hydrogels. *Adv. Funct. Mater.* **29**, 1808750 (2019).
169. Lee, D. *et al.* Hierarchical shape-by-shape assembly of microparticles for micrometer-scale viral delivery of two different genes. *Biomicrofluidics* **12**, 031102 (2018).
170. Bozuyuk, U. *et al.* Light-Triggered Drug Release from 3D-Printed Magnetic Chitosan Microswimmers. *ACS Nano* **12**, 9617–9625 (2018).
171. Ceylan, H. *et al.* 3D-Printed Biodegradable Microswimmer for Theranostic Cargo Delivery and Release. *ACS Nano* **13**, 3353–3362 (2019).
172. Yu, Y. *et al.* Bioinspired Helical Micromotors as Dynamic Cell Microcarriers. *ACS Appl. Mater. Interfaces* **12**, 16097–16103 (2020).
173. Rose, J. C. *et al.* Biofunctionalized aligned microgels provide 3D cell guidance to mimic complex tissue matrices. *Biomaterials* **163**, 128–141 (2018).
174. McGuigan, A. P. & Sefton, M. V. Vascularized organoid engineered by modular assembly enables blood perfusion. *Proc. Natl. Acad. Sci. U. S. A.* **103**, 11461–11466 (2006).
175. He, Y. & Park, K. Effects of the Microparticle Shape on Cellular Uptake. *Mol. Pharm.* **13**, 2164–2171 (2016).
176. Qu, H. *et al.* Slip Molding for Precision Fabrication of Microparts. *Langmuir* **36**, 585–590 (2020).
177. Tekin, H. *et al.* Responsive Micromolds for Sequential Patterning of Hydrogel Microstructures. *J. Am. Chem. Soc.* **133**, 12944–12947 (2011).
178. de Alteriis, R. *et al.* A method to tune the shape of protein-encapsulated polymeric microspheres. *Sci. Rep.* **5**, 12634 (2015).
179. Gratton, S. E. A. *et al.* The effect of particle design on cellular internalization pathways. *Proc. Natl. Acad. Sci.* **105**, 11613–11618 (2008).
180. Abbasi, N., Navi, M., Nunes, J. K. & Tsai, S. S. H. Controlled generation of spiky microparticles by ionic cross-linking within an aqueous two-phase system. *Soft Matter* **15**, 3301–3306 (2019).

181. Zhihong Nie, Shengqing Xu, Minseok Seo, Lewis, P. C. & Kumacheva, E. Polymer Particles with Various Shapes and Morphologies Produced in Continuous Microfluidic Reactors. *JACS* **127**, 8058–8063 (2005).
182. Nisisako, T., Ando, T. & Hatsuzawa, T. Capillary-Assisted Fabrication of Biconcave Polymeric Microlenses from Microfluidic Ternary Emulsion Droplets. *Small* **10**, 5116–5125 (2014).
183. Nisisako, T. & Hatsuzawa, T. A microfluidic cross-flowing emulsion generator for producing biphasic droplets and anisotropically shaped polymer particles. *Microfluid. Nanofluidics* **9**, 427–437 (2010).
184. Hu, Y., Azadi, G. & Ardekani, A. M. Microfluidic fabrication of shape-tunable alginate microgels: Effect of size and impact velocity. *Carbohydr. Polym.* **120**, 38–45 (2015).
185. Xu, S. *et al.* Generation of Monodisperse Particles by Using Microfluidics: Control over Size, Shape, and Composition. *Angew. Chemie Int. Ed.* **44**, 724–728 (2005).
186. Cai, Q.-W. *et al.* Fabrication and flow characteristics of monodisperse bullet-shaped microparticles with controllable structures. *Chem. Eng. J.* **370**, 925–937 (2019).
187. Kang, Z. *et al.* Engineering particle morphology with microfluidic droplets. *J. Micromechanics Microengineering* **26**, 075011 (2016).
188. Krüger, A. J. D. *et al.* Compartmentalized Jet Polymerization as a High-Resolution Process to Continuously Produce Anisometric Microgel Rods with Adjustable Size and Stiffness. *Adv. Mater.* 1903668 (2019). doi:10.1002/adma.201903668
189. Hwang, D. K., Dendukuri, D. & Doyle, P. S. Microfluidic-based synthesis of non-spherical magnetic hydrogel microparticles. *Lab Chip* **8**, 1640–1647 (2008).
190. Baah, D. *et al.* Microfluidic synthesis and post processing of non-spherical polymeric microparticles. *Microfluid. Nanofluidics* **12**, 657–662 (2012).
191. Haghgooie, R., Toner, M. & Doyle, P. S. Squishy Non-Spherical Hydrogel Microparticles. *Macromol. Rapid Commun.* **31**, 128–134 (2010).
192. Park, W. *et al.* Microfluidic-Printed Microcarrier for In Vitro Expansion of Adherent Stem Cells in 3D Culture Platform. *Macromol. Biosci.* **19**, 1900136 (2019).
193. Choi, K. *et al.* 3D shape evolution of microparticles and 3D enabled applications using non-uniform UV flow lithography (NUFL). *Soft Matter* **13**, 7255–7263 (2017).
194. Li, M. *et al.* Wrinkling Non-Spherical Particles and Its Application in Cell Attachment Promotion. *Sci. Rep.* **6**, 30463 (2016).
195. Nichol, J. W. & Khademhosseini, A. Modular tissue engineering: Engineering biological tissues from the bottom up. *Soft Matter* **5**, 1312–1319 (2009).
196. Guillotin, B. & Guillemot, F. Cell patterning technologies for organotypic tissue fabrication. *Trends Biotechnol.* **29**, 183–190 (2011).
197. Rouwkema, J., Rivron, N. C. & van Blitterswijk, C. A. Vascularization in tissue engineering. *Trends Biotechnol.* **26**, 434–441 (2008).
198. Gaspar, V. M., Lavrador, P., Borges, J., Oliveira, M. B. & Mano, J. F. Advanced Bottom-Up Engineering of Living Architectures. *Adv. Mater.* **32**, 1903975 (2020).
199. Correia, C. R., Bjørge, I. M., Nadine, S. & Mano, J. F. Minimalist Tissue Engineering Approaches Using Low Material-Based Bioengineered Systems. *Adv. Healthc. Mater.* **2002110**, 1–18 (2021).
200. Correia, C. R., Reis, R. L. & Mano, J. F. Design Principles and Multifunctionality in Cell Encapsulation Systems for Tissue Regeneration. *Adv. Healthc. Mater.* **7**, 1701444 (2018).
201. Ahrens, C. C., Dong, Z. & Li, W. Engineering cell aggregates through incorporated polymeric microparticles. *Acta Biomater.* **62**, 64–81 (2017).
202. Custódio, C. A., Cerqueira, M. T., Marques, A. P., Reis, R. L. & Mano, J. F. Cell selective chitosan microparticles as injectable cell carriers for tissue regeneration. *Biomaterials* **43**, 23–31 (2015).
203. Utech, S. *et al.* Microfluidic Generation of Monodisperse, Structurally Homogeneous Alginate Microgels for Cell Encapsulation and 3D Cell Culture. *Adv. Healthc. Mater.* **4**, 1628–1633 (2015).
204. Correia, C. R., Bjørge, I. M., Zeng, J., Matsusaki, M. & Mano, J. F. Liquefied Microcapsules as Dual-Microcarriers for 3D+3D Bottom-Up Tissue Engineering. *Adv. Healthc. Mater.*

1901221 (2019). doi:10.1002/adhm.201901221
205. Griffin, D. R., Weaver, W. M., Scumpia, P. O., Di Carlo, D. & Segura, T. Accelerated wound healing by injectable microporous gel scaffolds assembled from annealed building blocks. *Nat. Mater.* **14**, 737–744 (2015).
206. Lim, F. & Sun, A. M. Microencapsulated islets as bioartificial endocrine pancreas. *Science.* **210**, 908–10 (1980).
207. Slaughter, B. V., Khurshid, S. S., Fisher, O. Z., Khademhosseini, A. & Peppas, N. A. Hydrogels in Regenerative Medicine. *Adv. Mater.* **21**, 3307–3329 (2009).
208. Mao, A. S. *et al.* Deterministic encapsulation of single cells in thin tunable microgels for niche modelling and therapeutic delivery. *Nat. Mater.* **16**, 236–243 (2017).
209. de Vos, P., Faas, M. M., Strand, B. & Calafiore, R. Alginate-based microcapsules for immunoisolation of pancreatic islets. *Biomaterials* **27**, 5603–5617 (2006).
210. Correia, C. R., Reis, R. L. & Mano, J. F. Multilayered hierarchical capsules providing cell adhesion sites. *Biomacromolecules* **14**, 743–751 (2013).
211. Li, F. *et al.* Cartilage tissue formation through assembly of microgels containing mesenchymal stem cells. *Acta Biomater.* **77**, 48–62 (2018).
212. Riley, L., Schirmer, L. & Segura, T. Granular hydrogels: emergent properties of jammed hydrogel microparticles and their applications in tissue repair and regeneration. *Curr. Opin. Biotechnol.* **60**, 1–8 (2019).
213. Huang, G. Y. *et al.* Microfluidic hydrogels for tissue engineering. *Biofabrication* **3**, 012001 (2011).
214. Van Wezel, A. L. Growth of Cell-strains and Primary Cells on Micro-carriers in Homogeneous Culture. *Nature* **216**, 64–65 (1967).
215. Lima, A. C., Alvarez-Lorenzo, C. & Mano, J. F. Design Advances in Particulate Systems for Biomedical Applications. *Adv. Healthc. Mater.* **5**, 1687–1723 (2016).
216. Custódio, C. A., Reis, R. L. & Mano, J. F. Engineering Biomolecular Microenvironments for Cell Instructive Biomaterials. *Adv. Healthc. Mater.* **3**, 797–810 (2014).
217. Sheikhi, A. *et al.* Microfluidic-enabled bottom-up hydrogels from annealable naturally-derived protein microbeads. *Biomaterials* **192**, 560–568 (2019).
218. Mahou, R., Vlahos, A. E., Shulman, A. & Sefton, M. V. Interpenetrating Alginate-Collagen Polymer Network Microspheres for Modular Tissue Engineering. *ACS Biomater. Sci. Eng.* **4**, 3704–3712 (2018).
219. Skylar-Scott, M. A. *et al.* Biomanufacturing of organ-specific tissues with high cellular density and embedded vascular channels. *Sci. Adv.* **5**, eaaw2459 (2019).
220. Wang, Z. *et al.* Facile functionalization and assembly of live cells with microcontact-printed polymeric biomaterials. *Acta Biomater.* **11**, 80–87 (2015).
221. Onoe, H. & Takeuchi, S. Cell-laden microfibers for bottom-up tissue engineering. *Drug Discov. Today* **20**, 236–246 (2015).
222. Kang, E. *et al.* Microfluidic Spinning of Flat Alginate Fibers with Grooves for Cell-Aligning Scaffolds. *Adv. Mater.* **24**, 4271–4277 (2012).
223. Correia, C. R., Gil, S., Reis, R. L. & Mano, J. F. A Closed Chondromimetic Environment within Magnetic-Responsive Liquified Capsules Encapsulating Stem Cells and Collagen II/TGF-β3 Microparticles. *Adv. Healthc. Mater.* **5**, 1346–1355 (2016).
224. Kim, J., Staunton, J. R. & Tanner, K. Independent Control of Topography for 3D Patterning of the ECM Microenvironment. *Adv. Mater.* **28**, 132–137 (2016).
225. Paul, C. D. *et al.* Probing cellular response to topography in three dimensions. *Biomaterials* **197**, 101–118 (2019).
226. Kasza, K. E. & Zallen, J. A. Dynamics and regulation of contractile actin-myosin networks in morphogenesis. *Curr. Opin. Cell Biol.* **23**, 30–8 (2011).
227. Wei, D. *et al.* A biocompatible hydrogel with improved stiffness and hydrophilicity for modular tissue engineering assembly. *J. Mater. Chem. B* **3**, 2753–2763 (2015).
228. Unger, R. E., Dohle, E. & Kirkpatrick, C. J. Improving vascularization of engineered bone through the generation of pro-angiogenic effects in co-culture systems. *Adv. Drug Deliv. Rev.* **94**, 116–125 (2015).
229. Correia, C. R. *et al.* Semipermeable Capsules Wrapping a Multifunctional and Self-regulated

Co-culture Microenvironment for Osteogenic Differentiation. *Sci. Rep.* **6**, 21883 (2016).
230. Sun, T. *et al.* Magnetic alginate microfibers as scaffolding elements for the fabrication of microvascular-like structures. *Acta Biomater.* **66**, 272–281 (2018).
231. Flemming, R. G., Murphy, C. J., Abrams, G. A., Goodman, S. L. & Nealey, P. F. Effects of synthetic micro-and nano-structured surfaces on cell behavior. *Biomaterials* **20**, 573–588 (1999).
232. Dalby, M. J. Topographically induced direct cell mechanotransduction. *Med. Eng. Phys.* **27**, 730–742 (2005).
233. Bettinger, C. J., Langer, R. & Borenstein, J. T. Engineering substrate topography at the micro- and nanoscale to control cell function. *Angew. Chem. Int. Ed. Engl.* **48**, 5406–15 (2009).
234. Nie, Z. & Kumacheva, E. Patterning surfaces with functional polymers. *Nat. Mater.* **7**, 277–290 (2008).
235. Xu, Q. *et al.* Preparation of Monodisperse Biodegradable Polymer Microparticles Using a Microfluidic Flow-Focusing Device for Controlled Drug Delivery. *Small* **5**, 1575–1581 (2009).
236. Ko, J. A., Park, H. J., Hwang, S. J., Park, J. B. & Lee, J. S. Preparation and characterization of chitosan microparticles intended for controlled drug delivery. *Int. J. Pharm.* **249**, 165–174 (2002).
237. Yang, Y.-Y., Chung, T.-S. & Ping Ng, N. Morphology, drug distribution, and in vitro release profiles of biodegradable polymeric microspheres containing protein fabricated by double-emulsion solvent extraction/evaporation method. *Biomaterials* **22**, 231–241 (2001).
238. Lima, A. C., Song, W., Blanco-Fernandez, B., Alvarez-Lorenzo, C. & Mano, J. F. Synthesis of Temperature-Responsive Dextran-MA/PNIPAAm Particles for Controlled Drug Delivery Using Superhydrophobic Surfaces. *Pharm. Res.* **28**, 1294–1305 (2011).
239. Xie, J., Ng, W. J., Lee, L. Y. & Wang, C.-H. Encapsulation of protein drugs in biodegradable microparticles by co-axial electrospray. *J. Colloid Interface Sci.* **317**, 469–476 (2008).
240. Siepmann, J. & Siepmann, F. Modeling of diffusion controlled drug delivery. *J. Control. Release* **161**, 351–362 (2012).
241. Mo, R. & Gu, Z. Tumor microenvironment and intracellular signal-activated nanomaterials for anticancer drug delivery. *Mater. Today* **19**, 274–283 (2016).
242. Lin, X., Wu, Z., Wu, Y., Xuan, M. & He, Q. Self-Propelled Micro-/Nanomotors Based on Controlled Assembled Architectures. *Adv. Mater.* **28**, 1060–1072 (2016).
243. Wu, Z. *et al.* Water-Powered Cell-Mimicking Janus Micromotor. *Adv. Funct. Mater.* **25**, 7497–7501 (2015).
244. Xu, W., Yin, P. & Dai, M. Super-resolution Geometric Barcoding for Multiplexed miRNA Profiling. *Angew. Chemie - Int. Ed.* **57**, 14075–14079 (2018).
245. Sun, L. *et al.* Bioinspired programmable wettability arrays for droplets manipulation. *Proc. Natl. Acad. Sci. U. S. A.* **117**, 4527–4532 (2020).
246. Fu, F. *et al.* Bioinspired living structural color hydrogels. *Sci. Robot.* **3**, eaar8580 (2018).
247. Cai, L. *et al.* Stomatocyte structural color-barcode micromotors for multiplex assays. *Natl. Sci. Rev.* **7**, 644–651 (2020).
248. Harley, W. S. *et al.* Advances in biofabrication techniques towards functional bioprinted heterogeneous engineered tissues: A comprehensive review. *Bioprinting* **23**, e00147 (2021).
249. Burroughs, L. *et al.* Discovery of synergistic material-topography combinations to achieve immunomodulatory osteoinductive biomaterials using a novel in vitro screening method: The ChemoTopoChip. *Biomaterials* **271**, 120740 (2021).
250. Alisafaei, F., Jokhun, D. S., Shivashankar, G. V. & Shenoy, V. B. Regulation of nuclear architecture, mechanics, and nucleocytoplasmic shuttling of epigenetic factors by cell geometric constraints. *Proc. Natl. Acad. Sci. U. S. A.* **116**, 13200–13209 (2019).

2

Materials & Methods

Chapter II

Experimental methodologies and materials

Chapter II: Experimental methodologies and materials

This chapter summarises the materials and techniques applied in **Chapters III through VI**, as well as the reasons for their selection. In the experimental subsection of each chapter, the materials and corresponding commercial distributors can be found, as well as the experimental procedures and equipment suppliers.

1. Spheroidal hydrogel particles

Drug-loaded hydrogel particles are generally produced by precipitation or crosslinking while immersed in a liquid insoluble environment, which compromises the initial loading since molecules may be lost within the liquid phase. To solve this issue, superamphiphobic surfaces appear as attractive options to produce spherical hydrogel particles in a liquid-air interface, under mild processing conditions, compatible with drug and cell encapsulation. For example, photocrosslinking has been successfully applied to produce such particles spherical using water soluble methacrylated chitosan, a biocompatible and biodegradable natural polymer.[1,2] Based on these results, we envisioned the production of spheroidal hydrogel particles relying on the application of not one, but two superamphiphobic surfaces to "sandwich" the precursor solution prior to photocrosslinking (**Chapter III**).

1.1. Superamphiphobic coating of glass microscope slides

The method to produce superamphiphobic coating was adapted from Deng *et al*.[3] Briefly, a microscope slide was held above the flame of a paraffin candle to form a soot layer. Afterwards, the soot-coated substrates were exposed to chemical vapour deposition (CVD) of tetraethyl orthosilicate (TEOS) in the presence of ammonia for 24h in a desiccator, followed by calcination of the hybrid carbon/silica network at 550°C for 2h. Finally, the hydrophilic silica shell was coated with 1H,1H,2H,2H-perfluorodecyltriethoxysilane by CVD for 3 days at 50°C.

1.2. Synthesis of methacrylated chitosan

As described by Yu *et al*.,[4] a 3% w/v chitosan solution was prepared by dissolving chitosan in 2% v/v acetic acid overnight at RT with constant stirring. Subsequently, methacrylic

anhydride was added at 1 molar equivalents per chitosan repeat unit and left for 5h at RT. The mixture was dialysed against distilled water for 5 days, changing the water three times a day.

1.3. Production of spheroidal hydrogels

A volume of 4.5 μL of 2, 3, or 4% w/v methacrylated chitosan in distilled water was used to produce each hydrogel particle. Spacers were produced from polypropylene films with a thickness of 90 μm each, which were stacked to achieve the desired final height. The polymeric solution was placed between two superamphiphobic surfaces with a varying spacer height to control the shape of the polymer droplet. A UV-crosslinking method was employed using a curing system (λ = 320–500 nm) with a 90 second crosslinking period and 2-hydroxy-4'-(2-hydroxyethoxy)-2-methylpropiophenone as photoinitiator. For control spherical conditions, a second superamphiphobic surface was also placed above the precursor solution, without contact, to guarantee an equal UV intensity to spheroidal conditions.

1.4. Characterisation of spheroidal particles

1.4.1. Characterisation of circularity and surface area

The circularity and surface area of spheroidal hydrogel particles was calculated according to particle deformation. ImageJ software was used to calculate the circularity of particles from images taken using a contact angle measurement equipment between 0 to 1, with 1 corresponding to a perfectly spherical particle. In turn, particle deformation was calculated according to spacer height and an initial average particle diameter of 1.90 ± 0.05 mm. Particle surface area was calculated using formulas for oblate spheroids and spheres, where semi-axis values were measured from images of experimentally obtained particles with ImageJ. The specific equations applied in these calculations can be found in Chapter III.

1.4.2. Experimental *in vitro* drug release

To assess the impact of increasing surface area to volume ratio, drug release studies were performed using model drug BSA. The chitosan precursor was loaded with BSA and crosslinked according to the previously described methodology to produce apheres or spheroids. BSA-loaded hydrogel particles were placed in PBS at pH 7.4 and 37°C, under

gentle agitation. At pre-established time points, the supernatant was removed for analysis and replaced with an equal volume of fresh PBS. The amount of the drug released was quantified using the Micro BCA Protein Assay Kit upon spectrophotometrical quantification at 562 nm against a known calibration curve. Results were modelled using the Korsemeyer-Peppas equation for calculation of the diffusional exponent to characterise the transport mechanism, according to the exponential dependence of the amount of drug released and rate constant over time.[5]

1.4.3. Modelling of the liquid droplet compression and drug release

Under collaboration with Professor Miguel Nóbrega at the Institute for Polymers and Composites/i3N, University of Minho, Portugal, modelling of the liquid droplet deformation and of the drug release rate were performed. The droplet deformation was modelled with the computational library OpenFOAM, to simulate the structural behaviour of linear elastic materials. To mimic the experimental tests, the initially spherical droplet was deformed by a moving plate, to achieve the same deformation levels imposed experimentally. Additionally, numerical modelling studies were performed to assess the impact of the geometry of spheroidal particles on the evolution of a specific compound, transported by diffusion. In these studies, the OpenFOAM solver employed was the laplacianFoam, which was modified to accommodate a Neuman boundary condition at the spheroid surface.

2. Nanogrooved sandwich cell culture model

Optical media substrates (CDs) were previously identified as low-cost, attractive options to be used directly as substrates with grooved surface topography for tissue engineering applications, or to be used indirectly as moulds.[6,7] We envisioned CDs could also be used as moulds for the imprinting process, under a controlled temperature, time, and pressure. CDs are commonly manufactured using polycarbonate, which possesses a melt temperature of approximately 300ºC. In turn, polystyrene, one of the most widely applied thermoplastic polymers for cell culture materials, presents a glass transition temperature (T_g) of approximately 100ºC. Hence heating polystyrene substrates above the T_g would enable an effective imprinting, while safeguarding the grooved polycarbonate mould (**Chapter IV**).

2.1. Micromolding of polystyrene substrates

Polystyrene adherent petri dishes (15 cm diameter) were cut into 8 x 8 mm^2 substrates using a laser-cutting machine. CDs were used as nanogrooved templates to mould polystyrene substrates. Moulding was performed in a laboratory oven at 120ºC for 50 minutes with an applied pressure of approximately 130 mPa. Polystyrene substrates were plasma treated at 0.4-0.6 mbar and 30 V for 15 min using atmospheric air, followed by UV sterilisation during 30 min.

2.2. Sandwich culture model assembly

SW conditions were produced by assembling nanogrooved or non- nanogrooved substrates with or without MC3T3-E1 cells, and with variable relative orientations (0º or 90º) between nanogrooves of upper and lower substrates. Additionally, SW conditions with cells seeded on both lower and upper substrates were tested. Cells were seeded on respective substrates at a concentration of $1x10^4$ cells/cm^2 and left to adhere for 3 hours at 37ºC. SW conditions were produced by assembling upper substrates with lower substrates and ensuring contact between upper and lower substrates by placing a glass substrate (10x5x1 mm; 150 mg) over assembled SWs. For all assessed conditions, upon the initial 3h adhesion period, cells were cultured for 21h on single substrates or within the SW, totalling 24h of culture.

3. Microparticles: μspheres and topodiscs

To produce microdiscs with nanogrooved surface topography (topodiscs), imprinting technology was similarly applied on initially spherical microparticles. Furthermore, it was necessary to select an alternative thermoplastic polymer since polystyrene is not biodegradable. Due to its biocompatibility, biodegradability, melt temperature of approximately 60ºC, and extensive use in the fabrication of scaffolds and microparticles for tissue engineering applications, polycaprolactone (PCL) was selected. Yet initial trials to imprint PCL microparticles directly on CDs did not allow for topodisc collection. Hence, we idealised the use of sacrificial CD countermoulds, composed of water soluble poly(vinyl alcohol) (PVA), to enable collection. PVA presents a T_g of approximately 80ºC, hence the produced PVA membranes would be compatible with the temperature required for PCL melting during the imprinting process (75ºC). Immersion of PVA-entrapped PCL in water

enables dissolution of the PVA membrane and allows for topodisc collection (**Chapter V** and **VI**).

3.1. Production methodology

The production method of μspheres and topodiscs is illustrated in Scheme II.1. Step I relates to μsphere production, steps I-V relate to topodisc production, and step VI relates to surface modification.

Step I: A 5% w/v solution of PCL in dichloromethane was emulsified under agitation (1:5) with an aqueous 0.5% w/v solution of PVA for 48 hours to produce PCL microparticles. Spherical microparticles (μspheres) were sieved between distinct sizes: 25-40 μm and 50-80 μm diameters. μSpheres$_{25\text{-}40}$ were selected to be used for topodisc production in **Chapters V** and **VI**. For **Chapter V**, μspheres$_{25\text{-}40}$ serve as control non-grooved particles, whereas in **Chapter VI**, μspheres$_{50\text{-}80}$ were used as control. The use of μspheres$_{50\text{-}80}$ as a control particle with flat surface topography presented two main advantages. The first was related to the equivalent surface area per particle with regards to topodiscs. The second was due to the collapsing of particles, probably during production, rendering them less spherical and more flattened, similar in morphology to topodiscs.

Step II: PVA countermoulds of CDs were produced via solvent evaporation of a 12% w/v solution of PVA in distilled water on CDs at 40ºC. A 12% w/v solution was used to guarantee manageability of the membranes upon solvent evaporation, while aiming to reduce final membrane thickness and PVA content.

Step III: μspheres were dispersed on top of nanogrooved PVA membranes and pre-heated at 75ºC for 25 min prior to imprinting. A second nanogrooved PVA membrane was placed on top of pre-heated μspheres with an applied pressure of approximately 1 kPa for 5 min. Pressure, temperature, and time were optimised to obtain a homogeneous nanogrooved surface topography and disc-like shape.

Step IV: Upon cooling, PVA-entrapped PCL parrticles were dissolved in distilled water under stirring.

Step V: Topodiscs were collected by centrifugation, extensively washed in distilled water, and dried.

Step VI: Topodiscs and non-molded µspheres were subjected to plasma treatment at 0.4-0.6 mbar and 30 V for 15 min using atmospheric air. Particles were sterilised in 70% v/v ethanol for 30 min.

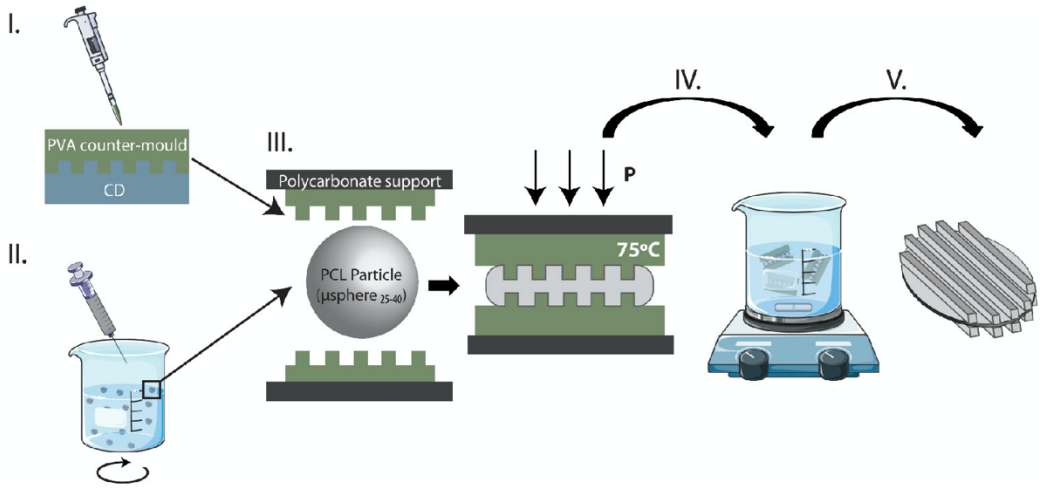

Scheme II.1. Illustration of the production method for topodiscs. I. Production of polyvinyl alcohol (PVA) counter-moulds of CDs by solvent evaporation of a 12% w/v PVA solution at 40ºC. II. Production of PCL particles via oil/water emulsion and subsequent sieving to collect particles with diameters comprised between 25-40 µm microparticles (µspheres$_{25\text{-}40}$). III. Micro-moulding of µspheres$_{25\text{-}40}$ between nanogrooved PVA membranes at an optimised applied force, time, and temperature. IV. Successive topodisc washing in distilled water to remove all traces of PVA. V. Topodisc recovery by centrifugation.

4. Liquefied-core, multi-layered capsules

Previously developed by our group, liquefied-core, multi-layered capsules are an attractive encapsulation strategy.[8–10] The multi-layered membrane guarantees an appropriate nutrient and oxygen diffusion into the capsule core, required for cell survival, and enables the exit of waste products. The liquefied core allows for free movement and promotes the interaction of the core components. Within the core, microparticles act as cell adhesion sites to enable cell survival and proliferation. Additionally, when subject to dynamic culturing in a simple spinner flask, each individual capsule functions as a microbioreactor. The technology was employed in **Chapter VI**.

Sodium alginate (ALG, low viscosity from brown algae) aqueous solution at 2% w/v containing 0.15 M sodium chloride (NaCl) and 25 mM MES hydrate at pH 6.7 are prepared and used as sacrificial template for membrane build-up. Desired core contents, namely cells

and microparticles of interest, are suspended in the ALG solution. The ALG solution containing desired core contents was added dropwise using a 21G needle into an aqueous calcium chloride solution (0.1 M, Sigma-Aldrich) buffered with NaCl and MES under stirring (200 rpm) for 20 min. Alginate hydrogels were rinsed in a washing buffer (0.15 M NaCl and 25 mM MES). To build up the multi-layered membrane via layer-by-layer technology, ALG hydrogels were sequentially immersed in poly-L-lysine (PLL, Mw~30,000–70,000, pH 6.7), ALG (pH 6.7), water-soluble highly purified chitosan (CHT, pH 6.3, viscosity 107 mPa.s, Mw = 2.7 × 105 $g.mol^{-1}$, 83% degree of deacetylation), and ALG again. This process was repeated three times to obtain a 12-layered membrane. A concentration of 0.5 $mg.mL^{-1}$ was used for the polyelectrolytes (ALG, CHT, PLL) dissolved in an aqueous 0.15 M NaCl and 25 mM MES solution. Polyelectrolyte immersion was performed during 10 min, followed by a 2 min washing step in washing buffer. Finally, the hydrogel core was liquefied via immersion in an aqueous 5 mM ethylenediaminetetraacetic acid (EDTA, pH 6.7) solution. All solutions were sterilized by filtration through a 0.22 µm filter.

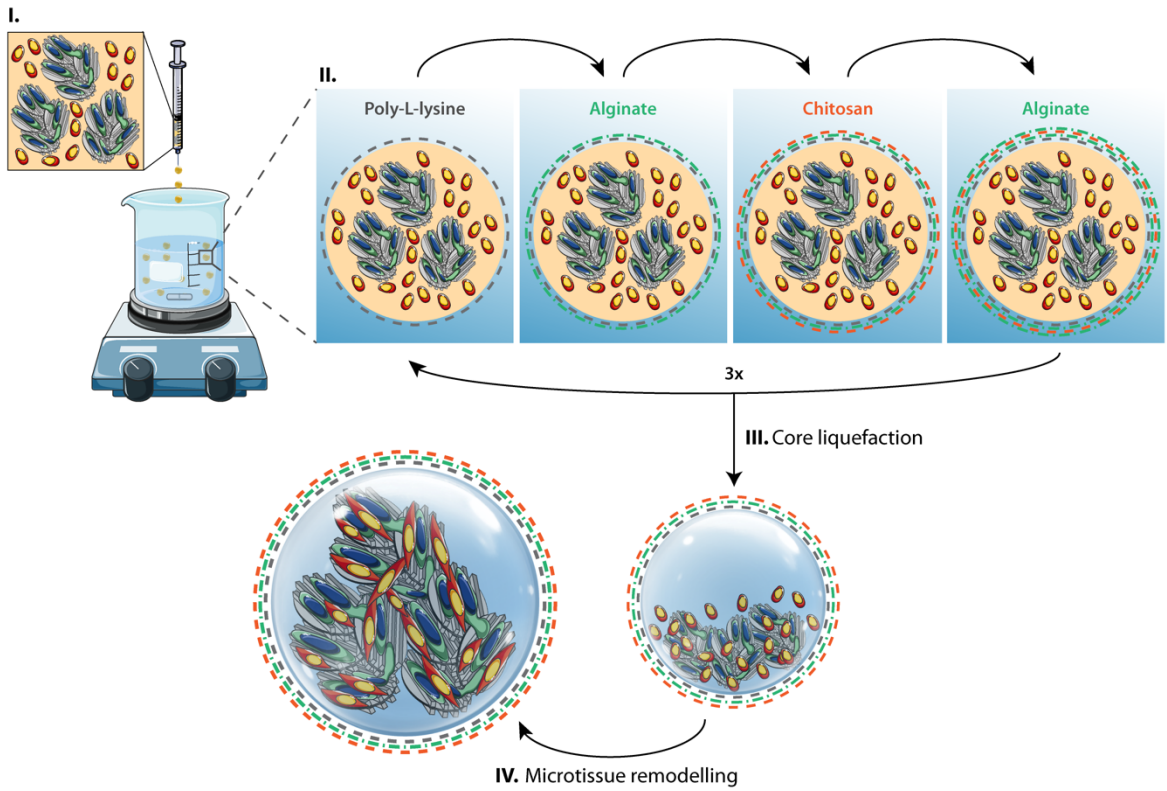

Scheme II.2. Schematic representation of the production method of liquefied-core, multi-layered capsules. I. Dropwise addition of ALG solution containing core components (illustrated: hASC and topodisc microaggregates, combined with suspended HUVECs) into an aqueous calcium chloride solution. II. ALG bead collection and sequential immersion in PLL, ALG, CHT, and ALG solutions to obtain a 12-layered

membrane. III. ALG core liquefaction with EDTA. IV. Ultimately, core contents are remodelled to for a microtissue.

5. Cell sources

5.1. Cell lines

Commercially available mouse fibroblast cell line L929 was used in **Chapter III**, whereas mouse pre-osteoblastic cell line MC3T3-E1 was used in **Chapters IV** and **V**. Both are standardised, immortalised cell lines, which proliferate indefinitely. Hence, they are attractive options for validation studies such as the ones described in aforementioned chapters.

5.2. Primary cells

Primary cells were either purchased (**Chapter V**) or isolated from adipose tissue (**Chapter VI**) and umbilical cord (**Chapter VI**). Adipose tissue is easily obtained and adipose-derived stromal cells (hASCs) retain their multipotency to differentiate into the adipogenic, chondrogenic, myogenic, and osteogenic lineages.[11] In turn, human umbilical cord-derived endothelial cells (HUVECs) are the most widely available human endothelial cell type.[12] Flow cytometry was used to confirm the phenotypic profile of isolated ASCs and HUVECs.

5.2.1. ASC isolation from adipose tissue

hASCs were isolated from subcutaneous adipose tissue derived from liposuction procedures. Collected tissues were obtained with informed patient consent and under a cooperation agreement between University of Aveiro and Hospital da Luz (Aveiro, Portugal), after approval of the Competent Ethics Committee (CEC) and were handled according to CEC guidelines. Samples were transported in PBS supplemented with 1% v/v antibiotic/antimycotic and stored at 4ºC until isolation. Lipoaspirate samples were washed with PBS five times and incubated in a 0.1% w/v collagenase type I solution at 37ºC for 45 minutes. Subsequently, the solution was centrifuged at 1200 rpm for 10 minutes, the supernatant was removed, and the pellet was resuspended in PBS and centrifuged again at 1200 rpm for 10 minutes. The resulting pellet containing isolated hASCs was resuspended in Minimum Essential Alpha Medium (α-MEM,) supplemented with 10% fetal bovine serum (FBS) and 1% antibiotic/antimycotic at 37ºC in a humidified air atmosphere of 5% CO_2.

5.2.2. EC isolation from umbilical cord

Umbilical cord was obtained under a cooperation agreement between the Aveiro Institute of Materials, University of Aveiro, and Hospital do Baixo Vouga (Aveiro, Portugal), upon approval from the Competent Ethics Committee (CEC). The human tissues received were handled in accordance with the guidelines approved by the CEC and informed consent was obtained from all subjects. HUVECs were isolated following well-established protocols in the group. The enzymatic mixture containing dispase II and collagenase type IV was used for the isolation of HUVECs from the cord vein. The cord vein was filled with the enzyme cocktail and incubated at 37 °C for 20 min. Subsequently, HUVECs were flushed out and seeded in culture flasks previously coated with 0.7% w/v gelatine (porcine skin type A) containing M199 growth medium at 5% CO_2 and 37 °C. 4–6 hours later, the medium was changed to M199 containing 20% v/v umbilical cord blood serum, 2 mM l-glutamine, 5 ng/mL vascular endothelial growth factor, 10 μg/mL heparin, 100 U/mL penicillin and 100 μg/mL streptomycin.

5.2.3. Characterisation of isolated cells

Phenotypic profile of hASCs and HUVECs was assessed by flow cytometry regarding mesenchymal (CD105-FITC, CD90-APC, and CD73-PE), endothelial (CD31-APC), and hematopoietic stem/progenitor cells (CD34-FITC) markers (**Chapter VI**). Isolated cells were harvested using TrypLE™ Express solution at 37 °C for 5 min. Samples were resuspended in PBS solution containing 3% w/v bovine serum albumin and abovementioned antibodies at dilutions defined by the manufacturer. Upon 20 min at RT, samples were washed with PBS, centrifuged, fixed in PBS with 1% v/v formaldehyde and analysed in a flow cytometer.

6. Cell seeding, encapsulation, and anchorage

3D culture strategies for cell anchorage to microparticles, namely μspheres and topodiscs, and cell encapsulation within hydrogels and liquefied-core capsules were employed in **Chapters III**, **V**, and **VI**. In **Chapter IV**, seeding was performed in a quasi-3D sandwich culture model.

6.1. Sandwich culture model

MC3T3-E1 cell line was selected for culturing within the sandwich culture model and assessment of cell elongation and morphology. MC3T3-E1 cells were cultured with α-MEM supplemented with 10% v/v FBS and 1% v/v AA at 37ºC in a humidified air atmosphere of 5% CO_2. Cells were detached at 90% of confluence via 0.05% w/v trypsin-EDTA treatment for 5 min at 37ºC. Cells were seeded on respective substrates at a concentration of $1x10^4$ cells/cm^2 and left to adhere for 3 hours at 37ºC after which each sandwich was closed accordingly. Upon 21h in culture, samples were fixed in in 4% v/v formaldehyde solution for 30 min at RT.

6.2. Cell anchorage

6.2.1. Macroaggregates

In **Chapter V**, macroaggregates were formed by cell-mediated, bottom-up assembly of cells with topodiscs and control μspheres. Pre-osteoblastic cell line MC3T3-E1 was used to initially assess the capability of microparticle populations to sustain cell survival and proliferation. To determine the potential of microparticles in inducing differentiation towards the osteogenic lineage, hASCs were utilised.

MC3T3-E1 cells and hASCs were cultured with α-MEM supplemented with 10% v/v FBS and 1% v/v AA, denominated basal medium (BAS) at 37ºC in a humidified air atmosphere of 5% CO_2. Cells were detached at 90% of confluence via 0.05% w/v trypsin-EDTA treatment for 5 min at 37ºC. A seeding density of $4x10^5$ cells.cm^{-2} was used for MC3T3-E1 cells, whereas $8x10^5$ cells.cm^{-2} was used for hASCs, calculated based on the average surface area of topodiscs. An equal weight of topodiscs and μspheres was used for each condition. Topodisc and μsphere MC3T3-E1-mediated aggregates were cultured in solely in BAS medium. To assess the osteogenic potential, hASC-mediated aggregates were cultured in both BAS medium and medium supplemented with osteoinductive factors (50 μg.mL^{-1} ascorbic acid, 10 mM β-glycerophosphate disodium salt, and 10 nM dexamethasone), aiming to pinpoint the role of topography in the absence of osteoinductive factors.

6.2.2. Microaggregates

In **Chapter VI**, microaggregates with approximately 200 µm in diameter were formed by cell-mediated, bottom-up assembly of hASCs with topodiscs and control µspheres. hASCs were cultured with α-MEM supplemented with 10% v/v FBS and 1% v/v AA, denominated BAS medium at 37ºC in a humidified air atmosphere of 5% CO_2. At 90% of confluence, hASCs were detached by 0.05% w/v trypsin-EDTA treatment for 5 min at 37ºC. hASC-particle (topodiscs or µspheres) microaggregates were produced using AggreWell400 24-well plates, according to manufacturer's recommendations. A concentration of $6x10^5$ cells and 1.5 mg particles (topodiscs or µspheres) was used per well. 24h after seeding, hASC-particle (topodiscs or µspheres) microaggregates were collected. Microaggregates produced for dynamic culturing were subjected to an additional coating with fibronectin from human plasma dissolved in PBS (5 $\mu g.cm^{-2}$, Sigma Aldrich) for 1h at 37ºC, followed by washing with PBS prior to encapsulation within liquefied-core capsules.

6.3. Cell encapsulation

6.3.1. Spheroidal hydrogels

To validate the use of spheroidal hydrogel particles and the impact of increasing surface area to volume ratio on cell survival, routinely applied L929 cells were encapsulated within hydrogel particles with varying circularity (**Chapter III)**. Cells were cultured with Dulbecco's Modified Eagle Medium (DMEM) low glucose supplemented with 3.7 g/L sodium bicarbonate, 10% v/v FBS and 1% pen-strep at pH 7.4, at 37°C in a humidified air atmosphere of 5% CO_2. At 90% of confluence the cells were washed with PBS and detached by a chemical procedure with trypsin solution for 5 min. The obtained cell suspension was centrifuged at 300 × g for 5 min and resuspended in the chitosan solution at a cell density of $1x10^6$ cells/mL. The resulting suspensions were used to produce spherical and spheroidal particles according to the methods previously described for spheroidal hydrogel production.

6.3.2. Liquefied-core and multi-layered capsules

In accordance with the previous section regarding liquefied-core capsule production, hASC-particle (topodiscs or µspheres) microaggregates and HUVECs were resuspended in a 2% w/v ALG aqueous solution containing 0.15 M NaCl and 25 mM MES hydrate at pH 6.7 to form the ALG core template for subsequent multi-layered membrane deposition (**Chapter**

VI). Within the core, a concentration of $3x10^6$ hASCs and 7.5 mg particles (topodiscs or μspheres) in microaggregates per mL of ALG were used for the monoculture, with an additional $3x10^6$ suspended HUVECs per mL of ALG for the co-culture system. Capsules containing only hASCs were cultured in complete α-MEM with or without osteoinductive factors (50 $\mu g.mL^{-1}$ ascorbic acid, 10 mM β-glycerophosphate disodium salt, and 10 nM dexamethasone). Capsules containing hASCs and HUVECs were cultured in complete M199 with or without osteoinductive factors.

7. *In vitro* biological performance assays

7.1. Cell metabolic activity

In **Chapter V**, mitochondrial metabolic activity quantification was tracked up to 21 days using a 3-(4,5-dimethylthiazol-2-yl)-5-(3-carboxymethoxyphenyl)-2-(4-sulphofenyl)-2H-tetrazolium (MTS) colorimetric assay. In viable cells, this assay relies on the reduction capability of mitochondrial dehydrogenase enzymes to convert MTS into a characteristically brown formazan product. This enabled to verify the ability of topodiscs and μspheres to sustain cell expansion for long term culture. Samples were incubated with an MTS solution diluted 1:5 in PBS at 37ºC for 4h. The amount of formazan product was measured by absorbance at 490 nm using a microplate reader.

7.2. Cell proliferation

In **Chapter V**, cell proliferation was assessed via double-stranded (ds) DNA quantification up to 21 days by Quant-iT™ Picogreen™ assay. This enabled to verify the ability of topodiscs and μspheres to sustain cell expansion for long term culture. Samples were collected in ultra-pure sterile water containing 2% v/v triton-X100 to induce cell lysis and placed at -80ºC. dsDNA quantification was performed according to the manufacturer's specifications. Fluorescence was read at an excitation wavelength of 485/20 nm and emission wavelength of 528/20 nm using a microplate reader.

7.3. Fluorescence staining

7.3.1. Live/Dead assay

In **Chapters III** and **VI**, cell viability was evaluated via the use of fluorescent dyes, namely calcein-AM and propidium iodide. Non-fluorescent calcein-AM is converted into green-

fluorescent calcein after acetoxymethyl ester hydrolysis by intracellular esterases in live cells. Propidium iodide is not permeant to live cells and is hence commonly used to detect dead cells, which have a disrupted membrane. Samples were collected in PBS, subsequently placed in 1 mL of PBS containing 2 µL of calcein-AM (1 $mg.mL^{-1}$) and 1 µL of PI (1 $mg.mL^{-1}$), and incubated at 37°C for 10 min protected from the light. After this period, samples were washed at RT protected from light several times with PBS to remove all traces of excessive dyes. Samples were visualised by fluorescence microscopy using appropriate red and green fluorescence filters to detect dead and live cells, respectively.

7.3.2. Nuclei and actin filaments

Actin filaments (F-actin) are a key component of the cytoskeleton and are considered mechanosensors involved in mechanotransduction of ECM cues.[13] Visualisation of F-actin can give information as to cell alignment and interaction with the substrate. Samples were fixed in 4% w/v formaldehyde solution for 30 min at RT, and permeabilised in 0.1 % v/v triton-X100 for 5 minutes at RT. DAPI (4',6-diamidino-2-phenylindole, dihydrochloride, 1 $mg.mL^{-1}$) and phalloidin (300U) were used to stain cell nuclei in blue and F-actin in red or green, respectively. Samples were incubated in phalloidin (red or green) solution diluted in PBS (5:200) for 45 min at RT, protected from light, and counterstained with DAPI solution diluted in PBS (1:1000) for 5 min at RT protected from light. This methodology was applied in **Chapters IV**, **V**, and **VI**.

7.3.3. Vinculin

Vinculin is a component of the integrin-based adhesion complex and is a major player in focal adhesions-mediated mechanotransduction.[14] In **Chapter III**, vinculin staining was performed to assess the interaction of cells with the substrate. Samples were fixed in 4% v/v formaldehyde solution for 30 min at RT, and permeabilised in 0.1 % v/v triton-X100 for 5 minutes at RT. Samples were incubated in 5% v/v FBS in PBS for 1h at RT. Cells were incubated with primary rabbit vinculin antibody diluted in 5% v/v FBS/PBS (0.5 $mg.mL^{-1}$, 1:50) overnight at 4ºC. Samples were then incubated with secondary antibody Alexa Fluor 594 anti-rabbit diluted in 5% v/v FBS/PBS (0.5 $mg.mL^{-1}$, 1:500) at RT protected from light.

7.3.4. Osteopontin

For detection of late osteogenic marker osteopontin, samples were incubated overnight at 4ºC with primary anti-osteopontin rabbit antibody (0.5 mg.mL^{-1}, 1:100 in 5% v/v FBS). Subsequently, samples were incubated in secondary antibody Alexa 647 anti-rabbit in 5% v/v FBS (0.5 mg.mL^{-1}, 1:500) for 1h at RT. Samples were counterstained with DAPI solution diluted in PBS (1 mg.mL^{-1}, 1:1000) for 5 min at RT protected from light. This assay was employed in **Chapter IV.**

7.3.5. Hydroxyapatite

Native bone is composed of hydroxyapatite-reinforced collagen type I fibrils.[15] Hence, characterizing the mineral component is crucial towards identifying the osteogenic potential of a system. This assay was employed in **Chapters V** and **VI**. Samples were fixed with 4% v/v formaldehyde solution in PBS for 30 min at RT and subsequently permeabilised with 0.1% v/v Triton-X100 in PBS for 5 minutes. Fluorescent staining of hydroxyapatite, the main mineral component of bone, was performed using the OsteoImage mineralization assay kit, according to the manufacturer's specifications. Samples were counterstained with DAPI (1 mg.mL^{-1}) at a 1:1000 ratio in PBS for 5 min at RT protected from light.

7.3.6. Lipophilic staining

Lipophilic staining can be performed prior to cell seeding or encapsulation for a long-term tracking of distinct cell populations since the dye is retained and transmitted upon cell division. To this end, cells were incubated with DiO (1 mM, Vybrant® DiO Cell-Labelling Solution), DiD (1 mM, Vybrant® DiD Cell-Labelling Solution), or DiL (1mM, 1,1'-Dioctadecyl-3,3,3',3'-Tetramethylindocarbocyanine Perchlorate) for 30 minutes at 37ºC. A quantity of 5 μL of dye was used per mL of cell suspension containing 1x10^{6} cells. Subsequently cells were washed with cell culture medium three times with intermediate centrifugation for 5 min at 300 × g and resuspended in fresh medium at RT protected from light. Lipophilic staining was applied in **Chapters IV**, **V**, and **VI**.

7.4. Histology

7.4.1. Sample processing and embedding

Histological assessment of samples was performed upon 21 days in culture (**Chapters V** and **VI**), after fixation in 4% w/v formaldehyde solution in PBS. Samples were routinely processed manually by initial dehydration in increasing ethanol series (70%, 80%, 95%, and 100% v/v), followed by xylene and paraffin infiltration, and ultimately paraffin embedding. Histological sections of 5 μm thickness were cut using a microtome.

7.4.2. Immunohistochemistry

In preparation for immunohistochemistry, histological sections were routinely deparaffinized in xylene/ethanol series and hydrated in distilled water. When required, samples were subjected to antigen retrieval in 10 mM tri-sodium citrate dihydrate buffer with 0.05% v/v Tween 20 at pH 6, 100ºC for 20 minutes, and blocked in FBS (5% v/v in PBS) for 1h at RT.

Osteopontin: For detection of late osteogenic marker osteopontin, histological cuts were incubated overnight at 4ºC with primary anti-osteopontin rabbit antibody (0.5 $mg.mL^{-1}$, 1:100 in 5% v/v FBS). Samples were incubated in secondary antibody Alexa 647 anti-rabbit (0.5 $mg.mL^{-1}$, 1:500 in 5% v/v FBS) for 1h at RT protected from light. Samples were visualised by fluorescence microscopy.

CD31: For detection of endothelial cell marker CD31, histological cuts were incubated overnight at 4ºC with anti-human CD31 mouse antibody (1:100 in 5% v/v FBS). Samples were incubated in secondary antibody Alexa 488 anti-mouse (0.5 $mg.mL^{-1}$, 1:500 in 5% v/v FBS) for 1h at RT protected from light. Samples were visualised by fluorescence microscopy.

von Willebrand Factor: von Willebrand Factor (vWF) is a glycoprotein produced in the cytoplasm of endothelial cells within Weibel-Palade bodies, commonly applied as an angiogenesis marker.[16] Samples were incubated with primary anti-vWF rabbit antibody (1:400 in 5% v/v FBS) overnight at 4ºC, followed by incubation in secondary antibody Alexa 647 anti-rabbit (0.5 $mg.mL^{-1}$, 1:500 in 5% v/v FBS) at RT protected from light. Samples were visualised by fluorescence microscopy.

Actin filaments: Staining with phalloidin (Flash Phalloidin™ Red 594, 300U) at a 1:40 ratio in PBS for 45 min, at RT protected from light, was performed for staining of actin filaments. Samples were visualised by fluorescence microscopy.

Laminins: Laminins are an endothelial basement membrane protein family and are hence useful for determining the presence of endothelial cells within the sample. Samples were incubated with primary anti-laminin rabbit antibody (0.7 $mg.mL^{-1}$, 1:200 in 5% v/v FBS) overnight at 4ºC, followed by incubation in secondary antibody Alexa 647 anti-rabbit (0.5 $mg.mL^{-1}$, 1:500 in 5% v/v FBS) at RT protected from light. Samples were visualised by fluorescence microscopy.

Podocalyxin: Podocalyxin, an endothelial plasma membrane sialoglycoprotein, allows for detecting the presence of endothelial cells within the sample.[17] Samples were incubated with primary anti-podocalyxin mouse antibody (0.5 $mg.mL^{-1}$, 1:200 in 5% v/v FBS) overnight at 4ºC, followed by incubation in secondary antibody Alexa 555 anti-mouse (0.5 $mg.mL^{-1}$, 1:500 in 5% v/v FBS) at RT protected from light. Samples were visualised by fluorescence microscopy.

Nuclei: Nuclei were stained with DAPI (1 $mg.mL^{-1}$) at a 1:1000 ratio in PBS for 5 min at RT protected from light. Samples were visualised by fluorescence microscopy.

Masson's Trichrome: Masson's Trichrome stains collagen, the main protein component of bone. Herein, it allowed to determine if a bone-like ECM, mostly rich in type I collagen, was deposited by the cells. Histological sections were routinely deparaffinized in xylene/ethanol series and subsequently mordant in pre-heated Bouin's solution at 56ºC for 15 min. Samples were stained in Weigert's Iron Hematoxylin solution for 5 min at RT and rinsed. Next, samples were stained in Biebrich Scarlet-Acid Fuchsin for 5 min at RT and rinsed. Then stained in Phosphotungstic/Phosphomolybic Acid for 5 min, followed by staining in Aniline Blue solution for 5 min. Samples were placed in 1% v/v acetic acid in distilled water for 30 s, rinsed, dehydrated, cleared in xylene, and mounted with DPX mountant. Samples were visualised by optical microscopy.

von Kossa: von Kossa staining is employed to specifically stain mineralisation deposits, thus herein used to complementary identify hydroxyapatite in samples. While amorphous

calcium phosphate does tend to evolve towards microcrystalline hydroxyapatite, the most thermodynamically stable calcium phosphate phase, the presence of phosphate is a sample alone cannot be an indication of hydroxyapatite. von Kossa staining is hence a useful technique to be applied in combination with alternative hydroxyapatite-identifying methodologies.[18,19] Samples were incubated in 5% w/v silver nitrate solution for 60 min with exposure to UV light and rinsed, followed by incubation in 5% w/v sodium thiosulfate solution for 3 min, rinsed, and incubated with Nuclear Fast Red solution for 5 min. Samples were rinsed, dehydrated, cleared in xylene, and mounted with DPX mountant. Samples were visualised by optical microscopy.

8. Proteomic assays

8.1. pFAK and FAK ELISA

Focal adhesions are dynamic multiprotein complexes that contain, among others, focal adhesion kinase (FAK).[20] Upon initial integrin-mediated adhesion, the increased local tension induces integrin clustering and phosphorylation of FAK (pFAK).[21] Hence, quantification of total FAK and pFAK gives important information regarding cell-substrate interactions. Via enzyme-linked immunosorbent assay (ELISA), it was possible to quantify FAK and pFAK. To this end, cell pellets were extracted using cell extraction buffer (Pierce RIPA Buffer) and frozen at -80ºC. Total FAK and phosphorylated FAK were quantified per manufacturer's recommendations (**Chapter III**).

8.2. Matrix microvesicle isolation and proteomic analyses

Extracellular vesicles play a crucial role in intercellular communication and have been pinpointed as important factors in osteogenesis and promotion of angiogenesis.[22–24] In collaboration with Professor Sandra Vieira at iBiMED, Institute of Biomedicine, University of Aveiro, Portugal, microvesicles (MVs) were isolated and characterized by nano Liquid Chromatography coupled to tandem Mass Spectrometry (nanoLC-MS/MS) (**Chapter VI**). This methodology has become increasingly used for proteomic analysis and is considered advantageous due to its greater sensitivity over conventional LC–MS/MS. In this process, proteins are initially cleaved by enzymatic digestion and separated by reversed phase nano LC, followed by data-dependent MS/MS analysis.[25]

Conditioned media was collected on predetermined timepoints and stored at −80°C until MV isolation by ultra-centrifugation. To this end, media from all timepoints was pooled and pre-cleared by centrifugation (300 × *g* at 25°C for 5 min and 18,500 × *g* at 4°C for 25 min). Resulting supernatants were ultracentrifuged at 50,000 rpm at 4°C for 60 min to pellet MVs. Obtained pellets were resuspended in 1% v/v protease inhibitors cocktail in PBS to guarantee sample integrity. Protein content was determined in each sample by the Pierce BCA assay kit and, due to low protein content, all isolated pellets were used for subsequent proteomic analyses through nanoLC-MS/MS. Samples were reduced, alkylated, and enzymatically digested using tris-(2-carboxyethyl)-phosphine (TCEP), chloroacetamide and trypsin, respectively. Resulting tryptic peptides were separated by liquid chromatography coupled to a high-resolution accurate mass spectrometer. Samples were loaded to a trapping capillary column (3 µm particle size, 300 µm internal diameter x 5 mm), with a mobile phase of 2% acetonitrile (ACN) and 0.1% formic acid (FA) at 10 µL/min, and subsequently another trapping column (2 µm particle size, 75 µm internal diameter x 50 cm) at 300 nL/min. Samples were eluted by mixing solvent A (0.1% FA) and solvent B (80% ACN), using a linear gradient: 5 min (2.5% B to 10% B), 120 min (10% B to 30% B), 20 min (30% B to 50% B), 5 min (50% B to 99% B) and 10 min (hold 99% B). The mass spectrometer was operated in the data-dependent (dd) acquisition mode. The analysis alternated between a full scan (*m/z* 380-1580) and a subsequent high-energy collisional dissociation (HCD) MS/MS of the 10 most intense peaks from full scan [normalized collision energy (NCE) 27%]. ESI spray voltage was 1.9 kV. Global settings: use lock masses best (*m/z* 445.12003); lock mass injection Full MS; chrom. peak width (FWHM) 15s. Full scan settings were: 70k resolution (*m/z* 200); automatic gain control (AGC) target 3e6; maximum injection time 120 ms. dd settings: minimum AGC target 8e3; intensity threshold 7.3e4; charge exclusion: unassigned, 1, 8, >8; peptide match preferred; exclude isotopes on; dynamic exclusion 45s. MS2 settings were: microscans 1; 35k resolution (*m/z* 200); AGC target 2e5; maximum injection time 110 ms; isolation window 2.0 *m/z*; isolation offset 0.0 *m/z*; spectrum data type profile.

Raw data were then analysed using the Proteome Discoverer software by comparison against the *Homo sapiens* proteome from the UniProt database. *Bos taurus* proteome was considered to identify possible contaminants from serum supplementation. Tryptic peptides were identified by the Sequest HT search engine. The ion mass tolerance was defined at 10 ppm (for precursor ions) and 0.02 Da (for fragment ions). A maximum of 2 missing cleavage sites

was allowed. Modifications were defined as follows: cysteine carbamidomethylation as constant modification; methionine oxidation and protein N-terminus acetylation as variable modifications. Peptide confidence settings were set as high. The following settings were applied to the processing node Percolator: maximum delta Cn 0.05; decoy database search target FDR 1%; validation based on q-value, which allows for more accurate determination of false positives for a given cut-off value, than using p-value alone. Protein levels were determined through label-free quantification. Upon excluding contaminants, uncharacterized proteins and bovine aliases, proteins identified with high confidence false discovery rate (FDR<0.01) and a minimum of 2 unique peptides were selected for further analysis. The abundances of proteins meeting the criteria above were compared. Through Volcano plot analysis, proteins with p-value < 0.05 were assigned into two groups: upregulated (UReg) or downregulated (DReg), considering abundance ratios > 2 or < 0.5, respectively. Gene ontology (GO) enrichment analyses was further performed based on experimental evidence for Biological Process and Molecular Function terms. All presented networks were obtained with medium specificity and were visually organized according to the UReg or DReg clusters, showing only significant GO term (p-value ≤ 0.05). Reactome open access database was also used for pathway analysis of UReg/Dreg datasets. The results presented were relative to the top 25 most significant pathways, excluding pathways related to diseases.

9. Characterisation techniques

9.1. Scanning electron microscopy

Scanning electron microscopy (SEM) was applied to visualise 2D and particle surface topography (**Chapters IV**, **V**, and **VI**), cell morphology (**Chapters IV**, **V**, and **VI**), and cell-microparticle aggregates (**Chapters V** and **VI**). 2D substrates and particles were sputtered with gold-palladium prior to analysis. Cell-seeded substrates or aggregates were prepared as follows: fixation in 4 % v/v formaldehyde solution (Sigma-Aldrich) in phosphate buffered saline (PBS, Corning) for 30 min at RT, followed by dehydration in increasing ethanol series (60, 70, 80, 90, 96, and 100 wt %, Fisher Chemical) for 10 min at RT in each solution. Lastly, samples were sputtered with gold-palladium.

9.2. Microtomography

In collaboration with Professor Håvard Haugen at the Institute of Clinical Dentistry, University of Oslo, Norway, microtomography was performed (**Chapter VI**). Microtomography is a useful technique for the acquisition of 2D projections and 3D rendering of samples, as well as the identification of zones with varying mass density due to differential X-ray absorption.

Samples were fixed in 4% w/v formaldehyde solution in PBS and stained with lead(II) acetate trihydrate solution in 2% w/v distilled water, which has been shown to enhance early mineralisation in microCT images.[26] Samples were washed in distilled water, immersed in the staining solution for 18 hours and washed again in distilled water. Subsequently, dehydration in ethanol series (40%, 50%, 60%, and 70% v/v) was performed and samples were mounted in 70% v/v ethanol. Scans were performed with acquisition parameters were set to 60 kV, 260 μA, rotation step of 0.29^{o} over 360^{o}, exposure time of 0.650 ms per projection and a frame-averaging of 2. The reconstruction of the virtual slices was performed with NRecon with a final voxel size of 0.7 μm. The 3D images were rendered using Dragonfly software.

References

1. Song, W., Lima, A. C. & Mano, J. F. Bioinspired methodology to fabricate hydrogel spheres for multi-applications using superhydrophobic substrates. *Soft Matter* **6**, 5868–5871 (2010).
2. Costa, A. M. S., Alatorre-Meda, M., Oliveira, N. M. & Mano, J. F. Biocompatible Polymeric Microparticles Produced by a Simple Biomimetic Approach. *Langmuir* **30**, 4535–4539 (2014).
3. Deng, X., Mammen, L., Butt, H. J. & Vollmer, D. Candle Soot as a Template for a Transparent Robust Superamphiphobic Coating. *Science.* **335**, 67–70 (2012).
4. Yu, L. M. Y., Kazazian, K. & Shoichet, M. S. Peptide surface modification of methacrylamide chitosan for neural tissue engineering applications. *J. Biomed. Mater. Res. Part A* **82A**, 243–255 (2007).
5. Ritger, P. L. & Peppas, N. A. A simple equation for description of solute release II. Fickian and anomalous release from swellable devices. *J. Control. Release* **5**, 37–42 (1987).
6. Anene-Nzelu, C. G. *et al.* Scalable cell alignment on optical media substrates. *Biomaterials* **34**, 5078–5087 (2013).
7. Anene-Nzelu, C. G. *et al.* Scalable alignment of three-dimensional cellular constructs in a microfluidic chip. *Lab Chip* **13**, 4124 (2013).
8. Correia, C. R. *et al.* Semipermeable Capsules Wrapping a Multifunctional and Self-regulated Co-culture Microenvironment for Osteogenic Differentiation. *Sci. Rep.* **6**, 21883 (2016).
9. Correia, C. R., Sher, P., Reis, R. L. & Mano, J. F. Liquified chitosan–alginate multilayer capsules incorporating poly(l-lactic acid) microparticles as cell carriers. *Soft Matter* **9**, 2125–2130 (2013).
10. Correia, C. R., Reis, R. L. & Mano, J. F. Multilayered hierarchical capsules providing cell

adhesion sites. *Biomacromolecules* **14**, 743–751 (2013).
11. Zuk, P. A. *et al.* Multilineage cells from human adipose tissue: implications for cell-based therapies. *Tissue Eng.* **7**, 211–228 (2001).
12. Baudin, B., Bruneel, A., Bosselut, N. & Vaubourdolle, M. A protocol for isolation and culture of human umbilical vein endothelial cells. *Nat. Protoc. 2007 23* **2**, 481–485 (2007).
13. Ladoux, B. & Mège, R. M. Mechanobiology of collective cell behaviours. *Nat. Rev. Mol. Cell Biol.* **18**, 743–757 (2017).
14. Omachi, T., Ichikawa, T., Kimura, Y., Ueda, K. & Kioka, N. Vinculin association with actin cytoskeleton is necessary for stiffness-dependent regulation of vinculin behavior. *PLoS One* **12**, e0175324 (2017).
15. Fratzl, P., Gupta, H. S., Paschalis, E. P. & Roschger, P. Structure and mechanical quality of the collagen–mineral nano-composite in bone. *J. Mater. Chem.* **14**, 2115–2123 (2004).
16. Ku, S. H. & Park, C. B. Human endothelial cell growth on mussel-inspired nanofiber scaffold for vascular tissue engineering. *Biomaterials* **31**, 9431–9437 (2010).
17. Horvat, R., Hovorka, A., Dekan, G., Poczewski, H. & Kerjaschki, D. Endothelial cell membranes contain podocalyxin--the major sialoprotein of visceral glomerular epithelial cells. *J. Cell Biol.* **102**, 484–491 (1986).
18. Bonewald, L. F. *et al.* von Kossa staining alone is not sufficient to confirm that mineralization in vitro represents bone formation. *Calcif. Tissue Int.* **72**, 537–547 (2003).
19. Haihua Pan, Yang Liu, X., Ruikang Tang & Yao Xu, H. Mystery of the transformation from amorphous calcium phosphate to hydroxyapatite. *Chem. Commun.* **46**, 7415–7417 (2010).
20. Ren, X. D. *et al.* Focal adhesion kinase suppresses Rho activity to promote focal adhesion turnover. *J. Cell Sci.* **113**, 3673–3678 (2000).
21. Kimura, K. *et al.* Regulation of Myosin Phosphatase by Rho and Rho-Associated Kinase (Rho-Kinase). *Science.* **273**, 245–248 (1996).
22. Bjørge, I. M., Kim, S. Y., Mano, J. F., Kalionis, B. & Chrzanowski, W. Extracellular vesicles, exosomes and shedding vesicles in regenerative medicine-a new paradigm for tissue repair. *Biomater. Sci.* **6**, (2018).
23. Hasegawa, T. Ultrastructure and biological function of matrix vesicles in bone mineralization. *Histochem. Cell Biol. 2018 1494* **149**, 289–304 (2018).
24. Kang, T. *et al.* Adipose-Derived Stem Cells Induce Angiogenesis via Microvesicle Transport of miRNA-31. *Stem Cells Transl. Med.* **5**, 440–50 (2016).
25. Gaspari, M. & Cuda, G. Nano LC-MS/MS: a robust setup for proteomic analysis. in *Methods in Molecular Biology* **790**, 115–126 (Springer, 2011).
26. Metscher, B. A simple nuclear contrast staining method for microCT-based 3D histology using lead(II) acetate. *J. Anat.* **238**, 1036–1041 (2021).

3
Results & Discussion

Chapter III

Tuneable spheroidal hydrogel particles for cell and drug encapsulation

Chapter IV

Cell behaviour within nanogrooved sandwich culture systems

Chapter V

Nanogrooved microdiscs for bottom-up modulation of osteogenic differentiation

Chapter VI

Bioengineered hierarchical bone-like compartmentalized microconstructs using nanogrooved microdiscs

Chapter III: Tuneable spheroidal hydrogel particles for cell and drug encapsulation[2]

Abstract

The need to better mimic native tissues has accompanied the research in tissue engineering and controlled drug delivery. The development of new platforms for cell and drug encapsulation followed the same trend, and studying the influence of the delivery material system's geometry has been gaining momentum. Aiming to investigate how an increase in surface area and varying particle shape could impact drug release and cell viability, a novel method was developed to produce spheroidal hydrogel particles with adjustable circularity, aiming to tune drug delivery. For this purpose, droplets of hydrogel precursor were squeezed between two superamphiphobic surfaces separated with spacers with different height, and then photo-crosslinked to maintain the acquired shape after "de-sandwiching". Numerical modelling studies were performed to study the polymeric droplet geometry deformation process, which were consistent with experimentally obtained results. The spheroidal particles were produced in mild conditions using methacrylated chitosan, capable of encapsulating proteins or cells. Likely due to their higher surface area to volume-ratio, comparatively to spherical-shaped ones, spheroids presented an improved viability of encapsulated cells due to an enhanced nutrient diffusion to the core, and lead to a significantly faster drug release rate from the polymer network. These results were also assessed numerically, in which the drug release rate was computed for different spheroidal-like geometries. Hence, the described method can be used to manufacture spheroidal particles with tailored geometry that can be broadly applied in the biomedical field, including for drug delivery or as cell encapsulation platforms.

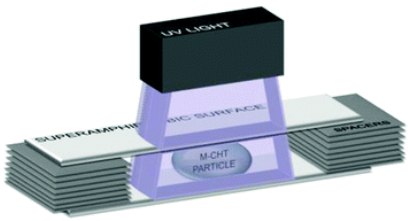

[2] Based on the publication: I.M. Bjørge, A.M.S. Costa, A.S. Silva, J.P.O. Vidal, J. M. Nóbrega, J.F. Mano. Tunable spheroidal hydrogel particles for cell and drug encapsulation, **Soft Matter**, 14 (2018) 5622-5627.

1. Introduction

Hydrogels are hydrated, crosslinked, highly porous structures that can be applied for microencapsulation of cells and active substances.[1,2] The fact that hydrogels can be produced using several biomaterials leads to an ample range of samples with varying viscoelasticity, porosity, and interaction with drugs.[3]

A key aspect for cell survival within a hydrogel matrix is the efficient diffusion of nutrients to the cells and removal of metabolites. Microspheres appear as an option for cell encapsulation, allowing for nutrient diffusion from the particle border to the core in all directions.[2] Yet, with increasing particle dimensions, diffusion is compromised, resulting in reduced cellular viability within the core.[4] Moreover, spherical objects present the lowest surface area to volume ratio, which is another impacting factor in diffusion.[5] The tailoring of geometry allows to produce hydrogels that can be adapted to specific requirements, imposed by the application.[6,7]

For drug delivery purposes, the effect of particle geometry has been studied as an impacting factor in opsonisation and targeted therapy. For example, particle geometry influences the phagocytosis of micron-sized particles, determined by the initial contact point and consequent orientation.[8] Particle accumulation in major organs has also been shown to be shape-dependent,[9] and an increased circulatory half-life has been verified for elliptical disks comparatively to micron and submicron spheres.[10]

From the above-mentioned arguments, it is interesting to consider the surface area associated with a given geometry, for the same volume of a microparticle. Geometries other than spherical may be more advantageous in cases where a larger ratio of surface area to volume is beneficial. The variety of geometries found in natural systems highlight the relevance of this parameter in evolution. For example, some bacteria acquire shapes with an increased surface area, enhancing nutrient up-take and disposal of waste products. Even though oblate spheroids present the highest surface area, other factors such as reduced sinking and enhanced swimming, lead these organisms to acquire a prolate spheroidal shape.[11] Another example is phytoplankton geometry, where various geometries such as spheroids, cylinders, and disks are preferentially adopted alternatively to spheres.[5]

Since varying microparticle geometry may lead to distinct cellular responses and drug release profiles, studying the impact of their geometry alongside the traditionally used microspheres would be of interest. Superhydrophobic and superamphiphobic surfaces have been widely applied to the production of individual spherical polymer particles using, for example, alginate,[12] chitosan,[13] dextran,[14] and PLGA.[15] These substrates have been used to manufacture liquid-core capsules [16] and multi-layered particles,[17] under mild processing conditions, as well as hydrogels with different shapes by patterning of wettable superhydrophilic domains.[18]

In this work we demonstrate, for the first time, the possibility to deform initially spherical liquid droplets, by the compressive action of another superamphiphobic surface, to produce spheroidal hydrogel particles with controlled deformation. We hypothesised that by varying the distance between the surfaces could deformed the droplets containing a photocrosslinkable polymer which, followed by a UV-light irradiation, would result in spheroidal particles with controlled heights along the *z* axis. Chitosan was selected due to its biocompatibility, and cell-adhesiveness, whereas its methacrylated derivative was chosen for its ability to crosslink using UV-light.[19]

We expected that the obtained spheroidal hydrogels could (*i*) improve cell viability due to an enhanced diffusion of nutrients to cells in the core, comparatively to spheres, and (*ii*) release the encapsulated drug at a faster rate due to the higher surface area to volume ratio. Spheroidal particles could therefore present advantages for certain applications when compared to conventional spheres. To confirm these hypotheses, particles were characterised experimentally and through numerical modelling studies of droplet deformation, aiming to provide additional insights into the behaviour of the system. Finally, particles were studied numerically and tested experimentally according to their performance for cell encapsulation and kinetics profile of drug delivery.

2. Materials & Methods

2.1. Materials

Tetraethyl orthosilicate (TEOS) was purchased from Merck (Germany); ammonia solution 25% from LabCHEM (Portugal); chitosan 95/20 (degree of deacetylation ≥ 92.6%; molecular weight = 40 – 150 kDa) from HMC Chitosan (Germany); and acetic acid from

Chem-Lab (Belgium). 1H,1H,2H,2H-perfluorodecyltriethoxysilane, methacrylic anhydride, dialysis tubing cellulose membrane (flat width 33 mm, MWCO 14 kDa), 2-Hydroxy-4'-(2-hydroxyethoxy)-2-methylpropiophenone, albumin from bovine serum (BSA), phosphate buffered saline (PBS), DMEM (Dulbecco's Modified Eagle Medium) low glucose, sodium bicarbonate were purchased from Sigma-Aldrich (USA). Fetal bovine serum (FBS) was purchased from Biochrom AG (Germany); penicillin-streptomycin (100U/100 $g.mL^{-1}$), trypsin (TrypleExpress), DPBS (PBS without calcium and magnesium), Calcein-AM, propidium iodide (PI), and Micro BCA Protein Assay Kit™ were supplied by ThermoFisher Scientific (USA).

2.2. Methods

2.2.1. Superamphiphobic coating of glass substrates

The method to produce the superamphiphobic coating was adapted from Deng *et al*.[20] Briefly, a microscope slide was held above the flame of a paraffin candle to form a soot layer. Afterwards, the soot-coated substrates were exposed to chemical vapour deposition (CVD) of TEOS (4 mL) in the presence of ammonia (4 mL) for 24h in a desiccator, followed by calcination of the hybrid carbon/silica network at 550°C for 2h. Finally, the hydrophilic silica shell was coated with 1H,1H,2H,2H-perfluorodecyltriethoxysilane (300 μL) by CVD for 3 days at 50°C. For surface morphology characterisation, samples were sputter-coated with gold-palladium and visualised by scanning electron microscopy (SEM Hitachi S4100), at a working distance of 15 kV.

2.2.2. Synthesis of methacrylated chitosan (M-CHT)

As described by Yu *et al*.,[19] a 3% w/v chitosan solution was prepared by dissolving chitosan in 2% v/v acetic acid overnight at room temperature (RT) with constant stirring. Subsequently, methacrylic anhydride was added at 1 molar equivalents per chitosan repeat unit and left for 5h at RT. The mixture was dialysed against distilled water for 5 days, changing the water three times a day.

2.2.3. Production of hydrogels

A volume of 4.5 μL of 2, 3, or 4% w/v M-CHT in distilled water was used to produce each hydrogel particle. Spacers where produced from polypropylene (PP) films with a thickness

of 90 μm, which were stacked to achieve the desired final height. The polymeric solution was placed between two superamphiphobic surfaces with a varying spacer height to control the shape of the polymer droplet. A UV-crosslinking method was employed using a curing system (λ = 320 – 500 nm; Omnicure-S2000 XLA) with a 90 second crosslinking period and 2-hydroxy-4'-(2-hydroxyethoxy)-2-methylpropiophenone as photoinitiator.

2.2.4. Characterisation of shape

ImageJ software was used to evaluate particle shape and size. The "Hull and Circle" plug-in allowed to calculate the circularity of particles from the images taken using a contact angle measurement equipment. Particle circularity was calculated using Equation 1, varies between 0 and 1, with 1 corresponding to a perfectly spherical particle.

$$Circularity = \frac{4\pi \times Area}{Perimeter^2} \quad \text{(Equation 1)}$$

Particle deformation was calculated according to spacer height and an initial average particle diameter of 1.90 ± 0.05 mm (Equation 2).

$$Particle\ deformation\ (\%) = \left(1 - \frac{Spacer\ height}{Initial\ particle\ diameter}\right) \times 100 \quad \text{(Equation 2)}$$

Particle surface area was calculated for oblate spheroids (Equation 3) and spheres ($4\pi a^3$), where a and c represent the semi-axis along the y axis and z axis, respectively. Semi-axis values were measured from experimentally obtained particles, with ImageJ, and used to calculate the surface area for each analysed particle deformation.

$$Surface\ area\ (oblate\ spheroid) = \\ = \frac{2\pi}{\sqrt{a^2 - c^2}}\left[a^2\sqrt{a^2 - c^2} + ac^2 ln\left(\frac{a + \sqrt{a^2 - c^2}}{c}\right)\right] \quad \text{(Equation 3)}$$

2.2.5. Modelling of the liquid droplet compression and drug release

The droplet deformation was modelled with the computational library OpenFOAM, using the elasticFoam solver, which can simulate the structural behaviour of linear and non-linear elastic materials. For this specific study, a linear elastic material was considered. To mimic the experimental tests, the initially spherical droplet was deformed by a moving plate, to

achieve the same deformation levels imposed experimentally. Additionally, numerical modelling studies were also performed to assess the impact of the geometry of spheroidal particles on the evolution of a specific compound, transported by diffusion. In these studies, the OpenFOAM solver employed was the laplacianFoam, which was modified to accommodate a Neuman boundary condition at the spheroid surface.

2.2.6. *In vitro* drug release

10 mg of BSA per millilitre were dissolved in the 2% w/v M-CHT solution prior to the production of spheres and spheroids. Four spheres or spheroids loaded with BSA were placed in each well containing 5 mL of PBS solution (pH 7.4) at 37°C, under gentle agitation (60 rpm). Assays were performed in triplicate (n=3). At pre-established time points, 150 µL of supernatant were removed for analysis and replaced with equal volume of fresh PBS. The amount of the drug released was quantified using the Micro BCA Protein Assay Kit™ upon spectrophotometrical quantification at 562 nm against the known calibration curve.

Results were modelled using the Korsemeyer-Peppas equation (Equation 4) for calculation of the diffusional exponent (n) to characterise the transport mechanism, according to the exponential dependence of the amount of drug released (M_t/M_∞) and rate constant (k) over time (t).[21] GraphPad software was used to perform a two-way analysis of variance (ANOVA) with a Bonferroni's multiple comparison test for a significance levels of 0.1 %, 1%, and 5%.

$$M_t/M_\infty = Kt \qquad \text{(Equation 4)}$$

2.2.7. Cell viability

L929 cells were cultured with DMEM low glucose supplemented with 3.7 g/L sodium bicarbonate, 10% FBS and 1% penicillin-streptomycin at pH 7.4. Cells were grown in 75 cm^2 tissue culture flasks and incubated at 37°C in a humidified air atmosphere of 5% CO_2. At 90% of confluence the cells were washed with PBS and detached by a chemical procedure with trypsin solution for 5 min at 37°C in a humidified atmosphere of 5% CO_2. After this period, fresh cell culture medium was added to inactivate the effect of trypsin. The obtained cell suspension was centrifuged at 300 x g and 25°C for 5 min. After discarding the supernatant, cells were resuspended in the polymer solution at a cell density of 1 x 10^6 cells/mL. The resulting suspensions were used to produce spherical and spheroidal particles

according to the methods previously described for hydrogel production. After 24h of culture the cell culture medium was removed and 1 mL of PBS containing 2 µL of calcein-AM and 1 µL of PI was added to each well and incubated at 37°C for 10 min protected from the light. After this period, samples were washed several times with PBS to remove all traces of excessive dyes. Samples were visualised by fluorescence microscopy (Axio Imager 2, Zeiss) using appropriate red and green fluorescence filters to detect dead and live cells, respectively.

3. Results & Discussion

3.1. Particle characterisation

The obtained superamphiphobic surfaces presented a contact angle of 165.2 ± 4.2°, consistent with previous reports.16 Oblate spheroidal particles (c < a) with different thickness were produced by sandwiching liquid M-CHT polymer precursor between superamphiphobic surfaces with varying spacer height, with subsequent UV-crosslinking, as shown in Figure III.1. The particle was thus compressed along the z axis (semi-axis c), whilst the length along the x and y axis increased equally (semi-axis a) (Figure III.1 inset).

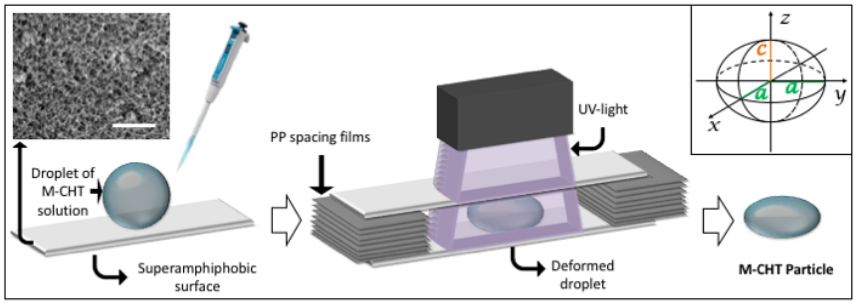

Figure III.1. Schematic representation of oblate spheroidal particle production method. Inset: Axis (*x, y, z*) and semi-axis (*a, c*) representation. M-CHT liquid precursor was squeezed between superamphiphobic surfaces separated using a known spacer height, followed by UV-crosslinking. Representative SEM image of topographical features present on superamphiphobic surfaces (scale bar corresponding to 10 µm).

In Figure III.2 it is possible to perceive the effect of decreasing spacer height on the shape of spheroidal particles. Figure 2A shows the droplet geometries predicted by the numerical modelling code, for each prescribed deformation, whilst Figure III.2B presents the experimentally observed particles upon deformation. Overlapping of the modelled geometry profile (red dotted lines in figure III.2B) on experimentally obtained particles demonstrates that there is a similarity in the disk-like shape for each deformation. Thus, experimental findings agreed with the numerical predictions. Figure III.2C evidences the spheroidal shape

that particles acquire upon removal of the upper superamphiphobic surface, as compared with the disk-like shape they present when "sandwiched" between the surfaces. Green dotted lines represent the theoretical *yz* plane profiles of spheroids, using the implicit equation of a spheroid $\left(\frac{x^2+y^2}{2}+\frac{z^2}{2}=1\right)$, which are in accordance with experimentally obtained particles.

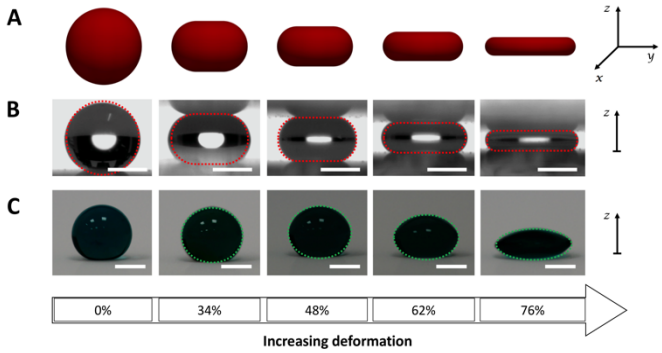

Figure III.2. A: Geometry predicted by numerical studies of the shape of the elastic liquid droplet upon deformation. B: Effect of decreasing spacer height on particle format. Dotted red lines correspond to the profiles of predicted particle geometry by numerical studies. C: Spheroidal particle shape acquired upon removal of upper superamphiphobic surface. Dotted green lines correspond to the *yz* plane representation of spheroids. The particle on the left was used as a spherical control with no deformation and was only in contact with the lower superamphiphobic surface. Increasing deformation was used for the following particles. Scales bars on both sets of images correspond to 1 mm.

Additionally, the effect of M-CHT concentration on spheroidal particle shape upon removal of the upper superamphiphobic was studied using 2, 3, and 4% w/v solutions. As can be observed in figure III.3, the recovery of particle shape was identical for all deformations studied, independently of the concentration of the precursor solution.

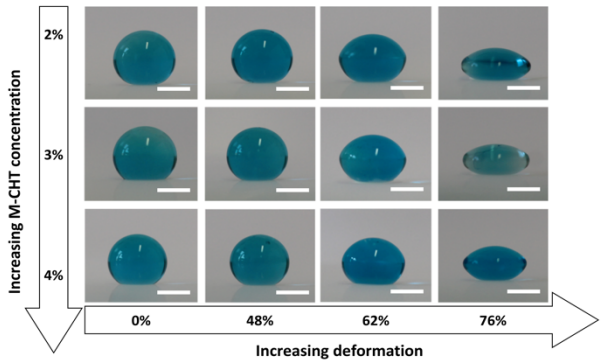

Figure III.3. Effect of chitosan concentration on UV-crosslinked spheroidal particles. Particles were produced with concentrations of 2%, 3%, and 4% w/v, and with equal deformations of 0%, 48%, 62%, and 76%. Scale bars correspond to 1 mm.

Figure III.4 presents the relationship of particle deformation with circularity and surface area, which were both calculated from the contour of the projected particle. The standard deviation values for circularity of each batch were small (≤0.04), indicating that the method was quite reproducible. As expected, an increase in particle deformation, was correlated with a decrease in particle circularity. As can also be observed from Figure III.3, there was an increase in surface area with increased particle deformation.

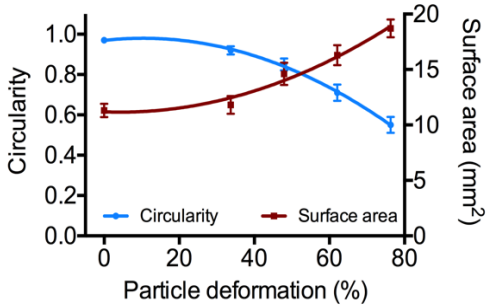

Figure III.4. Correlation of particle deformation with circularity (•, n>8) and surface area (▪, n>4). The values of circularity and surface area were obtained from particle images. Second order polynomial fittings are represented only as guidelines for the eye.

3.2. BSA release assay

The cumulative release profiles of BSA from M-CHT spheres and spheroids (62% deformation) (n = 3) are presented in Figure III.5A, as well as the data adjusted according to Korsmeyer-Peppas equation.

The cumulative BSA release from spheroids was faster than from spheres, with a statistical significance of at least 5% was observed for most time-points, including the initial 5 and 30 minutes. All particles presented the same initial volume. Therefore, the distinct results obtained may be attributed to the larger surface area of spheroids comparatively to spheres, thus facilitating diffusion across the particle surface. According to the Korsmeyer-Peppas model, spherical particles presented an n value of 0.0891, and spheroidal particles presented n=0.0757. According to Peppas *et al.*,[21] the diffusional exponent for Fickian release in spheres is $n = 0.432 \pm 0.007$. For values below this threshold the release kinetics can be classified as Quasi-Fickian diffusion, or partial diffusion, where another process in addition to diffusion is responsible for drug transport.[22,23] Hence, the release mechanism for both spherical and spheroidal particles studied can be classified as Quasi-Fickian.

Additionally, Figure III.5B presents the results obtained on the numerical modelling studies comparing the release of a compound from spherical and spheroidal particles with varying compression along the *c* semi-axis. As shown, the release tends to be more accelerated with increasing compression along the *c* semi-axis, with the spherical particle (1) presenting the slowest release. This is in accordance with experimentally obtained results, as the release curve for the studied particle with 62% deformation, should be between particles with relative height ½ and ¼.

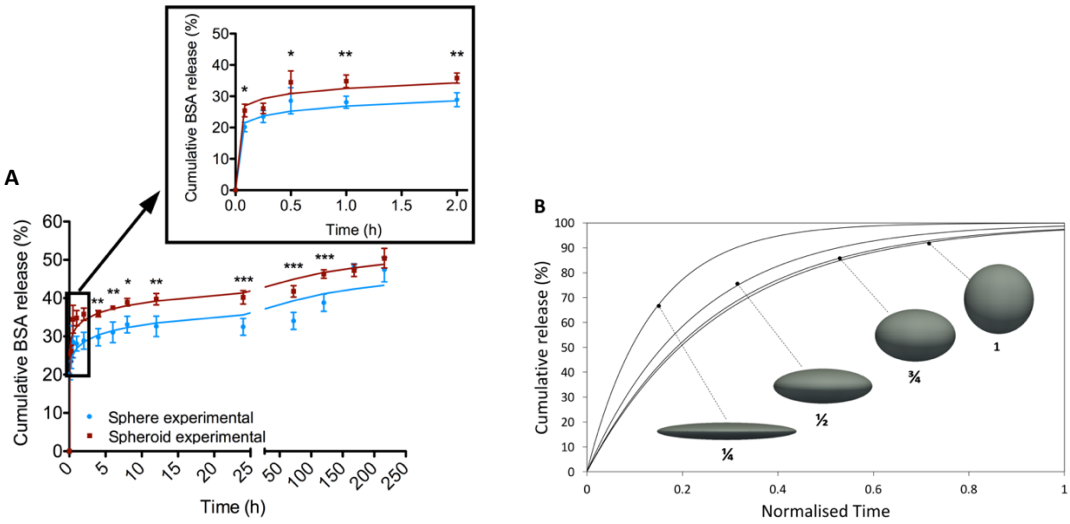

Figure III.5. A: Cumulative BSA release from 2% M-CHT spheres (●) and spheroids (62% deformation) (▪), up to 216 hours, with a zoom-in for the initial 2 hours (n=3). Values plotted are the mean ± error for 3 samples. Both experimental and curve fittings using Korsmeyer-Peppas equation are presented in the figure (lines with the same colour of the corresponding symbols). Statistical significance of $p<0.05$ (*), $p<0.01$ (**), and $p<0.001$ (***) are represented for time-points when applicable. B: Numerical modelling studies for the release of a compound from spherical versus spheroidal particles with varying particle height. Variation in height of spheroidal particles (¾, ½, and ¼) is presented relatively to spherical particles, corresponding to 1.

The loading efficiency of bioactive substances within particles produced using superhydrophobic or superamphiphobic surfaces has been previously reported to be approximately 100%, where the limiting condition is the solubility of the bioactive substance in the polymer aqueous solution.[12,17] This processing method renders a high encapsulation efficiency and thus a cumulative release of approximately 100% is also expected. Consistent with this finding, the work of Lima *et al.*[24] demonstrated a total release of low molecular weight model drug dexamethasone from within chitosan hydrogel particles. However, this was not the case in the present study, where the maximum cumulative release observed was 50.4 ± 2.6% for spheroids and 47.4 ± 3.2% for spheres. Taking into consideration that BSA is negatively charged at physiological pH (pH = 7.4) due to an isoelectric point (p*I*) between

4.7 and 5.3 (according to product specifications), the formation of complexes between BSA and positively charged chitosan molecules may explain the low cumulative release values.[25] This causes the entrapment of a fraction of the encapsulated BSA within the polymer matrix and blocks its capability to diffuse out of the network. The fact that both spheroidal and spherical particles tend towards similar final cumulative release values corroborates the theory of chitosan-entrapped proteins.

The initial hypothesis that spheroids would present a faster release rate comparatively to spheres was confirmed. This may be explained by the higher average distance between the points in the object and its surface, in the case of spherical particles, hence resulting in a larger travel distance for molecule diffusion. Thus, it was possible to significantly alter the release rate of an entrapped molecule by simply changing particle shape from spherical to spheroidal.

3.3. Live/Dead assay

Cells were successfully encapsulated within spherical and spheroidal hydrogel particles, showing an even cell distribution within all particles. In Figure III.6 it is possible to assess a higher viability degree within L929-laden spheroidal particles, when compared to spherical particles after 24 hours. Spherical particle (0% deformation) presented the highest number of dead cells, followed by 48% deformation spheroid. Spherical particles with 62% and 76% deformation presented virtually no dead cells (> 99% of live cells). Given the size of the particles studied, it was expected that spherical particles would contain dead cells within the core, seen as oxygen and nutrient diffusion is compromised by the crosslinked polymer network.[4,16] Interestingly, by increasing the particle deformation and thus increasing particle surface area, it was possible to bypass the size limitation and increase overall cell viability. Since the exchange of nutrients and waste is facilitated in the spheroidal particles, there is likely a promotion of cell growth and proliferation. Our hypothesis that spheroids would improve cell viability was therefore confirmed.

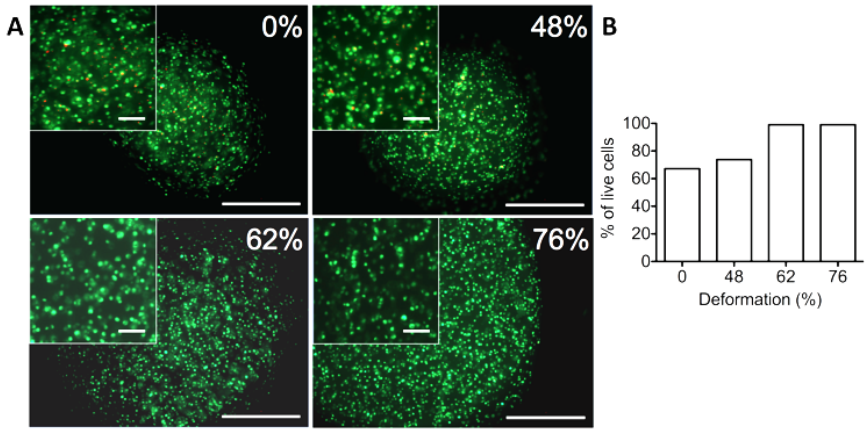

Figure III.6. Live/Dead assay of L929 cells encapsulated within 2% M-CH particles 24 hours after seeding. Spherical (0%) and spheroidal (48%, 62%, and 76%) particles are represented. A: Top views of particles and image magnifications in inset. Scale bars correspond to 750 µm for main images, and 440 µm for inset images. B: Quantification of the relative number of live cells per condition.

4. Conclusion

Spheroidal particles with varying thickness were successfully and reproducibly created using photocrosslinkable chitosan and superamphiphobic surfaces. Varying the distance between the superamphiphobic surfaces allowed to control the deformation of hydrogel precursor droplets, resulting in a range of particles after UV-crosslinking. Using chitosan as a model to prove this concept, the application of these particles was further studied as an encapsulation vehicle for either drugs/proteins or cells. For spheroids, a significantly faster cumulative BSA release, and an enhanced cell viability was observed, comparatively to spheres, greatly evidencing the impact of a larger surface area.

Furthermore, the good correlation obtained between the experimental results and the numerical predictions, both for droplet deformation and drug release rates, evidenced that numerical modelling can provide useful support on the design of these systems.

The proposed technology could expand the use of superhydrophobic and superamphiphobic platforms, which have been employed to process spherical particles, towards the production of spheroid-like objects with potential to be used in biomedical applications. These spheroidal particles could be, for example, applied for drug delivery by oral or rectal administration routes, where the size would not be a limitation. The production of smaller spheroidal particles could also be of interest, however this would require another dispensing

methodology, such as spray or jet-based techniques. In that case, other more precise equipment would also be needed to deform such particles between superamphiphobic surfaces.

Acknowledgments

I. M. Bjørge and A. M. S. Costa acknowledge financial support by the Portuguese Foundation for Science and Technology (FCT) with doctoral grants SFRH/BD/129224/2017 and SFRH/BD/101748/2014, respectively. This work was supported by the European Research Council grant agreement ERC-2014-ADG-669858 for the project "ATLAS". The work was developed within the scope of the project CICECO Aveiro Institute of Materials, POCI-01-0145-FEDER-007679 (FCT Ref. UID/CTM/50011/2013), and the project IPC/i3N Minho (FCT Ref. UID/CTM/50025/2013), financed by national funds through the FCT/MEC and when appropriate co-financed by FEDER under the PT2020 Partnership Agreement.

References

1. Seliktar, D. Designing Cell-Compatible Hydrogels for Biomedical Applications. *Science* **336**, 1124–1128 (2012).
2. Gasperini, L., Mano, J. F. & Reis, R. L. Natural polymers for the microencapsulation of cells. *J. R. Soc. Interface* **11**, 20140817 (2014).
3. Peppas, N. A., Hilt, J. Z., Khademhosseini, A. & Langer, R. Hydrogels in Biology and Medicine: From Molecular Principles to Bionanotechnology. *Adv. Mater.* **18**, 1345–1360 (2006).
4. Correia, C. R., Sher, P., Reis, R. L. & Mano, J. F. Liquified chitosan–alginate multilayer capsules incorporating poly(l-lactic acid) microparticles as cell carriers. *Soft Matter* **9**, 2125–2130 (2013).
5. Karp-Boss, L. & Boss, E. The Elongated, the Squat and the Spherical: Selective Pressures for Phytoplankton Shape. in *Aquatic Microbial Ecology and Biogeochemistry: A Dual Perspective* (eds. Glibert, P. M. & Kana, T. M.) 25–34 (Springer International Publishing Switzerland, 2016). doi:10.1007/978-3-319-30259-1_3
6. Soman, P., Chung, P. H., Zhang, A. P. & Chen, S. Digital microfabrication of user-defined 3D microstructures in cell-laden hydrogels. *Biotechnol. Bioeng.* **110**, 3038–3047 (2013).
7. Drury, J. L. & Mooney, D. J. Hydrogels for tissue engineering: scaffold design variables and applications. *Biomaterials* **24**, 4337–4351 (2003).
8. Champion, J. A. & Mitragotri, S. Role of target geometry in phagocytosis. *Proc. Natl. Acad. Sci. U. S. A.* **103**, 4930–4934 (2006).
9. Decuzzi, P. *et al.* Size and shape effects in the biodistribution of intravascularly injected particles. *J. Control. Release* **141**, 320–327 (2010).
10. Muro, S. *et al.* Control of Endothelial Targeting and Intracellular Delivery of Therapeutic Enzymes by Modulating the Size and Shape of ICAM-1-targeted Carriers. *Mol. Ther.* **16**, 1450–1458 (2008).
11. Dusenbery, D. B. Fitness landscapes for effects of shape on chemotaxis and other behaviors of bacteria. *J. Bacteriol.* **180**, 5978–5983 (1998).
12. Song, W., Lima, A. C. & Mano, J. F. Bioinspired methodology to fabricate hydrogel spheres

for multi-applications using superhydrophobic substrates. *Soft Matter* **6**, 5868–5871 (2010).
13. Leite, Á. J., Caridade, S. G. & Mano, J. F. Synthesis and characterization of bioactive biodegradable chitosan composite spheres with shape memory capability. *J. Non. Cryst. Solids* **432**, 158–166 (2016).
14. Lima, A. C., Song, W., Blanco-Fernandez, B., Alvarez-Lorenzo, C. & Mano, J. F. Synthesis of Temperature-Responsive Dextran-MA/PNIPAAm Particles for Controlled Drug Delivery Using Superhydrophobic Surfaces. *Pharm. Res.* **28**, 1294–1305 (2011).
15. Takei, T., Hamada, S., Terazono, K. & Yoshida, M. Air drying on superamphiphobic surfaces can reduce damage by organic solvents to microbial cells immobilized in synthetic resin capsules. *Process Biochem.* **54**, 28–32 (2017).
16. Costa, A. M. S. & Mano, J. F. Solvent-Free Strategy Yields Size and Shape-Uniform Capsules. *J. Am. Chem. Soc.* **139**, 1057–1060 (2017).
17. Lima, A. C., Custódio, C. A., Alvarez-Lorenzo, C. & Mano, J. F. Biomimetic Methodology to Produce Polymeric Multilayered Particles for Biotechnological and Biomedical Applications. *Small* **9**, 2487–2492 (2013).
18. Neto, A. I. *et al.* Fabrication of Hydrogel Particles of Defined Shapes Using Superhydrophobic-Hydrophilic Micropatterns. *Adv. Mater.* **28**, 7613–7619 (2016).
19. Yu, L. M. Y., Kazazian, K. & Shoichet, M. S. Peptide surface modification of methacrylamide chitosan for neural tissue engineering applications. *J. Biomed. Mater. Res. Part A* **82A**, 243–255 (2007).
20. Deng, X., Mammen, L., Butt, H. J. & Vollmer, D. Candle Soot as a Template for a Transparent Robust Superamphiphobic Coating. *Science.* **335**, 67–70 (2012).
21. Ritger, P. L. & Peppas, N. A. A simple equation for description of solute release II. Fickian and anomalous release from swellable devices. *J. Control. Release* **5**, 37–42 (1987).
22. Peppas, N. A. & Korsmeyer, R. W. Dynamically swelling hydrogels in controlled release applications. in *Hydrogels in medicine and pharmacy* **III**, 109–136 (CRC Press Boca Raton, Florida, 1987).
23. Rehman, K. & Zulfakar, M. H. Novel Fish Oil-based Bigel System for Controlled Drug Delivery and its Influence on Immunomodulatory Activity of Imiquimod Against Skin Cancer. *Pharm. Res.* **34**, 36–48 (2017).
24. Lima, A. C., Correia, C. R., Oliveira, M. B. & Mano, J. F. Sequential ionic and thermogelation of chitosan spherical hydrogels prepared using superhydrophobic surfaces to immobilize cells and drugs. *J. Bioact. Compat. Polym.* **29**, 50–65 (2014).
25. Kang, G. D. & Song, S.-C. Effect of chitosan on the release of protein from thermosensitive poly(organophosphazene) hydrogels. *Int. J. Pharm.* **349**, 188–195 (2008).

Chapter IV: Cell behaviour within nanogrooved sandwich culture systems[3]

Abstract

Grooved topography and inherent cell contact guidance has shown promising results regarding cell proliferation, morphology, and lineage-specific differentiation. Yet these approaches are limited to two-dimensional applications. Sandwich-culture conditions were developed to bridge the gap between two-dimensional and three-dimensional culture, enabling both ventral and dorsal cell surface stimulation. We assess the effect of grooved surface topography on cell orientation and elongation in a highly controlled manner, with simultaneous and independent stimuli on two cell sides. Nanogrooved and non-nanogrooved substrates are assembled into quasi-three-dimensional systems with variable relative orientations. A plethora of sandwich-culture conditions are created by seeding cells on lower, upper, or both substrates. Software image analysis demonstrates that F-actin of cells acquires the orientation of the substrate on which cells are initially seeded, independently from the orientation of the second top substrate. Contrasting cell morphologies are observed, with a higher elongation for nanogrooved two-dimensional substrates than nanogrooved sandwich-culture conditions. Correlated with an increased pFAK activity and vinculin staining for sandwich-culture conditions, these results point to an enhanced cell surface stimulation versus control conditions. The pivotal role of initial cell-biomaterial contact on cellular alignment is highlighted, providing important insights for tissue engineering strategies aiming to guide cellular response through mechanotransduction approaches.

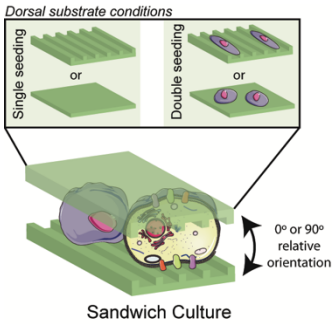

[3] Based on the publication: I.M. Bjørge, M. Salmerón-Sánchez, C.R. Correia, J.F. Mano. Cell behavior within nanogrooved sandwich culture systems, **Small**, 16 (2020) 2001975.

1. Introduction

Cell adhesion is mediated through integrins that tether to extracellular matrix (ECM) proteins, generally associated with an increased actin-myosin contractility to stabilize focal adhesions.[1,2] Integrin-mediated adhesions can be formed on only one cell face or on the entire cell surface in response to a two-dimensional (2D) or three-dimensional (3D) environment, respectively.[3] Therefore, cell morphology, cytoskeletal structure, and signaling are altered for cells cultured on 2D versus 3D environments, as well reported in the literature. For example, in a 2D versus 3D context, cells seeded atop of stiffer hydrogels tend to acquire a spread morphology, whereas cells encapsulated within the same stiff hydrogel are confined and adopt a rounded morphology.[4] As part of the focal adhesion complex, integrins are responsible for mechanotransduction, altering chemical signaling in response to the environment and physical cues to which cells are subjected.[5,6] Downstream signaling initiated by adhesion formation activates distinct pathways, including nuclear or cytoplasmic shuttling of Yorkie-homologues Yes-associated protein (YAP) and transcriptional coactivator with PDZ-binding motif (TAZ). YAP/TAZ have been indicated as sensors and mediators of mechanical cues, specifically adhesive areas and substrate stiffness, and have thus been linked to geometric control and stiffness-triggered cell differentiation.[7]

By means of contact guidance, topographical features may govern cell orientation, migration, and production of organized cytoskeletal arrangements.[8] There is also evidence that a greater cell deformation by topographical guidance can be correlated with a larger genome response regarding cell cytoskeleton, proliferation, transcription, translation, production of extracellular matrix, as well as inter- and intracellular signaling.[6] For example, larger focal adhesions (>5 mm) and greater actin-myosin contractility with consequent increased intracellular tension have been associated with cell differentiation towards the osteogenic lineage. This is likely due to the transfer of tensile forces to the nucleus, which impacts chromosomal arrangement. Conversely, mesenchymal stromal cells (MSCs) seeded on substrates that restrict spreading and lead to a rounded cell morphology impede the formation of mature adhesions, consequently directing adipogenic differentiation.[1] Other types of cells are also affected by contact guidance, such as pre-osteoblasts,[9] fibroblasts,[10] and myoblasts.[11] Moreover, the use of aligned substrates with different submicron groove

and ridge widths has shown promising results in directing the differentiation of MSCs towards osteogenic,[11] adipogenic,[11] myogenic,[12] and chondrogenic [13] lineages. We have recently proposed nanogrooved microdiscs, "topodiscs", as substrates for cell-mediated assembly structures,[14] which could be used in bottom-up tissue engineering strategies.[15] The osteogenic differentiation of adipose-derived stromal cells (ASCs) even in the absence of osteoinductive factors ascertains the effect of grooved topography in a 3D environment and warrants a more in-depth study of grooved topography.[14]

Sandwich-culture (SW) methods have been applied to bridge the gap between 2D and 3D cultures, allowing for both ventral and dorsal cell surface stimulation.[16–18] When placed in a 3D matrix, dorsal receptor integrins of fibroblasts undergo activation and conformational changes, leading to an altered cell morphology from well-spread to bipolar or stellate.[5] When placed in a SW, fibroblasts also acquire a stellate morphology, with the formation of smaller and fewer focal adhesions.[18] SW methods have been mainly applied to study the effect of dorsal and ventral protein-loading on cell proliferation, migration, and ECM reorganization.[16,18–20]

2. Materials & Methods

2.1. Micromolding of polystyrene substrates

Polystyrene adherent petri dishes (Plate Cell + 150, Sarstedt) were cut into 8 x 8 mm^2 substrates using a laser-cutting machine (Ignis, BCN3D). Optical media substrates (CDs; ridge width 1185±16 nm, groove width 412±12 nm, and ridge height 197±14 nm) were used as nanogrooved templates to mold polystyrene substrates. Molding was performed in an oven (Ecocell 55, MMM Medcenter Einrichtungen GmbH) at 120ºC for 50 minutes with an applied pressure of approximately 130 mPa. Polystyrene substrates were plasma treated (Plasma System ATTO, Electronic Diener) at 0.4-0.6 mbar and 30 V for 15 min using atmospheric air, followed by UV sterilization during 30 min.

2.2. Sandwich cell culture

MC3T3-E1 cells (American Type Culture Collection) were cultured with α-MEM supplemented with 10% v/v fetal bovine serum (ThermoFisher Scientific) and 1% v/v antibiotic-antimycotic (100x, ThermoFisher Scientific) in tissue culture flasks, incubated at

37ºC in a humidified air atmosphere of 5% CO_2. At 90% confluence, cells were detached by 0.05 % w/v trypsin-EDTA (from porcine pancreas 1:250, Sigma-Aldrich) treatment for 5 min at 37ºC. Cells were carefully seeded to avoid bubble formation at a density of $1.5x10^4$ cells/cm^2 and allowed to adhere for 3 h at 37ºC. SW conditions are produced by assembling nanogrooved or non- nanogrooved substrates with or without cells, and with variable relative orientations (0º or 90º) between nanogrooves of upper and lower substrates. Additionally, SW conditions with cells seeded on both lower and upper substrates were tested where MC3T3-E1 cells were incubated with DiO (Vybrant® DiO Cell-Labelling Solution, ThermoFisher Scientific) or DiD (Vybrant® DiD Cell-Labelling Solution, ThermoFisher Scientific) for 30 minutes at 37ºC (5 µL of dye per mL of cell suspension containing $1x10^6$ cells). Stained cells were seeded on respective substrates ($1x10^4$ cells/cm^2) and left to adhere for 3 hours at 37ºC. SW conditions were produced by assembling DiO-stained cell-seeded upper substrates with DiD-stained cell-seeded lower substrates. Contact between upper and lower substrates was ensured by placing a glass substrate (10x5x1 mm; 150 mg) over assembled SWs. For all assessed conditions, upon the initial 3h adhesion period, cells were cultured for 21h on single substrates or within the SW, totalling 24h of culture. Scheme IV.1 shows the different assembly conditions tested.

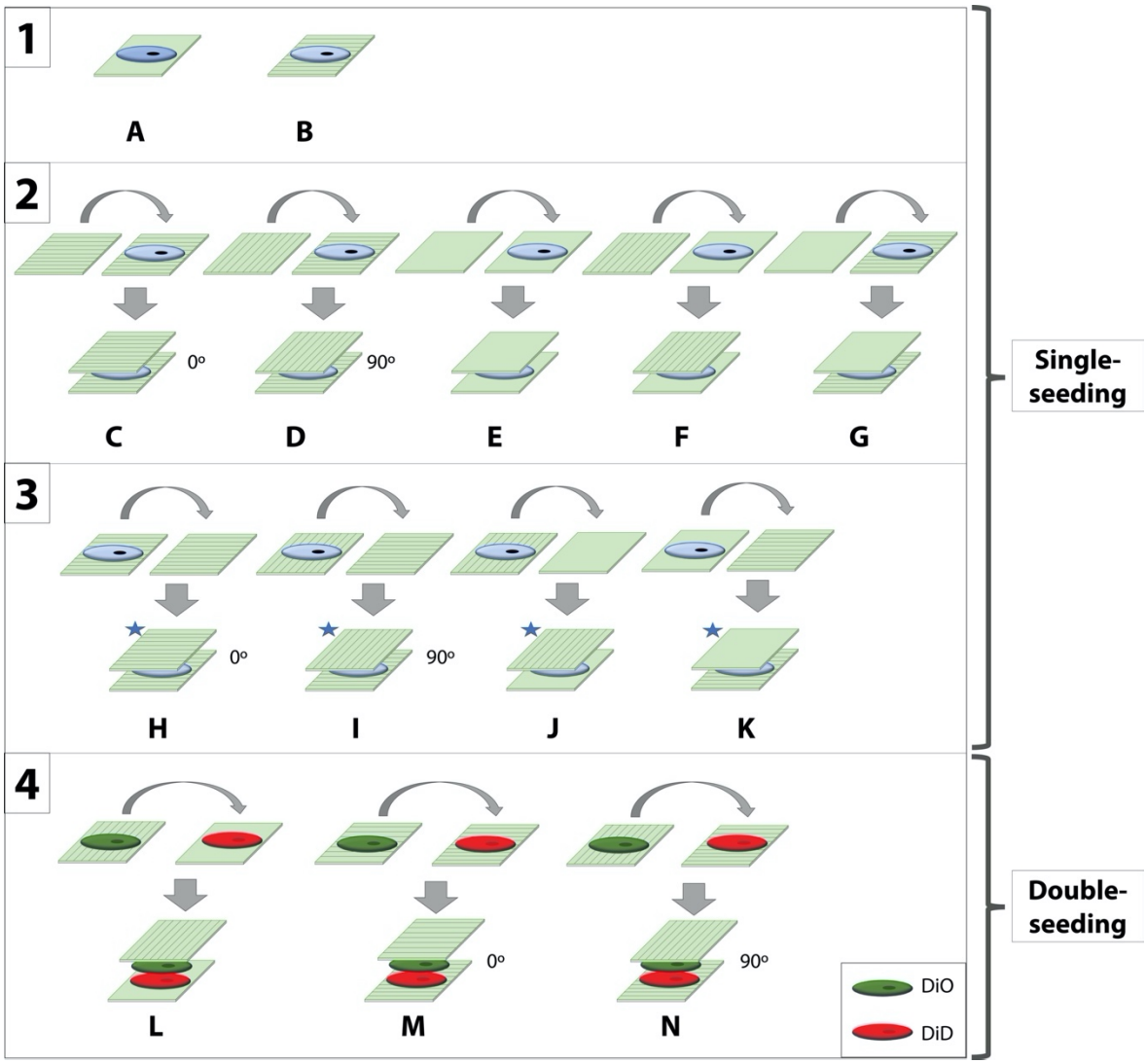

Scheme IV.1. Schematic representation of the different assembly conditions tested. MC3T3-E1 cells were seeded on polystyrene substrates with or without grooves and placed in sandwich-culture (SW) conditions. Cell seeding was performed on lower substrates unless marked with a star symbol. Relative orientations correspond to the angle between the nanogrooves of the upper and lower substrates. [Box 1] Control conditions without (A) or with (B) nanogrooves. [Box 2] SW conditions with cell-seeded lower substrates (single-seeding). The orientation of the nanogrooves between the upper and lower substrates is varied between 0º (C) and 90º (D). SW conditions with both substrates without nanogrooves (E) or presenting the nanogrooves on the upper (F) or lower (G) substrate. [Box 3] SW conditions with cell-seeded upper substrates (single-seeding). SW conditions with relative orientation of 0º (H) or 90º (I), and upper (J) or lower (K) grooved substrates. [Box 4] SW conditions with cell-seeded upper and lower substrates (double seeding). Cells adhered to upper or lower substrates are stained with DiO (green) or DiD (red) lipophilic dyes, respectively. SW conditions with the grooves only on the upper substrate (L), or with relative orientations of 0º (M) or 90º (N).

2.3. Scanning electron microscopy

The nanogrooved surface of substrates and cells was imaged by scanning electron microscopy (SEM; S4100, Hitachi). Cell-seeded substrates were prepared as follows: fixation in 4 % v/v formaldehyde solution (Sigma-Aldrich) in phosphate buffered saline

(PBS, Corning) for 30 min at RT, followed by dehydration in increasing ethanol series (60, 70, 80, 90, 96, and 100 wt %, Fisher Chemical) for 10 min at RT in each solution. Lastly, samples were sputtered with gold-palladium.

2.4. Fluorescence microscopy

DAPI (4',6-diamidino-2-phenylindole, dihydrochloride, 1 mg/mL, ThermoFisher Scientific) and phalloidin (Flash Phalloidin™ Red 594, 300U, BioLegend) were used to stain cell nuclei in blue and F-actin in red, respectively. Samples were fixed in 4% v/v formaldehyde solution (30 min at RT) and permeabilized in 0.1 % v/v triton-X100 (BioXtra, Sigma-Aldrich) (5 minutes at RT). Samples were incubated in phalloidin-red solution diluted in PBS (5:200) for 45 min at RT, protected from light, and counterstained with DAPI solution diluted in PBS (1:1000) for 5 min at RT protected from light. For vinculin immunofluorescence, samples were incubated in 5% v/v FBS in PBS (5% FBS/PBS) for 1h at RT upon fixation and permeabilization. Cells were incubated with primary antibody (Vinculin Antibody 42H89L44, ABfinity™ Rabbit Monoclonal, 0.5 mg/mL, ThermoFisher Scientific) diluted in 5% FBS/PBS (1:50) overnight at 4ºC. Samples were then incubated with secondary antibody (Alexa Fluor® 594 Donkey anti-rabbit IgG Antibody, BioLegend) diluted in 5% FBS/PBS (1:500). Lastly, F-actin and nuclei were stained as mentioned above with phalloidin (Flash Phalloidin™ Green 488, 300U, BioLegend) and DAPI. Samples were analyzed by fluorescence microscopy (Axio Imager 2, Zeiss) and confocal fluorescence microscopy (LSM 880, Zeiss).

2.5. Total FAK and FAK Y397 phosphorylation quantification

Conditions (B) and (C) were prepared as described above. Cell pellets were extracted using cell extraction buffer (Pierce RIPA Buffer, Thermo Scientific) and frozen at -80ºC. FAK (Total) Elisa Kit and FAK (Phospho) [pY397] Human ELISA Kit (ThermoFisher Scientific) were used for quantification.

2.6. Cell morphology characterization

OrientationJ plug-in for ImageJ was used to study the orientation of F-actin in fluorescence images. OrientationJ Analysis submenu was used to create a color-survey of images according to the local orientation. An orientation histogram was created using the

Distribution submenu, where a minimum energy of 2% was set in order to remove the background signal. Cell dimensions were measured using ImageJ to calculate the average elongation factor for each condition (Equation (1)).

$$\text{Elongation factor} = \frac{\text{Longest cell axis}}{\text{Maximal length perpendicular to longest axis}} \quad (1)$$

2.7. Statistical analysis

Statistical analysis was performed using one-way analysis of variance (ANOVA) with Tukey's multiple comparisons test, or Mann-Whitney U test (GraphPad Prism 6.0) A p-value < 0.05 was considered statistically significant.

3. Results & Discussion

With ever-growing evidence that the 2-dimensional approach is not the most appropriate to assess cellular behaviors, we herein propose the production of nanogrooved substrates to be implemented in SW systems, aiming to transpose grooved topography from a 2D to a quasi-3D approach by interacting with both ventral and dorsal cell receptors. Nanogrooved or non-nanogrooved substrates were assembled with different combinations and relative orientations, namely 0º and 90º. MC3T3-E1 pre-osteoblastic cells were seeded on bottom (Scheme IV.1-box 2) or top (Scheme IV.1-box 3) substrates prior to contact with the second substrate (single-seeded SW) to study the effect of substrate nanogrooves and relative orientation on cell morphology and alignment. Cell seeding on upper substrates was performed to rule out the effect of gravity as cells were allowed to adhere to the upper substrate prior to flipping upside-down onto the lower substrate. It is important to note that regardless the substrate on which cells are seeded (upper or lower), upon closing of the sandwich via placement of the second substrate, the ventral or dorsal substrate will always correspond to the lower or upper substrate, respectively. Additionally, cells were seeded on both substrates (double-seeded SW, Scheme IV.1-box 4) to evaluate if cell alignment would be affected by the presence of pre-existing cells. We hypothesized that these varying SW conditions would impact cell morphology and alignment due to direct contact with nanogrooved substrates (single-seeded SW) and via promotion of cell-cell contact (double-seeded SW).

To evaluate the effects of the different conditions on cell stimulation and behavior, results were analyzed using both qualitative (Figure IV.1) and quantitative (Figure IV.2) methods. Qualitatively it was observed that for cultures on single substrates, cells either spread randomly on the non-nanogrooved substrate (A) or aligned along the nanogrooves (B), thus evidencing the influence of substrate topography on cell orientation (Figure IV.1). Regarding SW conditions (C)-(K) cells generally acquired the morphology of substrates on which they were seeded, independently of the substrate later assembled to produce the SW conditions. Thus, SW conditions with cells seeded on non-grooved substrates (Figure IV.1 (E), (F), and (K)) tended to acquire a seemingly random orientation, whereas SW conditions with cells seeded on grooved substrates (Figure IV.1 (C), (D), (G), (H), (I) and (J)) tended to align along a specific direction. This specific orientation was established preferentially according to the initial substrate where cells were seeded, while the opposing substrate seemed to have no effect on cell orientation.

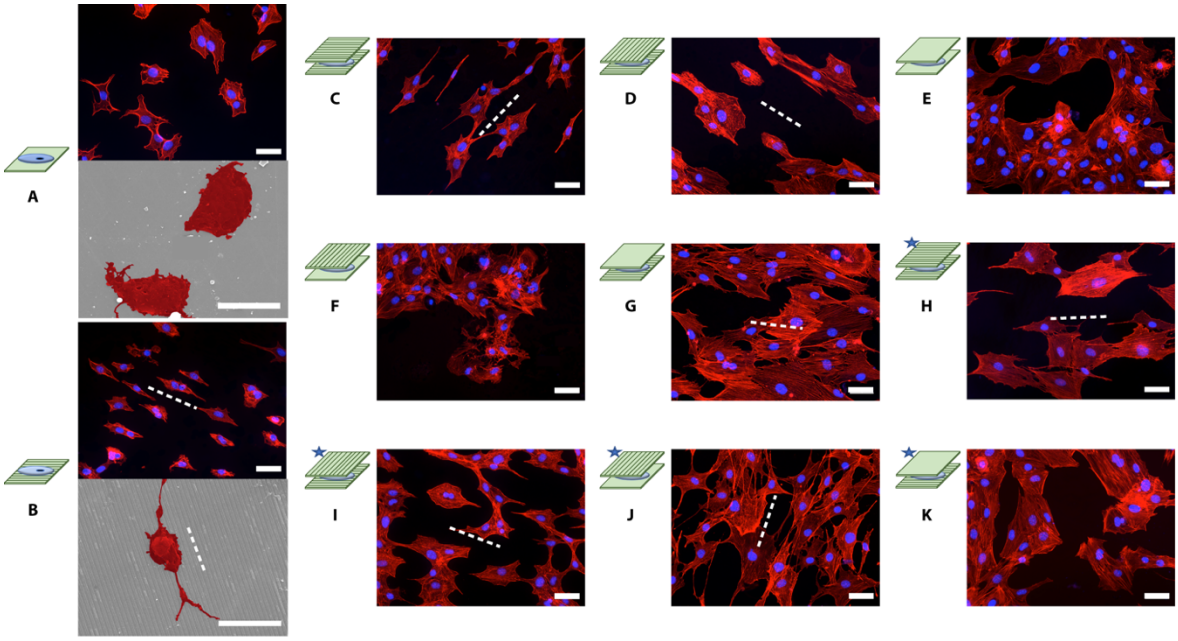

Figure IV.1. MC3T3-E1 cells seeded on 2D substrates or in SW conditions. F-actin stained in red and cell nuclei in blue. Cells seeded on lower substrates unless marked with a star. Images correspond to the substrate where cells were seeded (50 µm scale bars). Cells painted in red in SEM images for conditions (A) and (B) (20 µm scale bars). White dotted lines indicate nanogroove orientation of cell seeded substrates.

For a quantitative analysis, OrientationJ plug-in for ImageJ was used to create color-coded images of F-actin filament local orientations and translate this data into polar graphs (Figure IV.2I.). In accordance with the tendency qualitatively observed in Figure IV.1, in the absence

of grooves (condition (A)) cells acquired a random disposition, which was translated into the absence of a peak in the corresponding orientation plot and no dominant color in the image. Conversely, cells cultured on grooved substrates (condition (B)) aligned in a singular direction, which could be observed as a narrow peak and presence of a dominant color in Figure IV.2I. This cell behavior is also in accordance with previous studies using grooved substrates.[9,10] Regarding SW conditions, the software analysis also corroborated the findings from qualitative data of the disposition of F-actin cytoskeleton (Figure IV.1), *i.e.* cells aligned according to the groove direction of the substrate on which they were seeded. Cells on grooved substrates (Figure IV.2I (C), (D), (G), (H), (I) and (J)) tended to align along a dominant direction, whereas cells on non-grooved substrates (Figure IV.2I (E), (F), and (K)) presented a random distribution. Condition (E) was used as a control SW condition and, as expected, cells presented a random distribution in the absence of nanogrooves. Conditions (C) and (H) with substrates angled at 0º presented a narrow distribution of orientations. Analogously to what Ballester-Beltrán *et al.* [21] observed with cells seeded on aligned fibers with an upper flat substrate, condition (G) and (J) also presented a narrow distribution of orientations. Curiously, condition (D), and to some extent (I), with substrates angled 90º, presented a narrow distribution of orientations. This occurrence comes to reinforce the importance of initial contact and the finding that cells tend to align according to the substrate on which they were seeded, somewhat independently of further stimuli and also independent of gravity since it was also verified on upper cell-seeded substrates ((H)-(K)). In conditions (F) and (K), cells seeded on non-grooved substrates, placed in contact with opposing grooved substrates, acquired a random orientation. Previous studies did not describe such findings. This might be explained by the fact that MC3T3-E1 cells do not present a radial branching morphology,[21] contrarily to other cell types used in such studies, such as C2C12 and fibroblasts. Additionally, we have mapped cellular orientation based on the alignment of actin filaments, and not the orientation of the cell body by cytoplasmic staining, as has been described in previous works.[10,21] Therefore, our study highlights relevant findings that should be considered when designing surface engineering strategies aiming to control cell behavior.

Even though the formation of focal adhesions is a dynamic process, the initial three-hour adhesion time prior to closing the SW proves to be crucial on regulating cell morphology. It has been previously shown that if this initial step is bypassed, the elongation of cells is

jeopardized, and consequently a rounded morphology is acquired. This is in fact a limitation of the system, indicating that cell spreading is affected within SWs and that opposing substrate stimulation can only partially affect cell morphology.[22] In the assessed SW condition, a higher density in the activation of vinculin sites could be observed when compared to control single substrate condition, as shown in Figure 2II. The increased vinculin staining for SW condition (C) comparatively with control 2D-condition (B) may in fact be attributed to an enhanced engagement of the cell surface. Taking into consideration a previous SW culture study where upper substrate weight was deemed as not responsible for cell morphological changes,[18] this augmented engagement expectedly results from the effective contact of the cells to both substrates. However, since we did not directly assess the effects of varying substrate weight, we should consider that it may be driven by a greater ventral stimulation. Either way, these results confirm the greater stimulation within SW and corroborate our hypothesis. This is an important outcome for SW systems, since vinculin has recently emerged as a major player in focal adhesions-mediated mechanotransduction, facilitating 3D cell migration.[23] Even though focal adhesions have been extensively studied in 2D, studies in 3D such as cell encapsulation within hydrogels have yielded contradictory findings.[24,25] It has been previously proposed that focal and fibrillar adhesions observed in 2D studies are an amplification of *in vivo* 3D matrix adhesions.[26] Whereas the present study is not performed using a 3D model, it is a step further concerning 2D studies. When comparing the expression of focal adhesion kinase and its phosphorylation at Tyr-397 for control grooved condition (B) and SW condition (C), results showed a comparable FAK expression for both samples yet a significantly enhanced pFAK expression was observed for the SW condition (Figure IV.2III). Phosphorylation of FAK at Tyr-397 occurs upon integrin binding, denoting downstream signaling followed by integrin-mediated adhesion for the SW condition. Disassembly of integrin-based adhesion sites has in turn been linked to FAK signaling, indicating an equal degree of focal adhesion turnover, which has been linked to cell migration.[27,28] In accordance with a previous work that compared FAK and pFAK expression on fibroblasts cultured in regular 2D conditions and SW conditions, it was observed that the pFAK/FAK ratio was enhanced in SW culture conditions where cells were allowed to adhere for 3h prior to SW closing, as was performed in this study.[19] Taking together both the increased vinculin site activation and pFAK expression for SW condition (C) comparatively to nanogrooved control-2D condition (B), the enhanced interaction

provided by simultaneous dorsal and ventral stimulation of the cell surface is here demonstrated.

Cell elongation was another studied morphological aspect, corresponding to the ratio between the longest cell axis measured and the maximal perpendicular length. Grooved control condition (B) presented the highest elongation factor, followed by SW condition (C) with a 0º orientation angle between lower and upper substrates (Figure IV.2III). As expected, conditions (E), (F), and (K), where cells were seeded on non-patterned substrates, elongated the least. For these cases, cells were not subject to contact guidance and thus spread randomly on the substrate. Interestingly, grooved sandwich conditions (C), (D), (H), (I), and (J) presented a lower elongation factor than patterned control (B), even if not statistically significant for every condition. This may be due to the conjoint effect of ventral and dorsal stimuli, where cell spreading also occurs vertically, bridging both upper and lower substrates and acquiring an hourglass-like shape.[29] Comparatively to previously performed studies, Ballester-Beltrán *et al.* also observed alterations in morphology for fibroblasts seeded within sandwich conditions, comparatively to regular 2D conditions.[22] Therefore, although little or no effect was qualitatively found for cell orientation, cell elongation was actively affected.

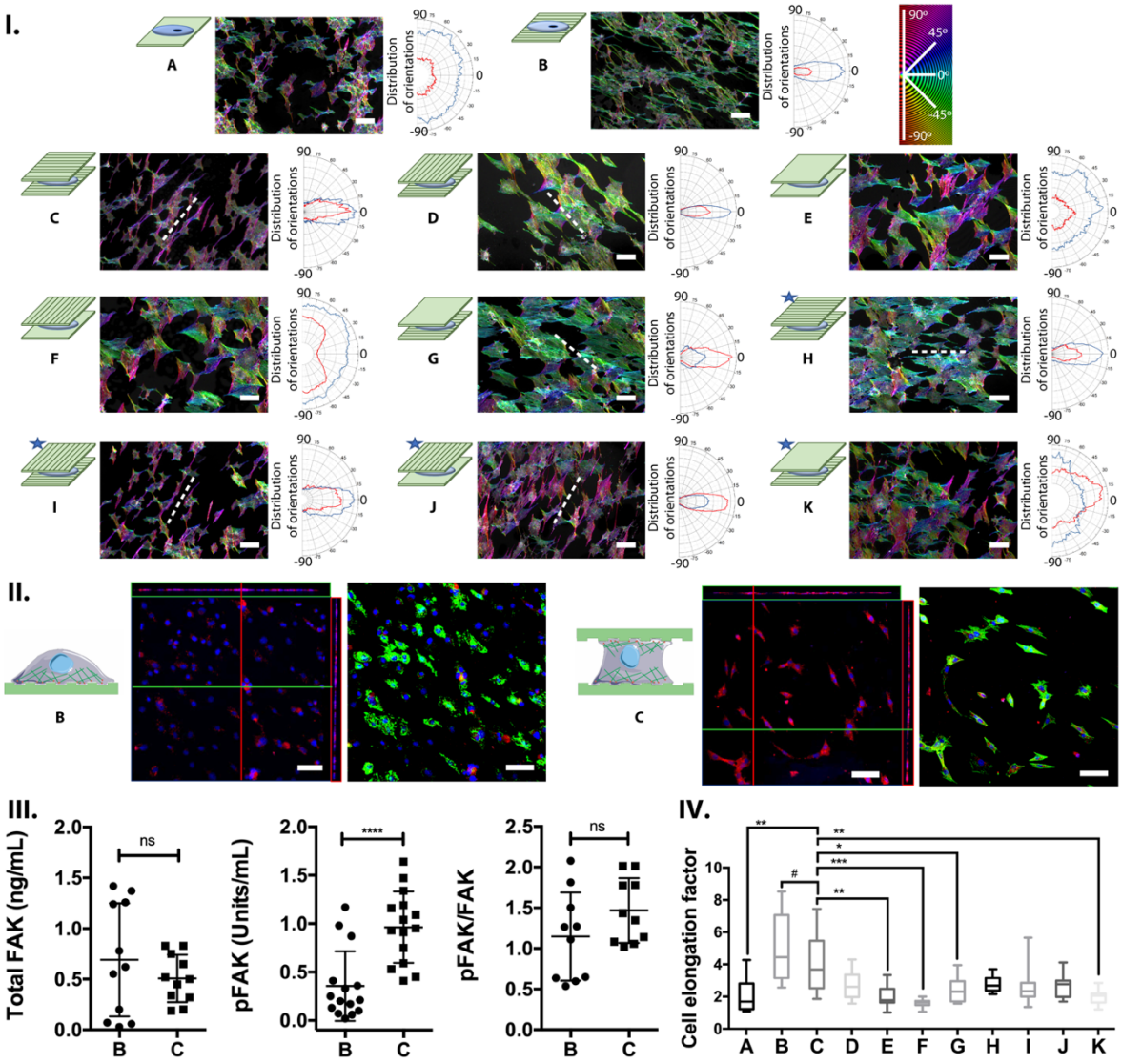

Figure IV.2. Analysis of 2D substrates ((A) and (B)) and single-seeded SW conditions ((C)-(K)). I. Orientation color-coded F-actin and corresponding orientation plots (n=2), ranging from -90 to 90º (circular color-coding map inset) (100 µm scale bars). Cells seeded on lower substrates unless marked with a star. White dotted lines indicate nanogroove orientation of cell seeded substrates. II. Cells for conditions (B) and (C) stained with vinculin (red) and nuclei (blue), with corresponding orthogonal views (left) and counterstaining of F-actin in green (right). III. Quantification via ELISA of total FAK (ng/mL) and phosphorylation of FAK at Tyr-397 (units/mL) for conditions (B) and (C) (n≥11) with corresponding pFAK/FAK ratio. Statistical significance of p≤0.0001 (****). IV. Cell elongation factor (n≥8). Statistical significance of p≤0.05 (*), p≤0.01 (**) and p≤0.001 (***) are represented when applicable. Statistical significance was observed between condition (B) and every other condition except (C), represented with # to facilitate reading.

Subsequently and in order to determine whether the presence of cells on both upper and lower substrates could be another influencing factor on cell behavior, double-seeded SW conditions were also studied. Cells stained with either DiO (green) or DiD (red) were seeded on independent substrates and closed onto each other for cells on both substrates to come in contact. Upon the disassembling of SW conditions, it was observed that few cells migrated

from the upper substrate to the lower substrate but none in the opposite direction; moreover, migrated cells (green) acquired a similar orientation to pre-seeded cells (red) (Figure IV.S1). By confocal microscopy of closed double-seeded SW conditions, the relative orientation of substrates could be observed, as well as the integration of cells from both substrates on one plane, further confirming contact between upper and lower substrates (Figure IV.3I; Figure IV.S2 illustrates the scenario when contact between substrates was not obtained). Cytoplasmic staining proved not to be sufficiently detailed for the development of rigorous orientation maps; thus, F-actin staining of conditions (L)-(N) was performed to obtain a precise cell mapping (Figure IV.3II). Similarly to single-seeded conditions, cells acquired the orientation of the substrate on which they were seeded. A narrow distribution of orientation could be observed for both lower and upper substrates of condition (M), which were angled at 0º. For condition (L), with a lower substrate presenting no grooves, or condition (N) with substrates angled at 90º, no significant differences were observed in cell orientation. For both conditions, cells initially seeded on grooved substrates aligned accordingly or spread randomly on non-grooved substrates.

When comparing single versus double-seeding, single-seeded conditions (G) and (J) and double-seeded condition (L) have grooved substrates versus non-grooved substrates, yet a greater alignment was found for condition (J) than for (G), which was similar to (L). With the same groove orientation, double-seeded condition (M) presented a narrow distribution of orientation, as was verified for conditions (C) and (H). When considering a 90º angle orientation between substrates, condition (N) also presented a narrow distribution, similarly to single-seeded conditions (D) and (I). In condition (L), cells on the lower non-grooved substrate presented a random distribution, whereas cells on the upper grooved substrate presented a definite trend towards a certain orientation, similarly to condition (G), even if not as narrow as condition (J).

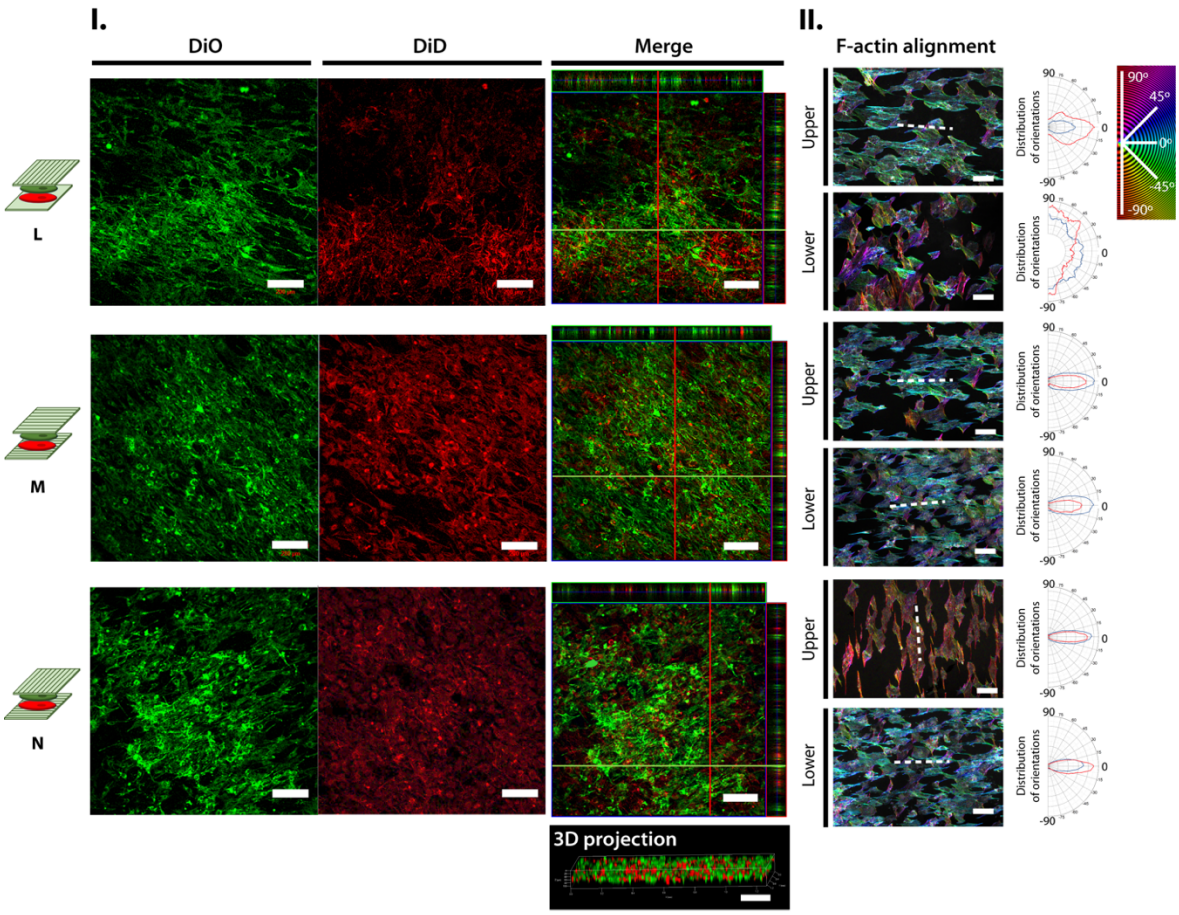

Figure IV.3. Double-seeded SW conditions (L)-(N) (100 µm scale bars). I. Confocal images of closed sandwich conditions: DiO (green) and DiD (red) stained cells, previously seeded on upper and lower substrates, respectively, with corresponding channel merging and orthogonal views. 3D projection of condition (L). II. Open SW orientation color-coded F-actin and corresponding orientation plots (n=2), ranging from -90 to 90º (circular color-coding map inset). White dotted lines indicate nanogroove orientation.

4. Conclusion

In conclusion, we proposed a sandwich culture model featuring varying combinations of nanogrooved topography on lower and upper substrates, with varying angles of nanogroove orientation between substrates, featuring single or double-seeding. For both single and double-seeded conditions, cells tended to acquire the orientation of the substrate on which they were seeded, evidencing the influence of initial contact over further stimuli from opposing substrates. Furthermore, cell elongation was effectively altered within SW conditions versus control 2D substrates, even if substrate orientation was not an impacting factor. This study explores for the first time the effect of nanogrooves on dorsal and ventral cell receptors under highly controlled orientation conditions, highlighting the significant impact of initial contact on cell morphology and orientation. Moreover, this is noteworthy

for tissue engineering strategies focusing on surface engineering, in particular on surface topography, as it brings new light into the role of the initial contact on cell behavior. Hence, even upon degradation or replacement of the biomaterial, the initial response of cells to the material may have an important influence on its bioperformance. We envision that a widespread application of SW cultures to distinct substrate materials, including soft materials (e.g. hydrogels), may deliver valuable information regarding the effects of mechanical cues on cells by combining stiffness and topography cues in an engineered quasi-3D environment more realistic compared to the conventional 2D platforms, and emphasize the contribution in the field of regenerative medicine through the development of mechanobiology platforms.

Acknowledgments

I. M. Bjørge acknowledges financial support by the Portuguese Foundation for Science and Technology (FCT) with doctoral grant SFRH/BD/129224/2017. This work was supported by the European Research Council grant agreement for the project "ATLAS" (ERC-2014-ADG-669858) and the FCT project "CIRCUS" (PTDC/BTM-MAT/31064/2017). This work was developed within the scope of the project CICECO-Aveiro Institute of Materials, UIDB/50011/2020 & UIDP/50011/2020, financed by national funds through the FCT/MEC and when appropriate co-financed by FEDER under the PT2020 Partnership Agreement. Image acquisition was performed in the LiM facility of iBiMED, a node of PPBI (Portuguese Platform of BioImaging): POCI-01-0145-FEDER-022122.

References

1. Donnelly, H., Salmeron-Sanchez, M. & Dalby, M. J. Designing stem cell niches for differentiation and self-renewal. *J. R. Soc. Interface* **15**, 20180388 (2018).
2. Alford, A. I., Kozloff, K. M. & Hankenson, K. D. Extracellular matrix networks in bone remodeling. *Int. J. Biochem. Cell Biol.* **65**, 20–31 (2015).
3. Baker, B. M. & Chen, C. S. Deconstructing the third dimension-how 3D culture microenvironments alter cellular cues. *J. Cell Sci.* **125**, 3015–3024 (2012).
4. Caliari, S. R., Vega, S. L., Kwon, M., Soulas, E. M. & Burdick, J. A. Dimensionality and spreading influence MSC YAP/TAZ signaling in hydrogel environments. *Biomaterials* **103**, 314–323 (2016).
5. Larsen, M., Artym, V. V, Green, J. A. & Yamada, K. M. The matrix reorganized: extracellular matrix remodeling and integrin signaling. *Curr. Opin. Cell Biol.* **18**, 463–471 (2006).
6. Dalby, M. J. Topographically induced direct cell mechanotransduction. *Med. Eng. Phys.* **27**, 730–742 (2005).
7. Dupont, S. *et al.* Role of YAP/TAZ in mechanotransduction. *Nature* **474**, 179–183 (2011).
8. Flemming, R. G., Murphy, C. J., Abrams, G. A., Goodman, S. L. & Nealey, P. F. Effects of

synthetic micro-and nano-structured surfaces on cell behavior. *Biomaterials* **20**, 573–588 (1999).
9. Wang, K., Cai, L., Zhang, L., Dong, J. & Wang, S. Biodegradable Photo-Crosslinked Polymer Substrates with Concentric Microgrooves for Regulating MC3T3-E1 Cell Behavior. *Adv. Healthc. Mater.* **1**, 292–301 (2012).
10. Sousa, M. P., Caridade, S. G. & Mano, J. F. Control of Cell Alignment and Morphology by Redesigning ECM-Mimetic Nanotopography on Multilayer Membranes. *Adv. Healthc. Mater.* **6**, 1601462 (2017).
11. Abagnale, G. *et al.* Surface topography enhances differentiation of mesenchymal stem cells towards osteogenic and adipogenic lineages. *Biomaterials* **61**, 316–326 (2015).
12. Wang, P.-Y., Li, W.-T., Yu, J. & Tsai, W.-B. Modulation of osteogenic, adipogenic and myogenic differentiation of mesenchymal stem cells by submicron grooved topography. *J. Mater. Sci. Mater. Med.* **23**, 3015–3028 (2012).
13. Wu, Y.-N. *et al.* Substrate topography determines the fate of chondrogenesis from human mesenchymal stem cells resulting in specific cartilage phenotype formation. *Nanomedicine Nanotechnology, Biol. Med.* **10**, 1507–1516 (2014).
14. Bjørge, I. M., Choi, I. S., Correia, C. R. & Mano, J. F. Nanogrooved microdiscs for bottom-up modulation of osteogenic differentiation. *Nanoscale* **11**, 16214–16221 (2019).
15. Gaspar, V. M., Lavrador, P., Borges, J., Oliveira, M. B. & Mano, J. F. Advanced Bottom-Up Engineering of Living Architectures. *Adv. Mater.* **32**, 1903975 (2020).
16. Dunn, J. C., Yarmush, M. L., Koebe, H. G. & Tompkins, R. G. Hepatocyte function and extracellular matrix geometry: long-term culture in a sandwich configuration. *FASEB J.* **3**, 174–177 (1989).
17. Gong, Y. Y. *et al.* A sandwich model for engineering cartilage with acellular cartilage sheets and chondrocytes. *Biomaterials* **32**, 2265–2273 (2011).
18. Beningo, K. A., Dembo, M. & Wang, Y. Responses of fibroblasts to anchorage of dorsal extracellular matrix receptors. *Proc. Natl. Acad. Sci. U. S. A.* **101**, 18024–9 (2004).
19. Ballester-Beltrán, J., Moratal, D., Lebourg, M. & Salmerón-Sánchez, M. Fibronectin-matrix sandwich-like microenvironments to manipulate cell fate. *Biomater. Sci.* **2**, 381 (2014).
20. Ballester-Beltrán, J., Lebourg, M., Rico, P. & Salmerón-Sánchez, M. Cell migration within confined sandwich-like nanoenvironments. *Nanomedicine* **10**, 815–828 (2015).
21. Ballester-Beltrán, J., Lebourg, M. & Salmerón-Sánchez, M. Dorsal and ventral stimuli in sandwich-like microenvironments. Effect on cell differentiation. *Biotechnol. Bioeng.* **110**, 3048–3058 (2013).
22. Ballester-Beltrán, J., Lebourg, M., Rico, P. & Salmerón-Sánchez, M. Dorsal and Ventral Stimuli in Cell–Material Interactions: Effect on Cell Morphology. *Biointerphases* **7**, 1–9 (2012).
23. Omachi, T., Ichikawa, T., Kimura, Y., Ueda, K. & Kioka, N. Vinculin association with actin cytoskeleton is necessary for stiffness-dependent regulation of vinculin behavior. *PLoS One* **12**, e0175324 (2017).
24. Kubow, K. E. & Horwitz, A. R. Reducing background fluorescence reveals adhesions in 3D matrices. *Nat. Cell Biol.* **13**, 3–5; author reply 5-7 (2011).
25. Fraley, S. I. *et al.* A distinctive role for focal adhesion proteins in three-dimensional cell motility. *Nat. Cell Biol.* **12**, 598–604 (2010).
26. Cukierman, E., Pankov, R., Stevens, D. R. & Yamada, K. M. Taking Cell-Matrix Adhesions to the Third Dimension. *Science.* **294**, 1708–1712 (2001).
27. Hamadi, A. *et al.* Regulation of focal adhesion dynamics and disassembly by phosphorylation of FAK at tyrosine 397. *J. Cell Sci.* **118**, 4415–25 (2005).
28. Mitra, S. K., Hanson, D. A. & Schlaepfer, D. D. Focal adhesion kinase: in command and control of cell motility. *Nat. Rev. Mol. Cell Biol.* **6**, 56–68 (2005).
29. Chaudhuri, O., Parekh, S. H., Lam, W. A. & Fletcher, D. A. Combined atomic force microscopy and side-view optical imaging for mechanical studies of cells. *Nat. Methods* **6**, 383–387 (2009).

Supporting Information

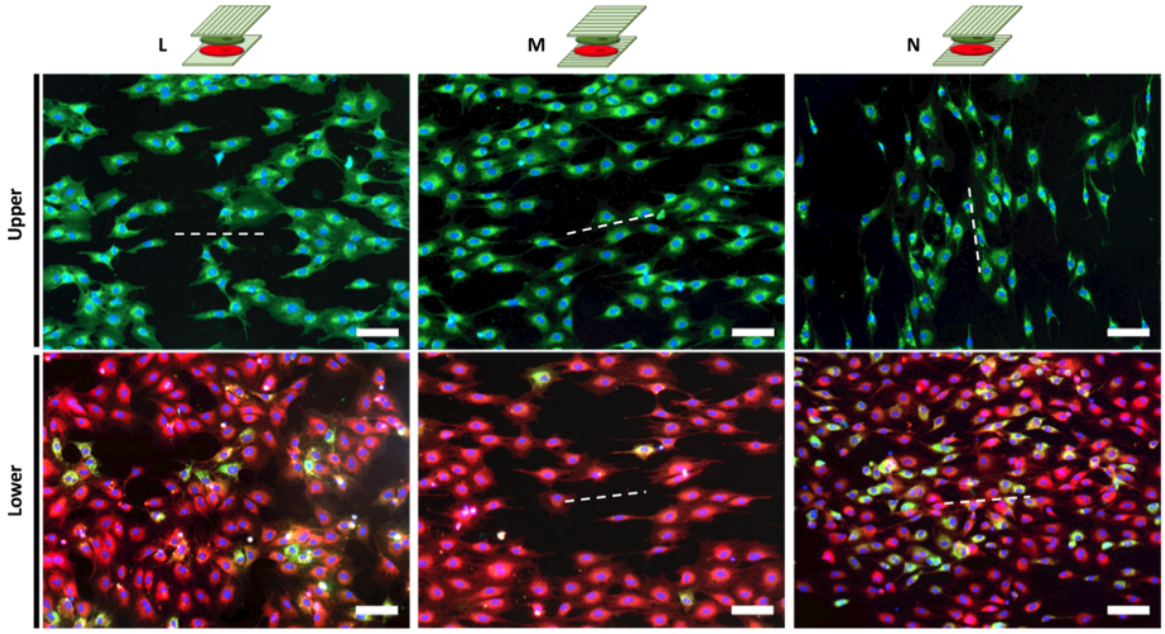

Figure IV.S1. Fluorescence images of SW conditions (L), (M), and (N) demonstrating the relative orientation of cells seeded on upper and lower substrates stained with DiO (green) and DiD (red), respectively. Some cells from the upper substrate tend to migrate and attach more firmly to the lower substrate, yet the opposite does not occur. Scale bars correspond to 200 μm.

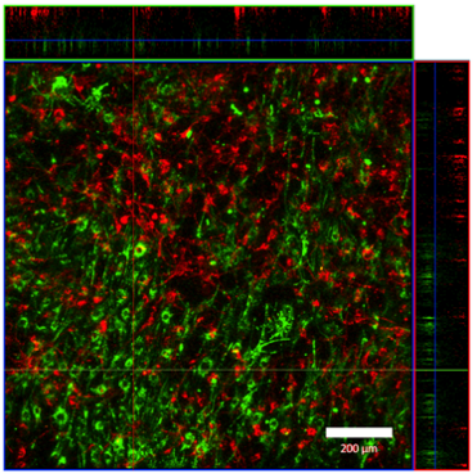

Figure IV.S2. Fluorescence confocal image of cells seeded in a closed SW condition stained with DiO (green) and DiD (red) for upper and lower substrates, respectively. Along the *z* axis it is possible to observe that cells from distinct substrates are in fact not in contact and opposing substrate stimulation will not impact cell behavior. To guarantee substrate contact, additional measures were taken to prevent this occurrence. Scale bar corresponds to 200 μm.

Chapter V: Nanogrooved microdiscs for bottom-up modulation of osteogenic differentiation[4]

Abstract

Grooved topographical features have effectively modulated cell differentiation on two-dimensional substrates. To transpose patterning into a 3D context, nanogrooved microdiscs, "topodiscs", are produced as cell-carriers for bottom-up cell-mediated assembly. While enhancing cell proliferation, topodiscs led to the formation of bone-like aggregates, even in culture medium lacking osteoinductive factors.

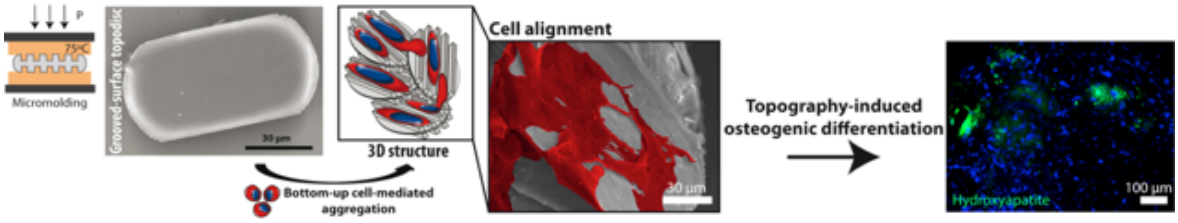

[4] Based on the publication: I.M. Bjørge, I.S. Choi, C.R. Correia, J.F. Mano. Nanogrooved microdiscs for bottom-up modulation of osteogenic differentiation, **Nanoscale**, 11 (2019) 16214-16221.

1. Introduction

At a nanometric scale, bone is mostly composed of hydroxyapatite reinforced collagen molecules.[1] Mineralized collagen molecules are arranged parallelly to form collagen fibrils, which, in turn, are also arranged parallelly to form fibers.[2] Understanding and taking advantage of bone physiology appears as an option to inspire bone tissue engineering strategies.[3] Both at a nano and micrometric level, the organization of the extracellular matrix (ECM) is a preponderant factor in cell-matrix signaling.[4,5] Topographical features deliver mechanical signals to cells, which are converted intracellularly into biochemical signals.[6] In order to take advantage of such mechanotransduction mechanisms, tailoring surface topography has gained momentum and several studies have explored the influence of ridges/grooves,[7] pillars,[8,9] bead monolayers,[10] and holes.[11] When cells are seeded on microgrooves, contact guidance directs cell alignment, growth, and migration along the microgroove direction.[12,13]

Furthermore, surface topography can actively guide the differentiation fate of mesenchymal stem cells (MSCs) into osteogenic or adipogenic lineages by directing cells to become elongated or rounded, respectively.[7,14] This effect has been linked to the mechanotransduction of surface cues. When cell spreading is stimulated, larger focal adhesions are formed and a greater actin- myosin contractility is observed, linked to an increased intracellular tension and transfer of tensile forces to the nucleus, which may in fact impact chromosomal arrangement. Conversely, when MSCs are seeded on substrates that restrict spreading, the rounded cell morphology impedes the formation of mature adhesions, consequently directing adipogenic differentiation.[15] Similarly, MSCs seeded on nanoholes or nanopillars are more likely to differentiate and form hyaline cartilage than when seeded on nanoridges in the same nanometric range.[11] In turn, myoblast fusion into multinucleated myotubes is enhanced when seeded on grooves, even in the absence of differentiation medium.[16] Additionally, grooved substrates with different nano and microgroove/ridge widths have been shown to direct the differentiation pathway of stem cells towards osteogenic,[17] myogenic,[18] neuronal,[19] and chondrogenic lineages.[11]

The osteogenic potential of grooved substrates has thus been previously established, however available studies are limited to a 2D approach, which does not mimic the native environment of cells.[12,20,21] Bottom-up approaches are an attractive option for the

development of 3D constructs for tissue engineering as they rely on the assembly of smaller units that can be implanted through minimally invasive procedures.[22] Microparticles support cell expansion and form 3D robust structures through cell-microparticle aggregation, which can be injected independently or encapsulated.[23–25]

Hence, we developed flat microparticles with topographical features, specifically grooves, here termed as topodiscs, that allow to transpose topographical cues to a 3D cell culture environment. This new class of microparticles features (1) disc-like shape with enhanced surface/volume ratio to maximize cell-adhesion sites; and (2) grooved patterning on the surface to control cell orientation or adhesion and direct osteogenic differentiation. Through a bottom-up cell-mediated approach, cells interact with topodiscs via not only ventral but also dorsal receptors, allowing for a three-dimensional cell stimulation. Topodiscs thus act as cell carriers, supporting cell expansion and adhesion, while also delivering topographical cues via surface patterning to direct osteogenic differentiation, even in the absence of osteogenic factors.

2. Materials & Methods

2.1. Grooved microdisc (topodisc) production

The production method of topodiscs was performed as illustrated in Scheme V.1. Step I: A 5% w/v solution of polycaprolactone (PCL, M_n=80 kDa, Sigma-Aldrich) in dichloromethane (DCM, Honeywell Chemicals) was emulsified under agitation (1:5) with an aqueous 0.5% w/v solution of polyvinyl alcohol (PVA, M_n=30 – 70 kDa, Sigma-Aldrich) for 48 hours to produce PCL microparticles (μpsheres) with a diameter range of 25-40 μm. Step II: Poly(vinyl alcohol) (PVA) counter-molds of optical media substrates (CDs) were produced via solvent evaporation of a 12% w/v solution of PVA in distilled water on CDs at 40ºC. PVA membranes sputtered with gold-palladium were visualized via scanning electron microscopy (SEM, S4100, Hitachi). Step III: μspheres were dispersed in patterned PVA membranes and pre-heated at 75ºC for 25 min prior to imprinting. A second patterned PVA membrane was placed on top of pre-heated μspheres with an applied pressure of approximately 1 kPa for 5 min. Step IV: Upon cooling, PVA-entrapped PCL membranes were dissolved in distilled water under stirring. Step V: Topodiscs were collected by centrifugation and extensively washed in distilled water. Topodiscs and non-molded μspheres were subjected to plasma treatment (Plasma System ATTO, Electronic Diener) at

0.4-0.6 mbar and 30 V for 15 min using atmospheric air, followed by UV sterilization during 30 min.

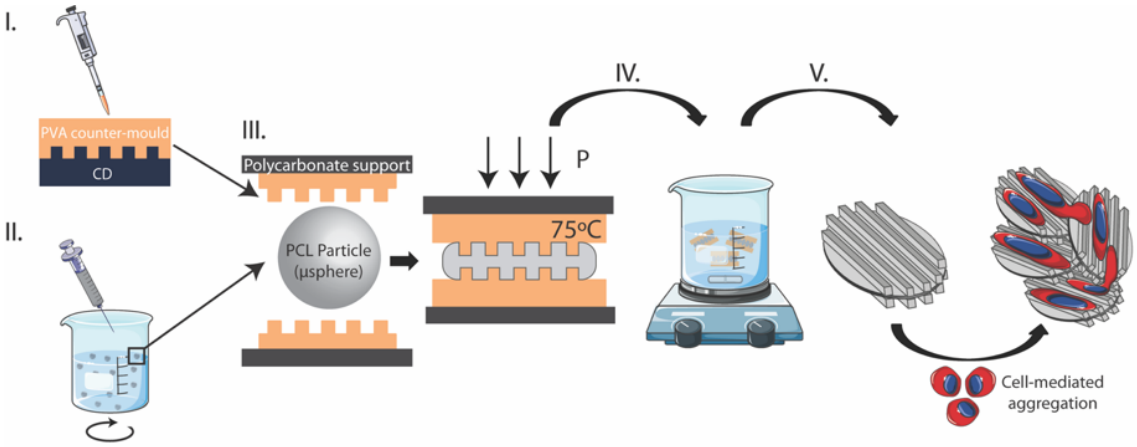

Scheme V.1. Schematic representation of production method for topodiscs. (I) Polyvinyl alcohol (PVA) counter-molds of CDs were produced by dispensing 12% w/v solution on top of CDs and allowing to dry at 40ºC. (II) PCL particles produced by oil/water emulsion were sieved to obtain [25-40] µm microparticles (µspheres). (III) Subsequently, µspheres were micro-molded between the patterned PVA membranes at an optimized time, temperature, and applied force. (IV) Topodiscs were subjected to several washings to eliminate the PVA counter-mold. (V) Recovery of topodiscs by centrifugation. Topodiscs sustained cell adhesion and proliferation via cell-mediated topodisc aggregation.

2.2. *In vitro* cell culture

MC3T3-E1 cells (American Type Culture Collection) were cultured with α-MEM supplemented with 10% fetal bovine serum (FBS, Gibco, ThermoFisher Scientific) and 1% antibiotic-antimycotic (100X, Gibco, ThermoFisher Scientific), denominated basal medium (BAS) at 37ºC in a humidified air atmosphere of 5% CO_2. Cells were detached at 90% of confluence via 0.05% w/v trypsin-EDTA (from porcine pancreas 1:250, Sigma-Aldrich) treatment for 5 min at 37ºC. An identical process was performed with human adipose-derived stem cells (hASCs, passage 4, American Type Culture Collection). A seeding density of $4x10^5$ cells.cm^{-2} was used for MC3T3-E1 cells, whereas $8x10^5$ cells.cm^{-2} was used for hASCs, calculated based on the average surface area of topodiscs. An equal weight of topodiscs and µspheres was used for each condition. Topodisc and µsphere MC3T3-E1-mediated aggregates were cultured in BAS medium, whereas hASC-mediated aggregates were cultured in both BAS and osteogenic (OST) medium supplemented with ascorbic acid (50 µg.mL^{-1}, Cayman Chemical), β-glycerophosphate disodium salt (10 mM, Santa Cruz Biotechnology), and dexamethasone (10 nM, ThermoFisher Scientific).

2.3. 3D aggregates with controlled shape

Cells were stained with DiL (1,1'-Dioctadecyl-3,3,3',3'-Tetramethylindocarbocyanine Perchlorate (DiIC18(3)), ThermoFisher Scientific) according to the manufacturer's specifications. Stained cells were seeded on previously developed surfaces[31] at a concentration of $5x10^7$ cells.mL^{-1} with 50 mg.mL^{-1} of topodiscs.

2.4. Cell-microparticle aggregate characterization

Samples were fixed with 4% v/v formaldehyde solution (Sigma-Aldrich) in PBS for 30 min at RT. For SEM morphological studies, samples were dehydrated in increasing ethanol series for 10 min at RT and sputtering with gold-palladium. For nuclei (blue) and actin filament (red) staining of MC3T3-E1 aggregates, DAPI (4',6-diamidino-2-phenylindole, dihydrochloride, 1 mg.mL^{-1}, ThermoFisher Scientific, 1:1000 ratio in PBS for 5 min, RT) and phalloidin (Flash Phalloidin™ Red 594, 300U, BioLegend, 1:40 ratio in PBS for 45 min, RT) were respectively used, posteriorly to permeabilization with 0.1% v/v Triton-X100 (BioXtra, Sigma-Aldrich) in PBS for 5 minutes. After 21 days in culture of hASC aggregates, hydroxyapatite (green) was stained using OsteoImage mineralization assay kit (Lonza) according to the manufacturer's specifications and counterstained with DAPI as previously described. Histological assessment of hASC aggregates upon 21 days was also performed after fixation in buffered formaldehyde 10% v/v. Samples were processed in an automatic tissue processor (STP120, Microm) and embedded in paraffin. Histological sections (5µm) were cut using a microtome (HM355E, Microm, ThermoFisher Scientific) and stained with Masson's Trichrome and von Kossa for visualization of collagen fibers and phosphate deposits, respectively. Samples were visualized by optical and fluorescence microscopy (Axio Imager 2, Zeiss).

2.5. Mitochondrial metabolic activity and cell proliferation quantification

Mitochondrial metabolic activity quantification (n=3) was performed at 1, 7, 14, and 21 days using an MTS colorimetric assay (CellTiter 96 AQueous One Solution Cell Proliferation Assay, Promega) according to the manufacturer's specifications. Absorbance was read at 490 nm using a microplate reader (Synergy HTX, BioTek). Total DNA quantification was performed according to kit specifications (Quant-iTTM PicoGreen® dsDNA assay kit, Life Technologies) after cell lysis in ultra-pure sterile water containing 2% v/v triton-X100.

Fluorescence was read at an excitation wavelength of 485/20 nm and emission wavelength of 528/20 nm using a microplate reader.

2.6. Statistical analysis

Statistical analysis was performed using two-way analysis of variance (ANOVA) with Tukey's or Sidak's post-hoc test (GraphPad Prism 6.0). A p-value<0.05 was considered statistically significant.

3. Results & Discussion

3.1. µSphere and topodisc characterization

Grooved substrates have been previously shown to impact cell alignment and differentiation into the osteogenic lineage, where pitch dimensions (groove plus ridge dimensions) ranging from 400 nm [17] to 200 µm [26] have been assessed. Furthermore, it has been demonstrated that grooved substrates tend to enhance osteogenic differentiation to a greater extent than flat substrates.[7,18,20,26–28] These studies have however been restricted to a two-dimensional approach, which does not fully mimic the native environment of cells. The present study aims to transpose the reaction of cells to patterning to a quasi-3D concept, as topodiscs were applied for a bottom-up cell-mediated assembly to form three-dimensional constructs.

CDs were used as grooved substrates, presenting ridge widths of 1185±16 nm, groove widths of 412±12 nm, and ridge heights of 197±14 nm. Initially, counter-molds of CDs were prepared using water-soluble poly(vinyl alcohol) (PVA). As can be observed in Figure V.1A, PVA counter-molds presented a homogeneously patterned surface, maintaining the fidelity of CD surfaces (Figure V.S1). Upon molding of polycaprolactone (PCL) microparticles (µspheres), the obtained topodiscs were collected and visualized by SEM. Topodiscs were successfully produced and presented the homogenous grooved patterning of the mold (Figure V.1A). The shape of topodiscs is elongated due to the preferential flow of PCL from the microparticles along the ridges of the mold during the processing. Topodiscs presented an average length of 92±20 µm and width of 55±19 µm (Figure V.1B), with patterning dimensions of 944±49 nm ridges, 358±23 nm grooves, and 201±45 nm ridge height. Furthermore, topodiscs presented on average the quadruple of the surface area comparatively to µspheres. The large standard deviation observed for all measured and calculated

parameters is due to the variance in size of the initial template used – μpsheres, which were sieved to be comprised between 25 and 40 μm. Of note, topodiscs allowed the adhesion of cells, which aligned along the microgrooves of the topodisc, as showed in Figure V.1A.

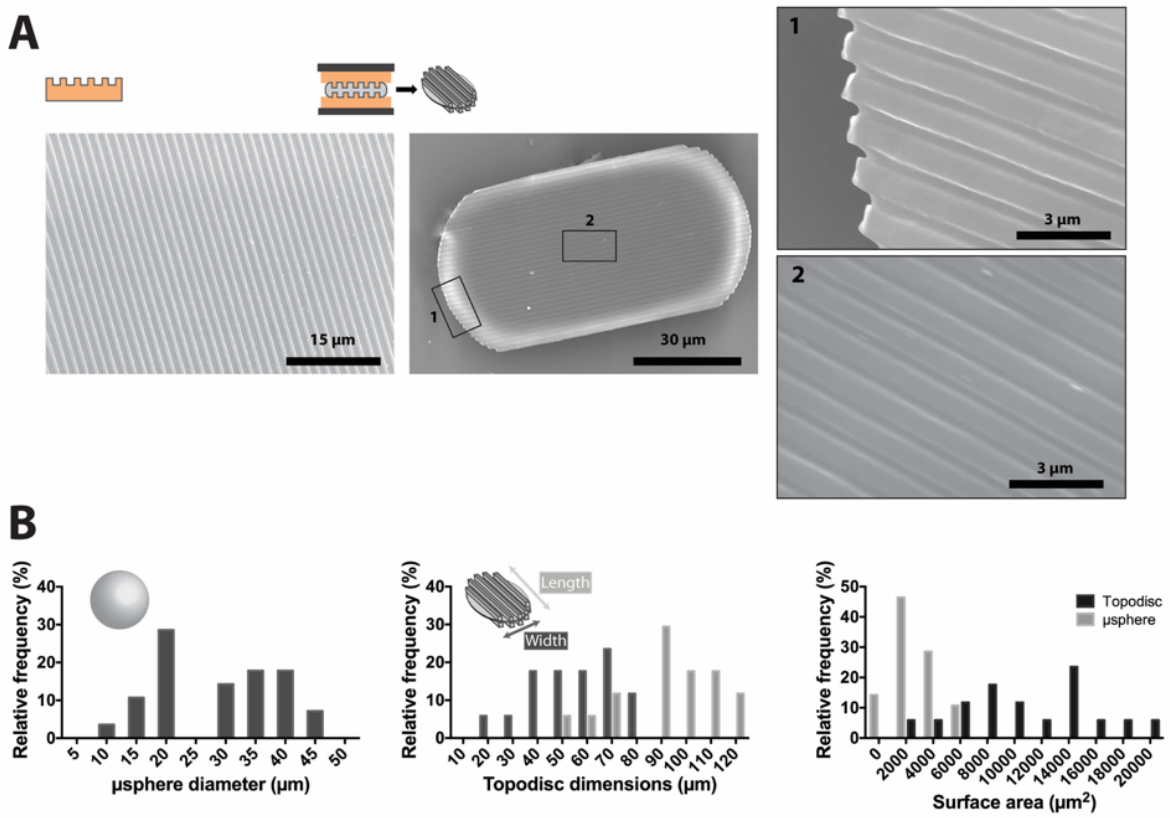

Figure V.1. μsphere and topodisc characterization. (A) SEM images from left to right of: PVA counter-mold; PCL grooved topodisc with higher magnification of topodisc patterning on border (1) and center (2). (B) μsphere and topodisc dimensions: μsphere diameter (left); topodisc length and width (center); topodisc and μsphere surface area (right).

3.2. Topodiscs as cell carriers for pre-osteoblastic MC3T3-E1 cell line

Topodiscs were then studied for their ability to perform as cell carriers, comparatively to μspheres. As a proof-of-concept, a MC3T3-E1 pre-osteoblastic cell line was used. Figure V.2A shows that both substrates supported cell adhesion. Additionally, cells' ability to proliferate was demonstrated since only small aggregates could be visualized on day 1, and larger cell-mediated aggregates were formed up to day 21. Spherical microparticles have been previously used as vehicles for cell proliferation via bottom-up approaches to form 3D constructs on their own [23] or when encapsulated.[29] Hence, it was expected that both μspheres and topodiscs would sustain cell culture, as was observed.

Upon 21 days of culture, the deposition of extracellular matrix (ECM) on the exterior of aggregates is evident for both types of substrates (Figure 2B). In cross-section images it is possible to observe cells bridging several microparticles. Cells can attach to more than one μsphere or topodisc, promoting the cohesion of cell-particle assembly. Hence, cells interact in both cases with particles via ventral and dorsal receptors, allowing for a complete cell stimulation, contrarily to what would occur in a 2D environment. The construction of aggregates is controlled by cells, which selectively remodel particle location, while depositing extracellular matrix. Whereas there is only a 3D aggregation of μpsheres mediated by cells, for topodiscs there is both a 3D aggregation and alignment of cells along surface microgrooves. The surface area of topodiscs is sufficiently large for the adherence of several cells, yet topodisc dimensions still allow for cell-mediated remodeling. Furthermore, higher magnification of formed aggregates allows to observe that the morphology of the ECM deposited on topodiscs and μspheres is quite distinct. Interestingly, a very fibrillar and highly aligned ECM was deposited on topodiscs, whereas a more compact ECM was deposited on μspheres, even if also seemingly aligned. During the 21-day assays, cells were allowed to interact freely with topodiscs and form randomly-shaped aggregates. The bottom-up assembly of microparticles has been previously established and pose as attractive options for minimally invasive injectable applications due to their ability to assemble *in situ*.[23,30] In order to demonstrate the potential of topodiscs for these same applications, cells and topodiscs were seeded at a higher density on hydrophilic spots engraved on superhydrophobic slides with varying shapes [31] and, upon a day in culture, it was verified that cell-topodisc aggregates acquired the different shapes, namely squares, circles, and hexagons (Figure V.S2).

To compare both types of microparticles as vehicles for cell culture, cell metabolic activity and cell proliferation was assessed. A significant difference in both metabolic activity and cell proliferation of MC3T3-E1 cells was observed between topodiscs and μspheres (Figure V.2C and D). Topodiscs clearly led to an increased cell expansion in both basal and osteogenic medium, likely due to the larger surface area to volume ratio for cells to proliferate.

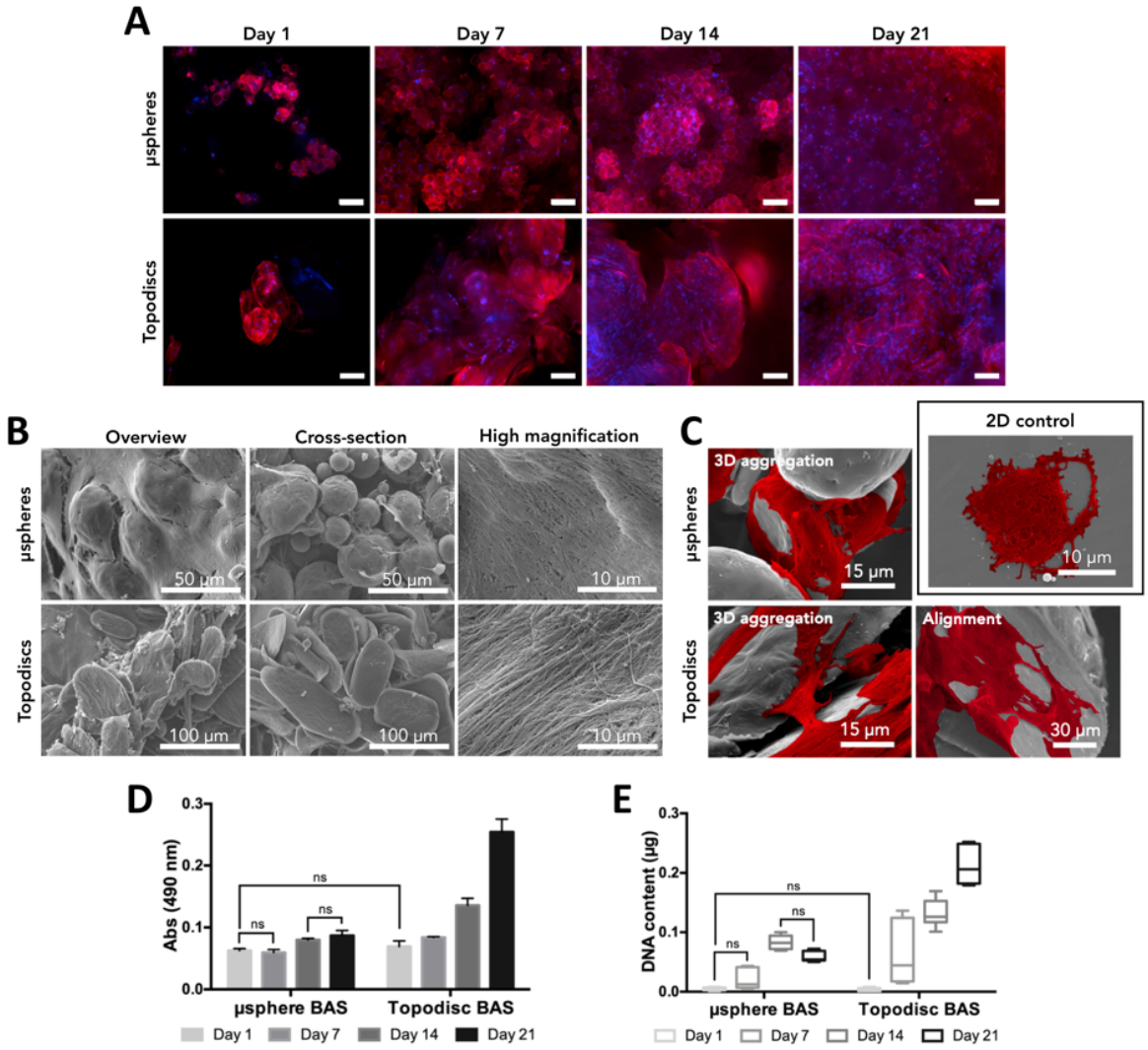

Figure V.2. Pre-osteoblastic MC3T3-E1 culture on topodiscs and µspheres. (A) Fluorescence images of stained F-actin filaments (red) and nuclei (blue) of cells seeded on topodiscs or µspheres at timepoints 1, 7, 14, and 21 days. Cells were seeded at a density of 40 000 cells/cm^2, calculated according to the average surface area of topodiscs, and cultured in basal medium. Scale bars correspond to 100 µm. (B) SEM images of cells seeded on topodiscs and µspheres on days 7 and 21 of culture in basal medium. Day 21 images from left to right correspond to cells and topodiscs/µspheres aggregation; cross-sections of respective aggregates with cells; and higher magnification of ECM. (C) SEM images of cells (red) cultured on µspheres or topodiscs, highlighting the 3D cell-mediated aggregation and alignment, for the case of topodiscs, upon 7 days in culture. Control image of cell cultured on a commercially available 2-dimensional polystyrene substrate. (D) Cell metabolic activity determined using an MTS colorimetric assay and (E) cell proliferation determined by DNA quantification. Cells were cultured up to 21 days in basal medium. Mean ± standard deviation for each condition (n=3). All results were significantly different unless marked with ns ($p > 0.05$), indicating no statistically significant differences between samples.

3.3. Topodiscs as osteogenic-inducing platforms in the absence of osteoinductive factors

To determine the osteogenic potential of topodiscs versus commonly used μspheres, mineralization upon 21 days in culture was assessed. To this end, hASCs were cultured in the presence (OST) or absence (BAS) of osteogenic factors. Histological cuts of hASC aggregates were stained with Masson's Trichrome and Von Kossa to specifically mark collagen (blue) and phosphate deposits (black), respectively. Hydroxyapatite (green) present in aggregates was specifically stained to further confirm mineralization (Figure V.3).

Regarding collagen deposition, a greater staining was observed for cells cultured with topodiscs, even in the absence of osteogenic factors, than for μsphere aggregates (Figure V.3). Collagen presence in μsphere aggregates in basal medium was nearly negligible and even in osteogenic medium was quite reduced when compared with topodiscs. Collagen is a prime component of bone, with 85 to 90% of the total bone protein consisting of collagen fibers.[1] Cell interaction with a collagen-containing ECM is also a requirement for the stimulation of osteogenic differentiation.[32] Hence, the enhanced collagen staining of topodisc aggregates, even without osteogenic factors, is an important indicator of commitment to the osteogenic lineage. In accordance, a previous study featuring 50 and 200 μm grooves composed of compacted osteogenic factor-loaded microspheres presented a significantly increased collagen secretion than flat substrates.[33] However, in the absence of osteogenic factors, collagen content and osteogenic quantifiers (ALP and osteocalcin) were only significantly enhanced on 50 μm grooves relatively to flat substrates and presented much lower results when compared to osteogenic factor-loaded substrates.[33]

To assess tissue mineralisation, the presence of phosphate deposits and hydroxyapatite was evaluated (Figure V.3). By Von Kossa staining, it was possible to observe that a similar phosphate deposition occurred in topodisc aggregates in both basal and osteogenic medium, as for μspheres in osteogenic medium. Virtually no phosphate deposits were observed for μsphere aggregates in the absence of osteogenic factors. A similar trend was observed for hydroxyapatite staining where topodisc aggregates clearly presented a greater hydroxyapatite content. Furthermore, a comparable amount of hydroxyapatite appeared to be present in cell-topodisc aggregates in both basal and osteogenic medium. Cell-μsphere aggregates required osteogenic factors to induce formation of hydroxyapatite, even if

slightly reduced when compared with topodiscs, and no hydroxyapatite staining was found in samples cultured in basal medium. Hence, it can be concluded that a mineralized matrix was effectively achieved. Considering both the enhanced collagen deposition and matrix mineralization, the osteogenic potential of topodiscs alone, without the need for osteogenic factors, as platforms for osteogenic differentiation was demonstrated.

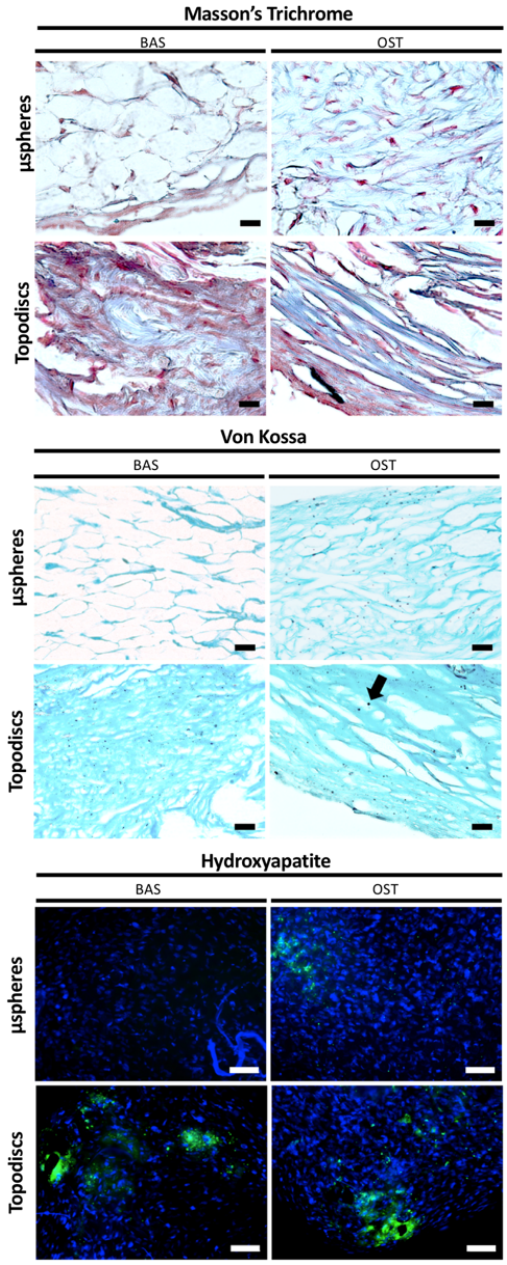

Figure V.3. hASCs seeded on topodiscs and µspheres after 21 days of culture in basal (BAS) or osteogenic (OST) medium. Staining of histological cuts with Masson's Trichrome and von Kossa was performed. For Masson's Trichrome, tissue is marked in red and collagen fibers in blue. Von Kossa staining of tissue (blue) and phosphate deposits (black), with arrow exemplifying the identification of deposits. Hydroxyapatite was fluorescently stained in green, whilst cell nuclei were stained in blue (DAPI). Black scale bars correspond to 20 µm, whereas white scale bars correspond to 100 µm.

Previous studies have been limited to a 2D approach, reporting that grooved patterning can effectively direct cell alignment and enhance osteogenic differentiation to a greater extent than flat surfaces.[7,26,27] The enhancement of osteogenic differentiation has also been shown to be cell-dependent, where optimal conditions may in fact be associated with maximal cell length, highlighting the effect of contact guidance and tensile stress on differentiation.[20,34] Kim *et al*. demonstrated that 0.5/1.8, 2/2, and 2/4 μm ridges/grooves, in the presence of osteogenic factors, induced osteogenic differentiation with a greater alizarin red staining observed for MC3T3-E1 cells seeded on 0.5/1.8 μm (500 nm depth) substrates, whereas hASCs presented an enhanced staining on 2/2 and 2/4 μm (1 μm depth) substrates. Additionally, half-doses of osteogenic supplements on hASCs grown on 2/2 μm substrates were comparable to full doses.[20] In accordance with these findings and also in the presence of osteogenic factors, Abagnale *et al.* [7] observed a greater alizarin red staining of hASCs on 2 μm ridges, than for other ridge widths studied up to 15 μm, somewhat independently of groove width, which was also varied between 2 and 15 μm. Watari *et al.* [17] demonstrated that human bone marrow-derived mesenchymal stem cells (hBMSCs) cultured on 200/200 nm ridges/grooves presented an enhanced calcium deposition and expression of osteogenic marker genes RUNX2 and BGLAP comparatively with non-patterned substrates in the absence of osteoinductive factors, yet a combination of topography with osteogenic factors yielded the best results. Ridge/groove widths of 700/700 nm and 2/2 μm were also studied yet did not present as promising results as 200 nm grooves, even if BGLAP expression was significantly higher than for flat surfaces. Ridge depth may also be an impacting factor for the differences observed between these studies as 1 or 2 μm depths were used by Kim *et al*. [20] and Abagnale *et al*.,[7] respectively, as opposed to 300 nm by Watari *et al*.[17] Hence, even though the 2D effect of patterning had previously been established, the effect in a 3D environment, which mimics the native environment in a more realistic manner, had yet to be proved.

In this study, ridge/groove dimensions present on topodiscs were approximately 944/358 nm, with 201 nm in depth. In accordance with 2D studies, hASC differentiation into the osteogenic lineage was effectively enhanced by the patterned surface of topodiscs, when compared with smooth surface μspheres.[7,26,27] It is complicated to reach a consensus regarding the optimal dimensions for patterned surfaces since ridges and grooves can be tailored at a nanometric scale, opening up an infinitude of possibilities. Despite this fact,

patterning dimensions in this study could to some extent be correlated with dimensions applied in previously mentioned studies. Hence, the enhancement of osteogenic potential due to the topographical features present on the surface of topodiscs is further corroborated. More importantly, a similar enhancement of osteogenic differentiation for cells cultured on patterned topodiscs in the absence or presence of osteogenic factors was observed. In previous studies, osteoinductive factors were required for osteogenic differentiation or for comparative results.[7,17,20] We previously used microspheres as cell carriers and showed their *in vitro* bioperformance using a co-culture of microvascular endothelial cells and hASCs. The cellular crosstalk led to the osteogenic differentiation of hASCs in the absence of two major osteogenic differentiation factors, namely dexamethasone and ascorbic acid. However, mineralization could only occur in the presence of β-glycerophosphate.[24] In this work, the proposed topodiscs allowed for a full osteogenic differentiation in the absence of osteoinductive factors, orchestrated by the patterned and three-dimensional environment offered to stem cells by the new engineered topodiscs. This opens up new potential applications, namely for *in vivo* studies, where an initial *in vitro* stimulation prior to implantation with osteoinductive factors may in fact be bypassed and still result in new localized mineralized bone tissue.

4. Conclusion

Topodiscs featuring nanogrooved patterning were produced for a bottom-up assembly of 3D cell-mediated micro-bone tissues. Topodiscs enabled cell adhesion and led to an enhanced proliferation comparatively with microspheres, likely due to the increased surface area to volume ratio. More importantly and in line with what is observed for 2D patterned substrates, topodiscs effectively led to the osteogenic differentiation of hASCs, even in the absence of osteoinductive factors. The formation of a three-dimensional tissue, which is more mimetic of the native cell environment, may in fact have contributed to the enhanced osteogenic effect. Patterned topodiscs were thus presented as novel cell carriers with nanotopographical cues for osteogenic differentiation, transposing the previously documented 2D osteogenic effect into a 3D setting, while bypassing the need for the osteogenic supplements. With tissue engineering strategies striving to reduce the complexity of systems and minimize the need for additional factors, the osteogenic potential of topodiscs was shown to be dependent on the grooved topographical surface cues. Although, the present work focused on osteogenic

differentiation, we envision that the application of these 3D patterned substrates could in fact be broadened to other topography-responsive cells. This technology could thus potentially be used, for example, in neuronal, myogenic, cardiac, or chondrogenic tissue engineering strategies.

Acknowledgments

I. M. Bjørge acknowledges the Portuguese Foundation for Science and Technology (FCT) with doctoral grant SFRH/BD/129224/2017. This work was financially supported by the European Research Council grant agreement ERC-2014-ADG-669858 (ATLAS) and FCT grant agreement PTDC/BTM-MAT/31064/2017 (CIRCUS). This work was developed within the scope of the project CICECO-Aveiro Institute of Materials, FCT Ref. UID/CTM/50011/2019, financed by national funds through the FCT/MCTES. I. S. Choi acknowledges the Basic Science Research Program through the National Research Foundation of Korea funded by the Ministry of Science, ICT and Future Planning (MSIP 2012R1A3A2026403).

References

1. Fratzl, P., Gupta, H. S., Paschalis, E. P. & Roschger, P. Structure and mechanical quality of the collagen–mineral nano-composite in bone. *J. Mater. Chem.* **14**, 2115–2123 (2004).
2. Fratzl, P. & Weinkamer, R. Nature's hierarchical materials. *Prog. Mater. Sci.* **52**, 1263–1334 (2007).
3. Lopes, D., Martins-Cruz, C., Oliveira, M. B. & Mano, J. F. Bone physiology as inspiration for tissue regenerative therapies. *Biomaterials* **185**, 240–275 (2018).
4. Bettinger, C. J., Langer, R. & Borenstein, J. T. Engineering substrate topography at the micro- and nanoscale to control cell function. *Angew. Chem. Int. Ed. Engl.* **48**, 5406–15 (2009).
5. Lamers, E. *et al.* The influence of nanoscale topographical cues on initial osteoblast morphology and migration. *Eur. Cells Mater.* **20**, 329–343 (2010).
6. Dobbenga, S., Fratila-Apachitei, L. & Zadpoor, A. A. Nanopattern-induced osteogenic differentiation of stem cells - a systematic review. *Acta Biomater.* **46**, 3–14 (2016).
7. Abagnale, G. *et al.* Surface topography enhances differentiation of mesenchymal stem cells towards osteogenic and adipogenic lineages. *Biomaterials* **61**, 316–326 (2015).
8. Fiedler, J. *et al.* The effect of substrate surface nanotopography on the behavior of multipotnent mesenchymal stromal cells and osteoblasts. *Biomaterials* **34**, 8851–8859 (2013).
9. Seo, J. *et al.* Nanotopography-Promoted Formation of Axon Collateral Branches of Hippocampal Neurons. *Small* **14**, 1801763 (2018).
10. Kang, K. *et al.* Cytoskeletal Actin Dynamics are Involved in Pitch-Dependent Neurite Outgrowth on Bead Monolayers. *Angew. Chemie Int. Ed.* **53**, 6075–6079 (2014).
11. Wu, Y.-N. *et al.* Substrate topography determines the fate of chondrogenesis from human mesenchymal stem cells resulting in specific cartilage phenotype formation. *Nanomedicine Nanotechnology, Biol. Med.* **10**, 1507–1516 (2014).
12. Wang, K., Cai, L., Zhang, L., Dong, J. & Wang, S. Biodegradable Photo-Crosslinked Polymer Substrates with Concentric Microgrooves for Regulating MC3T3-E1 Cell Behavior. *Adv.*

Healthc. Mater. **1**, 292–301 (2012).
13. Lenhert, S., Meier, M.-B., Meyer, U., Chi, L. & Wiesmann, H. P. Osteoblast alignment , elongation and migration on grooved polystyrene surfaces patterned by Langmuir – Blodgett lithography. *Biomaterials* **26**, 563–570 (2005).
14. Guvendiren, M. & Burdick, J. A. The control of stem cell morphology and differentiation by hydrogel surface wrinkles. *Biomaterials* **31**, 6511–6518 (2010).
15. Donnelly, H., Salmeron-Sanchez, M. & Dalby, M. J. Designing stem cell niches for differentiation and self-renewal. *J. R. Soc. Interface* **15**, 20180388 (2018).
16. Sousa, M. P., Caridade, S. G. & Mano, J. F. Control of Cell Alignment and Morphology by Redesigning ECM-Mimetic Nanotopography on Multilayer Membranes. *Adv. Healthc. Mater.* **6**, 1601462 (2017).
17. Watari, S. *et al.* Modulation of osteogenic differentiation in hMSCs cells by submicron topographically-patterned ridges and grooves. *Biomaterials* **33**, 128–136 (2012).
18. Wang, P.-Y., Li, W.-T., Yu, J. & Tsai, W.-B. Modulation of osteogenic, adipogenic and myogenic differentiation of mesenchymal stem cells by submicron grooved topography. *J. Mater. Sci. Mater. Med.* **23**, 3015–3028 (2012).
19. Lee, M. R. *et al.* Direct differentiation of human embryonic stem cells into selective neurons on nanoscale ridge/groove pattern arrays. *Biomaterials* **31**, 4360–4366 (2010).
20. Kim, C.-S. *et al.* A Specific Groove Pattern Can Effectively Induce Osteoblast Differentiation. *Adv. Funct. Mater.* **27**, 1703569 (2017).
21. Lamers, E. *et al.* The influence of nanoscale grooved substrates on osteoblast behavior and extracellular matrix deposition. *Biomaterials* **31**, 3307–3316 (2010).
22. Nichol, J. W. & Khademhosseini, A. Modular tissue engineering: Engineering biological tissues from the bottom up. *Soft Matter* **5**, 1312–1319 (2009).
23. Custódio, C. A., Cerqueira, M. T., Marques, A. P., Reis, R. L. & Mano, J. F. Cell selective chitosan microparticles as injectable cell carriers for tissue regeneration. *Biomaterials* **43**, 23–31 (2015).
24. Correia, C. R. *et al.* Semipermeable Capsules Wrapping a Multifunctional and Self-regulated Co-culture Microenvironment for Osteogenic Differentiation. *Sci. Rep.* **6**, 21883 (2016).
25. Neto, M. D., Oliveira, M. B. & Mano, J. F. Microparticles in Contact with Cells: From Carriers to Multifunctional Tissue Modulators. *Trends Biotechnol.* **in press**, (2019).
26. Shi, X. *et al.* Stretchable and Micropatterned Membrane for Osteogenic Differentation of Stem Cells. *ACS Appl. Mater. Interfaces* **6**, 11915–11923 (2014).
27. Sun, L. *et al.* Controlling Growth and Osteogenic Differentiation of Osteoblasts on Microgrooved Polystyrene Surfaces. *PLoS One* **11**, e0161466 (2016).
28. Matsuzaka, K., Walboomers, X. F., de Ruijter, J. E. & Jansen, J. A. The effect of poly-L-lactic acid with parallel surface micro groove on osteoblast-like cells in vitro. *Biomaterials* **20**, 1293–1301 (1999).
29. Correia, C. R., Sher, P., Reis, R. L. & Mano, J. F. Liquified chitosan–alginate multilayer capsules incorporating poly(l-lactic acid) microparticles as cell carriers. *Soft Matter* **9**, 2125–2130 (2013).
30. Oliveira, M. B. & Mano, J. F. Polymer-based microparticles in tissue engineering and regenerative medicine. *Biotechnol. Prog.* **27**, 897–912 (2011).
31. Neto, A. I. *et al.* Fabrication of Hydrogel Particles of Defined Shapes Using Superhydrophobic-Hydrophilic Micropatterns. *Adv. Mater.* **28**, 7613–7619 (2016).
32. Langenbach, F. & Handschel, J. Effects of dexamethasone, ascorbic acid and β-glycerophosphate on the osteogenic differentiation of stem cells in vitro. *Stem Cell Res. Ther.* **4**, 117 (2013).
33. Shi, X. *et al.* Directing Osteogenesis of Stem Cells with Drug-Laden, Polymer-Microsphere-Based Micropatterns Generated by Teflon Microfluidic Chips. *Adv. Funct. Mater.* **22**, 3799–3807 (2012).
34. Yang, Y. *et al.* Regulation of mesenchymal stem cell functions by micro–nano hybrid patterned surfaces. *J. Mater. Chem. B* **6**, 5424–5434 (2018).

Supplementary Information

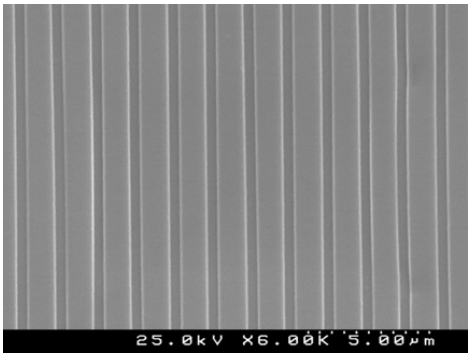

Figure V.S1. SEM image of topography of the used optical media substrate (CD).

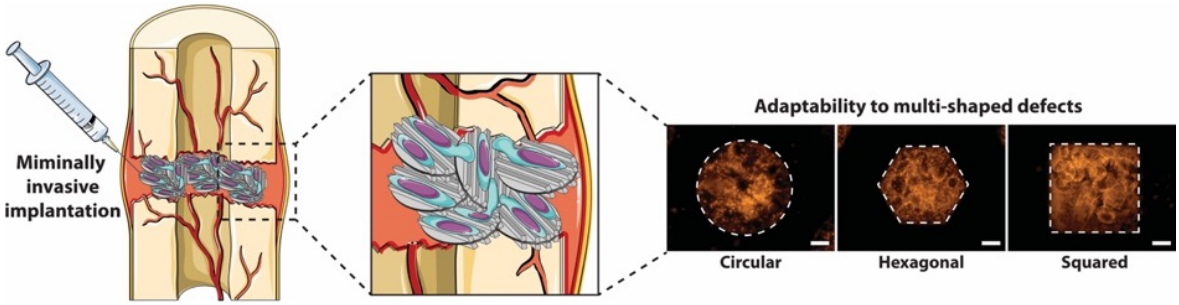

Figure V.S2. Schematic representation of the potential of topodiscs as injectable cell-carriers for bone regeneration upon fracture due to their adaptability to multi-shaped defects. Right: topodisc-cell aggregates acquire the shape of 2D patterned regions with circular, hexagonal, and squared geometries. Scale bars correspond to 200 µm.

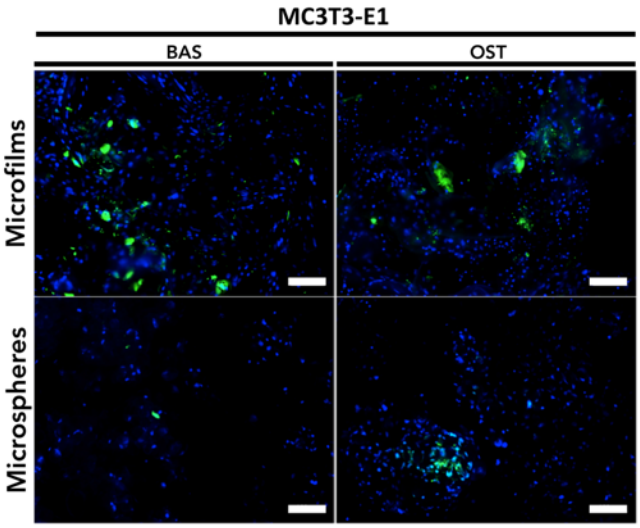

Figure V.S3. Hydroxyapatite staining in MC3T3-E1 cell line and µsphere or topodisc aggregates. Fluorescence images of MC3T3-E1 cells seeded on topodiscs and µspheres after 21 days of culture in basal (BAS) or osteogenic (OST) medium. Hydroxyapatite stained in green, whilst cell nuclei are stained in blue (DAPI). Scale bars correspond to 100 µm.

Chapter VI: Bioengineered hierarchical bone-like compartmentalized microconstructs using nanogrooved microdiscs[5]

Abstract

Fabrication of vascularized large-scale constructs for regenerative medicine remains elusive, since most strategies rely solely on cell self-organization or overly control cell positioning, failing to address nutrient diffusion limitations. We propose a modular and hierarchical tissue engineering strategy to produce bone-like tissues carrying signals to promote pre-vascularization. In these 3D systems, disc-shaped microcarriers featuring nanogrooved topographical cues guide cell behavior by harnessing mechanotransduction mechanisms. A sequential seeding strategy of adipose-derived stromal cells and endothelial cells is implemented within compartmentalized, liquefied-core macrocapsules in a self-organizing and dynamic system. Importantly, our system autonomously promotes osteogenesis and construct's mineralisation, while upregulating key proteins for the establishment of vascularization, as showed by proteomics analysis. Given its modular and self-organizing nature, our strategy may be applied for the fabrication of larger constructs with a highly controlled starting point, to be used for local regeneration upon implantation or as drug screening platforms.

[5] Based on the publication: I.M. Bjørge, B.M. de Sousa, S.G. Patrício, A.S. Silva, L.P. Nogueira, L.F. Santos, S.I. Vieira, H.J. Haugen, C.R. Correia, J.F. Mano. Bioengineered hierarchical bone-like compartmentalized microconstructs using nanogrooved microdiscs, *submitted*.

1. Introduction

Bottom-up tissue engineering strategies, with their possibility to combine heterogeneous building blocks into functional larger units, have an advantage over top-down strategies.[1] Building blocks may span various dimensions to recapitulate the hierarchical nature of tissues and be comprised of distinct elements.[2,3] The assembly of cell encapsulating micron-sized hydrogels,[4] cell anchorage platforms,[5] or a combination of both,[6,7] have shown promising results. Nevertheless, to step back from "over-engineering" it is necessary to approach each unit as an opportunity to deliver appropriate cues to drive cell behavior.[8] Furthermore, finding the right balance between guiding and constraining cell self-organization remains a challenge in the field. While cells possess an inherent capacity to form higher-order constructs, external guidance is crucial for developing functional characteristics.[9] For instance, a strategy aiming to guide tissue morphogenesis was recently proposed, where stem cells and organoids were allowed to spontaneously fuse and self-organize according to geometrical constraints generated by 3D printing.[10]

Topography poises itself as an ideal approach to modulate cell behavior. Cells sense subcellular changes in their local extracellular matrix (ECM) via integrin-mediated adhesions.[11] Through mechanotransduction, such physical cues are translated intracellularly into biochemical signals.[12] For instance, grooved surface topography has a proven track record in directing the differentiation of mesenchymal stem/stromal cells towards osteogenic,[13] adipogenic,[14] myogenic,[15] and chondrogenic lineages.[16] However, studies applying such nano- and micro-scale topographies are generally limited to a 2D approach, where cells are not fully engaged.

In the present study, we propose a highly controlled strategy to engineer bone-like microtissues from the nano to macro level. Using a bottom-up approach, we enable cell self-organization while delivering the appropriate topographical cues to guide cell orientation. This strategy hinges on the combination of surface nanogrooved microdiscs ('topodiscs') with human adipose-derived stromal cells (hASCs) to form living, micrometric supports for human umbilical cord-derived endothelial cells (HUVECs) anchoring. Such bioinspired nano-to-macro environment composes the core of liquefied capsules, cultured under dynamic conditions. At the nanoscale, topodiscs may deliver physical cues to hASCs, induce

cell alignment, and initiate mechanotransduction pathways.[17] Furthermore, they act as substrates to enable a bottom-up hASC-mediated assembly into micron-sized 3D constructs, the microaggregates. These living microaggregates are contained within the liquid core of multi-layered capsules, where they act as adhesion sites for HUVECs, enabling cell self-organization.[18–20] When subject to dynamic culturing in a spinner flask, each individual capsule functions as a microbioreactor. Ultimately, we anticipate capsule bursting to release the core contents of several capsules, further continuing the cell self-organization process that culminates in hybrid tissue-engineered macrostructures. The contribution and organization of the building blocks composing such structures is schematically represented in Figure VI.1.

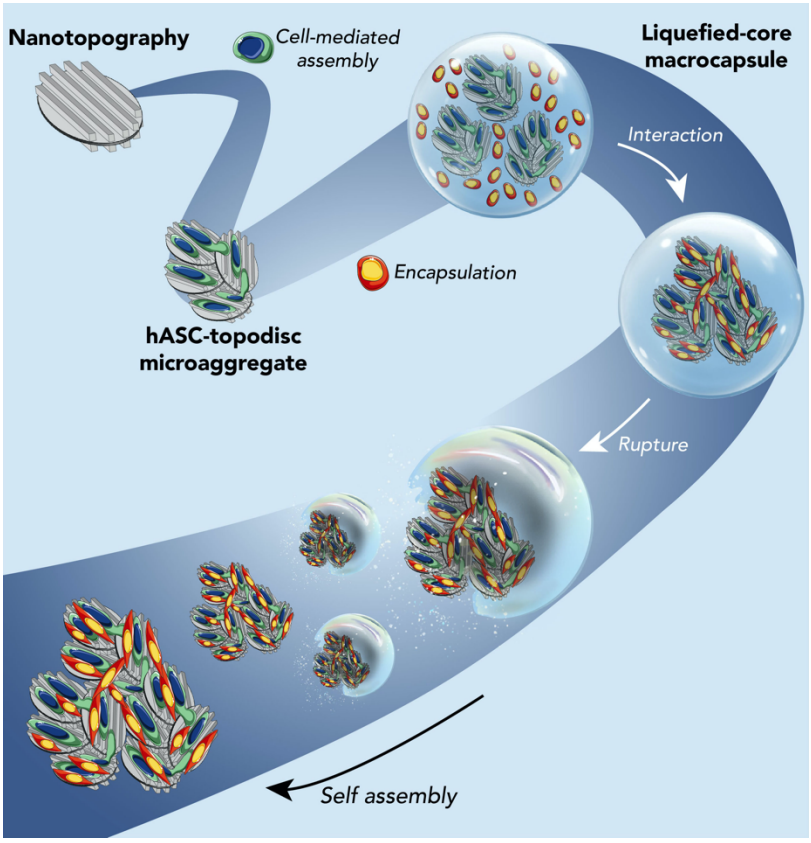

Figure VI.1. Schematic representation of the envisioned modular and hierarchical strategy to produce pre-vascularized, bone-like constructs. Nanogrooved microdiscs (topodiscs) interact with cells at the nanoscale level and are assembled into microaggregates containing various cells and particles, by cell-mediated action. Microaggregates of hASC-topodisc are placed in contact with suspended endothelial cells and compartmentalized within macrocapsules, whose core is further liquefied, promoting endothelial cell adhesion to living microaggregates. For initial culturing periods, the interaction of capsule core contents is promoted, leading to the formation of larger constructs. Upon prolonged culture, these capsules may rupture, and the core contents of several capsules become free to interact and create larger mineralized tissues interweaved with endothelial cells.

2. Results

2.1. Encapsulation of hASC-particles microaggregates with HUVECs

Nanogrooved microdiscs ('topodiscs') were successfully produced according to a method previously developed by the authors.[21] Topodiscs were characterized by a nanogrooved surface topography and a high surface area to volume ratio, delivering physical cues that induce cell alignment across a large cell adhesion area (Figure VI.2A). The average length and width of topodiscs was 92 ± 20 μm and 55 ± 19 μm, respectively (Figure VI.S2A). Regarding the dimensions of topographical features, ridges corresponded to 944 ± 49 nm, grooves were 358 ± 23 nm, and ridge height was 201 ± 45 nm. μSpheres with diameters of 50-80 μm were used as control due to the lack of surface grooves and similar surface area per particle to topodiscs (Figure VI.S1C). Notably, when leaning towards the upper diameter range, these μspheres presented a flattened and less spherical morphology, likely due to collapsing upon production (Figure VI.2B). Hence, they are good controls for the main variable to test in this study, nanogrooved topography.

The manufacturer's protocol for spheroid production using AggreWell400 plates was adapted to fabricate microaggregates composed of hASC with microparticles, namely topodiscs or μspheres. Upon 24h in culture in the plates, homogeneous microaggregates were retrieved and characterized (Figure VI.2C). The longest diameter average obtained was 205 ± 24 μm for μsphere microaggregates and 209 ± 29 μm for topodisc microaggregates, while circularity was 0.99 ± 0.01 and 0.97 ± 0.04, respectively (Figure VI.2D). Produced microaggregates were hence relatively similar in size and shape for both types of microparticles. The previously established protocol to produce liquefied-core capsules was employed to precisely compartmentalize core contents (Figure VI.2E).[18–20] For co-culture conditions, freely dispersed HUVECs were added within the capsule core at a 1:1 ratio with hASCs. Upon encapsulation within multilayered capsules and core liquefaction, a homogenous distribution of microaggregates (and HUVECs, for co-culture) could be observed within each capsule, for each condition (Figure VI.2E- day 0).

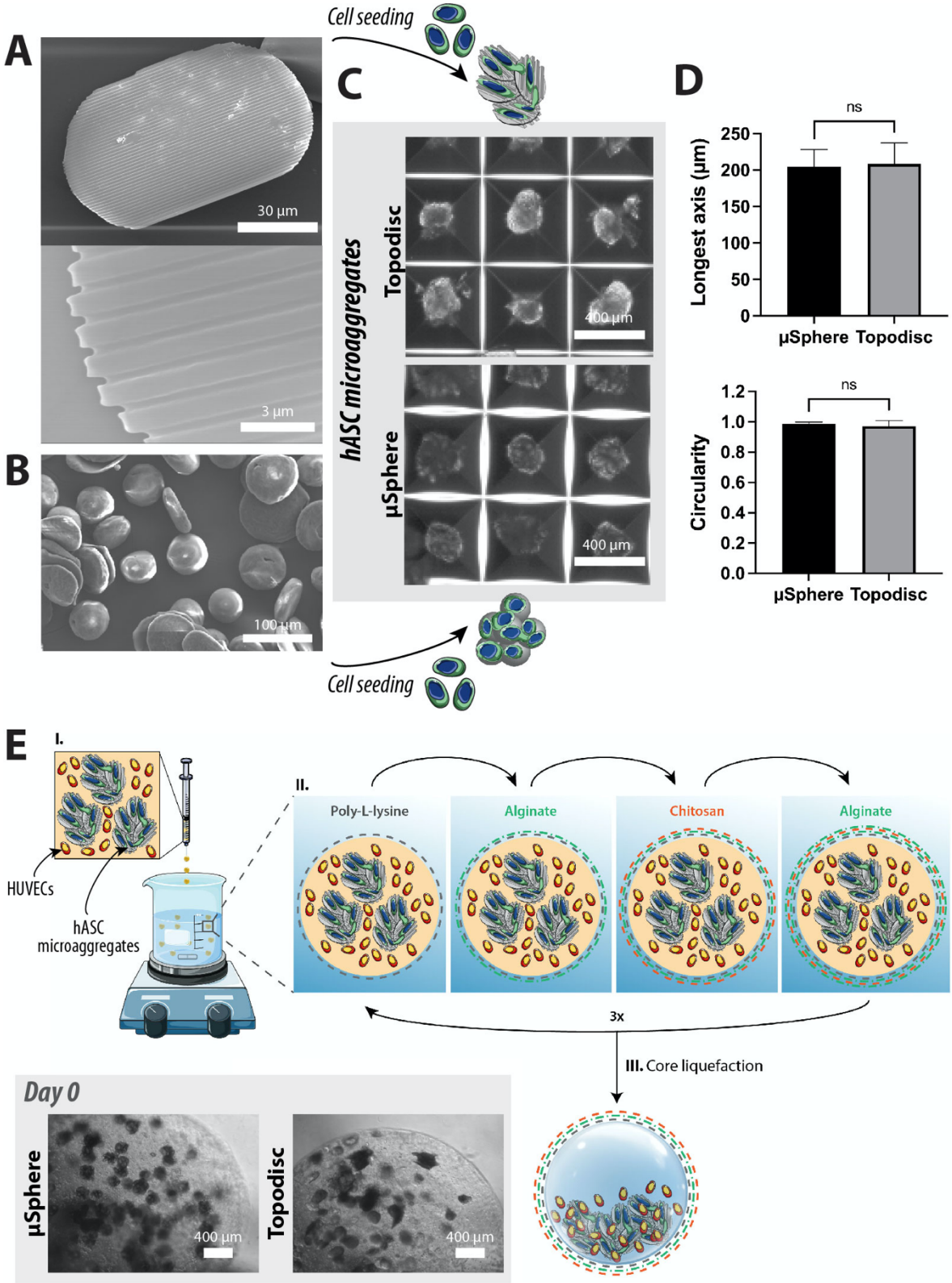

Figure VI.2. Particle populations (µspheres and topodiscs) sustain formation of homogeneous cell-mediated microaggregates, that are successfully encapsulated within liquefied-core capsules. A. SEM image of µspheres. B. SEM images of topodiscs. C. Brightfield image of microaggregates composed of hASCs and topodiscs or µspheres upon 24h within AggreWell400 plates. D. Characterization of microaggregates

concerning longest axis (μm) and circularity for each type of microparticle. E. Schematic representation of liquified-core, multi-layered capsule: *I.* Dropwise addition of ALG solution containing solely microaggregates (hASC-topodisc or hASC-μsphere) or combined with suspended HUVECs into an aqueous calcium chloride solution. *II*. ALG bead collection and sequential immersion in PLL, ALG, CHT, and ALG solutions to obtain a 12-layered membrane. *III.* ALG core liquefaction with EDTA. Brightfield image of capsules containing hASC microaggregates (topodiscs or μspheres) and HUVECs on encapsulation day (day 0).

2.2. HUVECs interact with hASC-particles microaggregates

The liquefied core of the multi-layered capsules enabled free movement of the core components and promoted the interaction between hASC-particle microaggregates and HUVECs. To track this interaction, hASCs and HUVECs were stained with lipophilic dyes in red and green, respectively, prior to microaggregates' formation and encapsulation. Core contents were imaged on days 1 and 7 post-encapsulation. On day 1 in static culturing, a clear separation of HUVECs and hASCs, with a more peripheral HUVEC localization, could be generally observed for both conditions, although slightly more evident for μpsheres. Dynamic culturing in turn led to a greater interaction of HUVECs and hASCs, for both types of particles, evidenced by a more significant number of dispersed green HUVECs between red hASCs, particularly on day 7 (Figure VI.3). In fact, in contrast to day 1, aggregates on day 7 presented a greater incorporation of HUVECs. Starker differences were observed at lower magnification at this time point, where dynamic conditions contributed to the formation of larger aggregates, generally combining most of the core contents of a single capsule, whereas static conditions promoted the conservation of smaller aggregates (Figure VI.3, brightfield).

The main differences here observed (Figure VI.3) may thus be attributed to static versus dynamic culturing and time in culture, although we cannot dismiss some cell-cell interaction effect of the particles' morphology in the case of 1 day in culture under static conditions. Of note, although the HUVEC population may slightly decrease from day 1 to day 7, cells remained viable for up to 21 days in all conditions (Figure VI.S3).

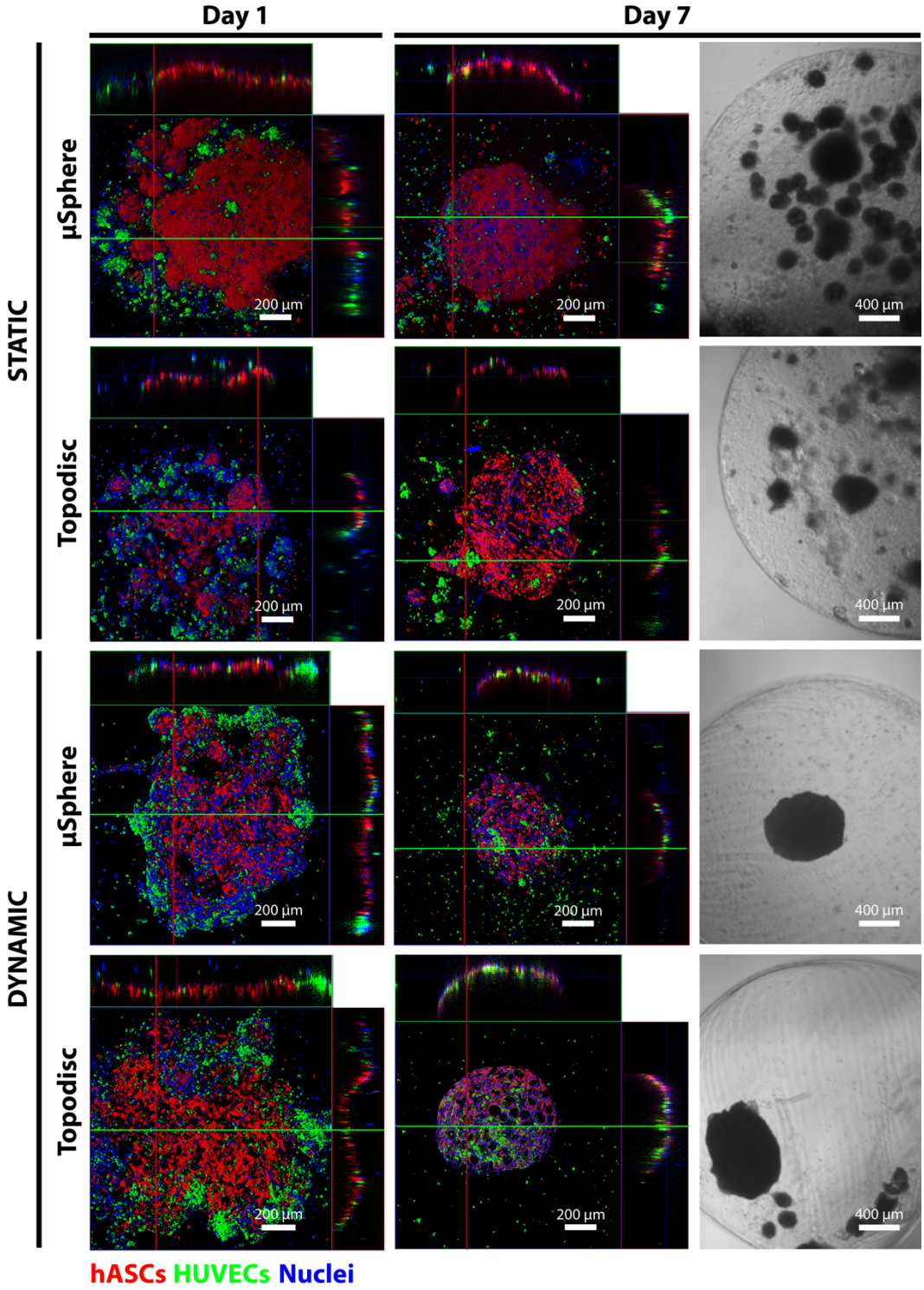

Figure VI.3. HUVECs interact and adhere to hASC-particle microaggregates (topodiscs and µspheres), forming larger aggregates, particularly under dynamic conditions. Left and center: Tracking of HUVECs (green) and hASCs (red), pre-stained with lipophilic dyes, at day 1 and day 7 post-encapsulation, under static and dynamic culturing, using confocal microscopy. Corresponding projections along the *x* and *y*-axis are shown. Right: brightfield images for samples at day 7.

2.3. Bone-like microtissues are formed with potential for pre-vascularization

Upon establishing the successful production of microaggregates composed of hASCs and particles (topodiscs or μpsheres), as well as their capability to sustain HUVEC adhesion and proliferation, we sought to analyze the impact of particles' surface topography on osteogenic differentiation and pre-vascularization, upon 21 days in culture. Furthermore, we aimed to determine the impact of static versus dynamic culturing in such a system.

Native bone is composed of hydroxyapatite-reinforced collagen type I fibrils.[22] When staining for hydroxyapatite, grooved topography appeared as a determinant factor for the static monoculture condition consisting solely of encapsulated hASC microaggregates ('MONO' in 'BAS' medium). In this condition, hydroxyapatite was visible even in the absence of osteogenic factors, while in the absence of grooves, namely the μsphere condition, osteogenic factors were required to induce hydroxyapatite deposition (Figure VI.4A). For the hASC and HUVEC co-culture conditions, the contact-dependent juxtracrine signaling and release of bioactive molecules between the two cell populations (paracrine signaling), appeared to be the determinant factor for hydroxyapatite deposition, overriding surface topography (Figure VI.4A). This was evidenced by the presence of hydroxyapatite in samples of co-cultures with μspheres without osteogenic factors, even in static conditions. In fact, when cultured with microdiscs without grooves (flat microdiscs), an identical trend was observed to that of μspheres (Figure VI.S4). In line with these results, a good expression of the late osteogenic marker osteopontin was observed for co-culture conditions under dynamic culturing, using either μspheres or topodiscs, and regardless of the presence or absence of osteogenic factors (Figure VI.S5).

Subsequently, we aimed to unveil the influence of the substrate topography on the content and structural organization of the enriched collagen matrix for co-culture conditions in basal medium. To this end, Masson's Trichrome was applied to stain collagen in blue for each sample. Furthermore, ATR-FTIR spectra within the amide I region were deconvoluted in well-established secondary structure components previously described for different collagen forms, particularly three main absorption bands centered at 1653, 1645 and 1637 cm^{-1}, assigned to α-helix, unordered structure (random coils) and triple helix (also known as

tropocollagen), respectively. Additional absorption bands, related to β-turns and β-sheet conformers, were also detected (Figure VI.4B and Figure VI.4C, Table VI.S1).[23–26]

Under static culturing conditions, the ATR-FTIR deconvoluted band at the amide I region of co-cultures with μsphere capsules exhibited a main band centered at 1643 cm^{-1}, which revealed unordered conformations as the dominant secondary structure of the secreted extracellular matrix (ca. 36%), when compared to triple helix at 1632 cm^{-1} (ca. 18%) and α-helix at 1653 cm^{-1} (ca. 17%). Under the same conditions, topodisc systems increased triple and α-helix relative contents up to 20% and 23%, respectively, with a concomitant decrease in the disordered structure contribution (from 36% in μspheres to 28% in topodiscs). Indeed, the total estimate contribution of the typical prime secondary structures of collagen molecules[27] – triple- and α-helices – was ca. 42%, higher than that of the unordered structures (ca. 28%). For μsphere systems, the sum of the triple- and α-helix contributions (ca. 35%) was close to the disordered secondary structures one (ca. 36%) (Figure VI.4B and Figure VI.4C). Collagen staining was also markedly different for both particle populations, with an evident collagen staining for topodiscs versus no staining for μspheres (Figure VI.4B). These findings highlight the impact of nanogrooved topography as a preponderant factor on triple collagen molecules' structural organization, under static conditions.

Under dynamic conditions, a different contour of the amide I band was found for both μsphere and topodisc biosystems. Spectral features were similar to those observed for native collagen type I,[27] thus suggesting a change in contents of the secreted collagen secondary structures. Indeed, the dynamic stimulus clearly led to a drastic decrease in disordered structures and the prominence of triple and α-helix contributions for both μsphere and topodisc conditions (Figure VI.4B). Additionally, the content of β-sheets, a more spacious and complex type of collagen secondary structure, is ca. 8 to 10% higher than in static conditions. However, an effect of the grooved topography alone could still be observed under dynamic conditions: a slightly decrease in the unordered structures (from 13% in μsphere to 11% in topodiscs) accompanied by an increase in the sum of triple- and α-helices contributions (from 43% in μsphere to 50% in topodiscs) (Figure VI.4C). Collagen staining confirmed these differences, with an enriched collagen presence for topodisc conditions, and a more sparse collagen staining for μspheres (Figure VI.4B).

MicroCT enabled the acquisition of 3D reconstructions and 2D projections of the larger hASCs-HUVECs co-culture constructs with topodiscs or μspheres, formed upon 21 days in dynamic cultures with osteogenic medium. Varying grey tones were indicative of a differential X-ray absorption and distinct mass density of microparticles, collagen, and hydroxyapatite. This difference in absorption was clearly noted for the topodiscs condition, with particles located in darker regions and the tissue evidenced in lighter shades (2D projection). Interestingly, the μsphere condition did not present such a clear distinction within these two regions (Figure VI.4D). As observed in Figure VI.4D, the deposited matrix appeared denser for topodisc conditions as opposed to μsphere conditions, which may cause such a difference.

To assess constructs' vascularization potential, staining for endothelial cell-specific markers and basement membrane proteins was performed for constructs grown under dynamic co-culture conditions in basal medium, 21 days post-encapsulation. Both CD31 and podocalyxin were detected, homogenously distributed throughout the entire samples (Figure VI.4E), which corroborated the successful integration of endothelial cells, observed at initial timepoints (Figure VI.2, day 7), further up to 21 days. Laminins were consistently found in both topodisc and μsphere conditions, coincident with podocalyxin. Von Willebrand factor (vWF) presented a dotted staining in both conditions, but its staining appeared slightly enhanced in the topodisc condition, where it could be found co-localizing with F-actin in denser regions (Figure VI.4E).

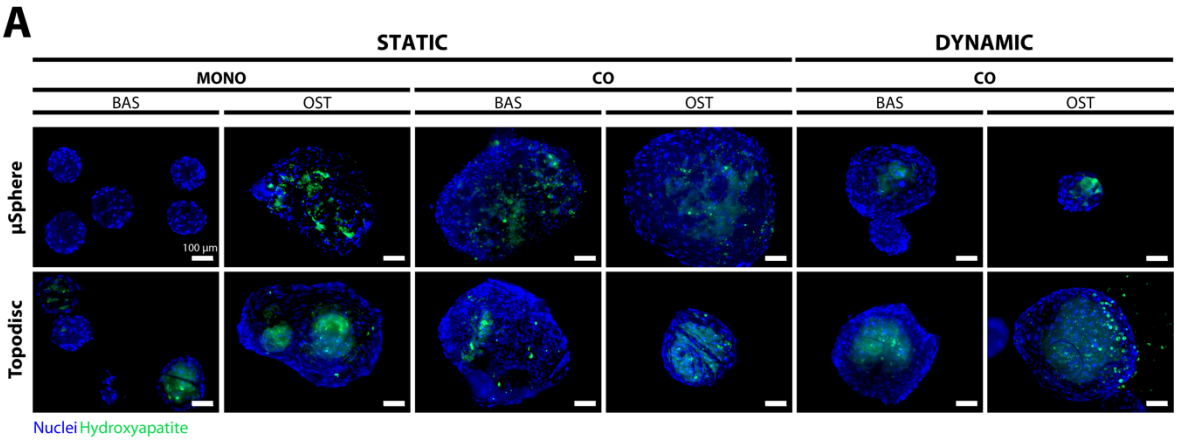
A
STATIC
DYNAMIC
MONO
CO
CO
BAS
OST
BAS
OST
BAS
OST
µSphere
Topodisc
100 µm
Nuclei Hydroxyapatite

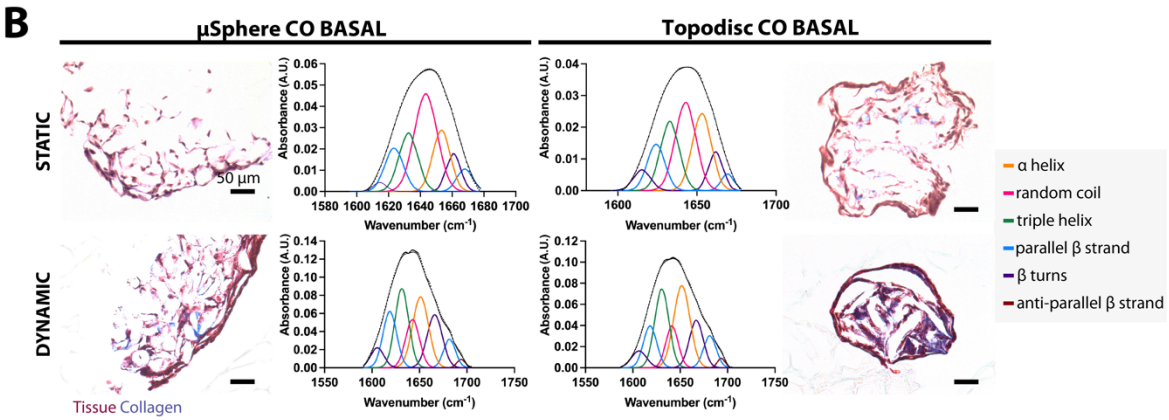
B
µSphere CO BASAL
Topodisc CO BASAL
STATIC
DYNAMIC
50 µm
Absorbance (A.U.)
Wavenumber (cm-1)
α helix
random coil
triple helix
parallel β strand
β turns
anti-parallel β strand
Tissue Collagen

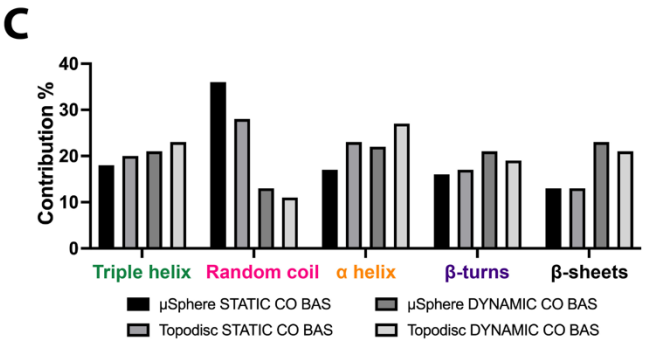
C
Contribution %
Triple helix
Random coil
α helix
β-turns
β-sheets
µSphere STATIC CO BAS
µSphere DYNAMIC CO BAS
Topodisc STATIC CO BAS
Topodisc DYNAMIC CO BAS

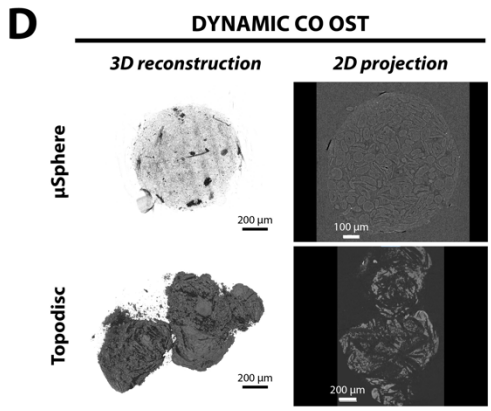
D
DYNAMIC CO OST
3D reconstruction
2D projection
µSphere
Topodisc
200 µm
100 µm

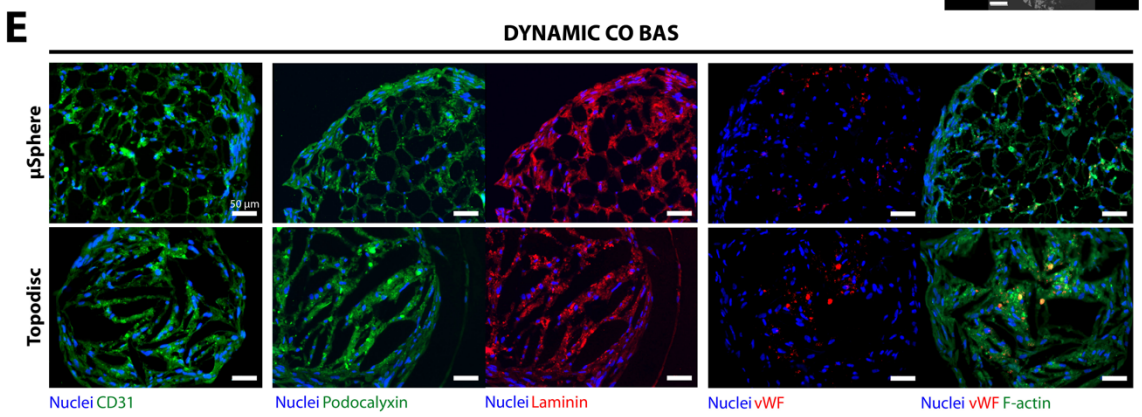
E
DYNAMIC CO BAS
µSphere
Topodisc
50 µm
Nuclei CD31
Nuclei Podocalyxin
Nuclei Laminin
Nuclei vWF
Nuclei vWF F-actin

Figure VI.4. Topography impacts mineralization, collagen structure, and pre-vascularization. A. Fluorescent staining of hydroxyapatite (green) counterstained with nuclei (blue) in dynamic and static environments for monoculture (MONO) and co-culture (CO) conditions, in basal (BAS) and osteogenic (OST) medium, with topodiscs or μspheres. B. Assessment of structural organization of secreted collagen matrix: Masson's Trichrome staining of collagen (purple) and surrounding tissue (red), with the corresponding deconvolution of ATR-FTIR spectra within the amide I region (absorbance in arbitrary units, A.U.). C. Contribution (%) of leading absorption bands assigned to triple helix, random coil, α-helix, β-turns, and β-sheets, for each dynamic versus static culturing of μsphere and topodisc CO BAS conditions. D. Microtomography (microCT) 3D reconstructions and 2D projections for topodisc and μsphere conditions in dynamic CO OST. E. Immunohistochemistry staining of CD31 (green), podocalyxin (green), laminin (red), von Willebrand Factor (vWF, red), and actin filaments (F-actin, green), counterstained with nuclei (blue).

2.4. Topography induces proteomic changes in cells-released extracellular microvesicles

Extracellular microvesicles (MV) play a role in intercellular communication and can be exploited for tissue engineering.[28,29] Given the role of MVs in the initialization of mineralization nuclei[30] and angiogenesis,[31] the protein content of extracellular MVs secreted by hASC and HUVEC co-cultures was assessed. Proteomic analyses were performed on MVs isolated from dynamic co-cultures, using μspheres or topodiscs, in basal (BAS) or osteogenic (OST) media, from day 7 to day 21 in culture. A total of 1711 proteins was identified, 538 of which with 2 or more unique peptides and high confidence false discovery rate (FDR<0.01), that were selected for further analysis. This selected dataset comprised several proteins previously identified in osteoblast-released MVs (Table VI.S2).[32,33] Of the 538 proteins set, 454 and 531 proteins appeared in the topodisc BAS and OST conditions, respectively, while 528 and 485 proteins appeared in the μsphere BAS and OST conditions, respectively (Data VI.S1). To focus on proteomic changes induced by topography, the presence/absence and abundance of MV proteins were compared in topodisc versus μsphere conditions.

In BAS medium, 44 proteins were upregulated in topodiscs condition, when compared to μspheres condition (UReg-TopoBAS, Table VI.S3), while 84 where downregulated (DReg-TopoBAS, Table VI.S4). Gene Ontology (GO) analysis revealed that the 44 UReg-TopoBAS were enriched in GO terms related to actin-binding and nucleotide biosynthetic processes, suggesting promotion of cell proliferation and cell morphology remodeling (Figure VI.5A). Accordingly, Reactome identified as most relevant, pathways related to cell cycle checkpoints, mitotic transitions, metabolism, and signal transduction (including Wnt signaling and negative regulation of Notch4 signaling) (Figure VI.5B). The 84 DReg-

TopoBAS were enriched in GO terms related to plasma membrane organization, protein modification, and positive regulation of apoptotic signaling (Figure VI.5A), with protein translation being the most relevant downregulated pathways (Figure VI.5C). These suggest that plasma membranes were less stable and more plastic, that there was a decrease in non-osteogenic differentiation and, importantly, decreased apoptosis.

In OST medium, 66 proteins were upregulated (UReg-TopoOST, Table VI.S5) in topodisc conditions, while 36 were downregulated (DReg-TopoOST, Table VI.S6), when compared to μspheres condition. The 66 UReg-TopoOST proteins were enriched in GO terms related again to metabolic processes, but also to ion binding and ubiquitin protein ligase binding (Figure VI.5D). Most relevant pathways included again cell cycle checkpoints, mitotic transitions, and signal transduction (again Wnt signaling and negative regulation of Notch4 signaling, besides absence of Hedgehog signaling) (Figure VI.5E). The 36 DReg-TopoOST were enriched in GO terms related to protease binding, cell-substrate adhesion, cell-matrix adhesion, and actin-binding (Figure VI.5D). Cell-cell communication and extracellular matrix organization, besides transcription and post-translational modifications were the most relevant pathways involving downregulated proteins (Figure VI.5F). These suggest that in osteogenic media, cells grown on topodiscs are even more prone to differentiate, and preferentially include in their MVs signals driving differentiation over those driving adhesion. As a result, cell membranes are more plastic and, in this way, facilitate differentiation, as seen before for other cells.[34]

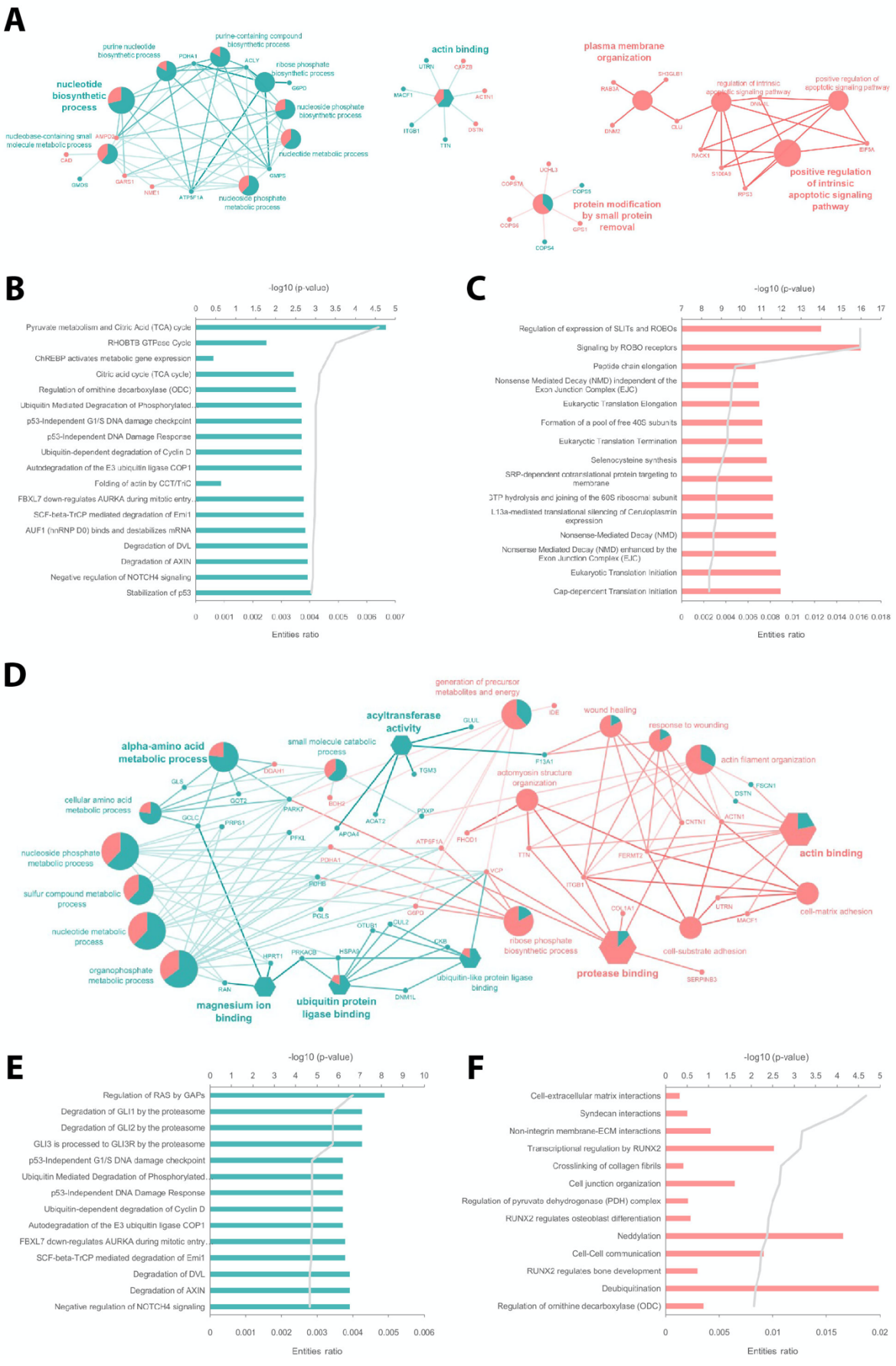
A
nucleotide biosynthetic process
purine nucleotide biosynthetic process
purine-containing compound biosynthetic process
ribose phosphate biosynthetic process
nucleoside phosphate biosynthetic process
nucleotide metabolic process
nucleoside phosphate metabolic process
nucleobase-containing small molecule metabolic process
actin binding
plasma membrane organization
regulation of intrinsic apoptotic signaling pathway
positive regulation of apoptotic signaling pathway
positive regulation of intrinsic apoptotic signaling pathway
protein modification by small protein removal
B
-log10 (p-value)
Pyruvate metabolism and Citric Acid (TCA) cycle
RHOBTB GTPase Cycle
ChREBP activates metabolic gene expression
Citric acid cycle (TCA cycle)
Regulation of ornithine decarboxylase (ODC)
Ubiquitin Mediated Degradation of Phosphorylated...
p53-Independent G1/S DNA damage checkpoint
p53-Independent DNA Damage Response
Ubiquitin-dependent degradation of Cyclin D
Autodegradation of the E3 ubiquitin ligase COP1
Folding of actin by CCT/TriC
FBXL7 down-regulates AURKA during mitotic entry...
SCF-beta-TrCP mediated degradation of Emi1
AUF1 (hnRNP D0) binds and destabilizes mRNA
Degradation of DVL
Degradation of AXIN
Negative regulation of NOTCH4 signaling
Stabilization of p53
Entities ratio
C
-log10 (p-value)
Regulation of expression of SLITs and ROBOs
Signaling by ROBO receptors
Peptide chain elongation
Nonsense Mediated Decay (NMD) independent of the Exon Junction Complex (EJC)
Eukaryotic Translation Elongation
Formation of a pool of free 40S subunits
Eukaryotic Translation Termination
Selenocysteine synthesis
SRP-dependent cotranslational protein targeting to membrane
GTP hydrolysis and joining of the 60S ribosomal subunit
L13a-mediated translational silencing of Ceruloplasmin expression
Nonsense-Mediated Decay (NMD)
Nonsense Mediated Decay (NMD) enhanced by the Exon Junction Complex (EJC)
Eukaryotic Translation Initiation
Cap-dependent Translation Initiation
Entites ratio
D
alpha-amino acid metabolic process
cellular amino acid metabolic process
nucleoside phosphate metabolic process
sulfur compound metabolic process
nucleotide metabolic process
organophosphate metabolic process
small molecule catabolic process
acyltransferase activity
generation of precursor metabolites and energy
wound healing
response to wounding
actin filament organization
actomyosin structure organization
actin binding
cell-matrix adhesion
cell-substrate adhesion
protease binding
ribose phosphate biosynthetic process
ubiquitin-like protein ligase binding
magnesium ion binding
ubiquitin protein ligase binding
E
-log10 (p-value)
Regulation of RAS by GAPs
Degradation of GLI1 by the proteasome
Degradation of GLI2 by the proteasome
GLI3 is processed to GLI3R by the proteasome
p53-Independent G1/S DNA damage checkpoint
Ubiquitin Mediated Degradation of Phosphorylated...
p53-Independent DNA Damage Response
Ubiquitin-dependent degradation of Cyclin D
Autodegradation of the E3 ubiquitin ligase COP1
FBXL7 down-regulates AURKA during mitotic entry...
SCF-beta-TrCP mediated degradation of Emi1
Degradation of DVL
Degradation of AXIN
Negative regulation of NOTCH4 signaling
Entities ratio
F
-log10 (p-value)
Cell-extracellular matrix interactions
Syndecan interactions
Non-integrin membrane-ECM interactions
Transcriptional regulation by RUNX2
Crosslinking of collagen fibrils
Cell junction organization
Regulation of pyruvate dehydrogenase (PDH) complex
RUNX2 regulates osteoblast differentiation
Neddylation
Cell-Cell communication
RUNX2 regulates bone development
Deubiquitination
Regulation of ornithine decarboxylase (ODC)
Entities ratio

Figure VI.5. Topodiscs topography induces changes in the proteome of microvesicles (MV) released by co-cultured cells. A. ClueGo analysis of proteins upregulated (UReg-TopoBAS) and downregulated (DReg-TopoBAS) by topography (topodiscs-to-µsphere relative abundances ratios) in basal (BAS) medium. B. Significant relevant pathways where UReg-TopoBAS proteins intervene. C. Significant relevant pathways where DReg-TopoBAS proteins intervene. D. ClueGo analysis of proteins upregulated (UReg-TopoOST) and downregulated (DReg-TopoOST) by topography (topodiscs-to-µsphere relative abundances ratios) in osteogenic (OST) medium. E. Significant relevant pathways where UReg-TopoOST proteins intervene. F. Significant relevant pathways where DReg-TopoOST proteins intervene. Functionally grouped networks in 'A' and 'D' represent Biological Process (BP) and Molecular Function (MF) terms as circular and hexagonal nodes, respectively. Terms are linked based on their kappa score level (>0.4). The node size represents the term enrichment significance. Each node shows the % of UReg and Dreg proteins per term has a 'pie-chart'. UReg and DReg proteins and related terms/pathways are in blueish and reddish colors, respectively. The bar length refers to the 'entities ratio', i.e., the number of proteins from each dataset that belong to the pathway divided by total number of *Homo sapiens* proteins known to belong to the pathway. Grey lines represent the -log10 (p-value), where the p-value represents the probability that the overlap between each dataset and the pathway has occurred by chance.

3. Discussion

Cells possess an inherent ability to self-organize, which can, and should, be harnessed to achieve functional histoarchitectures. Guiding cell organization into 3D hierarchical structures while delivering the appropriate cues appears an option to achieve self-driven morphogenesis.[8] Of note, the inclusion of endothelial cells in these systems and construct pre-vascularization have been identified as essential requirements to improve vascularization and overall tissue survival upon transplantation.[35–37] It is particularly challenging due to the tissue thickness limit of 100-200 µm to guarantee appropriate oxygen and nutrient supply.

Our strategy hinged on a nano-to-macro bottom-up strategy to develop bone-like 3D constructs with pre-vascularization potential. The basis of our approach relied on microdiscs with nanogrooved surface topography (topodiscs), a "low-material" strategy, designed to modulate cell behavior using physical surface cues.[8,21] Via a cell-mediated assembly, such particles gave rise to hASC microaggregates with diameters of approximately 200 µm, in line with tissue thickness limits. The macro component of our system hinged on previously reported liquefied-core multilayered capsules.[18–20] Within the compartmentalized liquefied core, hASC-topodisc microaggregates were placed in contact with suspended HUVECs, promoting HUVEC adhesion to existing living microaggregates. Dynamic culturing in easily accessible spinner flasks, possible due to the liquefied core of the capsules, turns each capsule into a microbioreactor, enabling the introduction of shear stress, an important aspect for endothelial cell sprouting and stabilization of cell-cell junctions.[38,39] For initial culturing

periods, dynamic conditions promote the interaction of capsule core contents, namely hASC-particle microaggregates and HUVECs, leading to the formation of larger constructs. Upon prolonged culture, capsules rupture and the core contents of several capsules are free to interact and create larger mineralized tissues interweaved with endothelial cells.

Produced topodiscs presented a discoidal geometry with a homogeneous surface topography. The use of μspheres, ranging between 50 and 80 μm in diameter, as a control particle with flat surface topography, presented two main advantages. The first related to their equivalent surface area per particle with regards to topodiscs. The second derived from the collapsing of particles, probably during production, that render them less spherical and more flattened, similar in morphology to flat microdiscs (Figure VI.S3). Total particle content per condition was normalized by weight, enabling a similar surface area per particle for both types of particles (Figure VI.S1C) and achieving hASC-particle microaggregates with equal dimensions (Figure VI.2D).

Upon encapsulation, cells remained viable up to 21 days in the mono and co-culture system (Figure VI.S3). Previously, a low adhesion of HUVECs to micro-objects has been reported, improved by co-culture with hMSCs, and hence hMSCs have been described as the driving force for compaction and remodeling.[40] Our strategy, using living microaggregates, also resulted in a similar outcome, with hASC microaggregates interacting in a good extension with HUVECs, which maintained in culture for 21 days and evaded anoikis. When comparing hASC and HUVEC localization and aggregation on days 1 and 7, the main differences observed were attributable to static versus dynamic culturing conditions, besides time (Figure 3). The maximized interaction of cells and microparticles under dynamic conditions within smaller scale liquefied-core capsules, as opposed to static culturing, has also been previously described.[26]

Next, we sought to characterize the mineral component and collagen organization, given their importance in native bone.[22] The role of grooved topography in directing osteogenic differentiation in a 2D context has been the focus of several studies.[13,14,41] Initial cell contact has been shown to play a crucial role in modulating cell behavior not only in 2D, as demonstrated in a quasi-3D grooved topography "sandwich" cell culture model.[42] Yet, the consistent use of biochemical factors to induce osteogenesis in many topography-based

studies does not allow to separate the effect of topography from the action of osteogenic factors.[14,43] Furthermore, these approaches lack the 3D element characteristic of the native environment, where cells are fully immersed and stimulated by the extracellular matrix and surrounding cells.

In our 3D culture system, grooved topography was an osteogenic impacting factor in static monoculture conditions since no deposition of hydroxyapatite was observed for μspheres in the absence of osteogenic factors (Figure VI.4A). This trend had been previously observed when comparing topodiscs and μspheres in an aggregation-based study.[21] On the other hand, all hASC and HUVEC co-culture conditions presented staining for hydroxyapatite, regardless of type of particle used or culturing conditions, highlighting the importance of co-culture systems (Figure VI.4A). Co-culturing endothelial cells with osteoprogenitor cells has been previously shown to improve tissue mineralization. Specifically, co-encapsulation within bulk RGD-modified alginate microspheres[44] or within liquefied-core capsules, with spherical microparticles as support, has shown promising results.[18] Furthermore, direct contact between these cell populations is a key factor, as opposed to sole culture with endothelial cell-conditioned media.[45] Inline, junctional communication between vasculogenic and osteogenic cells through connexin 43 has been highlighted as a potent regulator of osteogenesis and angiogenesis.[46,47] Furthermore, a synergistic effect between the use of nanogrooves and co-cultures of HUVECs and hASCs has been proposed. Whereas expression levels of bone morphogenetic protein 2 (BMP-2) and vascular endothelial growth factor (VEGF) were unaltered in 2D grooved versus non-grooved conditions, the expression of connexin 43 was significantly increased for nanogrooves.[48]

In native collagen type I, the secondary structure acquires a sum of triple- and α-helices of 37.1%, with unordered structures as low as 9.3%.[27] In the present study, the presence of topography contributed to the lowering of the percentage of unordered structures and the increase in the sum of triple- and α-helices for both static and dynamic conditions when compared to μsphere conditions (Figure VI.4B, Figure VI.4C). Accordingly, we previously reported that the morphology of the ECM deposited on topodiscs in static conditions was highly organized into fibrillar structures, in contrast to a dense and non-shaped morphology for μspheres.[21] Yet it is to note that dynamic culturing played a crucial role, even more so

than topography, in lowering the percentage of unordered structures to the values of native collagen. Interestingly, dynamic culturing was also shown to play a role in collagen organization in a co-culture of osteoblasts and hASCs.[26] As such, grooved topographical features impacted the lowest hierarchical structure, namely the formation of triple helical collagen molecules, while the dynamic stimulus impacted the supramolecular association of β-sheets into highly ordered collagen microfibrils.

The next step revolved around assessing construct pre-vascularization, focusing solely on the impact of the nanogrooved topography when the systems were cultured under dynamic conditions in the absence of osteogenic factors. Firstly, endothelial cell presence and homogeneous distribution throughout the constructs were confirmed using specific cell markers such as CD31, endothelial cell adhesion molecule, and podocalyxin, endothelial plasma membrane sialoglycoprotein.[49] Of note, endothelial cells appear to acquire a more elongated shape in the topodisc condition, which may be advantageous in later stages of vascularization.[50] Interestingly, vWF, a glycoprotein produced in the cytoplasm of endothelial cells within Weibel-Palade bodies,[51] partially co-localized with denser F-actin regions. This occurred in both particles' conditions, but was more evident in the topodiscs conditions (Figure VI.4E). The impact of grooves on HUVECs' vWF expression in 2D systems is not consistent in the literature. Whereas one study reported an increased vWF expression on grooved surfaces (of 500 nm and 1 μm features) versus flat ones,[52] another study observed no significant differences between 1 μm grooves and flat conditions.[53] In our case, for both topodiscs and μspheres, endothelial cells were shown to deposit laminins, an endothelial basement membrane protein required for endothelial cell reorganization into capillary-like tubes.[54] Lumen formation was not observed and hence we cannot affirm that vascularization occurred, yet the interplay between cells and the deposited ECM may be indicative of pre-vascularization. The delivery of vasculogenic factors or even the inclusion of an additional cell population such as fibroblasts or mural cells could be required.[55]

Given the role of MVs in the initialization of mineralization nuclei[30] and angiogenesis,[31] the protein content of extracellular MVs secreted by hASC and HUVEC co-cultures in dynamic conditions in basal and osteogenic medium, was assessed. Interestingly, grooved topography upregulated metabolic processes, namely nucleotide synthesis, cell cycle checkpoints, mitotic transitions, and ion binding, thus indicating that cell proliferation was promoted.

Additionally, grooved topography upregulated ubiquitin ligase binding, and signaling by Wnt, which are involved with cell differentiation. Indeed, ubiquitin ligases regulate transcription factors and signaling pathways relevant to osteoblast differentiation.[56] Furthermore, topography upregulated Wnt signaling and increased the abundance of proteins known to interact with hydroxyapatite and bind to calcium (Table VI.S2), particularly in the presence of osteogenic factors (OST medium). Of note, topography downregulated Notch4 signaling, an observation common for later stages of MSC osteogenic differentiation.[57] Topography also upregulated proteins related to axin degradation, which may promote osteogenesis since axin belongs to the β-catenin destruction complex that lowers β-catenin nuclear levels and prevents activation of osteogenic Wnt target genes.[58,59] Degradation of Hedgehog downstream effectors (Gli proteins) was also upregulated, linked to ASC osteodifferentiation.[60] Topography also downregulated signals related to apoptosis, protein transcription/translation, membrane stability and adhesion (this last in OST medium). These last are necessary for morphologic alterations occurring in proliferation differentiation cellular proccesses. Downregulation of proteins related to transcription has been previously observed during the osteogenic differentiation of MSC.[61] Taken together, these results point towards the impact of grooved topography in dynamic culturing. While pre-vascularization could not be observed during the experimental timepoints, proteomic data indicates that it may occur later on. Wnt signaling also plays a role in endothelial cell differentiation and stabilization of immature vasculature.[62] Additionally, a higher abundance of collagen type VI, specifically α1, α2, and α3 chains, was promoted by topography when combined with osteogenic factors. Collagen type VI acts as a substrate for cell attachment and interacts directly with collagen type IV, a significant component of endothelial basement membranes.[63]

Overall, our strategy enabled the production of mineralized bone-like micro-units enveloped by endothelial cells actively secreting crucial proteins of the vascular basement membrane. While grooved topography, in the absence of osteogenic factors, was required for the deposition of hydroxyapatite in hASC monoculture static conditions, the main contributor towards tissue mineralization was the co-culture of hASCs with HUVECs and the inherently associated juxtracrine and paracrine signaling. Collagen type I organization was greatly impacted by dynamic culturing and, to a lesser extent, by surface nanogrooved topography,

to achieve an organization similar to native collagen. Furthermore, pathways related to the promotion of osteogenesis were found to be upregulated by topography, under dynamic co-culturing conditions, as well as higher abundances of proteins known to interact with hydroxyapatite. The strategy here presented also enabled an adequate endothelial cell distribution and the deposition of vascular basement membrane proteins, necessary for future pre-vascularization. Here, topography proved to play a minor role.

4. Conclusion

With this study, we propose a three-dimensional, modular, and hierarchical tissue engineering strategy, with tunable and adaptable components. At the core, we have "low material"[8] nanogrooved microdiscs (topodiscs) delivering biophysical cues to cells within liquefied core of macrocapsules, with each capsule functioning as a small-scale bioreactor. We showcase this approach for bone tissue engineering using hASCs and HUVECs, where topographical cues act in synergy with the established cell co-culture under a dynamic environment. The formation of mineralized bone-like micro-units is promoted, which are enveloped by endothelial cells that can potentially foster pre-vascularization. Such a strategy could be employed for alternative tissues, such as cardiac[64] and neuronal,[65] where grooves have been shown to significantly impact on cell fate. Furthermore, additional components may be added to the system, such as the inclusion of mural cells or mural cell precursors, given their importance in vessel stabilization.[66] Due to our strategy's modular and self-organizing nature, we envision its application for the bioengineering of larger constructs with a highly controlled starting point, for local regeneration upon implantation or as advanced drug screening 3D platforms.

5. Experimental procedures

5.1. Resource availability

5.1.1. Lead contact

Further information and requests for resources and reagents should be directed to and will be fulfilled by the lead contact, João F. Mano.

5.1.2. Materials availability

This study did not generate new unique reagents.

5.1.3. Data and code availability

All data reported in this paper and any additional information required to reanalyze the data reported in this paper will be shared by the lead contact upon request is available from the lead contact upon request.

5.2. hASC-topodisc microaggregate production and encapsulation

Topodiscs were produced using a previously established protocol by the authors (Scheme S1).[21] At 90% of confluence, isolated hASCs were detached by 0.05% w/v trypsin-EDTA (from porcine pancreas 1:250, Sigma-Aldrich) treatment for 5 min at 37ºC. hASC-particle (topodiscs or µspheres) microaggregates were produced using AggreWell400 24-well plates (StemCell Technologies), according to the manufacturer's recommendations. A concentration of $6x10^5$ cells and 1.5 mg particles (topodiscs or µspheres) was used per well. Upon 24h of seeding, hASC-particle (topodiscs or µspheres) microaggregates were collected. Pre-formed microaggregates produced for dynamic culturing were subjected to an additional coating with fibronectin from human plasma (5 $\mu g.cm^{-2}$, Sigma Aldrich) dissolved in Dulbecco's phosphate buffered saline (DPBS, Corning) for 1h at 37ºC, followed by washing with DPBS prior to encapsulation. Encapsulation of hASC-particle (topodiscs or µspheres) microaggregates with (co-culture) or without (monoculture) HUVECs was performed within liquefieable-core and multi-layered capsules, which were previously developed by our group.[19,67] Samples were cultured up to 21 days in static versus dynamic conditions, in the absence or presence of osteogenic factors. Further information and characterization methodologies can be found in supplementary information.

Acknowledgments

I. M. Bjørge, B. M. de Sousa, and L. F. Santos acknowledge financial support by the Portuguese Foundation for Science and Technology (FCT) with doctoral grants SFRH/BD/129224/2017, 2020.06525.BD, and SFRH/BD/141523/2018, respectively. S. G. Patrício and A. S. Silva acknowledge the individual contracts 2020.00366.CEECIND and

2020.04344.CEECIND, respectively. This work was supported by the European Research Council grant agreement for the project "ATLAS" (ERC-2014-ADG-669858). This work was financed by national funds (OE) through (FCT/MCTES) in the scope of the projects "TETRISSUE", reference PTDC/BTM-MAT/3201/2020, "CIRCUS", reference PTDC/BTM-MAT/31064/2017, "MIMETIc", reference PTDC/BTM-MAT/31210/2017, and PROMENADE reference PTDC/BTM-MAT/29830/2017, supported, when applicable, by the Programa Operacional Competitividade e Internacionalização, in the component FEDER (POCI-01-0145-FEDER-031064 and POCI-01-0145-FEDER-031210). Mass spectrometry technique was performed at the Proteomics i3S Scientific Platform with the assistance of Hugo Osório. This work had support from the Portuguese Mass Spectrometry Network, integrated in the National Roadmap of Research Infrastructures of Strategic Relevance (ROTEIRO/0028/2013; LISBOA-01-0145-FEDER-022125). Image acquisition was performed in the LiM facility of iBiMED, a node of PPBI (Portuguese Platform of BioImaging): POCI-01-0145-FEDER-022122. This work was developed within the scope of the project CICECO-Aveiro Institute of Materials, UIDB/50011/2020 & UIDP/50011/2020, and iBiMED (UID/BIM/04501/2019), financed by national funds through the FCT/MEC and when appropriate co-financed by FEDER under the PT2020 Partnership Agreement.

References

1. Gaspar, V. M., Lavrador, P., Borges, J., Oliveira, M. B. & Mano, J. F. Advanced Bottom-Up Engineering of Living Architectures. *Adv. Mater.* **32**, 1903975 (2020).
2. Guven, S. *et al.* Multiscale assembly for tissue engineering and regenerative medicine. *Trends Biotechnol.* **33**, 269–279 (2015).
3. Nichol, J. W. & Khademhosseini, A. Modular tissue engineering: Engineering biological tissues from the bottom up. *Soft Matter* **5**, 1312–1319 (2009).
4. Yao, R., Zhang, R., Lin, F. & Luan, J. Injectable cell/hydrogel microspheres induce the formation of fat lobule-like microtissues and vascularized adipose tissue regeneration. *Biofabrication* **4**, 045003 (2012).
5. Leferink, A. *et al.* Engineered micro-objects as scaffolding elements in cellular building blocks for bottom-up tissue engineering approaches. *Adv. Mater.* **26**, 2592–2599 (2014).
6. McGuigan, A. P. & Sefton, M. V. Vascularized organoid engineered by modular assembly enables blood perfusion. *Proc. Natl. Acad. Sci. U. S. A.* **103**, 11461–11466 (2006).
7. Mahou, R., Vlahos, A. E., Shulman, A. & Sefton, M. V. Interpenetrating Alginate-Collagen Polymer Network Microspheres for Modular Tissue Engineering. *ACS Biomater. Sci. Eng.* **4**, 3704–3712 (2018).
8. Correia, C. R., Bjørge, I. M., Nadine, S. & Mano, J. F. Minimalist Tissue Engineering Approaches Using Low Material-Based Bioengineered Systems. *Adv. Healthc. Mater.* **2002110**, 1–18 (2021).

9. Laurent, J. *et al.* Convergence of microengineering and cellular self-organization towards functional tissue manufacturing. *Nat. Biomed. Eng.* **1**, 939–956 (2017).
10. Brassard, J. A., Nikolaev, M., Hübscher, T., Hofer, M. & Lutolf, M. P. Recapitulating macro-scale tissue self-organization through organoid bioprinting. *Nat. Mater.* **20**, 22–29 (2021).
11. Kim, D. & Wirtz, D. Focal adhesion size uniquely predicts cell migration. *FASEB J.* **27**, 1351–1361 (2013).
12. Dupont, S. *et al.* Role of YAP/TAZ in mechanotransduction. *Nature* **474**, 179–183 (2011).
13. Watari, S. *et al.* Modulation of osteogenic differentiation in hMSCs cells by submicron topographically-patterned ridges and grooves. *Biomaterials* **33**, 128–136 (2012).
14. Abagnale, G. *et al.* Surface topography enhances differentiation of mesenchymal stem cells towards osteogenic and adipogenic lineages. *Biomaterials* **61**, 316–326 (2015).
15. Wang, P.-Y., Li, W.-T., Yu, J. & Tsai, W.-B. Modulation of osteogenic, adipogenic and myogenic differentiation of mesenchymal stem cells by submicron grooved topography. *J. Mater. Sci. Mater. Med.* **23**, 3015–3028 (2012).
16. Wu, Y.-N. *et al.* Substrate topography determines the fate of chondrogenesis from human mesenchymal stem cells resulting in specific cartilage phenotype formation. *Nanomedicine Nanotechnology, Biol. Med.* **10**, 1507–1516 (2014).
17. Nikkhah, M., Edalat, F., Manoucheri, S. & Khademhosseini, A. Engineering microscale topographies to control the cell–substrate interface. *Biomaterials* **33**, 5230–5246 (2012).
18. Correia, C. R. *et al.* Semipermeable Capsules Wrapping a Multifunctional and Self-regulated Co-culture Microenvironment for Osteogenic Differentiation. *Sci. Rep.* **6**, 21883 (2016).
19. Correia, C. R., Reis, R. L. & Mano, J. F. Multilayered hierarchical capsules providing cell adhesion sites. *Biomacromolecules* **14**, 743–751 (2013).
20. Correia, C. R., Sher, P., Reis, R. L. & Mano, J. F. Liquified chitosan–alginate multilayer capsules incorporating poly(l-lactic acid) microparticles as cell carriers. *Soft Matter* **9**, 2125–2130 (2013).
21. Bjørge, I. M., Choi, I. S., Correia, C. R. & Mano, J. F. Nanogrooved microdiscs for bottom-up modulation of osteogenic differentiation. *Nanoscale* **11**, 16214–16221 (2019).
22. Fratzl, P., Gupta, H. S., Paschalis, E. P. & Roschger, P. Structure and mechanical quality of the collagen–mineral nano-composite in bone. *J. Mater. Chem.* **14**, 2115–2123 (2004).
23. Noreen, R. *et al.* FTIR spectro-imaging of collagen scaffold formation during glioma tumor development. *Anal. Bioanal. Chem.* **405**, 8729–8736 (2013).
24. Petibois, C., Gouspillou, G., Wehbe, K., Delage, J.-P. & Déléris, G. Analysis of type I and IV collagens by FT-IR spectroscopy and imaging for a molecular investigation of skeletal muscle connective tissue. *Anal. Bioanal. Chem.* **386**, 1961–1966 (2006).
25. Troullier, A., Reinstädler, D., Dupont, Y., Naumann, D. & Forge, V. Transient non-native secondary structures during the refolding of α-lactalbumin detected by infrared spectroscopy. *Nat. Struct. Biol.* **7**, 78–86 (2000).
26. Nadine, S., Patrício, S. G., Correia, C. R. & Mano, J. F. Dynamic microfactories co-encapsulating osteoblastic and adipose-derived stromal cells for the biofabrication of bone units. *Biofabrication* **12**, 15005 (2019).
27. Petibois, C. & Déléris, G. Chemical mapping of tumor progression by FT-IR imaging: towards molecular histopathology. *Trends Biotechnol.* **24**, 455–462 (2006).
28. Bjørge, I. M., Kim, S. Y., Mano, J. F., Kalionis, B. & Chrzanowski, W. Extracellular vesicles, exosomes and shedding vesicles in regenerative medicine-a new paradigm for tissue repair. *Biomater. Sci.* **6**, (2018).
29. Raposo, G. & Stoorvogel, W. Extracellular vesicles: exosomes, microvesicles, and friends. *J. Cell Biol.* **200**, 373–83 (2013).
30. Hasegawa, T. Ultrastructure and biological function of matrix vesicles in bone mineralization. *Histochem. Cell Biol. 2018 1494* **149**, 289–304 (2018).
31. Kang, T. *et al.* Adipose-Derived Stem Cells Induce Angiogenesis via Microvesicle Transport of miRNA-31. *Stem Cells Transl. Med.* **5**, 440–50 (2016).

32. Davies, O. G. *et al.* Osteoblast-Derived Vesicle Protein Content Is Temporally Regulated During Osteogenesis: Implications for Regenerative Therapies. *Front. Bioeng. Biotechnol.* **0**, 92 (2019).
33. Hasegawa, T. *et al.* Ultrastructural and biochemical aspects of matrix vesicle-mediated mineralization. *Jpn. Dent. Sci. Rev.* **53**, 34–45 (2017).
34. Marote, A. *et al.* A proteomic analysis of the interactions between poly(L-lactic acid) nanofibers and SH-SY5Y neuronal-like cells. *AIMS Mol. Sci. 2016 4661* **3**, 661–682 (2016).
35. Levenberg, S. *et al.* Engineering vascularized skeletal muscle tissue. *Nat. Biotechnol. 2005 237* **23**, 879–884 (2005).
36. Jain, R. K., Au, P., Tam, J., Duda, D. G. & Fukumura, D. Engineering vascularized tissue. *Nat. Biotechnol. 2005 237* **23**, 821–823 (2005).
37. Yu, H. *et al.* Improved tissue-engineered bone regeneration by endothelial cell mediated vascularization. *Biomaterials* **30**, 508–517 (2009).
38. Y. Rotenberg, M., Emil Ruvinov, Anna Armoza & Smadar Cohen. A multi-shear perfusion bioreactor for investigating shear stress effects in endothelial cell constructs. *Lab Chip* **12**, 2696–2703 (2012).
39. Hahn, C. & Schwartz, M. A. Mechanotransduction in vascular physiology and atherogenesis. *Nat. Rev. Mol. Cell Biol.* **10**, 53 (2009).
40. Leferink, A. M. *et al.* Shape-defined solid micro-objects from poly(d,l-lactic acid) as cell-supportive counterparts in bottom-up tissue engineering. *Mater. Today Bio* **4**, 100025 (2019).
41. Kim, C.-S. *et al.* A Specific Groove Pattern Can Effectively Induce Osteoblast Differentiation. *Adv. Funct. Mater.* **27**, 1703569 (2017).
42. Bjørge, I. M., Salmeron-Sanchez, M., Correia, C. R. & Mano, J. F. Cell Behavior within Nanogrooved Sandwich Culture Systems. *Small* **16**, 2001975 (2020).
43. Kim, M. J. *et al.* BMP-2 Peptide-Functionalized Nanopatterned Substrates for Enhanced Osteogenic Differentiation of Human Mesenchymal Stem Cells. *Biomaterials* **34**, 7236–7246 (2013).
44. Grellier, M. *et al.* The effect of the co-immobilization of human osteoprogenitors and endothelial cells within alginate microspheres on mineralization in a bone defect. *Biomaterials* **30**, 3271–3278 (2009).
45. Kaigler, D. *et al.* Endothelial cell modulation of bone marrow stromal cell osteogenic potential. *FASEB J.* **19**, 665–667 (2005).
46. Fan, X., Teng, Y., Ye, Z., Zhou, Y. & Tan, W.-S. The effect of gap junction-mediated transfer of miR-200b on osteogenesis and angiogenesis in a co-culture of MSCs and HUVECs. *J. Cell Sci.* **131**, (2018).
47. Correia, C. R., Bjørge, I. M., Zeng, J., Matsusaki, M. & Mano, J. F. Liquefied Microcapsules as Dual-Microcarriers for 3D+3D Bottom-Up Tissue Engineering. *Adv. Healthc. Mater.* 1901221 (2019). doi:10.1002/adhm.201901221
48. Kim, J. *et al.* Synergistic effects of nanotopography and co-culture with endothelial cells on osteogenesis of mesenchymal stem cells. *Biomaterials* **34**, 7257–7268 (2013).
49. Horvat, R., Hovorka, A., Dekan, G., Poczewski, H. & Kerjaschki, D. Endothelial cell membranes contain podocalyxin--the major sialoprotein of visceral glomerular epithelial cells. *J. Cell Biol.* **102**, 484–491 (1986).
50. Rouwkema, J., De Boer, J. & Van Blitterswijk, C. A. Endothelial Cells Assemble into a 3-Dimensional Prevascular Network in a Bone Tissue Engineering Construct. *Tissue Eng.* **12**, 2685–2693 (2006).
51. Ku, S. H. & Park, C. B. Human endothelial cell growth on mussel-inspired nanofiber scaffold for vascular tissue engineering. *Biomaterials* **31**, 9431–9437 (2010).
52. Ding, Y. *et al.* Directing Vascular Cell Selectivity and Hemocompatibility on Patterned Platforms Featuring Variable Topographic Geometry and Size. *ACS Appl. Mater. Interfaces* **6**, 12062–12070 (2014).
53. Ding, Y. *et al.* Cooperative control of blood compatibility and re-endothelialization by

immobilized heparin and substrate topography. *Acta Biomater.* **15**, 150–163 (2015).
54. Grant, D. S. *et al.* Two Different Laminin Domains Mediate the Differentiation of Human Endothelial Cells into Capillary-like Structures In Vitro. *Cell* **58**, 933–943 (1989).
55. Nishiguchi, A., Yoshida, H., Matsusaki, M. & Akashi, M. Rapid Construction of Three-Dimensional Multilayered Tissues with Endothelial Tube Networks by the Cell-Accumulation Technique. *Adv. Mater.* **23**, 3506–3510 (2011).
56. Shen, J. *et al.* E3 Ubiquitin Ligase-Mediated Regulation of Osteoblast Differentiation and Bone Formation. *Front. Cell Dev. Biol.* **0**, 2339 (2021).
57. Ballhause, T. M. *et al.* Relevance of Notch Signaling for Bone Metabolism and Regeneration. *Int. J. Mol. Sci.* **22**, 1325 (2021).
58. Kimelman, D. & Xu, W. β-Catenin destruction complex: insights and questions from a structural perspective. *Oncogene 2006 2557* **25**, 7482–7491 (2006).
59. Marcellini, S., Henriquez, J. P. & Bertin, A. Control of osteogenesis by the canonical Wnt and BMP pathways in vivo. *BioEssays* **34**, 953–962 (2012).
60. Plaisant, M. *et al.* Activation of Hedgehog Signaling Inhibits Osteoblast Differentiation of Human Mesenchymal Stem Cells. *Stem Cells* **27**, 703–713 (2009).
61. Granchi, D. *et al.* Gene Expression Patterns Related to Osteogenic Differentiation of Bone Marrow-Derived Mesenchymal Stem Cells During Ex Vivo Expansion.
62. Augustin, H. G. & Koh, G. Y. Organotypic vasculature: From descriptive heterogeneity to functional pathophysiology. *Science.* **357**, (2017).
63. Kuo, H.-J., Maslen, C. L., Keene, D. R. & Glanville, R. W. Type VI Collagen Anchors Endothelial Basement Membranes by Interacting with Type IV Collagen. *J. Biol. Chem.* **272**, 26522–26529 (1997).
64. Au, H. T. H., Cheng, I., Chowdhury, M. F. & Radisic, M. Interactive effects of surface topography and pulsatile electrical field stimulation on orientation and elongation of fibroblasts and cardiomyocytes. *Biomaterials* **28**, 4277–4293 (2007).
65. Yang, K. *et al.* Nanotopographical Manipulation of Focal Adhesion Formation for Enhanced Differentiation of Human Neural Stem Cells. *ACS Appl. Mater. Interfaces* **5**, 10529–10540 (2013).
66. Koike, N. *et al.* Creation of long-lasting blood vessels. *Nature* **428**, 138–139 (2004).
67. Correia, C. R., Ghasemzadeh-Hasankolaei, M. & Mano, J. F. Cell encapsulation in liquified compartments: Protocol optimization and challenges. *PLoS One* **14**, e0218045 (2019).

Supplementary Information

1. Supplementary methods

1.1. Cell isolation and characterisation

1.1.1. hASC isolation from adipose tissue

Human adipose-derived stromal cells (hASCs) were isolated from subcutaneous adipose tissue derived from liposuction procedures. Collected tissues were obtained with informed patient consent and under a cooperation agreement between University of Aveiro and Hospital da Luz (Aveiro, Portugal), after approval of the Competent Ethics Committee (CEC) and were handled according to CEC guidelines. Samples were transported in phosphate buffered saline (PBS) supplemented with 1% v/v antibiotic/antimycotic (AA,

Thermo Fisher Scientific) and stored at 4ºC until isolation. Lipoaspirate samples were washed with PBS five times and incubated in a 0.1% w/v collagenase type I (MP Biomedicals) solution at 37ºC for 45 minutes. Subsequently, the solution was centrifuged at 1200 rpm for 10 minutes, the supernatant was removed, and the pellet was resuspended in PBS and centrifuged again at 1200 rpm for 10 minutes. The resulting pellet containing isolated hASCs was resuspended in Minimum Essential Alpha Medium (α-MEM, Thermo Fisher Scientific) supplemented with 10% v/v fetal bovine serum (FBS, Thermo Fisher Scientific) and 1% v/v AA, termed complete α-MEM, at 37ºC in a humidified air atmosphere of 5% CO_2.

1.1.2. HUVEC isolation from umbilical cord

Umbilical cord was obtained under a cooperation agreement between the Aveiro Institute of Materials, University of Aveiro, and Hospital do Baixo Vouga (Aveiro, Portugal), upon approval from the Competent Ethics Committee (CEC). The human tissues received were handled in accordance with the guidelines approved by the CEC and informed consent was obtained from all subjects. HUVECs were isolated following protocols well-established in the group. The enzymatic mixture containing dispase II (Sigma-Aldrich) and collagenase type IV (Sigma-Aldrich) was used for the isolation of HUVECs from the cord vein. The cord vein was filled with the enzyme cocktail and incubated at 37 °C for 20 min. Subsequently, HUVECs were flushed out and seeded in culture flasks previously coated with 0.7% w/v gelatine (porcine skin type A, Sigma-Aldrich) containing M199 growth medium at 5% CO_2 and 37 °C. 4–6 hours later, the medium was changed to M199 (Sigma-Aldrich) containing 20% v/v FBS, 1% v/v AA, 1% v/v glutamax supplement (ThermoFisher Scientific), 0.05% w/v heparin (PanReac AppliChem), and 5% w/v endothelial cell growth supplement (ECGS, Sigma-Aldrich), termed complete M199, at 37ºC in a humidified air atmosphere of 5% CO_2.

1.1.3. Flow cytometry analysis

Phenotypic profile of ASCs and HUVECs was assessed regarding mesenchymal (CD105-FITC, Arium; CD90-APC and CD73-PE, BD Biosciences), endothelial (CD31-APC, BioLegend), and hematopoietic (CD34-FITC, BioLegend) markers. Isolated cells were harvested using TrypLE™ Express solution (Life Technologies) at 37 °C for 5 min. Samples

were resuspended in PBS solution containing 3% w/v bovine serum albumin (Sigma-Aldrich) and abovementioned antibodies at dilutions defined by the manufacturer. Upon 20 min at RT, samples were washed with PBS, centrifuged, fixed in PBS with 1% v/v formaldehyde (Sigma-Aldrich) and analyzed in a flow cytometer (forward and side scatter gating, CellQuest v3.3 software, BD Accuri C6, BD Biosciences).

1.2 Topodisc production

Topodiscs were produced using a protocol previously established by the authors (Scheme 1).[1] Initially, spherical polycaprolactone microparticles (diameter range 25-40 μm; μspheres$_{25\text{-}40}$) were produced via solvent emulsion evaporation of a 5% w/v solution of polycaprolactone (PCL, M_n=80 kDa, Sigma-Aldrich) in dichloromethane (DCM, Honeywell Chemicals) under agitation (1:5) with an aqueous 0.5% w/v solution of polyvinyl alcohol (PVA, M_n=30 – 70 kDa, Sigma-Aldrich) for 48 hours. Simultaneously, poly(vinyl alcohol) (PVA) counter-moulds of nanogrooved optical media substrates (CDs) were produced by solvent evaporation of an aqueous 12% w/v PVA solution, cast on CDs at 40ºC (Figure S1A). CDs presented ridge widths of 1185 ± 16 nm, groove widths of 412 ± 12 nm, and ridge heights of 197 ± 14 nm. Next, μspheres were nanoimprinted between water-soluble PVA counter-moulds: firstly, μspheres$_{25\text{-}40}$ were pre-heated for 25 min at 75ºC on top of PVA membranes and secondly, another PVA membrane was placed on top of pre-heated μspheres$_{25\text{-}40}$ for 5 min with an applied pressure of approximately 1 kPa. Subsequently, PVA-entrapped PCL was placed in distilled water to promote PVA dissolution and posterior topodisc collection. As a control, μspheres with a diameter ranging between 50 and 80 μm were selected since the average surface area is the equivalent to that of topodiscs. Topodiscs and μspheres were treated with plasma (Plasma System ATTO, Electronic Diener) at 0.4-0.6 mbar and 30 V for 15 min using atmospheric air, followed by sterilization in ethanol for 3h.

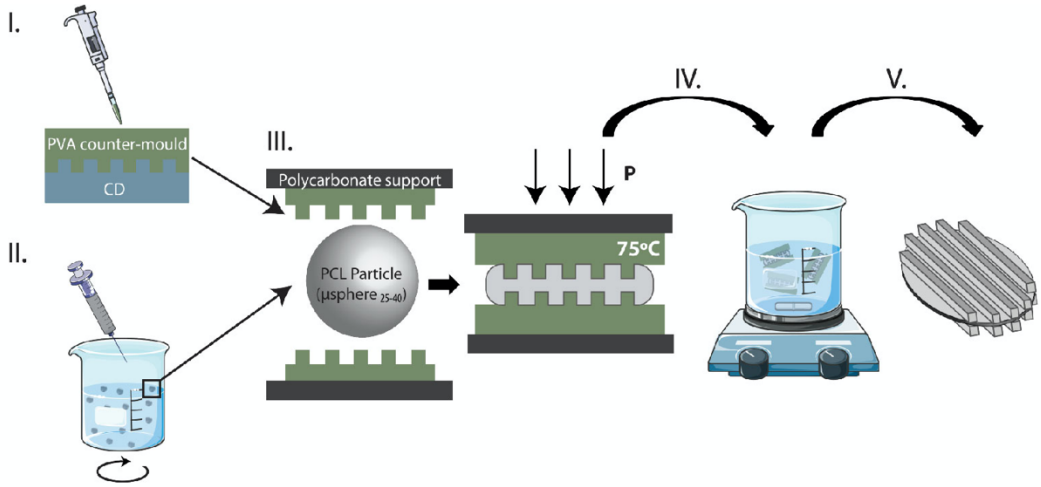

Scheme VI.1. Illustration of the production method for topodiscs. I. Production of polyvinyl alcohol (PVA) counter-moulds of CDs by solvent evaporation of a 12% w/v PVA solution at 40ºC. II. Production of PCL particles via oil/water emulsion and subsequent sieving to collect particles with diameters comprised between 25-40 μm microparticles (μspheres$_{25\text{-}40}$) by sieving. III. Micro-moulding of μspheres$_{25\text{-}40}$ between nanogrooved PVA membranes at an optimised applied force, time, and temperature. IV. Successive topodisc washings to remove all traces of PVA. V. Topodisc recovery by centrifugation.

1.3. Microaggregate production

At 90% of confluence, hASCs were detached by 0.05% w/v trypsin-EDTA (from porcine pancreas 1:250, Sigma-Aldrich) treatment for 5 min at 37ºC. Microaggregates of hASC-particles (topodiscs or μspheres) were produced using AggreWell400 24-well plates (StemCell Technologies), according to the manufacturer's recommendations. A concentration of $6x10^5$ cells and 1.5 mg particles (topodiscs or μspheres) was used per well. Upon 24h of seeding, hASC-particle (topodiscs or μspheres) microaggregates were collected. Pre-formed microaggregates produced for dynamic culturing were subjected to an additional coating with fibronectin from human plasma (5 $\mu g.cm^{-2}$, Sigma Aldrich) dissolved in Dulbecco's phosphate buffered saline (DPBS, Corning) for 1h at 37ºC, followed by washing with DPBS prior to encapsulation.

1.4. Encapsulation within liquefied-core, multilayered capsules

At 90% of confluence, HUVECs were detached by 0.05% w/v trypsin-EDTA (from porcine pancreas 1:250, Sigma-Aldrich) treatment for 5 min at 37ºC. Next, encapsulation of previously produced microaggregates of hASC-particles (topodiscs or μspheres), with (co-culture) or without (monoculture) HUVECs, was performed within multi-layered capsules with liquefiable-cores, which were previously developed by our group.[2,3] Microaggregates

of hASC-particles (topodiscs or μspheres) and HUVECs were resuspended in a 2% w/v sodium alginate (ALG, low viscosity from brown algae, Sigma-Aldrich) aqueous solution containing 0.15 M sodium chloride (NaCl, LabChem) and 25 mM MES hydrate (Alfa Aesar) at pH 6.7. A concentration of $3x10^6$ hASCs and 7.5 mg particles (topodiscs or μspheres) in microaggregates per mL of ALG were used for the monoculture, with an additional $3x10^6$ suspended HUVECs per mL of ALG for the co-culture system. The ALG solution containing hASC-particle (topodiscs or μspheres) microaggregates alone or in combination with suspended HUVECs was added dropwise using a 21G needle into an aqueous calcium chloride solution (0.1 M, Sigma-Aldrich) buffered with NaCl and MES under stirring (200 rpm) for 20 min. Alginate hydrogels were rinsed in a washing buffer (0.15 M NaCl and 25 mM MES). To build up the multi-layered membrane via layer-by-layer technology, ALG hydrogels were sequentially immersed in poly-L-lysine (PLL, Mw~30,000–70,000, pH 6.7, Sigma-Aldrich), ALG (pH 6.7), water-soluble highly purified chitosan (CHT, pH 6.3, Protasan UP CL 213, viscosity 107 mPa.s, Mw = 2.7 × 105 $g.mol^{-1}$, 83% degree of deacetylation, NovaMatrix), and ALG again. This process was repeated three times to obtain a 12-layered membrane. A concentration of 0.5 $mg.mL^{-1}$ was used for the polyelectrolytes (ALG, CHT, PLL) dissolved in an aqueous 0.15 M NaCl and 25 mM MES solution. Polyelectrolyte immersion was performed during 10 min, followed by a 2 min washing step in washing buffer. Finally, the hydrogel core was liquefied via immersion in an aqueous 5 mM ethylenediaminetetraacetic acid (EDTA, pH 6.7, Sigma-Aldrich) solution. Capsules containing only hASCs were cultured in complete α-MEM with ('OST' medium) or without ('BAS' medium) osteogenic factors [ascorbic acid (50 $μg.mL^{-1}$, Cayman Chemical), β-glycerophosphate disodium salt (10 mM, Santa Cruz Biotechnology), and dexamethasone (10 nM, ThermoFisher Scientific)]. Capsules containing hASCs and HUVECs were cultured in complete M199 with (OST) or without (BAS) the previous osteogenic factors. All solutions were sterilized by filtration through a 0.22 μm filter. For static conditions, capsules were cultured in non-treated 24-well plates. For dynamic culture, microcapsules were maintained within spinner flasks with double angled sidearms (ProCulture, Corning) set to 25 rpm. Capsules were maintained at 37ºC with 5% CO_2.

1.5. Particles' characterization

Topodiscs and μspheres particles were sputtered with gold-palladium and imaged using scanning electron microscopy (SEM, SU-70, Hitachi). ImageJ was used to measure corresponding dimensions.

1.6. Characterization of capsules' core contents

1.6.1. Lipophilic fluorescent labeling

For cell tracking studies, hASCs and HUVECs were stained prior to encapsulation with lipophilic dyes DiD (Vybrant DiD Cell Labelling Solution, ThermoFisher Scientific) and DiO (Vybrant DiO Cell-Labelling Solution, ThermoFisher Scientific), respectively, according to the manufacturer's instructions. Capsules were fixed on days 1 and 7, followed by permeabilization, nuclei counterstained with DAPI (4',6-diamidino-2-phenylindole, dihydrochloride, 1 $mg.mL^{-1}$, ThermoFisher Scientific), and assessment by confocal fluorescence microscopy (LSM 880, Zeiss).

1.6.2. Fluorescence staining of 3D structures and histological sections

Cell viability was assessed using a live/dead fluorescence assay, according to the manufacturer's recommendations (Live/Dead® Viability/Cytotoxicity Kit, ThermoFisher Scientific).

Fluorescent staining for hydroxyapatite using OsteoImage mineralization assay kit (Lonza) was performed according to the manufacturer's specifications after sample fixation with 4% w/v formaldehyde solution (Sigma Aldrich) in DPBS for 30 min at room temperature (RT), and subsequent permeabilization with 0.1% v/v Triton-X100 (BioXtra, Sigma Aldrich) in DPBS for 5 min. Samples were then counterstained with DAPI (1 $mg.mL^{-1}$) at a 1:1000 ratio in DPBS for 5 min at RT.

Histological assessment of samples upon 21 days in culture was performed after fixation, manual processing, and embedding in paraffin. Histological sections (5 μm) were cut using a microtome (HM340 E, Microm, ThermoFisher Scientific). Histological cuts were stained with Masson's Trichrome using Trichrome Stain (Masson) kit (Sigma) according to manufacturer's specifications for visualization of collagen fibers.

In preparation for immunohistochemistry, histological sections were routinely deparaffinized, subjected to antigen retrieval in 10 mM tri-sodium citrate dihydrate buffer (Pancreatic) with 0.05% v/v Tween 20 (Sigma Aldrich) at pH 6, 100ºC for 20 min, and blocked in FBS (5% v/v in DPBS) for 1h at RT.

For detection of the osteogenic marker osteopontin (OSP) and endothelial cell marker CD31, FBS-blocked histological cuts were incubated overnight at 4ºC with primary anti-osteopontin rabbit antibody (Merck Millipore, 1:100 in 5% v/v FBS) and anti-human CD31 mouse antibody (BioLegend, 1:100 in 5% v/v FBS). Samples were incubated with secondary antibodies Alexa 647 anti-rabbit (ThermoFisher Scientific, 1:500 in 5% v/v FBS) and Alexa 488 anti-mouse (ThermoFisher Scientific, 1:500 in 5% v/v FBS) for 1h at RT.

Similarly, for detection of angiogenesis marker von Willebrand Factor (vWF), FBS-blocked histological cuts were incubated with primary anti-von Willebrand Factor rabbit antibody (Abcam, 1:400 in 5% v/v FBS) overnight, followed by incubation in secondary antibody Alexa 647 anti-rabbit (ThermoFisher Scientific, 1:500 in 5% v/v FBS). Counterstaining with phalloidin (Flash Phalloidin™ Red 594, 300U, BioLegend, 1:40 ratio in DPBS for 45 min, RT), was performed to stain actin filaments.

For detection of laminin, FBS-blocked histological cuts were incubated with primary anti-laminin rabbit antibody (Abcam, 1:200 in 5% v/v FBS) overnight, followed by incubation with secondary antibody Alexa 647 anti-rabbit (1:500 in 5% v/v FBS). For detection of podocalyxin, FBS-blocked histological cuts were incubated with primary anti-podocalyxin mouse antibody (Alfagene, 1:200 in 5% v/v FBS) overnight, followed by incubation with secondary antibody Alexa 555 anti-mouse (Biolegend, 1:500 in 5% v/v FBS). All samples were counterstained with DAPI for nuclei staining. Samples were visualized by optical and fluorescence microscopy (Axio Imager 2, Zeiss).

1.6.3. Fourier transform infrared spectroscopy – attenuated total reflectance (ATR-FTIR)

Prior to Fourier transform infrared spectroscopy – attenuated total reflectance (ATR-FTIR) analysis, samples were fixed with 4% w/v formaldehyde solution, dehydrated in increasing ethanol concentrations (60-100% v/v), and incubated at 37 ºC. Spectra were acquired on a

Bruker Alpha infrared spectrometer controlled by the OPUS software package (version 7.0). Background and sample measurements were performed in the 4000 to 500 cm^{-1} range with the resolution of 4 cm^{-1} and averaging 256 scans, at RT and controlled humidity. Amide I bands were deconvoluted into individual components using symmetric Gaussian peak shapes, after a linear baseline correction. Curve fitting were applied using a non-linear least squares fitting routine (coefficient of determination $r^2 > 0.9999$). ATR-FTIR data treatment and quantitative analysis were carried out with PeakFit software.

1.6.4. Microtomography imaging

Prior to microtomography (microCT) imaging, fixed samples were stained with lead(II) acetate trihydrate ($Pb(CH_3COO)_2 \cdot 3H_2O$ solution in 2% w/v distilled water, which has been shown to enhance early mineralisation in microCT images.[4] Samples were washed for 30 min in distilled water, immersed in the staining solution for 18 hours and washed again in distilled water for 30 min. Subsequently, dehydration in ethanol was performed in 10 min intervals, starting from 40% up to 70% in steps of 10%.

For microCT imaging, samples were mounted in 70% ethanol. Scans were performed on a Skyscan 2211 system (Bruker, Kontich, Belgium), equipped with a CCD-camera 11Mpixels. The acquisition parameters were set to 60 kV, 260 µA, rotation step of 0.29º over 360º, exposure time of 0.650 ms per projection and a frame-averaging of 2. The reconstruction of the virtual slices was performed with NRecon (v. 1.7.5, Bruker, Kontich, Belgium) and a final voxel size of 0.7 µm was achieved. The 3D images were rendered using Dragonfly software (v. 2021.1 Object Research Systems (ORS) Inc, Montreal, Canada, 2021).

1.7. Matrix microvesicles isolation and proteomic analyses

For a pilot comparative analysis of the content of matrix microvesicles (MVs) released by each system, conditioned media from 4 different co-cultures (CO) in dynamic conditions (topodisc BAS, topodisc OST, µsphere BAS and µsphere OST) (n=1) were collected on days 7, 14, and 21, and stored at −80°C until MV isolation by ultra-centrifugation, as previously reported.[5–7] Conditioned medium from the 3 timepoints was pooled and pre-cleared by centrifugation: 300 x *g* at 25°C for 5 min (5424, Eppendorf) and 18,500 x *g* at 4°C for 25 min (5810R, Eppendorf). To pellet the MVs, the supernatants were ultracentrifuged (Optima

LE-80K, fixed-angle rotor 80Ti, Beckman Coulter GmbH, Krefeld, Germany) at 50,000 rpm at 4°C for 60 min. The obtained pellets were resuspended in 1% v/v protease inhibitors cocktail (P8340, Sigma-Aldrich) in DPBS. Protein content was determined in each sample by the Pierce BCA assay kit (Thermo Fisher Scientific) and, due to low protein content, all isolated pellets were used for subsequent proteomic analyses through nano Liquid Chromatography coupled to tandem Mass Spectrometry (nanoLC-MS/MS).[7]. All samples were reduced, alkylated, and enzymatically digested with 10 mM tris-(2-carboxyethyl)-phosphine (TCEP, Sigma-Aldrich), 40 mM chloroacetamide (CAA, Sigma-Aldrich) and Trypsin/Lys-C (Thermo Scientific), respectively. The resulting tryptic peptides were separated by liquid chromatography (nanoUHPLC) in an Ultimate 3000 system (Thermo Scientific) with a nanoelectrospray ionization (nanoESI) source coupled to a high-resolution accurate mass spectrometer (Q-Exactive Hybrid Quadrupole-Orbitrap, Thermo Scientific). Samples were loaded to a trapping capillary column Acclaim PepMap C18 100 Å [3 µm particle size, 300 µm internal diameter (i.d.) x 5 mm, 160454, Thermo Scientific], with a mobile phase of 2% acetonitrile (ACN) and 0.1% formic acid (FA) at 10 µL/min. Upon 3 min loading, the trap column was switched to an EASY-Spray column [PepMap RSLC C18, 2 µm particle size, 75 µm i.d. x 50 cm, ES803A, Thermo Scientific] at 250 nL/min. Samples were eluted by mixing solvent A (0.1% FA) and solvent B (80% ACN), using a linear gradient: 5 min (2.5% B to 10% B), 120 min (10% B to 30% B), 20 min (30% B to 50% B), 5 min (50% B to 99% B) and 10 min (hold 99% B). The mass spectrometer was operated in the data-dependent (dd) acquisition mode. The analysis alternated between a full scan (*m/z* 380-1580) and a subsequent high-energy collisional dissociation (HCD) MS/MS of the 10 most intense peaks from full scan [normalized collision energy (NCE) 27%]. ESI spray voltage was 1.9 kV. Global settings: use lock masses best (*m/z* 445.12003); lock mass injection Full MS; chrom. peak width (FWHM) 15s. Full scan settings were: 70k resolution (*m/z* 200); automatic gain control (AGC) target 3e6; maximum injection time 120 ms. dd settings: minimum AGC target 8e3; intensity threshold 7.3e4; charge exclusion: unassigned, 1, 8, >8; peptide match preferred; exclude isotopes on; dynamic exclusion 45s. MS2 settings were: microscans 1; 35k resolution (*m/z* 200); AGC target 2e5; maximum injection time 110 ms; isolation window 2.0 *m/z*; isolation offset 0.0 *m/z*; spectrum data type profile.

Raw data were analyzed using the Proteome Discoverer 2.4.0.305 software (Thermo Scientific) by comparison against the *Homo sapiens* proteome (74,811 entries) from the UniProt database (FASTA files obtained on 2nd March, 2020). At this stage, the *Bos taurus* proteome was also considered to identify possible contaminants from serum supplementation. Tryptic peptides were identified by the MSPepSearch and Sequest HT search engines. The ion mass tolerance was defined at 10 ppm (for precursor ions) and 0.02 Da (for fragment ions). A maximum of 2 missing cleavage sites was allowed. Modifications were defined as follows: cysteine carbamidomethylation as constant modification; methionine oxidation; protein N-terminus acetylation, methionine loss (met-loss) and met-loss + acetylation as variable modifications. Peptide confidence settings were set as high. The following settings were applied to the processing node Percolator: maximum delta Cn 0.05; decoy database search target false discovery rate (FDR) 1%; validation based on q-value. Protein levels were determined through label-free quantification (LFQ) methodologies.

Upon excluding contaminants, uncharacterized proteins and bovine aliases, proteins identified with high confidence (FDR<0.01) and a minimum of 2 unique peptides were selected for further analysis. The abundances of proteins that meet the above criteria were compared between topographic conditions (topodisc vs μsphere) in the same medium (BAS vs OST), using the Proteome Discoverer software. Through Volcano plot analysis, proteins with topodisc/μsphere abundance ratios > 2 or < 0.5 and p-value < 0.05 were assigned into groups of upregulated (UReg) or downregulated (DReg) proteins, cultured in BAS or OST.

Gene ontology (GO) enrichment analyses was further performed for the 4 UReg/Dreg datasets using the ClueGo v2.5.8 and CluePedia v1.5.8 plugins from Cytoscape v3.8.2. All GO enrichment analyses were based on experimental evidence for Biological Process and Molecular Function terms (GO databases from 1 June 2021). All presented networks were obtained with medium specificity and are visually organized according to the UReg or DReg clusters (color-coded), showing only significant GO terms (p-value < 0.05). Reactome open access database (database release v77, pathway browser v3.7) was also used for pathway analysis of the 4 UReg/Dreg datasets, and the top most significant pathways are presented (excluding pathways related to diseases).

1.8. Statistical analysis

Statistical analysis was performed using Mann-Whitney test. A p-value<0.05 was considered statistically significant.

2. Supplementary data

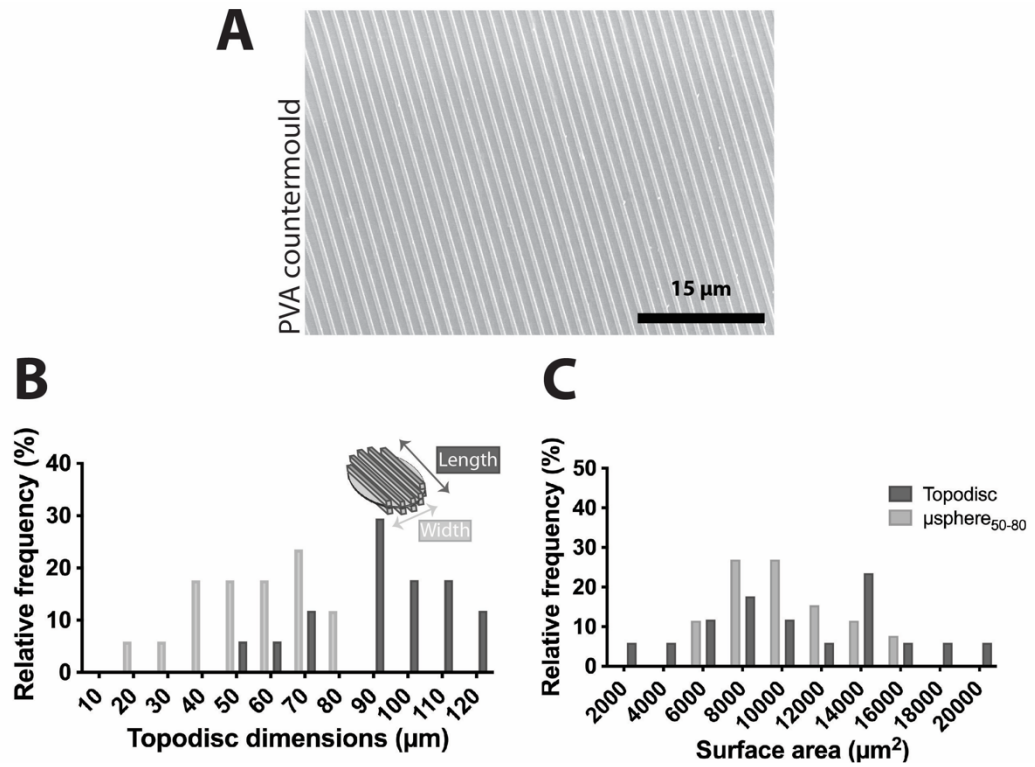

Figure VI.S1. A. SEM image of 12% w/v polyvinyl alcohol countermold of initial CD molds. B. Frequency distribution (%) of topodiscs' length (µm) and width (µm). C. Comparison of surface area for µspheres$_{50\text{-}80}$ (diameter ranging between 50-80 µm) and topodiscs.

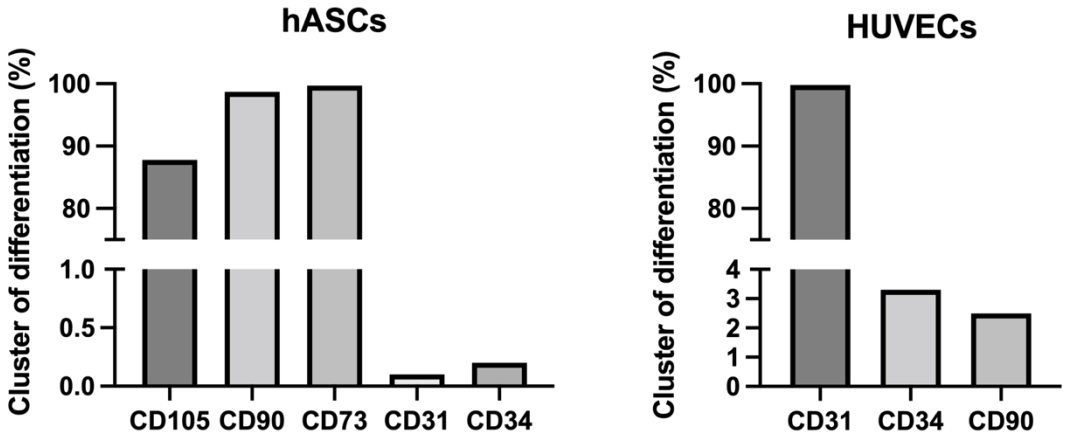

Figure VI.S2. Flow cytometry analysis of surface marker expression for isolated hASCs and HUVECs.

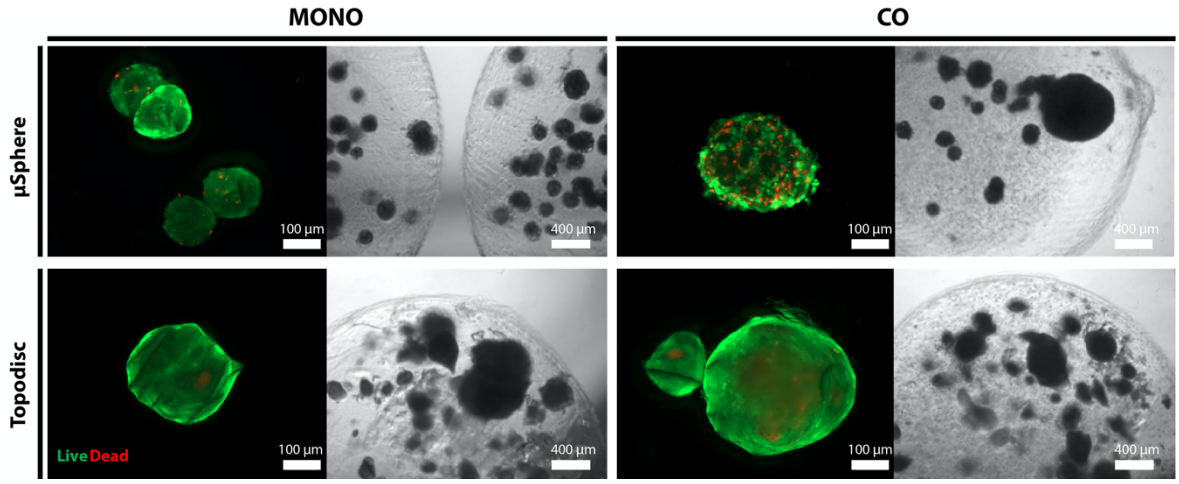

Figure VI.S3. Live/dead staining (live cells in green and dead cells in red) and corresponding brightfield images for hASC monoculture (MONO) and hASC-HUVEC co-culture (CO) with µspheres or topodiscs, on day 21 post-encapsulation under static culturing conditions. An apparent higher percentage of dead cells is visible in bigger aggregates, as expected.

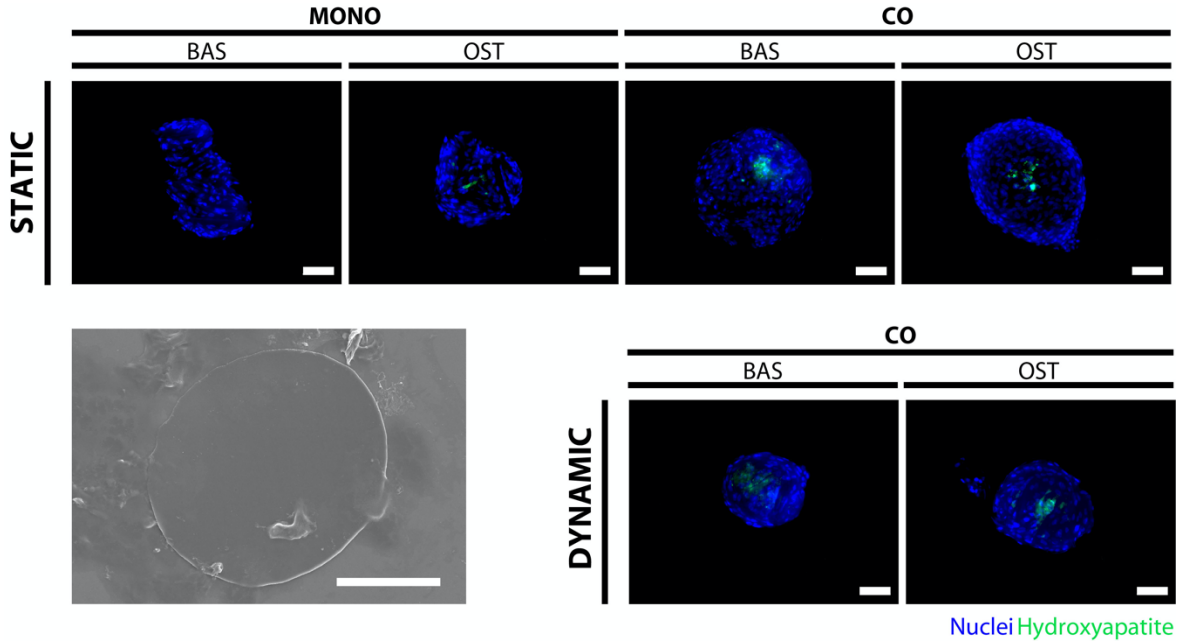

Figure VI.S4. Fluorescence images of hydroxyapatite (stained in green) and nuclei (in blue) in hASC monoculture (MONO) and hASC-HUVEC co-culture (CO) conditions, using flat microdiscs as particles, with (OST) or without (BAS) osteoinductive factors, in both static and dynamic environments. SEM image of a flat microdisc. Scale bars: 100 µm.

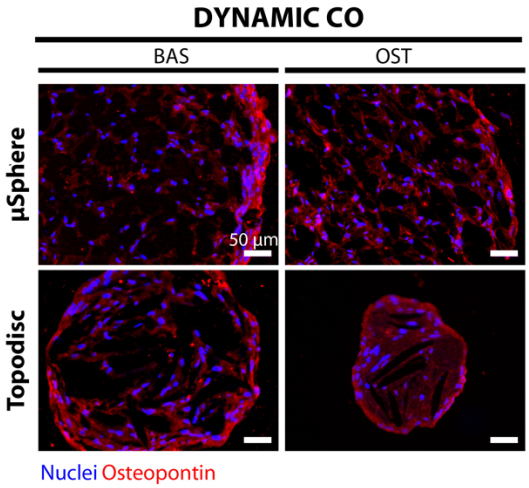

Figure VI.S5. Osteopontin expression (red) of hASC-HUVEC co-cultures (CO) with topodiscs or µspheres, cultured in medium with (OST) or without (BAS) osteoinductive factors, under dynamic conditions. Nuclei counterstained in blue.

Table VI.S1. Band positions of the different secondary structure contributions for co-culture microcapsule systems were obtained by curve fitting the corresponding IR spectra in the Amide I region.

Microcapsules	Environment	Triple helix/cm^{-1} (a)	Unordered/cm^{-1} (a)	α-helix/cm^{-1} (a)	β-turns/cm^{-1} (a)	β-sheets/cm^{-1} (a)
µSphere	Static	1632(14)	1643(17)	1653(13)	1614(10) 1661(9) 1668(6)	1623(14)
Topodisc		1633(14)	1643(15)	1653(14)	1615(13) 1662(11) 1669(9)	1624(13)
µSphere	Dynamic	1631(17)	1643(17)	1651(20)	1606(16) 1666(19)	1619(17) 1682(15) 1694(10)
Topodisc		1631(18)	1641(15)	1652(20)	1607(19) 1667(17)	1618(17) 1681(16) 1693(9)

[a] Values in brackets refer to the FWHM (full width at half maximum) of bands.

Table VI.S2. List of proteins detected in the proteomic analysis of cells-released microvesicles (MVs) that have previously been reported in proteomic studies and as mineral-binding proteins.

Function	Protein names (and gene symbols)	Ref.
Proteins reported in proteomic studies analysing osteoblast-released MVs	Lactate dehydrogenase (LDHA/LDHB) , annexins A2 and A5 (ANXA2, ANXA5), thrombospondin (THBS1), aminopeptidase N (ANPEP), integrin β3 (ITGB3), α-actinin-1 (ACTN1), vinculin (VCL), gelsolin (GSN), glyceraldehyde-3-phosphate dehydrogenase (GAPDH) , 3 members of the GTP-binding proteins family (RAN, RHOG, DIRAS2), 11 Rab proteins (RAB1A, RAB2A, RAB3A, RAB3D, RAB5B, RAB6A, RAB6C, RAB7A, RAB8A, RAB11B, RAB14) and 6 members of the 14-3-3 family (YWHAE, YWHAB, YWHAZ, YWHAH, YWHAG, YWHAQ)	[8,9]

Calcium-binding proteins	S100 proteins (S100A1, S100A7), annexins A2 andA11 (ANXA2, ANXA11), endoplasmic reticulum chaperone BiP (HSPA5), protein disulfide-isomerase A3 (PDIA3), coagulation factor X (F10), and periostin (POSTN)	[10–12]
Hydroxyapatite-binding proteins	Collagen type I α2 (COL1A2), lumican (LUM), thrombospondin-1 (THBS1), myosin-9 (MYH9), and α2-HS glycoprotein (AHSG)	[13]

Table VI.S3. Microvesicles' proteins upregulated by topography in basal medium (UReg-TopoBAS). Abundance ratio, ratio of the relative protein abundance in the topodiscs condition against the μspheres condition. Abundance ratios of 100: proteins only detected in the topodiscs condition and not in μspheres condition. Proteins were considered significantly upregulated by Volcano plot analysis: abundance ratio > 2 and p-value < 0.05.

Protein names (and gene symbols)	**Abundance ratio**	**Protein names (and gene symbols)**	**Abundance ratio**
Myoferlin (MYOF)	100	3-hydroxybutyrate dehydrogenase type 2 (BDH2)	10.732
Succinate--CoA ligase [ADP-forming] subunit beta, mitochondrial (SUCLA2)	100	Serpin B3 (SERPINB3)	8.727
Synaptic vesicle membrane protein VAT-1 homolog (VAT1)	100	Matrix Gla protein (MGP)	8.387
Microtubule-actin cross-linking factor 1, isoforms 1/2/3/5 (MACF1)	100	Isocitrate dehydrogenase [NAD] subunit alpha, mitochondrial (IDH3A)	8.239
NAD kinase 2, mitochondrial (NADK2)	39.221	Contactin-1 (CNTN1)	7.307
Xaa-Pro aminopeptidase 1 (XPNPEP1)	24.947	COP9 signalosome complex subunit 4 (COPS4)	7.252
Insulin-degrading enzyme (IDE)	24.145	Spondin-2 (SPON2)	6.098
Titin (TTN)	23.357	GTP-binding protein Di-Ras2 (DIRAS2)	5.515
C-type mannose receptor 2 (MRC2)	20.959	COP9 signalosome complex subunit 5 (COPS5)	5.29
Protein NDRG2 (NDRG2)	20.343	Elongation factor Tu, mitochondrial (TUFM)	5.25
Utrophin (UTRN)	15.682	Ras-related protein Rab-6C (RAB6C)	5.237
Thioredoxin-like protein 1 TXNL1)	5.074	Bifunctional glutamate/proline--tRNA ligase (EPRS1)	3.828
28S ribosomal protein S34, mitochondrial (MRPS34)	4.788	Heterogeneous nuclear ribonucleoproteins A2/B1 (HNRNPA2B1)	3.824
Glucose-6-phosphate 1-dehydrogenase (G6PD)	4.691	GDP-mannose 4,6 dehydratase (GMDS)	3.668
Fumarate hydratase, mitochondrial (FH)	4.474	Integrin beta-1 (ITGB1)	3.335
ATP-citrate synthase (ACLY)	4.36	GMP synthase [glutamine-hydrolyzing] (GMPS)	3.157

Lactotransferrin (LTF)	4.273	26S proteasome regulatory subunit 7 (PSMC2)	2.814
Beta-2-glycoprotein 1 (APOH)	4.273	Phosphoribosylformylglycinamidine synthase (PFAS)	2.676
26S proteasome non-ATPase regulatory subunit 11 (PSMD11)	4.18	Endoplasmic reticulum chaperone BiP (HSPA5)	2.487
Sodium/potassium-transporting ATPase subunit alpha-3 (ATP1A3)	4.068	Pyruvate dehydrogenase E1 component subunit alpha, somatic form, mitochondrial (PDHA1)	2.447
ATP synthase subunit alpha, mitochondrial (ATP5F1A)	4.058	Proteasome subunit alpha type-1 (PSMA1)	2.285
Retinal dehydrogenase 1 (ALDH1A1)	4.035	T-complex protein 1 subunit zeta (CCT6A)	2.154

Table VI.S4. Microvesicles' proteins downregulated by topography in basal medium (DReg-TopoBAS). Abundance ratio, ratio of the relative protein abundance in the topodiscs condition against the µspheres condition. Abundance ratios of 0.01: proteins only detected in µspheres condition and not in topodiscs condition. Proteins were considered significantly downregulated by Volcano plot analysis: abundance ratio < 0.05 and p-value < 0.05.

Protein names (and gene symbols)	**Abundance ratio**	**Protein names (and gene symbols)**	**Abundance ratio**
Destrin (DSTN)	0.088	GTPase KRas (KRAS)	0.01
Tubulin beta-1 chain (TUBB1)	0.077	Sialic acid synthase (NANS)	0.01
40S ribosomal protein S3 (RPS3)	0.077	Zymogen granule protein 16 homolog B (ZG16B)	0.01
Protein S100-A1 (S100A1)	0.071	Serine/threonine-protein phosphatase 2B catalytic subunit alpha isoform (PPP3CA)	0.01
Rab GDP dissociation inhibitor alpha (GDI1)	0.05	Endophilin-B1 (SH3GLB1)	0.01
Corneodesmosin (CDSN)	0.046	Olfactomedin-like protein 3 (OLFML3)	0.01
Protein S100-A9 (S100A9)	0.039	AMP deaminase 2 (AMPD2)	0.01
Ketimine reductase mu-crystallin (CRYM)	0.037	Dynamin-1-like protein (DNM1L)	0.01
Calpain small subunit 1 (CAPNS1)	0.01	Proteasome subunit alpha type-2 (PSMA2)	0.01
Glutamine synthetase (GLUL)	0.01	CAD protein (CAD)	0.01
Methanethiol oxidase (SELENBP1)	0.01	NEDD8-conjugating enzyme Ubc12 (UBE2M)	0.01
Annexin A6 (ANXA6) PE=1 SV=3	0.01	Ras-related protein Rab-3A (RAB3A)	0.01
26S proteasome non-ATPase regulatory subunit 8 (PSMD8)	0.01	Transforming growth factor beta-1-induced transcript 1 protein (TGFB1I1)	0.01

Nucleoside diphosphate kinase A (NME1)	0.01	Actin-related protein 2/3 complex subunit 5-like protein (ARPC5L)	0.01
Proteasome subunit beta type-5 (PSMB5)	0.01	Guanine nucleotide-binding protein G(i) subunit alpha-2 (GNAI2)	0.01
Nucleosome assembly protein 1-like 1 (NAP1L1)	0.01	Guanine nucleotide-binding protein G(o) subunit alpha (GNAO1)	0.01
Receptor of-activated protein C kinase 1 (RACK1)	0.01	COP9 signalosome complex subunit 1 (GPS1)	0.01
60S ribosomal protein L9 (RPL9)	0.01	Lactoylglutathione lyase (GLO1)	0.01
Hydroxyacylglutathione hydrolase, mitochondrial (HAGH)	0.01	60S ribosomal protein L28 (RPL28)	0.01
COP9 signalosome complex subunit 6 (COPS6)	0.01	Proteasome subunit beta type-1 (PSMB1)	0.01
Isovaleryl-CoA dehydrogenase isoform 1 (IVD)	0.01	26S proteasome regulatory subunit 8 (PSMC5)	0.01
60S ribosomal protein L18 (RPL18)	0.01	Cell division control protein 42 homolog (CDC42)	0.01
Ras-related protein Rab-8A (RAB8A)	0.01	Plakophilin-1 (PKP1)	0.01
60S ribosomal protein L4 (RPL4)	0.01	Protein MEMO1 (MEMO1)	0.01
V-type proton ATPase subunit H (ATP6V1H)	0.01	Protein S100-A14 (S100A14)	0.01
40S ribosomal protein S18 (RPS18)	0.01	40S ribosomal protein S2 (RPS2)	0.01
Lymphocyte cytosolic protein 2 (LCP2)	0.01	60S ribosomal protein L7a (RPL7A)	0.01
Geranylgeranyl transferase type-2 subunit alpha (RABGGTA)	0.01	Septin-2 (SEPTIN2)	0.01
AP complex subunit beta (AP2B1)	0.01	Lysozyme C (LYZ)	0.01
Procollagen C-endopeptidase enhancer 1 (PCOLCE)	0.01	Eukaryotic translation initiation factor 5A-1 (EIF5A)	0.01
Ribonucleoside-diphosphate reductase large subunit (RRM1)	0.01	Carbonyl reductase [NADPH] 1 (CBR1)	0.01
Serine/threonine-protein phosphatase 2A 55 kDa regulatory subunit B delta isoform (PPP2R2D)	0.01	Dynamin-2 (DNM2)	0.01
Multifunctional protein ADE2 (PAICS)	0.01	Ubiquitin carboxyl-terminal hydrolase isozyme L3 (UCHL3)	0.01
Exportin-2 (CSE1L)	0.01	Glutamine--fructose-6-phosphate aminotransferase [isomerizing] 1 (GFPT1)	0.01
Protein enabled homolog (ENAH)	0.01	Clusterin (CLU)	0.01

RAS guanyl-releasing protein 2 (RASGRP2)	0.01	Cytosolic non-specific dipeptidase (CNDP2)	0.01
F-actin-capping protein subunit beta (CAPZB)	0.01	Stress-70 protein, mitochondrial (HSPA9)	0.01
Alpha-actinin-1 (ACTN1)	0.01	Bisphosphoglycerate mutase (BPGM)	0.01
COP9 signalosome complex subunit 7a (COPS7A)	0.01	Calpain-1 catalytic subunit (CAPN1)	0.01
Mitogen-activated protein kinase 1 (MAPK1)	0.01	Proteasome subunit alpha type-7 (PSMA7)	0.01
N(G),N(G)-dimethylarginine dimethylaminohydrolase 1 (DDAH1)	0.01	Glycine--tRNA ligase (GARS1)	0.01
Sorting nexin-2 (SNX2)	0.01	Proline-rich protein 27 (PRR27)	0.01

Table VI.S5. Microvesicles' proteins upregulated by topography in osteogenic medium (UReg-TopoOST). Abundance ratio, ratio of the relative protein abundance in the topodiscs condition against the µspheres condition. Abundance ratios of 100: proteins only detected in topodiscs condition and not in µspheres condition. Proteins were considered significantly upregulated by Volcano plot analysis: abundance ratio > 2 and p-value < 0.05.

Protein names (and gene symbols)	**Abundance ratio**	**Protein names (and gene symbols)**	**Abundance ratio**
Ubiquitin carboxyl-terminal hydrolase 5 (USP5)	100	CAD protein (CAD)	100
Calpain small subunit 1 (CAPNS1)	100	Chromogranin-A (CHGA)	100
Elongation factor 1-alpha 2 (EEF1A2)	100	60S ribosomal protein L28 (RPL28)	100
Glutamine synthetase OS=Homo sapiens OX=9606 GN=GLUL PE=1 SV=1	100	Proteasome subunit beta type-1 (PSMB1)	100
26S proteasome non-ATPase regulatory subunit 8 (PSMD8)	100	Nuclear protein localization protein 4 homolog (NPLOC4)	100
Protein-glutamine gamma-glutamyltransferase E (TGM3)	100	26S proteasome regulatory subunit 8 (PSMC5)	100
26S proteasome regulatory subunit 6A (PSMC3)	100	Tripeptidyl-peptidase 2 (TPP2)	100
GTPase KRas (KRAS)	100	60S ribosomal protein L4 (RPL4)	100
Rho GDP-dissociation inhibitor 1 (ARHGDIA)	100	Lymphocyte cytosolic protein 2 (LCP2)	100
Synaptic vesicle membrane protein VAT-1 homolog (VAT1)	100	Geranylgeranyl transferase type-2 subunit alpha (RABGGTA)	100
Destrin (DSTN)	100	Glutamate--cysteine ligase catalytic subunit (GCLC)	100
Cullin-2 (CUL2)	100	AP complex subunit beta (AP2B1)	100

Dipeptidyl peptidase 3 (DPP3)	100	Serine/threonine-protein phosphatase 2A 55 kDa regulatory subunit B delta isoform (PPP2R2D)	100
Ribose-phosphate pyrophosphokinase 1 (PRPS1)	100	Protein enabled homolog (ENAH)	100
cAMP-dependent protein kinase catalytic subunit beta (PRKACB)	100	Sorting nexin-2 (SNX2)	100
Dynamin-1-like protein (DNM1L)	100	Acetyl-CoA acetyltransferase, cytosolic (ACAT2)	100
Proteasome subunit alpha type-2 (PSMA2)	100	Glutaminase kidney isoform, mitochondrial (GLS)	100
C1QTNF3-AMACR readthrough (NMD candidate) (C1QTNF3-AMACR)	100	Coagulation factor XIII A chain (F13A1)	13.571
ATP-dependent 6-phosphofructokinase (PFKL)	100	Creatine kinase B-type (CKB)	12.834
Filamin-B (FLNB)	100	Ubiquitin thioesterase (OTUB1)	12.618
Actin-related protein 3B (ACTR3B)	100	Secernin-1 (SCRN1)	11.518
Apolipoprotein A-IV (APOA4)	100	Hypoxanthine-guanine phosphoribosyltransferase (HPRT1)	11.355
Pyruvate dehydrogenase E1 component subunit beta, mitochondrial (PDHB)	100	Fascin (FSCN1)	11.059
Glutamine--fructose-6-phosphate aminotransferase [isomerizing] 1 (GFPT1)	100	Platelet-activating factor acetylhydrolase IB subunit alpha (PAFAH1B1)	10.384
Pyridoxal phosphate phosphatase (PDXP)	100	Cullin-associated NEDD8-dissociated protein 1 (CAND1)	10.197
Stress-70 protein, mitochondrial (HSPA9)	100	Echinoderm microtubule-associated protein-like 2 (EML2)	9.949
Sorting nexin-5 (SNX5)	100	Dihydropyrimidinase-related protein 3 (DPYSL3)	9.823
E3 ubiquitin-protein ligase UBR4 (UBR4)	100	Collectin-10 (COLEC10)	9.421
Proline-rich protein 27 (PRR27)	100	GTP-binding nuclear protein Ran (RAN)	9.255
Protein/nucleic acid deglycase DJ-1 (PARK7)	100	Isocitrate dehydrogenase [NADP], mitochondrial (IDH2)	9.058
Inorganic pyrophosphatase (PPA1)	18.91	Dual specificity mitogen-activated protein kinase kinase 1 (MAP2K1)	8.811
6-phosphogluconolactonase (PGLS)	18.727	Aspartate aminotransferase, mitochondrial (GOT2)	7.91
Glucose 1,6-bisphosphate synthase (PGM2L1)	15.703	Succinate--CoA ligase [ADP-forming] subunit beta, mitochondrial (SUCLA2)	13.962

Table VI.S6. Microvesicles' proteins downregulated by topography in osteogenic medium (DReg-TopoOST). Abundance ratio, ratio of the relative protein abundance in the topodiscs condition against the µspheres condition. Abundance ratios of 0.01: proteins only detected in µspheres condition and not in topodiscs condition. Proteins were considered significantly downregulated by Volcano plot analysis: abundance ratio < 0.05 and p-value < 0.05.

Protein names (and gene symbols)	Abundance ratio	Protein names (and gene symbols)	Abundance ratio
COP9 signalosome complex subunit 2 (COPS2)	0.474	Fermitin family homolog 2 (FERMT2)	0.419
Retinal dehydrogenase 1 (ALDH1A1)	0.474	Proteasome subunit alpha type-1 (PSMA1)	0.402
Glucose-6-phosphate 1-dehydrogenase (G6PD)	0.462	26S proteasome non-ATPase regulatory subunit 3 (PSMD3)	0.376
Utrophin (UTRN)	0.458	Contactin-1 (CNTN1)	0.367
Caspase-14 (CASP14)	0.455	Phosphoribosylformylglycinamidine synthase (PFAS)	0.365
Procollagen C-endopeptidase enhancer 1 (PCOLCE)	0.454	GDP-mannose 4,6 dehydratase (GMDS)	0.359
Elongation factor Tu, mitochondrial (TUFM)	0.452	Collagen alpha-1(I) chain (COL1A1)	0.352
Caldesmon (CALD1)	0.44	N(G),N(G)-dimethylarginine dimethylaminohydrolase 1 (DDAH1)	0.349
ATP synthase subunit alpha, mitochondrial (ATP5F1A)	0.427	Integrin beta-1 (ITGB1)	0.336
Tissue alpha-L-fucosidase (FUCA1)	0.308	Pyruvate dehydrogenase E1 component subunit alpha, somatic form, mitochondrial (PDHA1)	0.153
Titin OS=Homo sapiens OX=9606 GN=TTN PE=1 SV=4	0.281	Transitional endoplasmic reticulum ATPase (VCP)	0.146
40S ribosomal protein S26 (RPS26)	0.277	3-hydroxybutyrate dehydrogenase type 2 (BDH2)	0.113
FH1/FH2 domain-containing protein 1 (FHOD1)	0.277	Propionyl-CoA carboxylase beta chain, mitochondrial (PCCB)	0.093
28S ribosomal protein S34, mitochondrial (MRPS34)	0.261	Heterogeneous nuclear ribonucleoproteins A2/B1 (HNRNPA2B1)	0.085
Insulin-degrading enzyme (IDE)	0.252	NAD kinase 2, mitochondrial (NADK2)	0.084
Serpin B3 (SERPINB3)	0.234	Alpha-actinin-1 (ACTN1)	0.016
V-type proton ATPase subunit E 1 (ATP6V1E1)	0.206	Microtubule-actin cross-linking factor 1, isoforms 1/2/3/5 (MACF1)	0.01
COP9 signalosome complex subunit 5 (COPS5)	0.17	Ribonucleoside-diphosphate reductase large subunit (RRM1)	0.01

References

1. Bjørge, I. M., Choi, I. S., Correia, C. R. & Mano, J. F. Nanogrooved microdiscs for bottom-up modulation of osteogenic differentiation. *Nanoscale* **11**, 16214–16221 (2019).
2. Correia, C. R., Ghasemzadeh-Hasankolaei, M. & Mano, J. F. Cell encapsulation in liquified compartments: Protocol optimization and challenges. *PLoS One* **14**, e0218045 (2019).
3. Correia, C. R., Reis, R. L. & Mano, J. F. Multilayered hierarchical capsules providing cell adhesion sites. *Biomacromolecules* **14**, 743–751 (2013).
4. Metscher, B. A simple nuclear contrast staining method for microCT-based 3D histology using lead(II) acetate. *J. Anat.* **238**, 1036–1041 (2021).
5. Schmidt, J. R. *et al.* Osteoblast-released Matrix Vesicles, Regulation of Activity and Composition by Sulfated and Non-sulfated Glycosaminoglycans. *Mol. Cell. Proteomics* **15**, 558 (2016).
6. Xiao, Z. *et al.* Analysis of the extracellular matrix vesicle proteome in mineralizing osteoblasts. *J. Cell. Physiol.* **210**, 325–335 (2007).
7. de Sousa, B. M. *et al.* Capacitive interdigitated system of high osteoinductive/conductive performance for personalized acting-sensing implants. *npj Regen. Med. 2021 61* **6**, 1–14 (2021).
8. Davies, O. G. *et al.* Osteoblast-Derived Vesicle Protein Content Is Temporally Regulated During Osteogenesis: Implications for Regenerative Therapies. *Front. Bioeng. Biotechnol.* **0**, 92 (2019).
9. Hasegawa, T. *et al.* Ultrastructural and biochemical aspects of matrix vesicle-mediated mineralization. *Jpn. Dent. Sci. Rev.* **53**, 34–45 (2017).
10. Santamaria-Kisiel, L., Rintala-Dempsey, A. C. & Shaw, G. S. Calcium-dependent and -independent interactions of the S100 protein family. *Biochem. J.* **396**, 201 (2006).
11. Coe, H. & Michalak, M. Calcium binding chaperones of the endoplasmic reticulum. *Gen. Physiol. Biophys* **28**, 96–103 (2009).
12. Coutu, D. L. *et al.* Periostin, a Member of a Novel Family of Vitamin K-dependent Proteins, Is Expressed by Mesenchymal Stromal Cells. *J. Biol. Chem.* **283**, 17991–18001 (2008).
13. HY, Z. Proteomic analysis of hydroxyapatite interaction proteins in bone. *Ann. N. Y. Acad. Sci.* **1116**, 323–326 (2007).

4
Conclusion

Chapter VII

Conclusions and future perspectives

Chapter VII: Conclusions and future perspectives

1. General conclusion

While the impact of biophysical cues has been studied in a 2D context, the translation of these cues into a 3D context, holding more resemblance to the native cell environment, is lacking. Throughout this thesis, the role of biophysical cues, specifically geometry and topography, are described, and the advantageous application of such cues is illustrated for strategies in the Tissue Engineering and Regenerative Medicine (TERM) field.

In **Chapter III**, geometry took centre stage as we investigated how an increase in surface area and varying particle shape could impact drug release and cell viability. By resorting to superamphiphobic surfaces and a "sandwich" method, spheroidal hydrogel particles with adjustable circularity were produced. Likely due to their higher surface area to volume-ratio, comparatively to spherical-shaped ones, spheroids presented an improved viability of encapsulated cells, due to an enhanced nutrient diffusion to the core, and led to a significantly faster drug release rate from the polymer network. The proposed technology could expand the use of superhydrophobic and superamphiphobic platforms, which have been employed to process spherical particles, towards the production of spheroid-like objects. Spheroidal particles with tailored geometry may hence be broadly applied in the biomedical field, including for drug delivery or as cell encapsulation platforms.

In **Chapters IV** to **VI**, we focused on the role of topography in controlling cell behaviour in quasi-3D environments, firstly applying the sandwich culture model and secondly, with microcarriers through a bottom-up tissue engineering strategy. In **Chapter IV**, sandwich-culture conditions featuring grooved surface topography were developed to bridge the gap between two-dimensional and three-dimensional culture, enabling both ventral and dorsal cell surface stimulation. The effect of nanogrooves on dorsal and ventral cell receptors under highly controlled orientation conditions was assessed and the significant impact of initial contact on cell morphology and orientation was pinpointed. This is noteworthy for tissue engineering strategies focusing on surface engineering, specifically surface topography, as it brings new light into the role of the initial contact on cell behaviour and bioperformance of the substrate. This study set the basis for the following chapters, where nanogrooves were introduced on the surface of microdiscs, termed "topodiscs", for a bottom-up, cell-mediated

aggregation to form 3D bone-like constructs. With this approach, we aimed to recapitulate the well-documented pro-osteogenic effects of 2D grooved topography in a 3D environment. To this end, **Chapter V** focused on the development and characterisation of topodiscs, as well as the assessment of cell response to these tailored microdiscs. In fact, topodiscs effectively led to the osteogenic differentiation of hASCs, even in the absence of osteoinductive factors. With tissue engineering strategies striving to reduce the complexity of systems and minimise the need for additional factors, the osteogenic potential of topodiscs was shown to be dependent on the grooved topographical surface cues, bypassing the need for osteogenic supplements. Thus, in **Chapter VI**, we aimed to further explore the potential of topodiscs and develop a highly controlled strategy to engineer bone-like microtissues from the nano to macro level. This approach relied on the nanogrooves of topodiscs, microaggregates composed of cells and topodiscs, and liquefied core macrocapsules for compartmentalisation. Combined with dynamic culturing, the liquefied environment allowed for the interaction of endothelial cells and hASCs to enable an appropriate construct pre-vascularisation. With this strategy, we intended to find the right balance between guiding and confining cell self-organisation. Although the focus was the effect of topodiscs for osteogenic differentiation, we envision that the application of these 3D nanogrooved substrates could be broadened to other topography-responsive cells. This technology could thus potentially be used in neuronal, myogenic, or cardiac tissue engineering strategies.

2. Future perspectives for biophysical cues[6]

In the native environment, cell behaviour is constantly modelled by biochemical and biophysical cues, and are hence relevant key criteria that should be integrated during the design of biomaterials.[1–3] These cues arise from the extracellular matrix, neighbouring cells, soluble factors, and physical forces. Biochemical cues are potent regulators of cell function and are in fact the most studied and generally applied in tissue engineering. For example, ascorbic acid and β-glycerophosphate are almost ubiquitously applied in bone tissue engineering strategies. Yet problematic local delivery and dosage-related issues may arise from the use of biochemical signals. Although less explored, biophysical cues have similarly been shown to enable control over cell fate. Biophysical cues such as stiffness, viscoelasticity, topography, and geometry, are converted intracellularly into biochemical signals via mechanotransduction pathways. While a promising strategy, several hurdles still exist to bring biophysical cues universally closer to the clinical reality. Aside from the usage of micro-roughened implant surface topography for an improved osseointegration, alternative applications are scarce.

To date, several major challenges have been addressed, such as the mitigation of host responses through immunomodulation, and improved vascularization strategies. In fact, one of the major problems hampering the clinical outcome of TE strategies is the absence of a functional vascular supply or its delayed establishment.[6] As a consequence of being deprived from the exchange of essential molecules, including the inflow of nutrients and oxygen, as well as the release of waste metabolites, cell death occurs. Additionally, cell-cell interactions may be blocked, hampering the exchange of important cell signalling molecules indispensable in the orchestration of cellular crosstalk events towards tissue healing.[7] Such blockages can result from the presence of a physical barrier imposed by an excessive *in situ* volume of engineered material implanted into the defect site, and/or due to an excessive amount of ECM, when considering strategies that rely on a pre-seeding approach. Physical barriers block the ingrowth of host vessels and prevent the establishment of vascular supply. These physical constraints surpass the pro-angiogenic strategies often imprinted into the biomaterial, thus explaining the major discrepancy between scientific research efforts and

[6] Partially based on the publication: C.R. Correia, I.M. Bjørge, S. Nadine, J.F. Mano. Minimalist tissue engineering approaches using low material-based bioengineered systems, **Advanced Healthcare Materials**, 10 (2021) e2002110.

the clinical applications of such strategies. Concerns related to "over-engineering" approaches and their effect in hampering the innate cell self-organization have also been recently pointed out by others.[8,9]

This paves the way for "minimalist-engineering" approaches, which rely on minimising of the amount of implanted biomaterials, as opposed to an excessive *in situ* overloading that ultimately leads to the failure of the TE strategy. Such "developmental" strategies rely on an engineering-based narrative, where an integrative cell-material approach paves the way for cells to self-organize, while underlining the importance of the ECM and cell-cell contacts towards tissue reconstruction. The influence biomaterials exert on cell behaviour is highly dependent on surface and localised mechanical, topographical, and geometrical properties. This is in line with platforms or devices with low material content, where such cues guide cell migration, function, and organization. On the other hand, properties such as porosity, degradation, mechanical performance, namely viscoelasticity and stiffness, and the release of absorbed biomolecules are highly dependent on the bulk properties of the scaffold. As schematically represented in Figure VII.1, a higher number of surface properties, and thus with low dependence on the amount of material of the scaffold, can be pointed out compared to bulk properties. This reinforces the concept of "minimalist-engineering" approaches, that have resulted in a multitude of low-material based bioengineered systems. The main idea is to fine-tune the spatial balance occupied by the inanimate region of the regenerative niche towards maximum actuation of the key living components within the healing process.

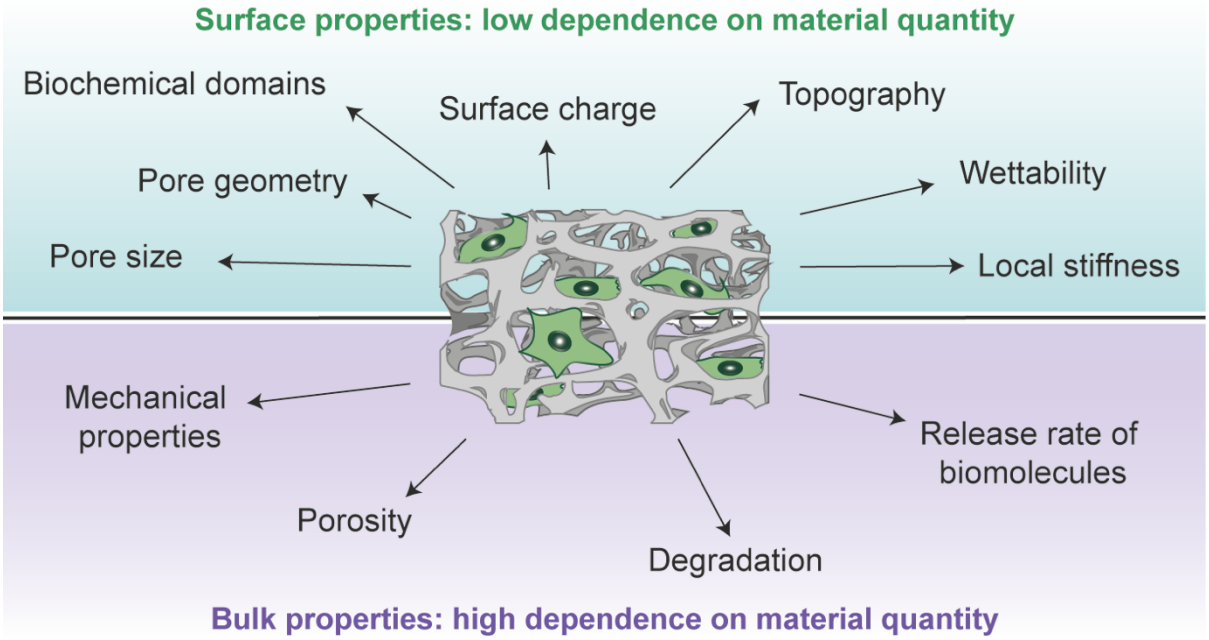

Figure VII.1. Surface versus bulk properties of biomaterials for tissue regeneration. Surface properties, such as pore size and geometry, exposure of biochemical domains to guide the cellular behaviour (e.g., signalling biomolecules, growth factors, drugs, and reprogramming factors), topography (e.g., random or aligned patterns, roughness), surface chemistry, including charge and wettability, and local stiffness, have low dependence on the quantity/volume of material used to produce the bioengineered scaffold. On the contrary, bulk properties, such as mechanical performance, porosity, degradation, and the release rate of absorbed biomolecules, are highly dependent on the quantity/volume of material [Reprinted with permission from [4], Copyright (2021) John Wiley and Sons].

Concerns related to "over-engineering" approaches and their effect in hampering the innate self-organization of cells have inspired the development of low-material based bioengineering systems, such as the ones addressed in this thesis. According to their complexity and architectural features, these strategies can be divided in a range of dimensions from "zero-dimensional" (0D) to "three-dimensional" (3D) approaches (Figure VII.2). We consider such low-materials strategies to be a promising route for the development of functional tissues. Of note, we are aware of the great challenge in defining such minimal amount, and thus low-material based approaches should be carefully analysed and take into consideration tissue- and biomaterial-specific factors, ranging from the physicochemical characteristics of the damaged tissue, mechanical loading, resident cell characteristics, namely proliferation ratio and density, biodegradation, as well as the extent of the lesion. Upon implantation, "minimalist material engineering" approaches are aimed to work *in tandem* with recruited cells, including endogenous progenitor or stromal/stem and immune cells. For that, low-material based bioengineered systems can express surface biochemical cues to facilitate or suppress cellular reprogramming towards a specific

differentiation route, and thus, match the type of tissue to be regenerated. Although a wide range of epigenetic drugs are currently used in the clinics for the treatment of different cancers, their use for tissue regeneration is still limited. Simultaneously, immunomodulatory cues may aid to orchestrate the kinetics of the recruited immune cells towards tissue remodelling and healing. Alternatively, microcarriers such as the ones proposed in this thesis could be adapted to introduce alternative topographical cues such as pits, pillars, or curvature. Likewise, alternate tissues containing topography-responsive cells could be targeted to engineer or regenerate. Furthermore, the combination of distinct biophysical cues, e.g., stiffness and topography, could be exploited to deliver a synergistic effect. Ultimately, the combination of minimal guiding and harnessing cell self-organisation may be the driving force to develop functional histoarchitectures *in vitro*, with regenerative potential *in vivo*.

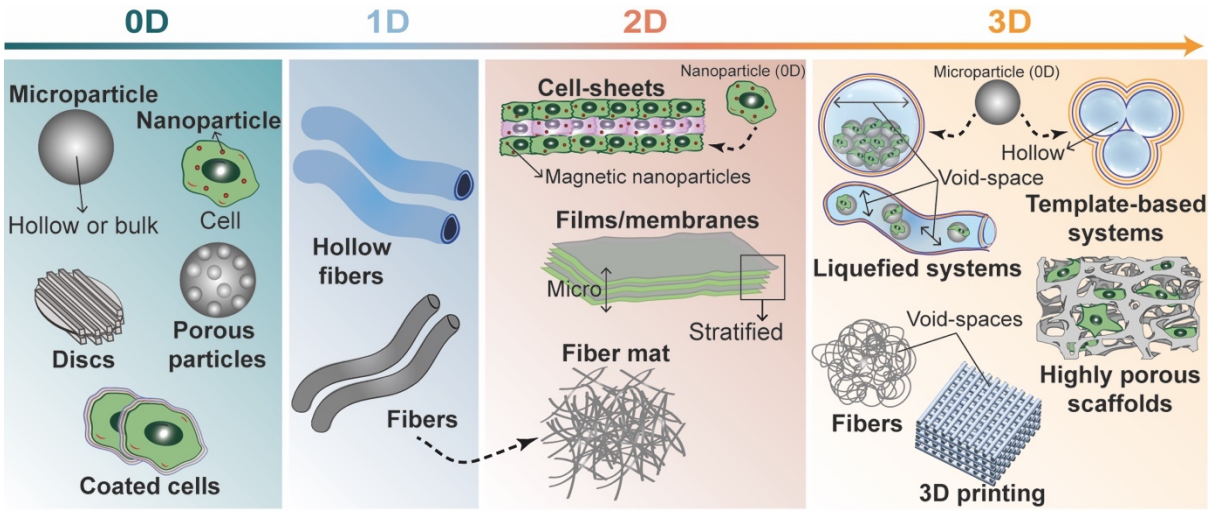

Figure VII.2. Approaches to engineer low-material based bioengineering systems according to their dimension ranging from "zero-dimensional" (0D) to "three-dimensional" (3D). Dotted lines connect each building block to the correspondent higher hierarchical order structure, namely *(i)* microparticles (0D) can be incorporated within liquefied systems to provide cell adhesion cells or used to produce template-based systems (3D), *(ii)* cells containing nanoparticles (0D) can be used to produce magnetic cell sheets (2D), and *(iii)* fibres (1D) can be assembled to produce fibre mats (2D) [Reprinted with permission from [4], Copyright (2021) John Wiley and Sons].

References

1. Khademhosseini, A. & Langer, R. A decade of progress in tissue engineering. *Nat. Protoc.* **11**, 1775–1781 (2016).
2. Gaharwar, A. K., Singh, I. & Khademhosseini, A. Engineered biomaterials for in situ tissue regeneration. *Nat. Rev. Mater.* **5**, 686–705 (2020).
3. Correia, C. R., Nadine, S. & Mano, J. F. Cell Encapsulation Systems Toward Modular Tissue Regeneration: From Immunoisolation to Multifunctional Devices. *Adv. Funct. Mater.* **30**, 1–

23 (2020).
4. Correia, C. R., Bjørge, I. M., Nadine, S. & Mano, J. F. Minimalist Tissue Engineering Approaches Using Low Material-Based Bioengineered Systems. *Adv. Healthc. Mater.* **2002110**, 1–18 (2021).
5. Engler, A. J., Sen, S., Sweeney, H. L. & Discher, D. E. Matrix Elasticity Directs Stem Cell Lineage Specification. *Cell* **126**, 677–689 (2006).
6. Nguyen, L. H. *et al.* Vascularized bone tissue engineering: Approaches for potential improvement. *Tissue Eng. - Part B Rev.* **18**, 363–382 (2012).
7. Takeo, M. & Tsuji, T. Organ regeneration based on developmental biology: past and future. *Current Opinion in Genetics and Development* **52**, 42–47 (2018).
8. Sthijns, M. M. J. P. E., Lapointe, V. L. S. & Van Blitterswijk, C. A. Building Complex Life through Self-Organization. *Tissue Eng. - Part A* **25**, 1341–1346 (2019).
9. Takebe, T. & Wells, J. M. Organoids by design. *Science* **364**, 956–959 (2019).